



UNIVERSITY OF GENOA  
PHYSICS DEPARTMENT  
PH.D. IN PHYSICS

Growth, coalescence and equilibration of  
metallic nanoparticles and nanoalloys studied  
by computational methods

CANDIDATE:  
Diana Nelli

SUPERVISOR:  
Prof. Riccardo Ferrando

MAY, 4 2022

# List of publications

## PAPERS PUBLISHED IN PEER-REVIEWED JOURNALS

1. Impurity diffusion in magic-size icosahedral clusters; D. Nelli, F. Pietrucci and R. Ferrando; *The Journal of Chemical Physics*, 2021, 155, 144304
2. Octahedral growth of PtPd nanocrystals; D. Nelli, C. Roncaglia, S. Ahearn, M. Di Vece, R. Ferrando, and C. Minnai; *Catalysts*, 2021, 11(6), 718
3. Shape control of size-selected naked platinum nanocrystals; Y. Xia, D. Nelli, R. Ferrando, J. Yuan, and Z. Y. Li, *Nature Communications*, 2021, 12, 3019
4. Shape changes in AuPd alloy nanoparticles controlled by anisotropic surface stress relaxation; D. Nelli, C. Roncaglia, R. Ferrando, and C. Minnai, *The Journal of Physical Chemistry Letters*, 2021, 12(19), 4609–4615
5. From metastability to equilibrium during the sequential growth of Co–Ag supported clusters: a real-time investigation; P. Andreatza, A. Lemoine, A. Coati, D. Nelli, R. Ferrando, Y. Garreau, J. Creuze, and C. Andreatza-Vignolle, *Nanoscale*, 2021, 13, 6096–6104
6. Tuning the coalescence degree in the growth of Pt–Pd nanoalloys; D. Nelli, M. Cerbelaud, R. Ferrando, and C. Minnai, *Nanoscale Advances*, 2021, 3, 836–846
7. One-step growth of core–shell (PtPd)@Pt and (PtPd)@Pd nanoparticles in the gas phase; D. Nelli, A. Krishnadas, R. Ferrando, and C. Minnai, *The Journal of Physical Chemistry C*, 2020, 124(26), 14338–14349
8. Structure and orientation effects in the coalescence of Au clusters; D. Nelli, G. Rossi, Z. Wang, R. E. Palmer, and R. Ferrando, *Nanoscale*, 2020, 12, 7688–7699
9. Core–shell vs. multi-shell formation in nanoalloy evolution from disordered configurations; D. Nelli and R. Ferrando, *Nanoscale*, 2019, 11, 13040–13050
10. Central vacancy creation in icosahedral nanoparticles induced by the displacement of large impurities; D. Nelli, *The European Physical Journal Applied Physics*, 2022, 97, 18

#### PAPERS ACCEPTED IN PEER-REVIEWED JOURNALS

11. Growth of size-matched nanoalloys - A comparison of AuAg and PtPd; E. El koraychy, D. Nelli, C. Roncaglia, C. Minnai, and R. Ferrando, accepted in *The European Physical Journal Applied Physics*

#### PAPERS SUBMITTED TO PEER-REVIEWED JOURNALS

12. Growth mechanisms from tetrahedral seeds to multiply twinned Au particles revealed by atomic level simulations; E. El koraychy, C. Roncaglia, D. Nelli, M. Cerbelaud, and R. Ferrando

#### PAPERS IN PREPARATION

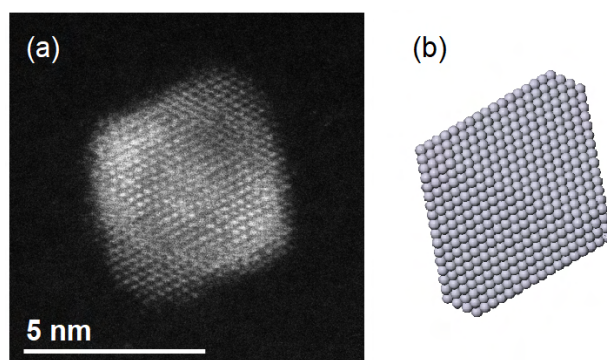
13. Solidification pathways of AgCu, AgNi and AgCo nanodroplets revealed by molecular dynamics simulations; D. Nelli, R. Ferrando, M. Cerbelaud, B. Crespín, and A. Videcoq
14. Interdiffusion in nanoalloys evolving from phase-separated to intermixed configurations; D. Nelli, C. Mottet and R. Ferrando

This thesis is based on the content of papers n. 1, 3, 4, 6, 7, 8, 9 and 10.

## Introduction

AMONG NANOSCALE SYSTEMS, metallic nanoparticles (NPs) certainly play a primary role, due to their highly tunable properties and to the wide variety of their applications. The possibility to efficiently exploit NPs in the catalytical and optical fields has been soon understood, and many studies in this sense have been carried out in the last decades [1–3]. More recently, applications in energy and data storage, biosensing and nanomedicine have been explored [4–6]; the interest in NPs has therefore increased, crossing the borders of the pure chemical and physical areas and moving towards new interdisciplinary fields. Nowadays, NPs are produced by a wide variety of synthesis techniques, and can be characterized by imaging tools with atomic-level resolution, as in the example shown in the figure below.

The properties of NPs are known to strongly depend on their size and geometric shape. Size varies in the range between few angstrom and hundreds of nanometers, and it is finely selected according to the desired application; for example, optical properties such as the peak wavelength of the NP plasmon resonance can be tuned by changing the NP size [7–9]. The optical response of the NPs is determined also by the overall geometric shape [10]. Catalytical properties have been proved to be shape-dependent as well: NPs of different shapes exhibits different crystallographic facets and have different fraction of surface atoms on their corners and edges, which considerably affects the catalytic activity of various organic and inorganic reactions [11]. In the case of bimetallic



(a) Electron microscope image of a Pt-Pd NP of octahedral shape; close-packed atomic planes are clearly visible. Courtesy of Dr. Chloé Minnai. (b) Computer model of the NP.

nanoparticles, also known as nanoalloys, further parameters can be exploited, i.e. the NP composition and the spatial arrangement of the two atomic species within the NP volume, here referred to as chemical ordering. Nanoalloy properties are especially affected by such arrangement; for example, the composition of the surface layer mostly determines the catalytical properties of the nanoalloy.

Within this framework, the fine control of the NP configuration (here intended as the interplay between size, shape, composition and chemical ordering) is essential in sight of the possible technological applications. To this aim, a deep understanding of the NP formation process is highly desirable: one has to clearly know what are the different stages of such process, and what are the physical forces and the chemical effects involved. Moreover, a clear knowledge of the thermodynamic stability of the produced phases under the operating conditions is desirable as well.

In general, such issues are quite complex because of the rich variety of phenomena involved, which in most cases are the non-trivial result of the competition between equilibrium and kinetic effects. The NP formation is an inherently kinetic process, often taking place in strongly out-of-equilibrium conditions. Both equilibrium and kinetic driving forces act at the same time, the former pushing the NP toward configurations closer to the thermodynamic equilibrium, the latter slowing down the evolution and trapping the NP in metastable far-from-equilibrium states. According to the outcome of such competition, a wide variety of configurations can be obtained, corresponding to different degrees of equilibration. The out-of-equilibrium configurations produced can then evolve towards equilibrium by shape transformations and, in the case of nanoalloys, chemical ordering rearrangements; peculiar equilibration pathways can be observed, and, again, kinetic trapping effects may take place at some stage of the process.

Due to the complexity and variety of the physical effects involved, in many cases it is difficult to correctly interpret the experimental results and observations. For example, it may be non-trivial to understand whether the produced NPs are at the thermodynamic equilibrium or not; moreover, by solely observing the final NP, it is almost impossible to reconstruct the complete formation pathway that has produced it. Computer simulations can be of great help in this sense, as they can provide clear information on both the equilibrium properties and the kinetic behaviour of the NPs. Specifically, the most thermodynamically favourable configurations of a given system can be determined, and the evolution pathways can be simulated and analysed at the atomic level, therefore allowing to rationalize the experimental findings. The combined experimental-theoretical approach has indeed proved to be the most effective method to study mono- and bi-metallic NPs; by employing this approach, multiple results have been obtained in the last years, that have greatly increased our knowledge of such nanoscale systems.

This Ph.D. thesis is devoted to the computational study of mono- and bi-metallic NPs, with particular attention to some of the nonequilibrium phenomena undergone by them. Different examples are presented and discussed; specifically, different metallic systems are treated, all of which are of great interest due to their practical applications, and different phenomena are analysed. In most cases, the results presented in this thesis have been achieved by the above mentioned experimental-theoretical approach, as we have worked in close collaboration with two experimental groups who

have produced and characterized different types of mono- and bi-metallic NPs. Since the comparison between experiments and simulations has been essential to deeply understand the phenomena under investigation, here we also present the main experimental findings, along with our simulation results.

The investigated nonequilibrium processes are here presented to reflect the subsequent stages of a NP life, going from its formation to its ageing. Firstly, the NP growth process is analysed, for both mono- and bi-metallic systems. During growth, the NP size increases mainly because of the addition of monomers from the surrounding environment. The configuration obtained at the end of the process strongly depends on the growth conditions, so that a wide variety of structures can be produced by tuning the experimental growth parameters; however, the atomic-level driving forces leading to specific shapes or chemical arrangements are often unclear. Our simulations have allowed us to identify peculiar growth pathways, and therefore to explain the experimental outcomes; in Chapter 3, such pathways are described in details, and the analysis of the elemental mechanisms and of the physical driving forces involved in the processes is provided as well. This is done in the case of pure Pt NPs and Pt-Pd nanoalloys, which are among the most used systems for applications to catalysis.

The out-of-equilibrium configurations obtained at the end of the growth process are expected to evolve towards more favourable configurations, until finally reaching thermodynamic equilibrium. In the case of nanoalloys, intra-nanoparticle diffusion of the atoms of the two species takes place, therefore producing transformations in the overall chemical ordering. Such equilibration processes are analysed in Chapter 4; specifically, we show our simulation results on both the elemental mechanisms of atomic diffusion in NPs, and on more global chemical ordering rearrangements, involving many atoms at the same time. In this case, different bimetallic systems are considered, such as Au-Co, Ag-Cu, Ag-Ni, Ag-Co, Au-Pt and Au-Rh, which are the subject of many experimental and theoretical studies due to their optical, magnetic and catalytical properties.

Finally, in Chapter 5 we analyse the coalescence process, in which two preformed NPs collide and merge to form a single larger aggregate. For both mono- and bi-metallic systems (specifically pure Au NPs and Pt-Pd nanoalloys), we investigate the different stages of the equilibration of the coalescing NP, the atomic-level mechanisms leading to the transformation of the overall geometric shape, and the dependence of the coalescence outcome on the two initial colliding units. Again, our simulation results are compared with experimental observations.

In all these examples, kinetic trapping effects turn out to play a major role; as a consequence, peculiar evolution pathways are observed, and metastable out-of-equilibrium configurations are obtained during the processes. In our analysis we particularly focus on such kinetic trapping effects: we show at what stage of the process they take place, how they are able to direct the evolution toward a specific configuration, and in what conditions they are dominant over equilibration effects.

In order to provide a more complete overview of the possible behaviours of NPs, we include, in Chapter 6, one final example in which, at variance with the previous cases, equilibrium driving forces are the main responsible of the experimentally observed Au-Pd nanoalloy structures. Here,

our simulations are not aimed at reproducing the NP evolution pathway, but at deeply understanding the atomic-level equilibrium effects involved, which have allowed us to explain the experimental observations where a composition-dependent shape change is found.

Our results have been obtained by different computational techniques, whose purpose is the identification of the most energetically favourable configurations for a given NP, and the accurate reproduction of the evolution pathways. To allow a better understanding of the simulation results, such techniques are briefly presented in Chapter 2; a brief description of the general features of the systems studied in this thesis is provided in Chapter 1.

# Contents

LIST OF PUBLICATIONS	<b>iii</b>
INTRODUCTION	<b>vii</b>
1 GEOMETRIC STRUCTURES AND CHEMICAL ORDERING OF NANOPARTICLES AND NANOALLOYS	<b>1</b>
1.1 Geometric structures . . . . .	1
1.2 Chemical ordering . . . . .	9
2 THEORETICAL MODELS AND COMPUTATIONAL TECHNIQUES FOR THE STUDY OF NANOPARTICLES	<b>12</b>
2.1 Modelling nanoparticles: energy landscape, atomistic approach and SMATB potential . . . . .	13
2.2 Looking for lowest-energy structures: global optimization . . . . .	14
2.3 Computational techniques for the simulation of kinetic phenomena . . . . .	17
3 OUT-OF-EQUILIBRIUM GROWTH PATHWAYS OF PURE Pt AND ALLOYED Pt-Pd NANOPARTICLES	<b>23</b>
3.1 Gas phase synthesis of mono- and bi-metallic nanoparticles . . . . .	25
3.2 Molecular dynamics growth simulations . . . . .	26
3.3 Defect-driven symmetry-breaking pathways in the growth of Pt nanocrystals . . . . .	27
3.4 Spontaneous formation of different core-shell arrangements in the growth of Pt-Pd nanoalloys . . . . .	43
4 CHEMICAL ORDERING TRANSFORMATIONS IN NANOALLOYS: ATOMIC DIFFUSION AND EQUILIBRATION PATHWAYS	<b>52</b>
4.1 Elementary diffusion mechanisms in icosahedral nanoparticles . . . . .	53
4.2 Chemical ordering equilibration pathways in phase-separating bimetallic systems	72
5 KINETIC TRAPPING AND EQUILIBRATION IN THE COALESCENCE OF PURE Au AND ALLOYED Pt-Pd NANOPARTICLES	<b>86</b>
5.1 Memory effects in the coalescence of Au clusters . . . . .	88



5.2	Equilibration steps in the coalescence of Pt-Pd crystalline nanoparticles . . . . .	101
6	SURFACE STRESS RELAXATION AND SHAPE TRANSFORMATIONS IN AU-PD NANOALLOYS	109
	CONCLUSIONS	121
A	PARAMETERS OF THE SMATB FORCE FIELD	123
B	ATOMIC STRESS AND PRESSURE	126
B.1	Hydrostatic pressure . . . . .	126
B.2	Stress tensor . . . . .	129
B.3	Energy and forces . . . . .	131
	REFERENCES	145

# 1

## Geometric structures and chemical ordering of nanoparticles and nanoalloys

NANOPARTICLES can take several different geometric shapes. Such a rich variety, besides being an interesting subject for basic research, is one of the main reasons behind the impressive versatility of these systems in many application fields. For example, the catalytic and optical properties of nanoparticles have been shown to strongly depend on their geometric structure [10–12]. In the case of nanoalloys, in which two metallic components are present, the variety of possible structures is even richer, since the pattern in which the two elements are arranged within the nanoparticle volume, i.e. the *chemical ordering*, has to be considered as well.

In this chapter, we describe some of the most common geometric shapes and chemical ordering types of nanoparticles and nanoalloys. We would point out that the following description is far from being exhaustive; we focus on the shapes and chemical arrangements that are relevant in the framework of the results of this thesis. A more complete and detailed discussion can be found in Refs. [13], [14] and [15].

### 1.1 GEOMETRIC STRUCTURES

In the analysis of NP geometric shapes we can identify some structural families, also called *structural motifs*, which are common to many different mono- and bi-metallic systems. Among them, we usually distinguish between *crystalline* and *noncrystalline* structural motifs.

NPs belonging to crystalline motifs are fragments of bulk crystals. The symmetry of the bulk

crystal is therefore preserved, namely the face-centered cubic (fcc), body-centered cubic (bcc) or hexagonal close-packed (hcp) lattice, and the interatomic distances within the cluster are roughly the same as in the bulk.

Noncrystalline NPs cannot be seen as fragments of any crystal lattice. Such structures are possible as the constraint of translational invariance of infinite bulk crystals does not apply to nanoscale systems. The most common noncrystalline structures are the decahedron (Dh) and the icosahedron (Ih).

### 1.1.1 CRYSTALLINE STRUCTURES

Here we consider fcc nanocrystals, as most of the metallic systems studied in this thesis (Au, Ag, Cu, Ni, Pt and Pd) exhibit fcc symmetry in the bulk. The only exception is Co, which crystallizes in the hcp lattice at sufficiently low temperatures [16]. Two regular geometric structures (Platonic polyhedra) are consistent with the fcc lattice, the *tetrahedron* and the *octahedron*.

The regular tetrahedron (Th) has four faces, six edges and four vertices; all four faces are equilateral triangles. A Th can be characterized by a single integer index  $n_l$ , which is the number of atoms in each edge. The total number of atoms in the Th is

$$N_{\text{Th}} = \frac{1}{6}(n_l + 2)(n_l + 1)n_l, \quad (1.1)$$

which gives the series of geometric magic numbers  $N_{\text{Th}} = 1, 4, 10, 20, 35, 56, \dots$ , i.e. the NP sizes for which a perfect Th can be built. Truncated tetrahedral structures are also possible: they are obtained by eliminating some atomic layers from the four tetrahedral vertices.

The regular octahedron (Oh) has eight faces, twelve edges and six vertices. Again, all faces are equivalent equilateral triangles. The total number of atoms in the octahedron is

$$N_{\text{Oh}} = \frac{1}{3}(2n_l^3 + n_l), \quad (1.2)$$

where  $n_l$  is again the number of atoms in each octahedral edge. The resulting series of magic numbers is  $N_{\text{Oh}} = 1, 6, 19, 44, 85, \dots$ . We notice that a perfect Oh can be obtained by performing symmetric truncations at the vertices of a larger Th, which underlines the close relationship between the two geometric motifs.

The main geometrical features of Th and Oh are summarized in Tab. 1.1.1. In both cases the surface contains only (111) closed-packed facets, i.e. the ones with the lowest possible surface energy for the fcc metals considered in this thesis. However, by comparing the dihedral angles of the two motifs, we can notice that tetrahedral edges are considerably sharper. Atoms on tetrahedral edges and vertices have therefore lower connectivity compared to the corresponding atoms on the Oh. The surface-to-volume ratio is much larger in the Th than in the Oh. For these reasons, Th are typically much less favourable from an energetic point of view. Despite their high energetic cost,

structural motif	Th	Oh
faces	4	8
edges	6	12
vertex	4	6
surface facets	(111)	(111)
dihedral angle	$70.5^\circ$	$109.5^\circ$
edge connectivity	6	7
vertex connectivity	3	4
number of symmetries	24	48

**Table 1.1.1:** Comparison between Th and Oh crystalline motifs.

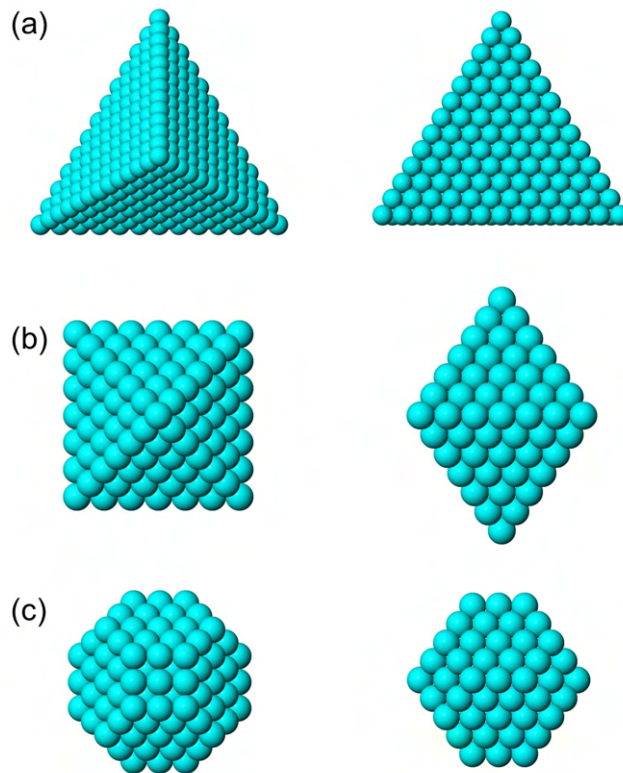


**Figure 1.1.1:** From top to bottom, tetrahedron, octahedron and regular truncated octahedron. Each structure is shown in two views. (a) Tetrahedron of size 455, corresponding to  $n_l = 13$ . (b) Octahedron of size 231, corresponding to  $n_l = 7$ . This octahedron can be obtained from the tetrahedron in (a), by cutting three atomic layers from each vertex. (c) Regular truncated octahedron of size 201, obtained from the octahedron in (b) by cutting two atomic layers from each vertex ( $n_l = 7$  and  $n_{\text{cut}} = 2$ ).

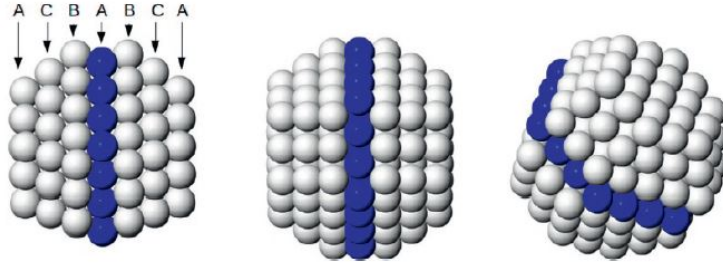


**Figure 1.1.2:** Twinned nanoparticle of 201 atoms, shown from three different views. Atoms of the twin plane are coloured in blue.  
 Reproduced from R. Ferrando, *Structure and Properties of Nanoalloys, Volume 10, Elsevier, 2016.*

tetrahedral NPs can actually be obtained in the experiments in specifically tailored growth conditions; we will discuss this point more extensively in Chapter 3. Examples of Th and Oh structures are shown in Fig. 1.1.1(a) and (b), respectively. The Oh of Fig. 1.1.1(b) can be obtained by cutting three atomic layers from the vertices of the Th of Fig. 1.1.1(a).

Although Oh are more favourable than Th, they still have a large surface-to-volume ratio, which can be improved by performing truncations at the vertices of the structure. These truncations create six (100) facets, whose surface energy is typically higher compared to the (111) ones, as their atoms are less densely packed. The energetic cost of the truncations is paid off with the achievement of a more compact structure. The optimal degree of truncation is usually close to the regular truncation, in which the (111) facets are regular hexagons. This is possible when  $n_l = 3n_{\text{cut}} + 1$ ,  $n_{\text{cut}}$  being the number of atomic layers removed at each vertex. The size of the truncated octahedron (TO) obtained in this way is

$$N_{\text{TO}}^{\text{reg}} = \frac{1}{27}(16n_l^3 - 3n_l^2 + 12n_l + 2), \quad (1.3)$$

which gives the series  $N_{\text{TO}}^{\text{reg}} = 38, 201, 586, 1289, \dots$  for  $n_l = 4, 7, 10, 13, \dots$ . The TO of size 201 is shown in Fig. 1.1.1(c). For some metals such as Au and Pt, the optimal truncation from the energetic point of view is less deep, so that the best TO present somewhat sharper tips than the regular ones [17].

### 1.1.2 NONCRYSTALLINE STRUCTURES

Noncrystalline structures are often composed of fcc subunits, which are joined together through *twin planes*. A twin plane is a mirror symmetry plane, which interrupts the stacking of the perfect fcc lattice and introduces a local hcp zone. In the simplest case one single twin plane is present in the central part of the cluster (see Fig. 1.1.2), but *multiply twinned* structures are possible as well. Decahedra and icosahedra are the most common; they can be obtained by joining 5 and 20 fcc tetrahedra, respectively. In order to build these structures, the fcc tetrahedra need to be somewhat distorted, so that the resulting decahedra and icosahedra present non-ideal interatomic distances, i.e. atomic-level strain (see for example Ref. [13]). The strain is much stronger in icosahedra than

in decahedra.

The regular *decahedron* is made of two pentagonal pyramids sharing their base (see Fig. 1.1.3(a)). A fivefold rotational axis is therefore present, which makes clear the noncrystalline character of this geometric structure. All the ten faces of the Dh are close-packed (111)-like, but, as in the case of the Oh, the surface-to-volume ratio is quite large, as the structure is highly non-spherical. Better Dh can be obtained by performing truncations. In the Ino decahedron [18] atoms are eliminated symmetrically from the edges along the common base (see Fig. 1.1.3(b)). In this way a more compact structure is achieved, but five rectangular (100) facets are created. An even better structure is the Marks decahedron [19], in which further truncations are made in order to create (111) re-entrant facets (see Fig. 1.1.3(c)). Marks Dh is characterized by three integer indices ( $m, n, p$ ).  $m$  and  $n$  are the number of atoms on the sides of the (100) facets, perpendicular and parallel to the fivefold axis, respectively.  $p$  is the depth of the Marks re-entrance ( $p = 1$  corresponds to no re-entrance, i.e. to the Ino Dh). Typically, the most favourable Dh have  $m = n$ , corresponding to square (100) facets, whereas the optimal value for  $p$  depends on the system; for example,  $p = m/2$  for Ag clusters,  $p = m$  for Au ones [17].

The regular *icosahedron* has 20 faces, 30 edges and 12 vertices; all faces are equilateral triangles. Each pair of opposite vertices lie along a fivefold symmetry axis. Icosahedral nanoparticles can be obtained by putting together concentric atomic layers; this construction is called Mackay icosahedron [20]. The number of atoms in an Ih is given by

$$N_{\text{Ih}} = \frac{1}{3}(10k^3 - 15k^2 + 11k - 3), \quad (1.4)$$

where  $k$  is the number of icosahedral layers. The corresponding series of magic number is  $N_{\text{Ih}} = 1, 13, 55, 147, 309, 561, 923, \dots$ . In Fig. 1.1.4 we show the Ih made of  $k = 5$  atomic layers. Other structures of icosahedral symmetry are possible, which can be obtained from the Mackay Ih by modifying the outer atomic layer. One possibility is the anti-Mackay Ih, in which the surface atoms occupy the hcp-like sites on the underlying layer instead of the fcc-like sites [21] (see Fig. 1.1.5(b)). The chiral Ih can be obtained by applying a chiral distortion to the surface of the anti-Mackay Ih [22] (see Fig. 1.1.5(c)). In anti-Mackay and chiral icosahedra surface atoms are packed less densely than in standard Mackay icosahedra. As a consequence, they are typically much less favourable, with the exception of some bimetallic systems [22].

### 1.1.3 SURFACE DEFECTS

In most cases, although it is possible to clearly identify the geometric motif (fcc-like, Dh or Ih) to which the NP belongs, some defects are present. Defects are especially found in the NP surface, as surface atoms can rearrange quite easily due to their low coordination. Defects are common when the NP size does not match any of the magic sizes for the chosen geometric motif; in that case,

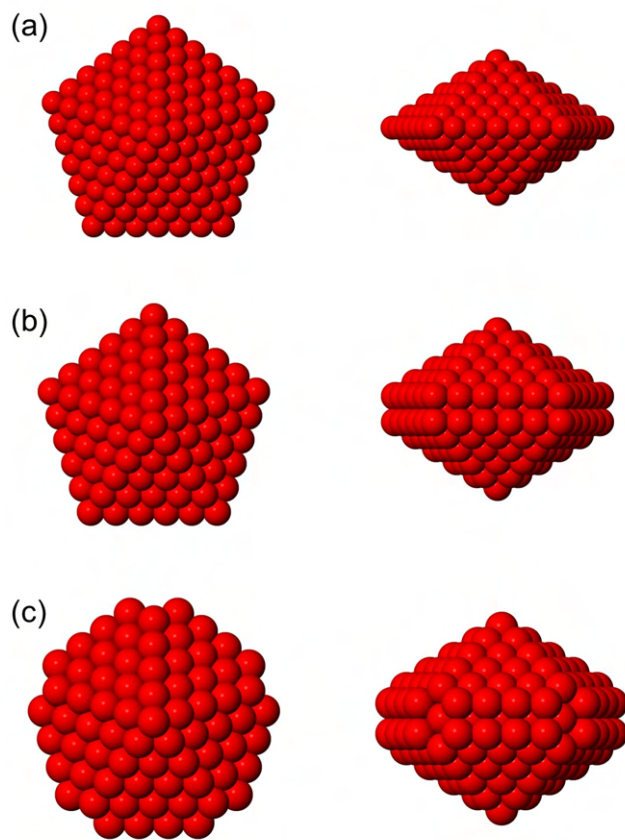


**Figure 1.1.3:** Dh structures with different type of truncation. Each structure is shown in two views. (a) Regular decahedron with  $(m, n, p) = (7, 1, 1)$ , containing 287 atoms. (b) Ino decahedron with  $(m, n, p) = (6, 2, 1)$  and of size 257, obtained from the structure in (a) by removing 30 atoms. (c) Marks decahedron with  $(m, n, p) = (4, 2, 2)$  and of size 247, obtained from the structure in (b) by removing further 10 atoms to create reentrances.

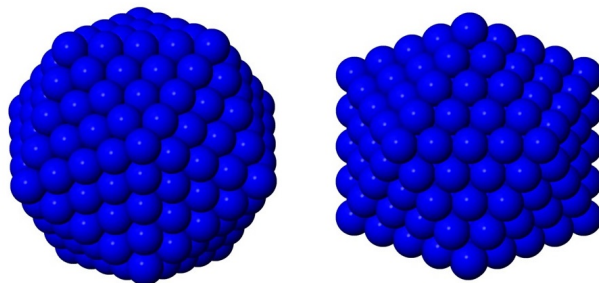


**Figure 1.1.4:** Icosahedron of 309 atoms, corresponding to  $k = 5$  atomic layers. The structure is shown in two views.

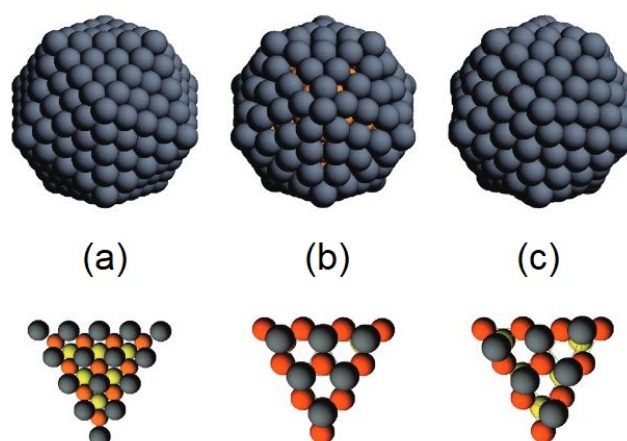


**Figure 1.1.5:** (a) Mackay, (b) anti-Mackay and (c) chiral icosahedra. For each structure, the surface (top row) and the stacking of the three outer atomic shell (bottom row) are shown. Reproduced from D. Bochicchio and R. Ferrando, *Size-dependent transition to high-symmetry chiral structures in AgCu, AgCo, AgNi, and AuNi nanoalloys*, *Nano Lett.* 10:4211-4216, 2010.

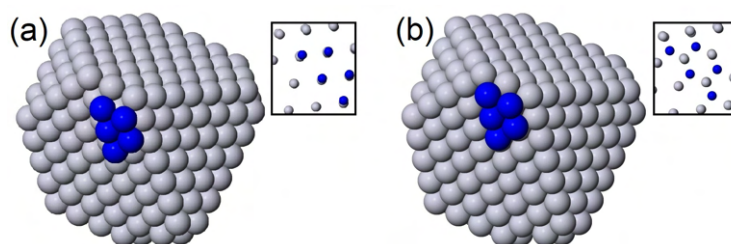


**Figure 1.1.6:** Possible stackings for a small atomic island (highlighted in blue) on the surface of a fcc cluster. (a) fcc stacking: extra atoms arrange themselves according to the overall symmetry; alignment between the extra atoms and the underlying atomic columns is observed (small box in the upper right). (b) hcp stacking (stacking fault): extra atoms arrange themselves in a local hcp symmetry, therefore they are not aligned with the underlying atomic columns.

the most external atomic layer is incomplete, and, as a consequence, rearrangements are even more likely. However surface defects can be observed also in magic-size structures.

In the case of crystalline NPs, some portion of the surface layer can be in hcp stacking. This hcp-like area can be a small “island” made of few atoms, as in Fig. 1.1.6(b), but in some cases it can be an extended layer that covers a whole face of the perfect fcc structure.

Icosahedral structures may undergo different types of surface reconstructions. A common surface reconstruction pattern is the *rosette* [23], in which a vertex atom enters the cluster surface and forms a hexagonal ring together with its former five surface neighbours. Multiple rosette reconstructions may be present, as shown in Fig. 1.1.7.

Surface defects are typically unstable, as their presence is associated with an increase of the total energy of the NP in most cases. However, under certain conditions they can survive for long; an interesting example of metastable surface defects in fcc NPs will be given in Chapter 3. In some



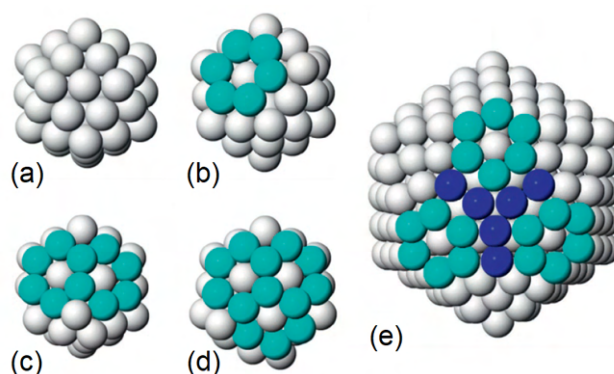


**Figure 1.1.7:** Rosette reconstruction on the surface of icosahedral structures. Icosahedron of 55 atoms with (a) no rosettes, (b) one rosette, (c) two rosettes and (d) three rosettes. (e) Icosahedron of 309 atoms with three rosettes. Hexagonal rings are highlighted in cyan, whereas in (d) further edge atoms in the reconstructed region are highlighted in blue.

*Reproduced from R. Ferrando, Structure and Properties of Nanoalloys, Volume 10, Elsevier, 2016.*

cases surface defects are energetically favourable, as it happens for rosette reconstructions in Pt and Au icosahedral NPs [23].

#### 1.1.4 ENERGETIC STABILITY OF THE DIFFERENT GEOMETRIC MOTIFS

Here we briefly discuss the energetic stability of the geometric motifs we have described so far. For precise energy evaluations we should consider each metallic system separately; however, some general trends can be identified.

The stability of the different geometric motifs strongly depends on the NP size. Icosahedra exhibit quasi-spherical shape and closed-packed surface, but also large volume strain coming from the non-ideal interatomic distances. Due to these features, icosahedra are expected to be favourable at small sizes, when the surface contribution to the total energy is dominant, and unfavourable at large sizes, when the dominant contribution comes from the NP volume. On the contrary, crystalline structures have no volume strain, but less compact surface; therefore they are expected to be energetically favourable for large sizes and unfavourable for small sizes. Decahedra are intermediate, for what concerns both volume strain and surface compactness. By this line of reasoning, we can expect a crossover from icosahedra to decahedra and then to crystalline structures as the NP size increases. This behaviour has been confirmed by energy calculations for different metals. Crossover sizes between the different motifs strongly depend on the material; for example, in the case of Ag NPs the two crossover sizes roughly correspond to 300 and 20000 atoms [17]. We note that the crossover between two motifs is usually not sharp. For example, decahedral and fcc structures present wide size ranges in which their energies are quite close [14, 17].

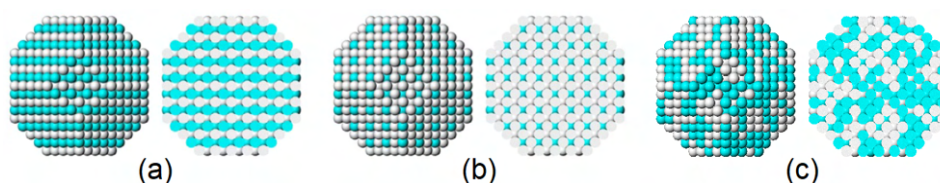


**Figure 1.2.1:** Mixing patterns in crystalline bimetallic nanoparticles. Two different colours (grey and cyan) are used to highlight atoms of the two different species. In all cases both the nanoparticle surface (left) and a cross-section (right) are shown. (a)  $L_{10}$  phase at 1:1 composition, with alternating (100) atomic planes of the two elements. (b)  $L_{12}$  phase at 3:1 composition; the two alternating (100) atomic planes are made of: (i) the most abundant element, and (ii) both elements arranged in a chessboard. (c) Randomly intermixed chemical ordering at 1:1 composition.

Adapted from R. Ferrando, *Structure and Properties of Nanoalloys*, Volume 10, Elsevier, 2016.

## 1.2 CHEMICAL ORDERING

Chemical ordering is the pattern in which the different elements of a multi-metallic NP are arranged. Here we describe the most common chemical ordering types in bimetallic NPs.

Two main classes of chemical ordering can be identified, the *mixing patterns* and the *nonmixing* or *phase-separated patterns*.

Mixing patterns may exhibit different degrees of ordering, ranging from perfectly ordered phases to completely random solid solutions. Ordered phases observed at the nanoscale can be the same as in bulk alloys; two examples of such phases are displayed in Fig. 1.2.1(a) and (b), for 1:1 and 3:1 composition respectively, whereas in Fig. 1.2.1(c) a randomly intermixed chemical ordering at 1:1 composition is shown.

A rich variety of nonmixing chemical ordering patterns may occur in bimetallic NPs, as we show in Fig. 1.2.2. In the core-shell arrangement we can identify a core made of atoms of species A, surrounded by a shell of species B (see Fig. 1.2.2(a)); the abbreviation A@B is commonly used in this case. Multi-shell arrangements are also possible, with multiple concentric layers entirely made of either A or B atoms; in Fig. 1.2.2(b) a three-shell A@B@A nanoparticle is shown. In some cases the core-shell arrangement is not perfect: the inner core may be off-centered, or the outer shell may be incomplete, as in Fig. 1.2.2(c). In Janus nanoparticles the two elements are separated so that they occupy opposite sides of the structure (Fig. 1.2.2(d)). In quasi-Janus nanoparticles the same kind of phase separation occurs, but the surface is completely made of one of the two elements, as shown in Fig. 1.2.2(e).

The energetic stability of the different chemical ordering patterns is mainly due to the behaviour of the bulk bimetallic alloy. The tendency towards mixing in the bulk induces the formation of mixing patterns also at the nanoscale. On the other hand, a weak mixing tendency is the main driving force for the formation of stable phase-separated patterns. Other driving forces for nonmixing behaviour at the nanoscale are the difference in surface energy and the size mismatch between the two elements; the element with lower surface energy segregates to the nanoparticle surface, and the

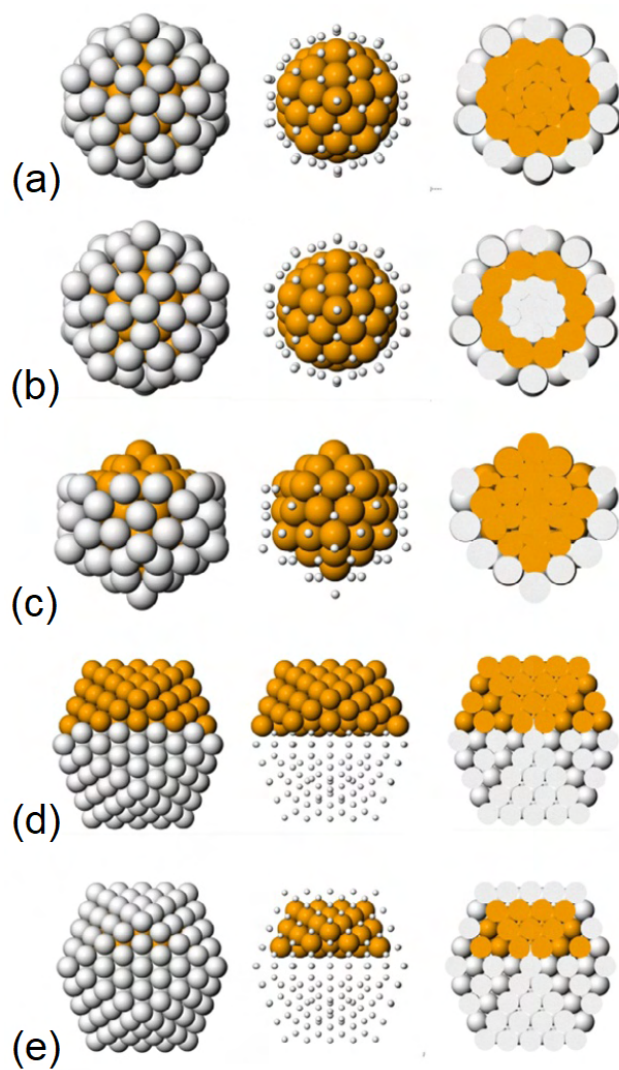


**Figure 1.2.2:** Nonmixing patterns in bimetallic nanoparticles with icosahedral geometric structure. A and B atoms are shown in orange and grey, respectively. In all cases the nanoparticle is shown in three different views. Left column: nanoparticle surface. Middle column: B atoms are shown as small spheres. Right column: cross-section of the nanoparticle. (a) Core-shell A@B; (b) three-shell A@B@A; (c) core-shell A@B with incomplete B shell; (d) Janus; (e) quasi-Janus with B surface layer.

*Reproduced from R. Ferrando, Structure and Properties of Nanoalloys, Volume 10, Elsevier, 2016.*

same is expected for the element with larger atomic radius, leading to chemical ordering patterns of the core-shell type [24, 25]. The surface segregation of the larger atoms is able to partially decrease the atomic stress, which is larger in the internal part of the structure [13]. Mixing patterns are observed, for example, in Co-Pt, Fe-Pt, Au-Cu, Au-Pd, Ag-Pd and Ag-Au bimetallic nanoparticles, whereas phase-separated patterns are common in Ag-Cu, Ag-Ni, Au-Co, Ag-Co and Au-Pt.

Though we have described the the most common chemical ordering patterns, we have to remark that, in real systems, more complicated arrangement are often observed. In some cases the real behaviour is somewhat intermediate between mixing and nonmixing, with the presence of an intermixed core and of an outer shell completely made of the element with lower surface energy; such structures have been observed, for instance, in Pt-Co and Ag-Pt nanoparticles [26, 27].

In addition, the chemical ordering of a bimetallic NP is not independent from its geometric shape. Sometimes a close correlation can be established, as these two features may influence each other: in noncrystalline icosahedral structures, where the internal stress is particularly large [13], the effect of surface segregation of the larger atoms is stronger compared to other geometries [25]; due to similar stress considerations, phase-separated chemical ordering patterns may stabilize a specific geometry in bimetallic nanoparticles, which would be unlikely in both the corresponding pure monometallic systems [28]. We will deal with this last point more extensively in Chapter 6.

# 2

## Theoretical models and computational techniques for the study of nanoparticles

THE COMPUTATIONAL APPROACH has been widely employed in the study of nanoscale systems since many decades; nowadays, the number of computational studies on nanoparticles is constantly increasing, as well as the variety of computational techniques exploited in the field. Results obtained by computational methods may be very useful to interpret the experimental findings; moreover, the computational approach allows to investigate atomic-level phenomena taking place on very short time scales, which cannot be easily accessed by present experimental techniques.

In general, the computational approach requires the description of the system by some theoretical model. The model shall consist of a method for calculating the potential energy of the system as a function of the coordinates of its components, which, in the case of nanoparticles, are the atoms building up the structure. The computational approach is used to study both equilibrium properties and dynamical behaviours, by the use of different specifically tailored techniques.

In this chapter, we describe the theoretical model and the computational techniques used in the framework of this thesis for the study of nanoparticles. Two main kinds of techniques have been employed. Methods based on Monte Carlo sampling [29, 30] have been used to find the lowest-energy structures of mono- and bi-metallic NPs, which are likely to represent thermodynamic equilibrium at sufficiently low temperatures. Molecular dynamics has been employed to study nonequilibrium phenomena, such as growth, coalescence and evolution at constant temperature. Both techniques are widely used in the computational study of several different systems; in the following, we describe

their general aspects, as well as some specific adjustments to the study of nanoparticles.

## 2.1 MODELLING NANOPARTICLES: ENERGY LANDSCAPE, ATOMISTIC APPROACH AND SMATB POTENTIAL

In the theoretical-computational framework, any system is fully described by its energy landscape, i.e. the potential energy  $U$  as a function of the coordinates of its  $N$  atoms  $\{\mathbf{R}\} = (\mathbf{R}_1, \mathbf{R}_2, \dots, \mathbf{R}_N)$ . Different approaches are used to evaluate the function  $U(\{\mathbf{R}\})$ . In *ab initio* approaches,  $U(\{\mathbf{R}\})$  is calculated by numerically solving the quantum electronic problem for each position of the atomic nuclei; in the study of nanoscale systems, the most widely employed *ab initio* method is density functional theory (DFT) [31, 32]. In atomistic approaches, the function  $U(\{\mathbf{R}\})$  is directly given by analytical formulas or numerical tables. In this case, electrons do not appear explicitly, but their effect is taken into account to build up effective force fields between atoms.

Both DFT and atomistic models are used in the computational study of NPs. The choice of one or the other model depends mainly on the desired accuracy, on the size of the system and on the time scale of the phenomena under investigation. DFT is usually more accurate, but much more computationally demanding; DFT calculations are therefore employed when high accuracy is needed, but their range of applications is quite limited. Local minimization, i.e. the search of the closest local minimum of the energy profile starting from a given structure, can be performed at DFT level for nanoparticles of few thousands atoms. However, in Monte Carlo and molecular dynamics simulations, which require a large number of energy evaluations, much smaller sizes can be considered. For example, in *ab initio* molecular dynamics, rather short time scales can be reached: typically, the evolution of NPs of a few tens of atoms can be simulated up to a maximum time of a few hundred ps with a reasonable computational effort.

The atomistic approach allows to treat much larger systems, and to simulate the dynamics on longer time scales. Though the accuracy is usually lower compared to *ab initio* calculations, satisfactory results can be obtained in many cases. In this thesis, the atomistic approach has been employed in all global optimization and molecular dynamics simulations; specifically, we have used an atomistic potential developed on the basis of the second-moment approximation to the tight-binding model [33–35], which is commonly referred to as SMATB, Gupta or Rosato-Guillopé-Legrand (RGL) potential. Here we report the analytical form and main properties of the SMATB potential; the derivation from the tight-binding model can be found in Refs. [36] and [37].

In the SMATB model, the potential energy of the system is calculated as the sum of single atom contributions  $E_i$ , each one depending on the relative distance  $R_{ij} = |\mathbf{R}_i - \mathbf{R}_j|$  between atom  $i$  and all other atoms  $j$ . Two terms are included: a repulsive term, which is a sum of pair contributions, and an attractive term of many-body character. The form of the SMATB potential is

$$U(\{\mathbf{R}\}) = \sum_{i=1}^N E_i, \quad (2.1)$$

where

$$E_i = \sum_{j, r_{ij} \leq r_{a\beta}^c} A_{a\beta} \exp \left[ -p_{a\beta} \left( \frac{r_{ij}}{r_{a\beta}^o} - 1 \right) \right] - \sqrt{\sum_{j, r_{ij} \leq r_{a\beta}^c} \xi_{a\beta}^2 \exp \left[ -2q_{a\beta} \left( \frac{r_{ij}}{r_{a\beta}^o} - 1 \right) \right]}. \quad (2.2)$$

Here  $a$  and  $\beta$  are the species of atoms  $i$  and  $j$ , respectively. The parameter  $r_{a\beta}^o$  is commonly chosen as the equilibrium distance in the bulk crystal for homogeneous pairs, and the average of the two equilibrium distances for heterogeneous pairs, whereas the parameters  $p_{a\beta}$ ,  $q_{a\beta}$ ,  $A_{a\beta}$  and  $\xi_{a\beta}$  are usually fitted on properties of the bulk metals and alloys [34, 35, 38, 39]. Cutoff distances  $r_{a\beta}^c$  for the interaction are often taken as second or third neighbour distances in the bulk crystal. In this thesis, cutoff distances on the interactions are imposed as follows. The exponential functions in Eq. 2.2 are replaced by fifth-order polynomials, of the form  $a_3(r - r_{c2})^3 + a_4(r - r_{c2})^4 + a_5(r - r_{c2})^5$ , between distances  $r_{c1}$  and  $r_{c2}$ , with  $a_3$ ,  $a_4$ ,  $a_5$  fitted in each case to obtain a function which is always continuous, with first and second derivative for all distances, and goes to zero at  $r_{c2}$ . The parameters of the potential for the different systems studied in this thesis are reported in Appendix A.

The SMATB potential is a common choice for modelling NPs made of transition or noble metals. The accuracy of this model has been verified in many studies, by comparing its results and prediction with DFT calculations on small systems and with experimental data. For the metals considered in this thesis, results of tests against DFT calculations can be found in Refs. [22, 28, 40–43]. A good agreement has been obtained in all cases.

As already mentioned, the greatest part of the results of this thesis has been obtained within the atomistic approach, by using the SMATB model. DFT calculations have been performed to find the energy of some specific configurations of small Pt clusters; results are reported in Chapter 3, in which more details on the procedure of DFT calculations can be found.

## 2.2 LOOKING FOR LOWEST-ENERGY STRUCTURES: GLOBAL OPTIMIZATION

In the computational study of NPs, a very important subject is the *global optimization* problem, i.e. the search of the *global minimum*. The global minimum is the atomic configuration at which the potential energy  $U(\{\mathbf{R}\})$  takes its minimum value; this corresponds to the thermal equilibrium structure in the limit  $T \rightarrow 0$ <sup>1</sup>, but, in the case of metallic NPs, the statistical weight of the global minimum can be considerably high also at room temperature. The knowledge of the lowest-energy configuration is therefore necessary for understanding the equilibrium properties of NPs in the temperature range of experiments and applications; for this reason, in the last decades much effort has been devoted to efficiently address the global optimization problem.

The problem is indeed rather complex. Since potential energy is a function of a large number of atomic coordinates, an analytical minimization is not possible. To identify the global minimum,

<sup>1</sup>More precisely, the global minimum is the one with the lowest-energy after taking into account quantum zero-point energy. Cases where zero-point energy alters the order of the lowest energy minima are rare. In this thesis, such cases have not been found.

one should in principle find all the local minima, i.e. the locally stable configurations, and compare their energy. Again, this is not feasible as the number of local minima is huge even for NPs of quite small size [44, 45].

In practical terms, only a partial sampling of the local minima of the potential energy landscape can be made; therefore we need to come up with some strategies to bolster the efficiency of such sampling, in order to maximize the probability of finding the global minimum and to minimize the time needed for the search. Several algorithms have been developed to this aim, with a large variety of largely different approaches. However, global optimization algorithms share some common features. Typically, an initial structure is chosen, which corresponds to the first estimate of the searched global minimum. This initial structure may be chosen by attributing random coordinates to the atoms in the simulation box. Starting from this structure, a new configuration is build by applying some elementary moves that modify the positions of the atoms. The energy of the new configuration is evaluated and, according to some energy-based criteria which are specific for each algorithm, the move is either accepted or rejected; if it is accepted, the exploration of the potential energy landscape continues from the new structure, otherwise the initial configuration is restored. This scheme is repeated for a predetermined number of steps, or until some convergence criterion is satisfied. In many algorithms, a family of structures is evolved in parallel.

To successfully apply this scheme, we have to properly choose the elementary moves to switch from one structure to the other, and the acceptance criterion of the newly build structures. In the following, we describe the acceptance criterion of the basin hopping algorithm [45, 46], which has been applied in all the global optimization searches of this thesis. Then we describe two types of elementary moves which are commonly used for exploring the energy landscape of mono- and bi-metallic NPs.

We point out that, in the framework of the global optimization procedure, it is not possible to rigorously demonstrate that the global minimum has been actually found. The final output of the global optimization search is indeed only an estimate of the global minimum, i.e. the best estimate according to the performed calculations, which is often referred to as the *putative* global minimum. However, a precise knowledge of the global minimum is usually not necessary for the NP sizes considered in this thesis. In most cases, the identification of the best geometric motif and, in the case of bimetallic systems, of the best type of chemical ordering is sufficient to understand the most relevant equilibrium properties of the NPs and to make a comparison with the experimental observations, whereas the details of the precise optimal placement of every single atom are not essential.

### 2.2.1 BASIN HOPPING ALGORITHM

In the *basin hopping* (BH) algorithm [47, 48], a newly generated structure is either accepted or rejected according to the Metropolis Monte Carlo rule. The acceptance rule is not applied directly to the potential energy  $U$  of the two structures under comparison, but to the energy of their closest local minima. In other words, we are sampling a new potential energy function  $\tilde{U}(\{\mathbf{R}\})$ , which is



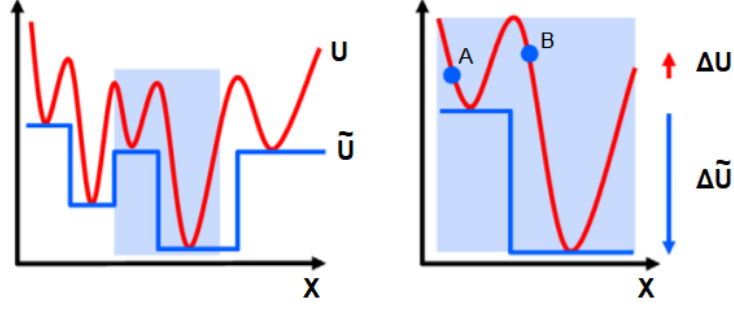


**Figure 2.2.1:**  $U \rightarrow \tilde{U}$  transformation in the simple case of one-dimensional potential energy function (left panel). Effect of the transformation on the BH algorithm (right panel): moving from A to B the potential energy  $U$  increases but the transformed potential energy  $\tilde{U}$  decreases as B is associated to a lower-energy basin; therefore the move is accepted with probability 1.

defined as

$$\tilde{U}(\{\mathbf{R}\}) = \min [U(\{\mathbf{R}\})]. \quad (2.3)$$

The local minimization is started from the configuration identified by the set of atomic coordinates  $\{\mathbf{R}\}$ . Different local minimization methods can be used; in this thesis the L-BFGS algorithm [49] has been employed.

The new structure is accepted with probability

$$\min [1, \exp(-\Delta\tilde{U}/(k_B T))], \quad (2.4)$$

where  $\Delta\tilde{U}$  is the transformed potential energy difference between the new and the current structure. If  $\Delta\tilde{U} < 0$ , the new structure is accepted and substitutes the previous one. If  $\Delta\tilde{U} > 0$ , a random number  $r$ , uniformly distributed in the interval  $(0, 1]$ , is extracted, and the new structure is accepted only if

$$r \leq \exp(-\Delta\tilde{U}/(k_B T)). \quad (2.5)$$

The application of the acceptance rule to the transformed potential energy  $\tilde{U}(\{\mathbf{R}\})$  instead of  $U(\{\mathbf{R}\})$  considerably improves the efficiency of the global minimization procedure, as it facilitates the transition between nearby minima. Specifically, there is no barrier for moving towards configurations belonging to the energy basin of a lower minimum, as it is shown in Fig. 2.2.1.

The only parameter of the BH algorithm is the simulation temperature  $T$ , which has to be properly tuned to ensure the efficiency of the minimization procedure. The simulation temperature affects the acceptance probability of moves towards higher-energy basins: by increasing  $T$ , the acceptance probability of such moves increases as well.  $T$  should be sufficiently high to ensure a good sampling of the potential energy surface, i.e. to avoid that the system gets trapped around some particularly stable local minimum during the simulation. On the other hand, if  $T$  is too high, the probability of locating the lowest-energy minimum becomes small. The most effective choice of the simulation temperature depends on the properties of the system and on the type of elementary

move, as we discuss in the following.

### 2.2.2 ELEMENTARY MOVES FOR THE EXPLORATION OF NANOPARTICLES ENERGY LANDSCAPE

The choice of the elementary moves is an essential point in the global optimization procedure. If we are able to identify the “right” moves, we can increase the probability of finding the global minimum, therefore speeding up the search. The choice of the most effective elementary moves depends on the system under consideration. Here we describe two types of elementary moves: the *Brownian move* and the *exchange move*, which are commonly used to optimize the geometric structure and chemical ordering of NPs.

In a Brownian move the system is evolved following its internal forces; the evolution is simulated by molecular dynamics (see Section 2.3.1 for more details), with very short runs (200-300 steps with a timestep of few fs) at high temperature, typically in the range 2000-3000 K [50]. The molecular dynamics algorithm is of Langevin type [29].

Exchange moves are used in the case of bimetallic NPs; a pair of atoms of different species is selected, and their positions are exchanged. The atomic pair may be selected randomly, but in some cases tailored exchanges are employed, in which atoms are chosen with different probability depending on their position [22, 41, 51]. Tailored exchange moves require some knowledge of the system equilibrium properties, specifically its tendency towards mixing or phase separation, and the tendency towards surface segregation of the two metals. For example, in the case of mixing systems, it is useful to design moves in which atoms surrounded by neighbours of the same type are more likely to be chosen for the exchange [52].

Brownian moves are mainly used for optimizing the geometric shape of pure NPs, whereas exchange moves are mainly used for optimizing the chemical ordering of nanoalloys at fixed geometry. The optimal acceptance temperature is different for the two moves: the best results in terms of final energy and convergence time have been obtained for  $T$  in the range 1000-2000 K for structure optimization by Brownian moves, and in the range 100-300 K for chemical ordering optimization by exchange moves [13, 53]. In the case of nanoalloys, it is possible to optimize geometry and chemical ordering at the same time by combining Brownian and exchange moves. Good results have been obtained by simulations with 80% of Brownian moves and 20% of exchange moves [13]; two different acceptance temperatures must be set, in the same ranges as in pure Brownian/exchange moves optimizations.

## 2.3 COMPUTATIONAL TECHNIQUES FOR THE SIMULATION OF KINETIC PHENOMENA

Along with equilibrium properties, the kinetic behaviour of metallic NPs is a widely investigated subject. The computational study of kinetic phenomena, such as phase transitions, growth and coalescence, requires the simulation of NP time evolution. To this end, many techniques have been proposed in the literature, from atomistic to coarse-grained and to semi-macroscopic approaches (see for example Refs. [54-63], and the recent review articles in Refs. [64, 65]). Here we focus on

the techniques that has been used in this thesis.

A commonly used technique is *molecular dynamics*, which is able to reproduce the evolution of the system in a realistic way, by identifying physical trajectories in the phase space. The main drawback of molecular dynamics is the time scale of the simulations, which is presently limited to few tens of  $\mu\text{s}$  even if atomistic potentials are employed to describe the system. In some cases such limitations can be overcome by the use of different types of *accelerated techniques* [66]. Accelerated techniques are usually rather complex, and some of them have to be carefully adjusted to each particular system before being employed. However, when used properly, they are really effective in accelerating the dynamics of the system and in enhancing the time scale of the simulations. In this thesis *metadynamics* [67], a well-known accelerated technique, has been employed; the main aspects of this technique are discussed in the following, after a brief description of molecular dynamics.

### 2.3.1 MOLECULAR DYNAMICS

In classical molecular dynamics (MD), the Newton equations of motion of each atom are numerically solved. Forces are calculated as the gradient of the potential energy. The numerical resolution consists of discretizing the time in steps of duration  $\delta t$ , and by applying some recursive algorithm; in this thesis the velocity Verlet algorithm [29] has been used. To ensure the precision of the MD trajectories,  $\delta t$  should be small enough to provide a sufficiently dense sampling of the motions of the system. In the case of metallic nanoparticles, typical oscillation periods of atoms around their local equilibrium positions are in the range of few ps, therefore  $\delta t$  values in the range of few fs are commonly used. A recent study has shown that the timestep can be increased up to 20 fs in the case of Au nanoparticles, without affecting the precision of the MD simulations [68]. In this thesis, unless otherwise specified,  $\delta t = 5$  fs has been employed.

MD simulations can be performed at constant energy (in the microcanonical ensemble) or at constant temperature (in the canonical ensemble). Constant temperature simulations require the employment of a *thermostat*, an algorithmic tool which ensures the correct sampling of the canonical distribution at the selected temperature. In this thesis all MD simulations have been performed at constant temperature. The Andersen thermostat [29] has been employed: at each MD step, each atom may interact with the thermostat with a probability of  $\eta_c \delta t$ , where  $\eta_c$  is a properly chosen collision frequency; if the collision takes place, a new velocity is extracted from the Maxwell distribution at the desired temperature, and it is used in the propagation of the atomic trajectory. The parameter  $\eta_c$  must be large enough to ensure a stable temperature during the simulation; however, too high values would perturb the atomic trajectories too much, thus producing nonphysical effects. In this thesis we have used  $\eta_c = 5 \times 10^{11} \text{ s}^{-1}$ , which has been proved to not alter atomic diffusion coefficients on the surfaces of noble-metal nanoparticles [69].

### 2.3.2 METADYNAMICS

Metadynamics [67] (MetaD) is one of the most widely used accelerated techniques. It is able to considerably speed up the evolution of the system, therefore allowing the observation of rare events within an affordable simulation time. MetaD simulations can be employed to induce the system to abandon metastable states with long lifetimes, and to explore new configurations. Another use of this technique, which is here mentioned briefly, is the reconstruction of the free energy profile.

The basic idea of MetaD is very simple, but its implementation requires the definition of a set of new variables, called *collective variables* (CVs). CVs are calculated from the atomic positions, and their purpose is to simplify the description of the system. In the following, we present the main aspects of the CVs-based description and of MetaD technique; to this end, we follow the treatment made in Ref. [70], of which the same notation is used. We refer to Ref. [70] and to Ref. [71] for further details.

Let us consider a system described by a set of coordinates  $x$ , typically the spatial coordinates of the atoms, and by a potential energy  $V(x)$ . The system evolves at constant temperature  $T$ . Here we want to describe the properties of the system as a function of a set of CVs  $S_a(x)$ ,  $a = 1, \dots, d$ .  $d$  is a small number: in most cases,  $d = 1$  or  $d = 2$  is chosen, which corresponds to a considerable simplification of the system description. The choice of the most proper CV set is discussed later on.

The equilibrium probability distribution of these new variables is given by

$$P(s) = \frac{\exp\left(-\frac{1}{k_B T} F(s)\right)}{\int ds \exp\left(-\frac{1}{k_B T} F(s)\right)}, \quad (2.6)$$

where  $s = (s_1, \dots, s_d)$  denotes the generic state in the  $d$ -dimensional space of the CVs, and the free energy  $F(s)$  is calculated as

$$F(s) = -k_B T \ln \left( \int dx \exp\left(-\frac{1}{k_B T} V(x)\right) \delta(s - S(x)) \right). \quad (2.7)$$

All configurations  $x$  corresponding to the CV value  $s$ , i.e. those for which  $S(x) = s$ , give nonzero contributions to the free energy  $F(s)$ .

Let us now consider the case in which the system gets trapped in a metastable state during its evolution. In this situation, the dynamics of the system is confined in a narrow region of the CV space, around a local minimum of  $F(s)$ , at the bottom of a deep free energy well. In order to force the system to abandon such metastable state, the MetaD algorithm acts by modifying the free energy profile in a small area around the system position in the CV space: every  $\tau_G$  MD steps, a small repulsive Gaussian potential is added, and it is used in the calculation of the forces and of the atomic trajectories in the subsequent MD steps. The total MetaD potential acting on the system at the time

$t$  is given by

$$V_G(S(x), t) = w \sum_{\substack{t' = \tau_G, 2\tau_G, \dots \\ t' < t}} \exp \left( - \sum_{a=1}^d \frac{(S_a(x) - s_a(t'))^2}{2 \delta s_a^2} \right). \quad (2.8)$$

Three parameters of the Gaussian functions have to be tuned:

1. The Gaussian height  $w$
2. The Gaussian width  $\delta s_a$  for each CV
3. The period  $\tau_G$  at which the Gaussians are added.

A proper choice of these parameters is needed to ensure the efficiency and the precision of the MetaD simulations, as we discuss later.

In order to better understand how MetaD is able to influence the system evolution, it is useful to consider a simple example. In Fig. 2.3.1(a) we show the free energy profile of a system described by a single CV, namely  $s$ . At the beginning of the simulation, the system is in the central minimum, which corresponds to  $s \simeq 0$ . Here the free energy barriers separating the central minimum from the two nearby minima are much higher compared to the thermal energy at the simulated temperature; therefore the probability of escaping from the central free energy well during a standard MD simulation is quite low. MetaD acts by depositing Gaussian functions along  $s$  during the simulation; in this example,  $w = 0.3$  and  $\delta s = 0.4$  are used (free energy values are expressed as a fraction of the thermal energy  $k_B T$ ), and  $\tau_G$  corresponds to 300 MD steps. After the addition of 20 Gaussians, the central well is filled (see Fig. 2.3.1(b)); the free energy barrier on the left does not exist anymore, and the system can therefore easily move to the left region of the  $s$  space. In this way, a new minimum is reached, at  $s \simeq -4$ . If we want to observe the transition to the lowest free energy minimum, at  $s \simeq 4$ , we have to continue the MetaD simulation: after the deposition of 69 Gaussians also the left well is filled (Fig. 2.3.1(c)), so that the system can freely move in the  $s$  region corresponding to the left and central minima. The level of the free energy barrier on the right is eventually reached, and the system moves to the lowest minimum. The action of the MetaD algorithm has therefore forced the system to explore different configurations, corresponding to all possible values of  $s$  within the displayed interval. Moreover, it has allowed to observe the transitions from the initial metastable minimum to the left minimum, and then to the lowest minimum, which would have been unlikely in a standard MD simulation.

If the MetaD simulation is continued, the free energy well on the right is eventually filled; this happens after the deposition of 180 Gaussian functions, as shown in Fig. 2.3.1(d). At this stage, the modified free energy profile exhibits no barriers, and the system can move freely through all the  $s$  interval (Fig. 2.3.1(e)). This situation is called *diffusive regime*.

In the top panels of Fig. 2.3.1 the MetaD potential  $V_G$  is shown.  $V_G$  increases as the simulation proceeds, and at the end of the simulation, when the diffusive regime is reached, it exactly compen-

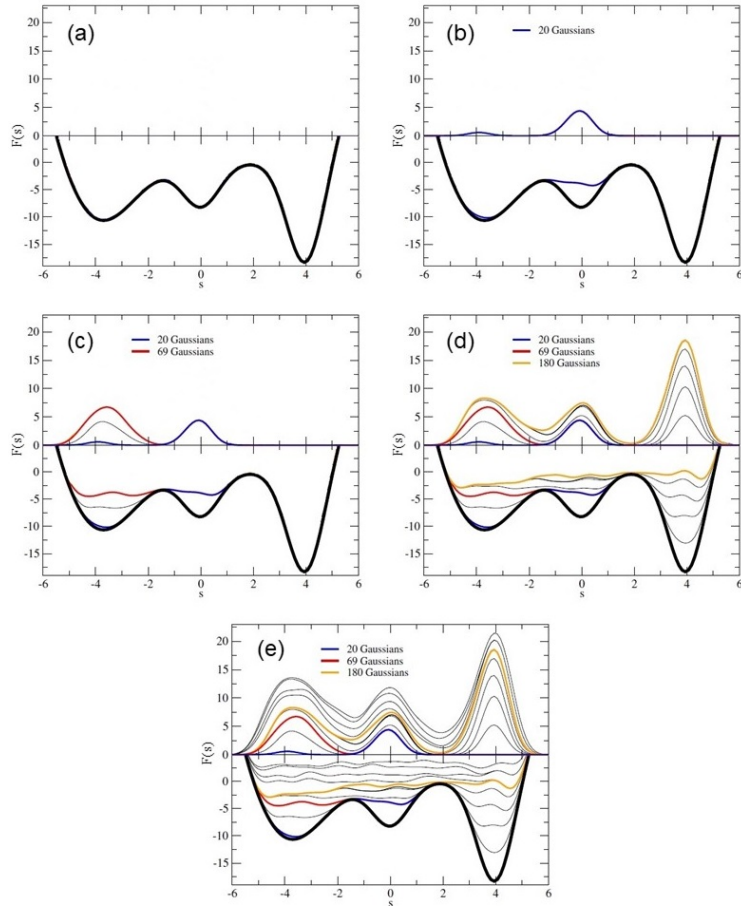


**Figure 2.3.1:** Action of the MetaD algorithm in the case of a one-dimensional CV space. The parameters are:  $w = 0.3$ ,  $\delta_s = 0.4$  and  $\tau_G = 300$ . Free energy values are expressed as fractions of the thermal energy  $k_B T$ . The five graphs correspond to subsequent stages of the MetaD simulation. Top panel: MetaD bias potential  $V_G$ . Bottom panel: unbiased free energy profile (thick black line) and how it is modified by the addition of  $V_G$  (thin black lines and coloured lines). (a) Beginning of the simulation, with the system in the central minimum. (b) The central free energy well has been filled. (c) The free energy well on the left has been filled. (d) The lowest free energy well on the right has been filled. (e) Diffusive regime: the system moves freely through all the  $s$  space.

*Adapted from A. Laio and F. L. Gervasio, Metadynamics: a method to simulate rare events and reconstruct the free energy in biophysics, chemistry and material science, Rep. Progr. Phys., 71:126601, 2008*

sates the underlying free energy profile. The reconstruction of the free energy profile in the space of the chosen CVs is indeed a common application of MetaD. In this thesis, MetaD has not been employed to this aim, but solely to study transitions from initial metastable configurations with long lifetime. Although some attempts have been made to obtain a partial free energy profile, we have never achieved satisfactory results. The problems in reconstructing the free energy profile in the case of NPs will be discussed in Chapter 4.

As anticipated, a proper choice of the parameters of the MetaD bias potential is essential. Specifically, we need to find a balance between efficiency and accuracy of the sampling during the simulation. Large values of  $w$  and  $\delta s$ , along with high deposition frequency, allow for a fast sampling of the CV space, whereas the accuracy of the sampling is higher if small  $w$ ,  $\delta s$  and deposition frequency are chosen. In most cases it is possible to make a rough estimate of the energy barriers involved, whereas the width of the CV region visited during the evolution is typically known, at least approximately, from the definition of the CVs employed. The parameters  $w$  and  $\delta s$  have to be chosen accordingly, so that they are small with respect to such estimated values.

Finally, the efficiency of the MetaD simulations and the reliability of the results obtained are largely based on the proper choice of the CVs. In the study of the transitions, a good set of CVs must be able to distinguish between the initial state, the final state and all relevant intermediate states appearing during the evolution. Moreover, as already mentioned, the number of the CVs must not be too large; otherwise, a long simulation time would be required and the use of MetaD would therefore be of little advantage. In the literature, many examples of CVs can be found. Such a great variety is due to the highly specific nature of most CVs: very often, a set of CVs is suitable for describing the class of systems for which it was originally proposed, but it cannot be used just as effectively in other cases. As a consequence, when we face the analysis of a new system or transition by MetaD, a major initial effort is required to determine the best variables to use.

In the field of NPs, MetaD has been employed to investigate structural transformations of mono- and bi-metallic systems [59, 72–74], coalescence [61] and solidification pathways [62]. In this thesis we have used MetaD simulations to study the diffusion of impurities within NPs; details on the MetaD simulations and results, and on the choice of the CVs, will be given in Chapter 4.

# 3

## Out-of-equilibrium growth pathways of pure Pt and alloyed Pt-Pd nanoparticles

THE GROWTH of metallic nanoparticles is the subject of several studies, in both experimental and theoretical fields. The interest in growth processes arises from the observation that the final size, geometric shape and chemical ordering of nanoparticles and nanoalloys are deeply influenced by the synthesis technique employed to produce them, and by the specific growth conditions chosen in the experiments. On the experimental side, much effort has been made to design and refine growth procedures aimed at producing specific nanoparticle configurations, with a view to their possible applications. Theoretical and computational studies are very often focused on describing the possible growth mechanisms at the atomic level, and on identifying the physical driving forces that are able to direct the growth towards a specific geometric motif or chemical arrangement.

Here, the term “growth” refers to a particular stage of the nanoparticle synthesis, in which a stable nucleus progressively increases its size mainly by the addition of monomers from the surrounding environment. The size of a growing nanoparticle may increase also because of coalescence, i.e. the collision and merging with other nanoparticles. However, coalescence usually takes place in the final part of the synthesis, whereas in the first stages its effects are almost completely negligible. Coalescence will be analysed separately in Chapter 5.

In general, growth is a complex phenomenon, in which many different effects are involved. In some cases the interaction with the environment plays a major role; this typically happens in wet-chemistry synthesis, in which nanoparticles are grown in liquid solution in the presence of organic



and inorganic molecules. In gas phase synthesis, the growth takes place in highly clean conditions, under the sole influence of interatomic attractive forces between metal atoms and of the interaction with an inert (carrier) gas. However, growth processes are usually rather complex also in this case: the final outcome strongly depends on the selected synthesis conditions, often in a somewhat unpredictable way; in addition, different metallic systems can exhibit rather different behaviours when the same growth conditions are employed.

The driving forces of nanoparticles growth can be divided into two groups, namely equilibrium and out-of-equilibrium driving forces. Equilibrium driving forces are responsible for those structural and chemical rearrangements leading the system towards thermodynamic equilibrium; conversely, under the action of out-of-equilibrium or kinetic driving forces the system takes far-from-equilibrium configurations. From the competition between equilibrium and kinetic driving forces, different growth pathways arise, leading to a rich variety of possible final outcomes.

In general, two growth regimes can be identified. In the *equilibrium regime*, equilibrium driving forces are dominant, so that the system is close to thermodynamic equilibrium at each stage of the growth. In the *out-of-equilibrium regime*, the opposite holds: kinetic trapping effects play a major role, and the system is not able to approach equilibrium. Typically, the degree of equilibration is related to the speed of the growth process; specifically, it increases when the growth is slowed down.

A combined regime is also possible, in which equilibration is achieved in the first part of the growth, whereas in the second part kinetic effects are dominant. This is due to the size-dependence of typical equilibration times, which become longer and longer as the nanoparticle becomes bigger.

In this chapter, two examples of out-of-equilibrium growth are presented. In the first one, the growth pathways of far-from-equilibrium geometric shapes are described, in the case of monometallic Pt nanoparticles. In the second one, we discuss the formation of different out-of-equilibrium chemical arrangements in Pt-Pd nanoalloys. In both cases, the presented results have been achieved by a combined experimental-theoretical approach: nanoparticles have been produced in controlled growth conditions and characterized by high-precision observation techniques, and long-scale molecular dynamics simulations have been performed to analyse the growth at the atomic level. A remarkable agreement between experimental and computational results has been obtained; moreover, we have been able to provide a detailed atomic-level description of the growth mechanisms leading to the observed out-of-equilibrium structures, and of the kinetic driving forces responsible for them.

Here we mostly focus on the computational part of these studies. The main experimental results are shown, but we do not dwell on experimental details; a complete description of the experimental methods can be found in Refs. [75] and [76], respectively for Pt and Pt-Pd growth.

As all synthesis experiments have been performed in the gas phase, in the first paragraph of this chapter a brief description of this technique is provided; such description will be useful also for understanding the experimental results presented in the following chapters. The second paragraph is dedicated to the computational details of growth simulations by molecular dynamics. Finally, the results on the growth of pure Pt and binary Pt-Pd nanoparticles is shown and discussed.

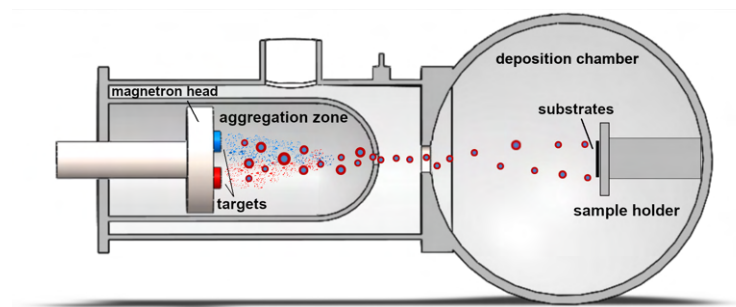


**Figure 3.1.1:** Schematic representation of bimetallic nanoalloys synthesis by magnetron sputtering.

Reproduced from D. Nelli, A. Krishnadas, R. Ferrando and C. Minnai, *One-Step Growth of Core–Shell (PtPd)@Pt and (PtPd)@Pd Nanoparticles in the Gas Phase*, *J. Phys. Chem. C*, 124:14338-14349, 2020.

### 3.1 GAS PHASE SYNTHESIS OF MONO- AND BI-METALLIC NANOPARTICLES

In gas phase synthesis, a beam of NPs is produced from the condensation of a metallic vapour. The metallic vapour is obtained from a solid target, which is either heated or bombarded according to the specific cluster beam source employed in the experiment. All experimental results presented in this thesis refer to NPs and nanoalloys obtained by magnetron sputtering sources [77], in which inert-gas ions are ignited over the metallic target by applying a DC potential, and confined by a magnetic field. In the case of bi- or multi-metallic NPs, different pure metallic targets are used simultaneously; the sputtering current applied to each target can be adjusted separately, thus providing control over the mole fraction of metals in the metallic vapour, and therefore over the NPs composition. The metallic vapour is cooled down by a tunable flux of inert gas (typically Ar or He), which induces the aggregation of the atoms and the progressive growth of the NPs. The region of the experimental apparatus in which aggregation and growth take place is called *aggregation* or *condensation zone*. Finally, the obtained NP beams enters a lower-pressure *deposition chamber*, and NPs are deposited on a solid substrate. The acceleration towards the substrate is provided by a DC potential, as the NP beam produced by magnetron sputtering is usually positively charged [78]. Before deposition, NPs can be selected in size through a mass filter, in order to obtain monodisperse samples. A schematic representation of bimetallic nanoalloys synthesis by magnetron sputtering is shown in Fig. 3.1.1.

In most cases, NPs are directly deposited on an amorphous carbon-coated microgrid, and they are then observed and characterized by Transmission Electron Microscopy (TEM) techniques [79]. TEM allows to precisely identify both the geometric shape and the chemical ordering of the produced NPs: high-resolution aberration-corrected scanning TEM (STEM) enables atomic imaging at sub-angstrom resolution; in addition, it can be combined with X-ray energy-dispersive spectroscopy (STEM-EDX) [80] to obtain a map for the distribution of the different elements within the NP [81].

Gas phase techniques are usually costly and time-consuming, and allow to produce much smaller quantities of NPs compared to other synthesis methods. However, the obtained NPs are highly

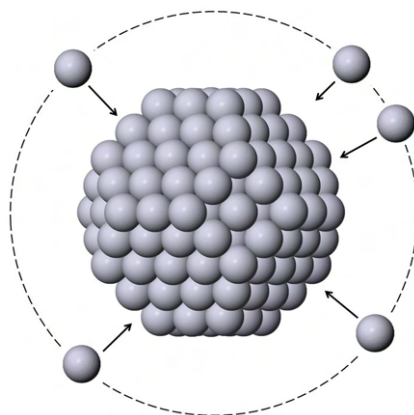


**Figure 3.2.1:** Schematic representation of a MD growth simulation. Atoms are deposited one by one, from random directions. The initial position of the incoming atom is chosen on a sphere containing the growing cluster, whereas the magnitude of the initial velocity is extracted from a Maxwell distribution at the chosen deposition temperature, and the direction is toward the cluster.

pure and contaminant-free, as the growth takes place in ultra-high vacuum conditions, which is an extremely clean environment. This makes gas phase synthesis experiments the ideal platform to study the fundamental mechanisms at the basis of NP growth.

### 3.2 MOLECULAR DYNAMICS GROWTH SIMULATIONS

MD is an effective simulation method for studying NP growth in the gas phase. In our simulations, an initial seed is selected, and atoms are isotropically deposited on it from random directions. Specifically, the starting position of each deposited atom is randomly chosen on a sphere centered on the geometric centre of the growing cluster, whose radius is larger by 0.6 nm than the maximum radius of the cluster. The initial velocity of the deposited atom is directed towards the cluster, and its modulus is extracted from a Maxwell distribution at the growth temperature. A schematic representation of our MD growth simulations is shown in Fig. 3.2.1. Atoms are deposited one by one, at a fixed deposition rate. The simulation results presented in this chapter have been obtained by depositing one atom every 1 or 10 ns, corresponding to deposition rates of 1 and 0.1 atoms/ns. Time scales up to 10  $\mu$ s have been reached; these times scales approach the typical experimental growth times, which are estimated to range from a fraction of ms to a few ms [14].

The action of the carrier inert gas is mimicked by a thermostat (see Section 2.3.1). Simulations with explicit carrier gases can be performed as well, but the number of atoms in the simulation would become quite large, therefore limiting the time scale. The experimental temperature of the NPs during the growth is not known exactly. We expect that in first stages of nucleation and growth the temperature is quite high, and then the NPs cool down while moving along the aggregation zone due to the interaction with the carrier gas; however, it is difficult to precisely estimate the initial temperature and then how fast it decreases as the NP grows. Our growth simulations are performed

at constant temperature; different temperatures have been considered, in the range of 300-900 K, depending on the system and on the initial NP size. This wide temperature range has been chosen to encompass the experimental growth temperatures related to the stages after nucleation.

MD growth simulations are able to reproduce NP formation in a simple non-interacting environment, such as that provided by gas phase synthesis experiments. A direct comparison between simulation and experimental results is therefore possible, and it can help us to unravel the physical mechanisms taking place during the growth.

### 3.3 DEFECT-DRIVEN SYMMETRY-BREAKING PATHWAYS IN THE GROWTH OF Pt NANOCRYSTALS

Here we discuss the growth of *nanocrystals*, i.e. NPs with crystalline geometric shape. In Section 1.1.1 we have described the crystalline motifs consistent with the fcc lattice: tetrahedron, octahedron and truncated octahedron. All three motifs have been obtained in NP synthesis experiments, for different metallic systems; moreover, growth pathways have been identified in which transformations between the different motifs occur. A TO can grow towards a perfect Oh by completing the six initially truncated tips, and a Th can be obtained starting from a Oh of smaller size. Such shape transformations, which are suggested by the close geometric relationship between the three crystalline motifs, have been observed in synthesis experiments and in growth simulations. However, though the TO  $\rightarrow$  Oh transformation is well understood in the literature since long time (we will discuss it later), the Oh  $\rightarrow$  Th transformation has remained an open problem since its first unambiguous observation in the growth of Pd NPs synthesized by wet-chemistry methods [82]. Indeed, this shape transformation requires the growth of tetrahedral tips on four symmetrically-placed faces of the initial Oh; since the eight Oh faces are equivalent and the growth environment is perfectly isotropic, with atoms landing on the nanocrystals randomly from all directions, the underlying mechanisms of such specific symmetry-breaking process are hard to guess.

We have addressed this problem in the case of the growth of Pt NPs and, for the first time, we have provided an explanation of the atomic mechanism responsible for the growth of a Th nanocrystal from an initial Oh seed. This explanation has been obtained through a detailed analysis of MD growth simulations; it is provided in the following, after showing the experimental results on Pt NPs produced in the gas phase<sup>1</sup>.

#### 3.3.1 EQUILIBRIUM AND OUT-OF-EQUILIBRIUM CRYSTALLINE STRUCTURES

In Fig. 3.3.1 we show the two most abundant shapes obtained in the experiments, in case of size-selected NPs with a nominal mass of 5000 Pt atoms: the Th (Fig. 3.3.1(a)) and the Oh (Fig. 3.3.1(b)).

---

<sup>1</sup>Experiments have been conceived, performed and analysed by Yu Xia (University of Birmingham, UK), Jun Yuan (University of York, UK) and ZiYou Li (University of Birmingham, UK). Experimental and simulation results have been published in Ref. [75].

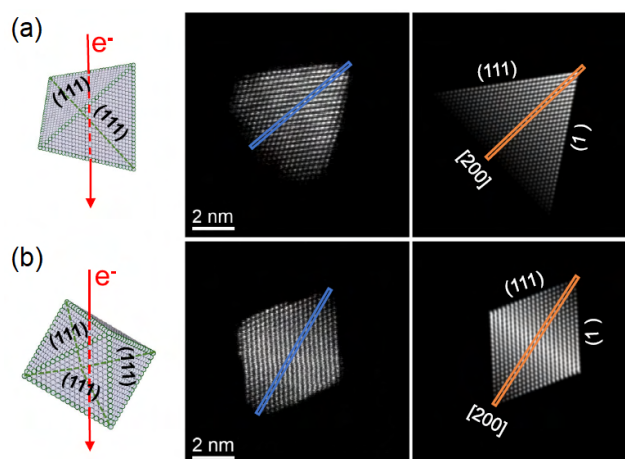


**Figure 3.3.1:** Shape identification of (a) Th and (b) Oh nanocrystal by STEM imaging. Left column: schematic representation of the three-dimensional structures, crossed by the electron beam. Middle column: experimental HAADF-STEM images. Right panel: simulated HAADF-STEM images based on the idealized models shown in the left column. *Reproduced from Y. Xia, D. Nelli, R. Ferrando, J. Yuan and Z. Y. Li, Shape control of size-selected naked platinum nanocrystals, Nat. Commun, 12:3019, 2021.*

Shape identification has been performed by STEM imaging. A STEM image corresponds to the two-dimensional projection of the NP on the plane perpendicular to the electron beam; when the resolution is sufficiently high, atomic columns can be identified, as in central panel of Fig. 3.3.1. To precisely identify the corresponding three-dimensional structures, experimental images have been compared with simulated STEM images of ideal Th and Oh fcc nanocrystals of comparable sizes at all possible orientations (right panel of Fig. 3.3.1).

As already discussed in Section 1.1.1, both Th and Oh are typically out-of-equilibrium structures for fcc NPs, due to the poorly compact shape and the high number of low-coordinated edge and vertex atoms. In the case of Pt, this has been verified by annealing experiments and simulations, and by calculations of the excess energy.

The results of annealing experiments and simulations are shown in Fig. 3.3.2. In the experiments, Th and Oh NPs of nominal size 2057 atoms have been heated in situ from room temperature to different final temperatures in the range 500-900 °C; then NPs have been cooled down to room temperature, where the STEM images shown in the figure have been acquired. In both cases, the initial shape is stable up to 700 °C, even though some rearrangements of the atoms occur. Further heating to 800 and 900 °C induces the transformation to a much more rounded shape, well corresponding to a compact TO. The same behaviour has been observed in annealing simulations, in which the equilibration of a Oh of size 2030 to a TO has been achieved, even though the total duration of the simulations is much shorter compared to the experimental time scales.

Our results suggest that the equilibrium structure for Pt NPs is the TO; this is further confirmed by excess energy calculations for regular TO, Oh, Th and truncated Th structures with different

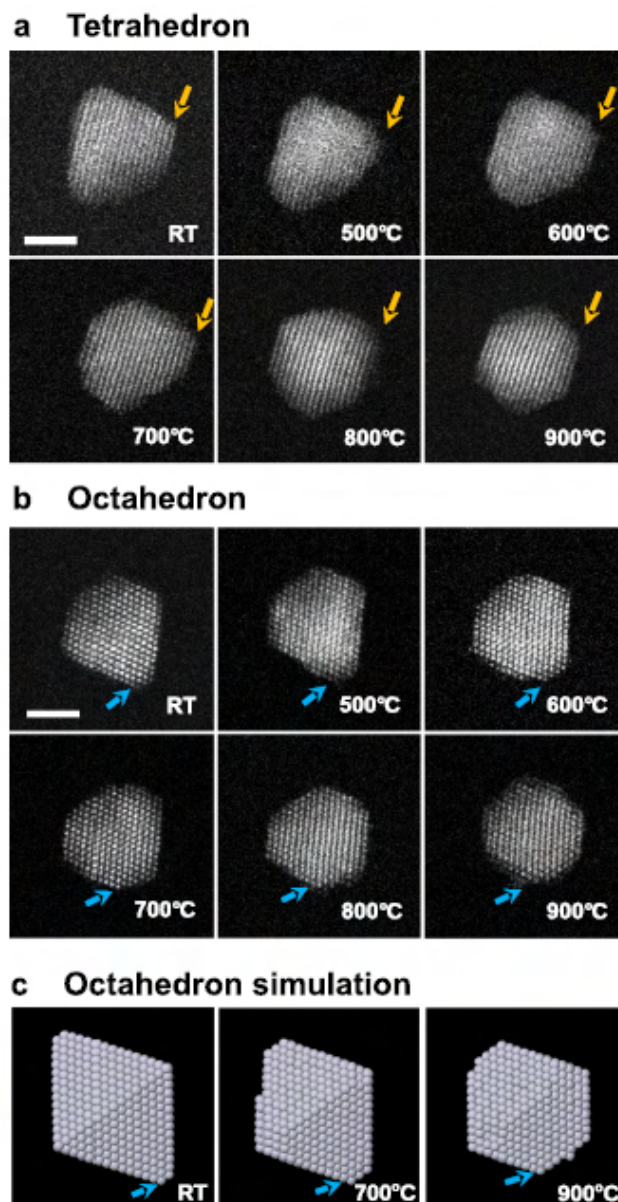


**Figure 3.3.2:** Shape transformation of (a) Th and (b) Oh NPs of nominal size 2057 atoms during annealing experiments, and of (c) Oh NP of size 2030 during annealing simulations. In each panel, the annealing temperature is shown, i.e. the maximum temperature reached before the NP is cooled down again to room temperature (RT). All images have been acquired at RT. Heating and cooling rates in annealing simulations are 1 K/ns and -1 K/ns, respectively. *Reproduced from Y. Xia, D. Nelli, R. Ferrando, J. Yuan and Z. Y. Li, Shape control of size-selected naked platinum nanocrystals, Nat. Commun., 12:3019, 2021.*

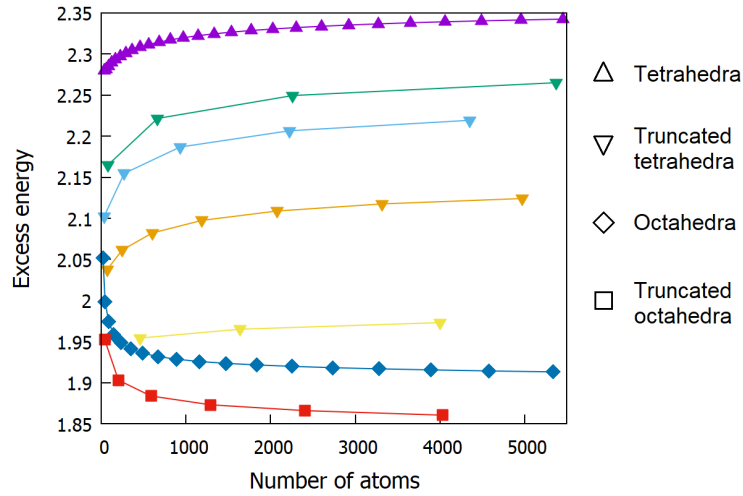


**Figure 3.3.3:** Excess energy of Pt NPs with different structural motifs. Excess energy is shown as a function of number of atoms in the NP, for regular TO, Oh, truncated Th and Th. Reproduced from the Supplementary Information of Y. Xia, D. Nelli, R. Ferrando, J. Yuan and Z. Y. Li, *Shape control of size-selected naked platinum nanocrystals*, *Nat. Commun.*, 12:3019, 2021.

degrees of symmetric truncation. The excess energy  $E_{exc}$  is defined as [14]:

$$E_{exc} = (E + N\varepsilon)/N^{2/3}, \quad (3.1)$$

where  $\varepsilon$  is the cohesive energy per atom in bulk Pt,  $E$  and  $N$  are the binding energy and the number of atoms of the NP. The excess energy allows to compare the energetic stability of different structural motifs:  $E_{exc}$  is lower for motifs closer to equilibrium. The results for Pt NPs shown in Fig. 3-3-3 clearly demonstrate that regular TO are the most energetically stable structures, followed by Oh, truncated Th and Th. Lesser and lesser truncations give tetrahedral structures of higher energy.

It is therefore evident that the growth of out-of-equilibrium Th and Oh NPs observed in the experiments must be due to kinetic processes, which have been investigated by further experiments and simulations.

### 3.3.2 EXPERIMENTAL EVIDENCE OF THE OH $\rightarrow$ TH SHAPE TRANSFORMATION DURING NANOPARTICLE GROWTH

The mean value of the NP size distribution can be varied by tuning the experimental parameters of the growth, specifically the He flow rate introduced in the condensation chamber. The use of a mass filter before the NP deposition allows to strongly reduce the dispersion of the size distribution, thus obtaining almost perfectly monodisperse samples. The shape distribution of such size-selected samples has been analysed for different NP sizes, namely 3900, 5000, 10000 and 20000 Pt atoms. The results of the shape characterization are shown in Fig. 3-3-4. The most prominent finding is that the dominant shape of the Pt<sub>5000</sub> NPs is Oh (73% of the NPs counted) while the dominant shape of the Pt<sub>20000</sub> NPs is Th (52% of the NPs counted). The results for Pt<sub>10000</sub> NPs are in between. It

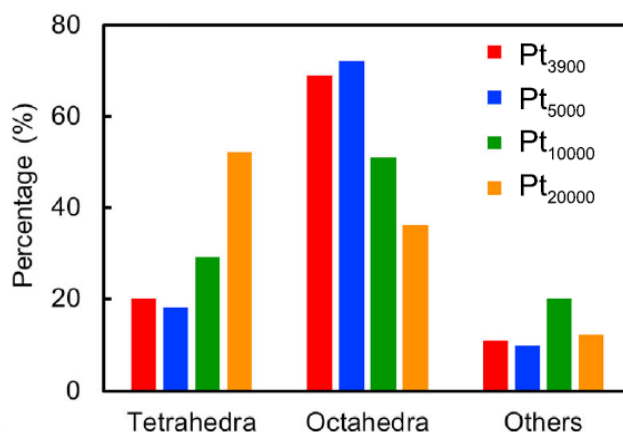


**Figure 3.3.4:** Shape distribution of size-selected NP samples, for different NP sizes. The percentage of Th, Oh and other structures is shown. “Others” refer to single or multiply twinned particles, hexagonal-shaped particles or elongated particles. Reproduced from Y. Xia, D. Nelli, R. Ferrando, J. Yuan and Z. Y. Li, *Shape control of size-selected naked platinum nanocrystals*, *Nat. Commun.*, 12:3019, 2021.

seems that as the size increases, there is a higher percentage of NPs with the Th shape. In other words, at least some of the Th NPs are grown from the smaller Oh.

NPs classified as “others” in Fig. 3.3.4 consist of some single or multiply twinned particles, hexagonal-shaped particles or elongated particles. The absolute numbers of these NPs are small and comparable in all measured samples, so they may not play significant roles in the growth pathway from Oh to Th. Anyway, this does not exclude the possibility that a few Th may grow without passing through the Oh structure, but data indicate that the Oh route is dominant.

In summary, the experimental results described so far have confirmed the possibility of the Oh → Th growth pathway for crystalline NPs, as already observed in Ref. [82]. Such shape transformation has been obtained in highly clean growth conditions, without the use of precursors or surfactants, meaning that it can arise from driving forces inherent to the kinetics of the pure metal condensation.

### 3.3.3 TWO-STEP OUT-OF-EQUILIBRIUM GROWTH SEQUENCE OF FCC NANOCRYSTALS

We can identify a kinetic growth pathway in which the NPs progressively move further and further away from equilibrium, while growing in the context of crystalline structural motifs. This pathway comprises two steps: (i) TO → Oh and (ii) Oh → Th, as schematically shown in Fig. 3.3.5.

Small nuclei formed in the early stage of the growth from the high-temperature atomic vapour are likely to easily equilibrate [14, 17], so that nearly equilibrium TO shapes are formed. They can become Oh after growth on all six (100) facets to complete their vertices, through adatom adsorption and diffusion. Then, the further transformation into Th can only be obtained by growing tips on four (111) facets of the Oh out of eight, in such a way that Oh symmetry is broken in a very specific pattern.



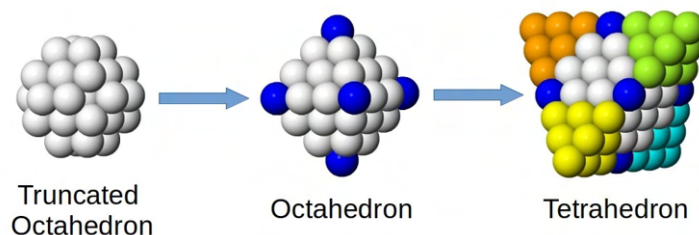


**Figure 3.3.5:** Schematic representation of the two main steps of the growth sequence. A TO (white atoms) becomes a Oh after growth on all (100) facets to complete six vertices (blue atoms). The Th is then obtained by growing equivalent tips on only four (111) facets of the Oh over eight, in such a way that Oh symmetry is broken with a specific pattern. These tips are colored in yellow, green, cyan and orange.

*Reproduced from Y. Xia, D. Nelli, R. Ferrando, J. Yuan and Z. Y. Li, Shape control of size-selected naked platinum nanocrystals, Nat. Commun., 12:3019, 2021.*

The initial TO presents both (111) and (100) facets. Adsorption on (100) facets is more energetically favourable than on (111) facets, by about 0.5 eV in our model. It is well known that atoms deposited on (111) facets can move to the (100) facets where they get trapped, thus growing the octahedral tips [69]. This growth step follows the classical Kinetic Wulff Construction (KWC) model [83, 84], with the out-of-equilibrium growth driven by the growth rates of different facets: (100) facets grow faster so that they tend to disappear.

However, the KWC cannot be applied to the second step of the growth sequence, i.e. the Oh  $\rightarrow$  Th shape transformation: both structures expose the same type of (111) facets only, and therefore we cannot in principle assume different growth rates. A subtler growth mechanism must take place, which is able to break the Oh symmetry and direct the growth towards the more out-of-equilibrium Th shape. In the following paragraph we explain such kinetic mechanism, with the aid of MD simulations.

#### 3.3.4 SYMMETRY-BREAKING ATOMIC PROCESS UNRAVELLED BY MD GROWTH SIMULATIONS: THE ROLE OF METASTABLE SURFACE DEFECTS

In Fig. 3.3.6 we show some representative snapshots of a MD growth simulation performed at 400 K, with a deposition rate of 0.1 atoms/ns (the total duration of the simulation is 8  $\mu$ s). The simulation originally starts from a TO structure of size 201 atoms, which becomes the perfect Oh of size 231 atoms by completing its six vertices, as shown in Fig. 3.3.6(a). The subsequent Oh  $\rightarrow$  Th growth takes place in three fundamental steps:

1. **Formation of a tetrahedral edge.** When the growth starts on a given facet of the Oh, steps are created on that facet. These steps work as traps for adatoms, which are likely to diffuse to the growing facet to stick there. This depletion effect renders the nucleation of islands on nearby facets less likely, and leads to configurations of the type shown in Fig. 3.3.6(b), in which initially growing (G) facets are separated by initially non-growing (NG) facets. NG

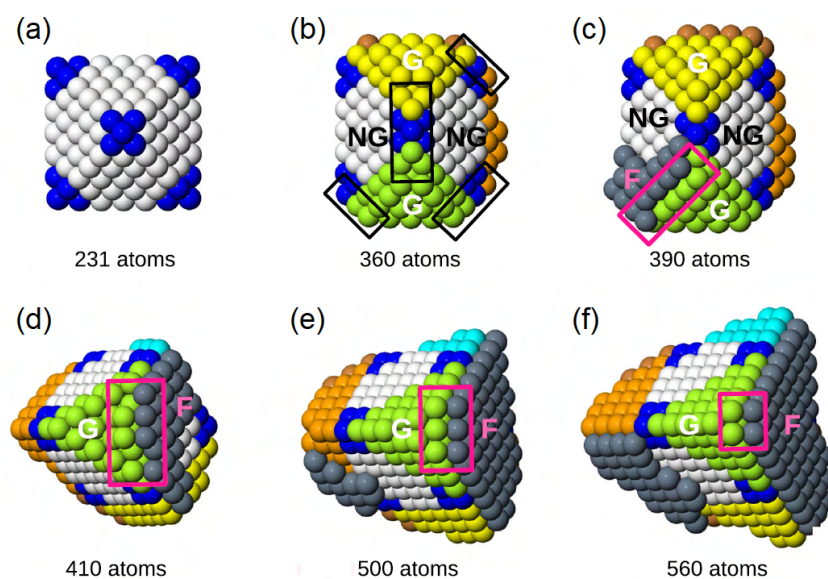


**Figure 3.3.6:** Oh  $\rightarrow$  Th growth pathway. Snapshots from a MD simulation at temperature 400 K and deposition rate 0.1 atoms/ns. Atoms are coloured as follows. Initial TO: white. Atoms completing the Oh: blue; growing Th tips: yellow, green, orange and cyan. Surface atoms in hcp stacking: dark grey. Growing (G) and non-growing (NG) facets are highlighted, as well as the island in stacking fault (F). Tetrahedral edges are enclosed by black rectangles. Fourfold adsorption sites are enclosed by pink rectangles. See the main text for a detailed explanation of the steps of the growth.

Reproduced from Y. Xia, D. Nelli, R. Ferrando, J. Yuan and Z. Y. Li, *Shape control of size-selected naked platinum nanocrystals*, *Nat. Commun.*, 12:3019, 2021.

facets may indeed grow, but at a lower rate than G facets. The growth of a layer on a G facet initiates the formation of a Th edge in its nearby NG facets, as shown in Fig. 3.3.6(b).

2. **Nucleation of an island in stacking fault.** Sharp Th edges present favourable sites for adatom adsorption on the NG facet, so that a small island can nucleate and grow on it, at the border of a G facet. The key symmetry-breaking step starts if the island is in stacking fault, as in Fig. 3.3.6(c). Small islands in fault position are common surface defects of crystalline nanoparticles (see Section 1.1.3). In general, they are expected to eventually revert to the more favourable fcc stacking; however, if the island is able to temporarily maintain the stacking fault placement, the Th growth can start.
3. **Growth of the tetrahedral tips.** The presence of an island in stacking fault on the NG facet creates fourfold adsorption sites on the nearby G facet (Fig. 3.3.6(c)). These sites act as traps for new incoming adatoms, which contributes to locking the island in fault position. These adatoms create further new fourfold adsorption sites, causing an autocatalytic self-replicating process which can lead to the fast growth of a tetrahedral tip (Fig. 3.3.6(e, f)). The fast kinetics of tip growth over the layer-by-layer growth, combined with the symmetric placement of the growing tips, drives the Oh  $\rightarrow$  Th shape transformation.

The scheme above is able to rationalize the symmetry breaking of the growing crystalline NP, and the final achievement of a complete Th. We note that two essential conditions are required. The first condition is the mobility of atoms between nearby facets: atoms must be able to diffuse on the NP surface until finding the most favourable adsorption sites, i.e. the initial step-sites and the fourfold sites on the growing tip. We have verified that in our simulations inter-facet atom mobility occurs by exchange, and is activated already at relatively low temperatures.

The second condition is the stability of islands in fault position close to the Th edges. We have shown that, during the growth of the Th tips, the island is locked in fault position by the growth process itself; however, the small newly-formed island must be stable enough to initiate such process. Atom adsorption is indeed known to be more favourable in the vicinity of edges, from both experimental and computational results on Pt(111) surfaces [85, 86]. Moreover, our calculations of adsorption energies on the surface of small Pt tetrahedral NPs confirm that the most favourable adsorption site for an adatom is the hcp site close to the edge, both at the atomistic and DFT level. These results will be shown and discussed later.

Further evidence of the key role of islands in stacking fault in the growth of Th tips can be found in the analysis of a second MD simulation, performed at 600 K and with a deposition rate of 0.1 atoms/ns. Snapshots of this simulation are shown in Fig. 3.3.7. At size 470 atoms a stable island in hcp stacking is formed (displayed in dark grey in the figure). We notice that this threshold size, which marks the beginning of the Th growth, is larger compared to what observed at 400 K. This means that the system is able to grow within the closer-to-equilibrium Oh motif for longer; we will discuss this point extensively later. The newly-formed island triggers the fast growth of the three

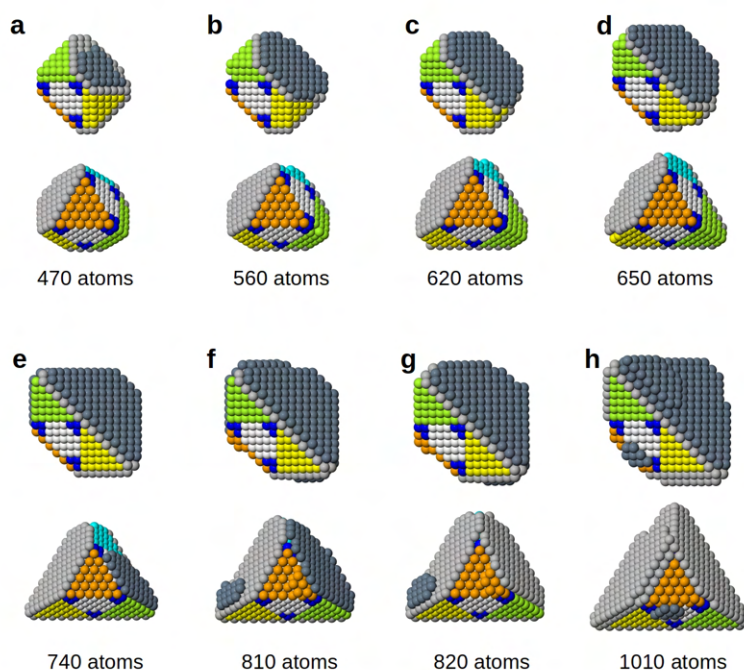


**Figure 3.3.7:** Role of the island in stacking fault in the growth of Th tips. Snapshots from a MD simulation at temperature 600 K and deposition rate 0.1 atoms/ns. Atoms are coloured as in Fig. 3.3.6; further layers in fcc stacking are coloured in light grey. See the main text for a detailed explanation of the steps of the growth.

*Reproduced from the Supplementary Information of Y. Xia, D. Nelli, R. Ferrando, J. Yuan and Z. Y. Li, Shape control of size-selected naked platinum nanocrystals, Nat. Commun., 12:3019, 2021.*

tetrahedral tips over four (those in yellow, green and cyan in the figure) that have borders in common with it, while the orange tip, which has no faulted islands at its border, does not grow (see Fig. 3.3.7(a-d)). At a later stage of the growth, a second faulted island is formed at the border of the orange tip (at its right in Fig. 3.3.7(e)) and the orange tip starts growing one layer (Fig. 3.3.7(f)). This second faulted island reverts back to fcc stacking (Fig. 3.3.7(g)), and the growth of the orange tip stops again, no further layers nucleating beyond the second. The final structure, shown in Fig. 3.3.7(h), is of tetrahedral type, but with three sharp tips and one truncated tip.

We have monitored the number of atoms on the four Th tips during the simulation. Results are shown in Fig. 3.3.8. Here, each curve refers to the correspondingly colored tip of Fig. 3.3.7, and red vertical lines mark the steps of the growth at which islands in hcp stacking are formed. Before the formation of the first faulted island, the green and yellow tips have completed two layers whereas the cyan and orange tips have completed only one layer. After the formation of the island, the green, yellow and cyan tips grow quickly until they complete the last layer. The growth of the orange tip, which is the only one not connected to the first faulted island, is much slower: the tip is blocked at the first layer until a second faulted island is formed at its border. The difference in the growth

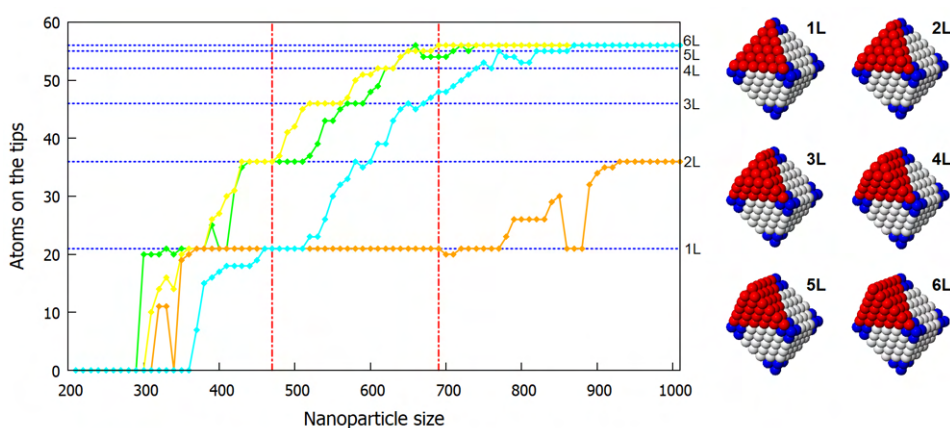


**Figure 3.3.8:** Growth velocity of the Th tips. The graph refers to the growth sequence of Fig. 3.3.7. The number of atoms on the four Th tips during the growth is shown, each curve referring to the correspondingly colored tip of Fig. 3.3.7. Th tips are made of smaller and smaller triangular layers stacked one on another (see the right part of the figure). Blue horizontal lines on the graph point out the number of atoms at which the different layers of the tips are completed, whereas red vertical lines mark the steps of the growth at which islands in hcp stacking are formed.

*Reproduced from the Supplementary Information of Y. Xia, D. Nelli, R. Ferrando, J. Yuan and Z. Y. Li, Shape control of size-selected naked platinum nanocrystals, Nat. Commun., 12:3019, 2021.*

velocities is striking, and it can be unambiguously related to the different positions of the tips with respect to the island in stacking fault.

### 3.3.5 EVIDENCES AND GENERALITY OF THE PROPOSED TH GROWTH MECHANISM

To study the growth of Pt NPs, we have performed 70 independent simulations. The initial seed was the TO of size 201 in all cases, and different growth conditions have been selected: temperature in the range 300-900 K and deposition rate 1 or 0.1 atoms/ns. The Th motif has been obtained in 24 simulations; in all cases, the defect-mediated growth mechanism previously described has been observed. The results of the other simulations, as well as their relationship with the growth conditions, will be discussed later.

Further simulations have been done to reach larger growth sizes, up to more than 14000 atoms, which is in the same size range as those studied in experiments. Significant snapshots of these large-size simulations are shown in Fig. 3.3.9. These simulations have been performed by using the version of our code running on GPUs. Our results confirm that the transitions from TO to Oh and then to Th take place by the same growth mechanisms observed at smaller sizes.

The generality of the defect-mediated Th growth mechanism is supported by many simulations results, which we have obtained for different fcc metals: pure Au, Ag and Pd, and alloyed Au-Ag and Pt-Pd [76, 87].

On the experimental side, a real-time observation of such growth process is difficult to achieve; in our case, such as in most NP synthesis experiments, only the observation of the final outcome of the growth is possible. The high-resolution TEM images of Pt tetrahedral NPs grown in the gas

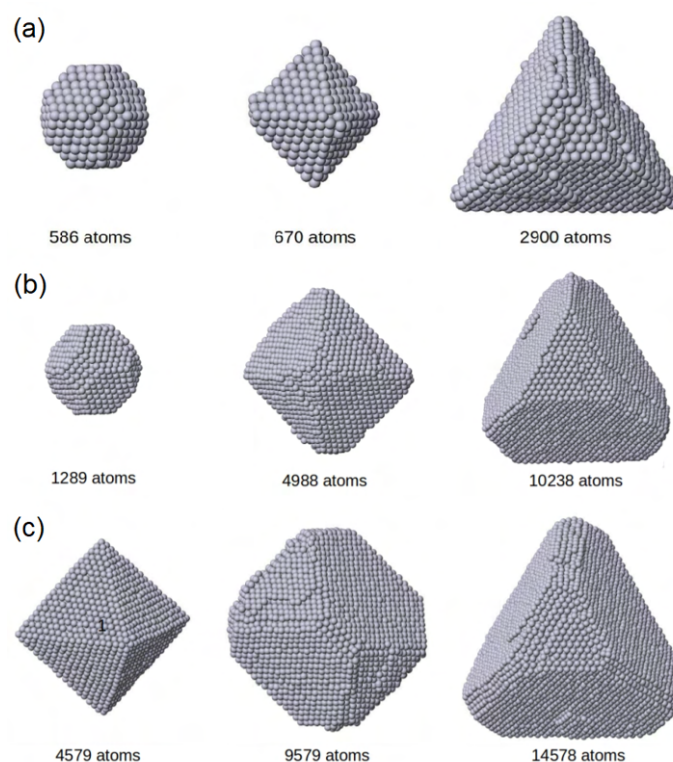


**Figure 3.3.9:** Growth simulations of larger NPs. (a)  $T = 700\text{K}$  and deposition rate of 1 atoms/ns. The simulation is started from a TO of 586 atoms, which grows to a Oh and then to a Th of 2900 atoms. (b)  $T = 900\text{K}$  and deposition rate of 1 atoms/ns. The simulation is started from a TO of 1289 atoms, which grows to a somewhat asymmetric Oh for sizes around 5000 atoms and then evolves towards a Th shape at about 10000 atoms. (c)  $T = 900\text{K}$  and deposition rate of 1 atoms/ns. The simulation starts from a perfect Oh of about 4600 atoms, then it evolves to a deeply truncated Th at about 10000 atoms, which becomes sharper growing up to sizes close to 15000 atoms.

Reproduced from the Supplementary Information of Y. Xia, D. Nelli, R. Ferrando, J. Yuan and Z. Y. Li, *Shape control of size-selected naked platinum nanocrystals*, *Nat. Commun.*, 12:3019, 2021.

phase have been checked, but surface islands in hcp stacking have not been observed. We believe that this is due to their shift to the more favourable fcc stacking at the end of the Th growth process, which indeed frequently takes place in the last stages of our growth simulations (see for example Fig. 3.3.7(f, g)). However, stacking fault islands are visible in Pd tetrahedral NPs grown in the liquid phase (for example on the left of the Th in Fig. 3.3.10, reproduced from Ref. [82]), where those islands may have been stabilized by ligands after growth completion.

### 3.3.6 TH VS. OH GROWTH: EFFECT OF THE GROWTH CONDITIONS

The first step of the out-of-equilibrium growth pathway, i.e. the growth of octahedral tips on the initial TO, has been observed in all our simulations. The symmetry breaking and the evolution

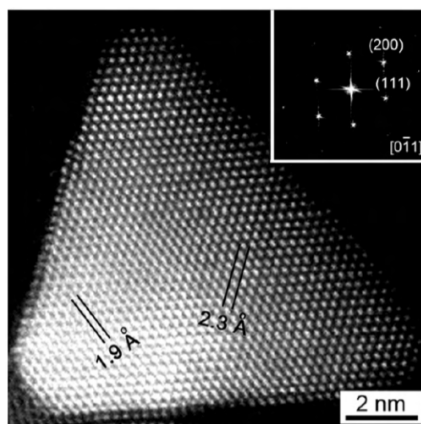


**Figure 3.3.10:** HAADF-STEM image of a Pd truncated tetrahedron grown in the liquid phase. On the left we can see a surface island in hcp stacking, which could be responsible of the development of the Th tips according to the growth mechanism that we have proposed. Reproduced from Y. Wang, S. Xie, J. Liu, J. Park, C. Z. Huang and Y. Xia, *Shape-Controlled Synthesis of Palladium Nanocrystals: A Mechanistic Understanding of the Evolution from Octahedrons to Tetrahedrons*, *Nano Lett.*, 13:2276-2281, 2013.

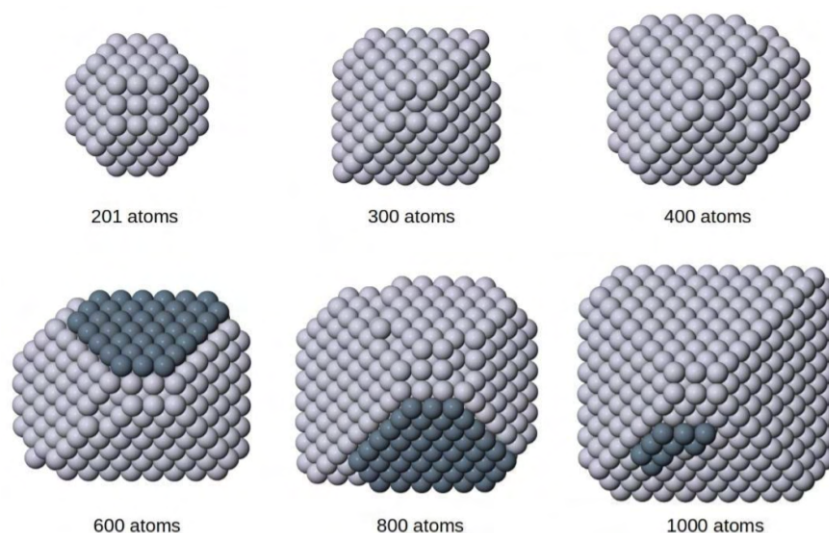


**Figure 3.3.11:** Growth within the Oh motif. Snapshots from a MD simulation at temperature 800K and deposition rate 0.1 atoms/ns. All images are taken from the same perspective. Islands in hcp stacking are shown in dark grey. Reproduced from the Supplementary Information of Y. Xia, D. Nelli, R. Ferrando, J. Yuan and Z. Y. Li, *Shape control of size-selected naked platinum nanocrystals*, *Nat. Commun.*, 12:3019, 2021.

Temperature and deposition rate	Oh	Th	Twins and hexagons	Disordered
300 K, 1 atoms/ns	0	0	0	5
300 K, 0.1 atoms/ns	0	1	0	4
400 K, 1 atoms/ns	0	1	0	4
400 K, 0.1 atoms/ns	0	5	0	0
500 K, 1 atoms/ns	0	5	0	0
500 K, 0.1 atoms/ns	1	4	0	0
600 K, 1 atoms/ns	2	2	1	0
600 K, 0.1 atoms/ns	1	4	0	0
700 K, 1 atoms/ns	4	1	0	0
700 K, 0.1 atoms/ns	5	0	0	0
800 K, 1 atoms/ns	4	0	1	0
800 K, 0.1 atoms/ns	4	0	1	0
900 K, 1 atoms/ns	4	0	1	0
900 K, 0.1 atoms/ns	4	0	1	0

**Table 3.3.1:** Final structures of MD growth simulations at different temperatures from 300 to 900 K and for two deposition rates (1 and 0.1 atoms/ns). Simulations start from a truncated octahedral structure of 201 atoms and are stopped when the NP size reaches 1001 atoms. As regards twins and hexagons, the only structure with hexagonal shape is the one grown at 600 K, whereas the structures grown at 800 and 900 K are triangular twins.

*Reproduced from the Supplementary Information of Y. Xia, D. Nelli, R. Ferrando, J. Yuan and Z. Y. Li, Shape control of size-selected naked platinum nanocrystals, Nat. Commun., 12:3019, 2021.*



towards a complete Th may then take place as previously described, or alternatively the growth can continue within the Oh motif. An example of Oh growth is shown in Fig. 3.3.11. Here snapshots are taken from a simulation at high temperature  $T = 800$  K and deposition rate of 0.1 atoms/ns. In this case, islands in hcp stacking often form but they always revert back to the fcc stacking. At variance with the simulations analysed before, the fourfold adsorption sites formed at the border of faulted islands are not as effective as atom traps because of the higher temperature, so that tetrahedral tip growth is not started.

The results of the MD growth simulations are summarized in Table 3.3.1, in which the frequency of the different structural motifs at the end of the simulation is reported, for the different growth conditions. A correlation can be established between the final geometric shape and the growth conditions, especially the simulation temperature: Th are frequent in simulations performed for temperatures in the range 400-600 K, and they are rarely observed at higher temperatures (indeed only one Th structure has been obtained for  $T = 700$  K and flux 1 atoms/ns), when Oh structure are by far dominant.

We have observed that, in the case of Th growth, the size of the growing NP at which the Oh symmetry breaks depends on the simulation temperature. Specifically, such critical size is larger for higher temperatures, as we can see by comparing the growth sequences at 400 and 600 K shown in Fig. 3.3.6 and 3.3.7, respectively. Therefore we can guess that, if the simulations at  $T \geq 700$  K are continued to reach larger sizes, the growth of tetrahedral tips will eventually begin.

In summary, the overall picture arising from our simulations is that nanocrystals initially grow close to their equilibrium shape, until they reach a critical size at which they are not able to equilibrate anymore. In fact, the larger the NP size, the slower the equilibration of its shape. After that critical size, kinetic trapping begins to dominate, so that Oh grow into Th. This critical size depends both on the growth time scale and on temperature, being small for short growth times and for low temperatures. It can be increased in two ways, namely by growing on longer time scales and by increasing the temperature.

Data in Table 3.3.1 show that final structures different from Oh and Th have sometimes been obtained in our simulations. Disordered structures have been obtained at 300 K, and at 400 K in the case of fast deposition (1 atoms/ns); in these conditions, typical time scales for surface atom diffusion are larger than the interval between subsequent depositions, therefore atoms tend to pile up, and regular shapes cannot be achieved. A flat hexagonal shape have been obtained in one simulations (600 K, 1 atoms/ns). In this case, two islands in stacking fault have formed almost simultaneously on parallel faces of the Oh; from then on, the growth mechanisms were the same as in the Th growth, i.e. the accumulation of atoms in the fourfold sites at the border of the hcp islands and the concurrent enlargement of the islands themselves. However, because of the peculiar relative position of the two islands, a flat-shaped structure have been obtained instead of the usual Th tips. *Triangular twins* have been obtained at 800 and 900 K. These are flat triangular structures, made of two truncated Th connected by a twin plane. They can form if, in the very first part of the simulation, a shift of the atomic planes of the growing NP occurs, so that an internal twin plane appears. Such

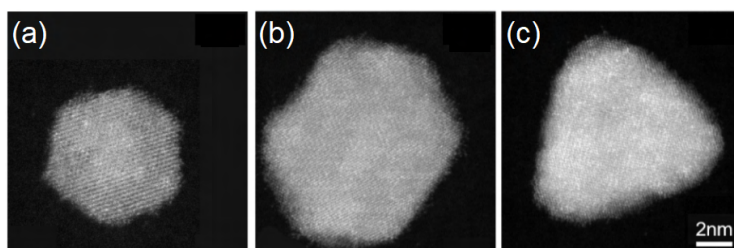


**Figure 3.3.12:** HAADF-STEM images of some of the NPs classified as “others” in Fig. 3.3.4. (a,b) Hexagonal NPs; (c) triangular NP. Reproduced from the Supplementary Information of Y. Xia, D. Nelli, R. Ferrando, J. Yuan and Z. Y. Li, *Shape control of size-selected naked platinum nanocrystals*, *Nat. Commun.*, 12:3019, 2021.

structural rearrangement is made possible by the small size of the NP, and by the high simulation temperature. We have obtained similar hexagonal structures and triangular twins in MD growth simulations of pure Au, Ag and Pd, and alloyed Au-Ag and Pt-Pd NPs [76, 87]. Some hexagonal and triangular Pt NPs have been obtained and observed in our experiments (they have been classified as “others” in Fig. 3.3.4); three examples are shown in Fig. 3.3.12. The agreement between the geometric structures of the observed NPs and the simulated ones is remarkable, and it is an important evidence in favor of the reliability of the model used in our simulations, and of the reliability of the proposed growth mechanisms.

### 3.3.7 ADSORPTION ENERGY ON THE DIFFERENT SURFACE SITES

As already mentioned, the favourable adsorption in the vicinity of the sharp edges of tetrahedral type is needed to initiate the growth process of sharp tetrahedral tips. This is a key point, which deserves to be investigated by more sophisticated calculations; to this end, we have employed DFT calculations, using three different exchange-correlation functionals: Perdew-Burke-Ernzerhof (PBE) [88] functional, a revised version of PBE which improves the description of bulk solids (PBEsol) [89] and the Local Density Approximation (LDA) [90].

All DFT calculations have been made by the open-source QUANTUM ESPRESSO software [91]. For all functionals, the convergence thresholds for the total energy, total force, and for electronic calculations have been set to  $10^{-4}$  Ry,  $10^{-3}$  Ry and  $5 \times 10^{-6}$  Ry respectively. We have used a periodic cubic cell, whose size has been set to 30 Å. Cutoffs for wavefunction and charge density have been set to 39 and 424 Ry for LDA, and to 39 and 401 Ry for PBE and PBEsol, according to Pt.pz-n-kjpaw\_psl.o.1.UPF, Pt.pbe-n-kjpaw\_psl.1.o.o.UPF and Pt.pbesol-n-kjpaw\_psl.1.o.o.UPF, as provided by the QUANTUM ESPRESSO pseudopotential library available at [http://pseudopotentials.quantum-espresso.org/legacy\\_tables/ps-library/pt](http://pseudopotentials.quantum-espresso.org/legacy_tables/ps-library/pt).

In Table 3.3.2 we compare the Gupta and DFT adsorption energies of Pt adatoms on a tetrahedron of 56 atoms (i.e. for total size of the cluster of 57 atoms). The positions of the adsorption sites

	Gupta	PBE	PBEsol	LDA
(a) hcp edge	0.000	0.000	0.000	0.000
(b) fcc edge	0.062	0.261	0.265	0.248
(c) hcp terrace	0.181	0.541	0.553	0.558
(d) fcc terrace	0.185	0.636	0.652	0.612

**Table 3.3.2:** Energies (in eV) of a Pt adatom on the surface of a Pt tetrahedron of 56 atoms according to the Gupta potential and to our DFT calculations with different exchange-correlation functionals. (a-d) refer to the adsorption sites of Fig. 3.3.13. The adsorption energy in site (a) is set to zero.

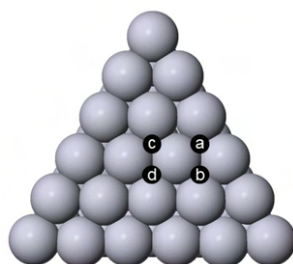


**Figure 3.3.13:** Adsorption sites on the face of a Pt tetrahedron of 56 atoms. (a) hcp site at the facet edge; (b) fcc site at the facet edge; (c) hcp site on the terrace; (d) fcc site on the terrace.

are shown in Fig. 3.3.13.

DFT calculation confirm the results of the Gupta force field: the most favourable adsorption sites turn out to be those in the vicinity of the edge; furthermore, the best site is the hcp one, which is the closest to the edge. We note that, compared to Gupta results, energy differences between the edge hcp site and other adsorption sites are even larger according to all DFT calculations, whose results are very similar.

If we compare the two terrace sites, we find that the hcp is more favourable. This may be due to different reasons. First of all we note that the hcp terrace site is closer to the edge than the fcc site (see Fig. 3.3.13), and this may favour a better relaxation of interatomic distances. Second, we recall that field-ion microscopy experiments of the diffusion of isolated Ir adatoms on Ir(111) showed the preference for hcp sites, even though Ir is a fcc metal [92]. These points deserve a more complete investigation, by considering larger clusters, and also the adsorption of small islands besides isolated adatoms. This work is in progress. However, we have already some data for isolated Au adatoms on Au Th, and the behaviour of Au is of the same type as that of Pt, with a clear preference for adsorption on hcp edge sites [93].

### 3.4 SPONTANEOUS FORMATION OF DIFFERENT CORE-SHELL ARRANGEMENTS IN THE GROWTH OF Pt-Pd NANOALLOYS

In the previous section we have discussed the formation out-of-equilibrium geometric shapes during the growth of monometallic nanoparticles. In the case of nanoalloy growth, the evolution of the chemical ordering must be considered as well. Out-of-equilibrium arrangements are frequently obtained; for example, it is possible to synthesize phase-separated patterns such as core-shell for mixing systems, by subsequent growth of the two atomic species. Here we discuss the formation of such out-of-equilibrium core-shell orderings under a different growth condition, i.e. from an initial metallic vapour in which the two elements are homogeneously mixed.

The system we have considered is Pt-Pd, which is known to have some tendency towards intermixing in the bulk [94]; this tendency have been observed also at the nanoscale, together with some degree of Pd surface segregation [95, 96]. Our experimental results have shown that different types of core-shell nanoparticles can be produced in the gas phase, in one step, according to the composition of the vapour. This peculiar behaviour has been rationalized by global optimization searches and MD growth simulations, which have allowed us to describe the overall growth pathway. Again, an initial close-to-equilibrium growth stage can be identified, which is followed by a second stage dominated by kinetic trapping phenomena. Our experimental and simulation results are shown and discussed in the following<sup>2</sup>.

#### 3.4.1 COMPOSITION-TUNABLE CHEMICAL ORDERING OF NANOPARTICLES GROWN IN THE GAS PHASE

In gas-phase synthesis, the composition of bimetallic NPs can be tuned by adjusting the ratio between the powers applied to the two targets (see Fig. 3.1.1); in this way, it is possible to choose the composition of the initial metallic vapour, which will correspond, at least on average, to the composition of the produced NPs. In our experiments, two composition of the Pt-Pd vapour have been considered, namely a Pd-rich ( $\text{Pt}_{0.2}\text{Pd}_{0.8}$ ) and a Pt-rich ( $\text{Pt}_{0.7}\text{Pd}_{0.3}$ ) composition. The main finding of our experimental results is that the composition of the vapour strongly affects the chemical ordering of the final structures.

In Fig. 3.4.1 we show two NPs, which are representative of the Pt-rich sample (top row) and of the Pd-rich one (bottom row). Their chemical composition has been mapped by STEM-EDX, so that the colors in Fig. 3.4.1(a) are based on the local chemical composition of the NP, and the overall chemical ordering can be identified. Both images are consistent with a core-shell chemical ordering, in which we can clearly distinguish a central core and an outer shell of considerably different composition. Moreover, the arrangement of the two elements is different in the two cases: in the Pt-rich NP, Pd atoms are concentrated in the core and almost absent in the shell, whereas in the

---

<sup>2</sup>Experiments have been conceived, performed and analysed by Chloé Minnai (Okinawa Institute of Science and Technology Graduate University, Okinawa, Japan). Experimental and simulation results have been published in Ref. [76].

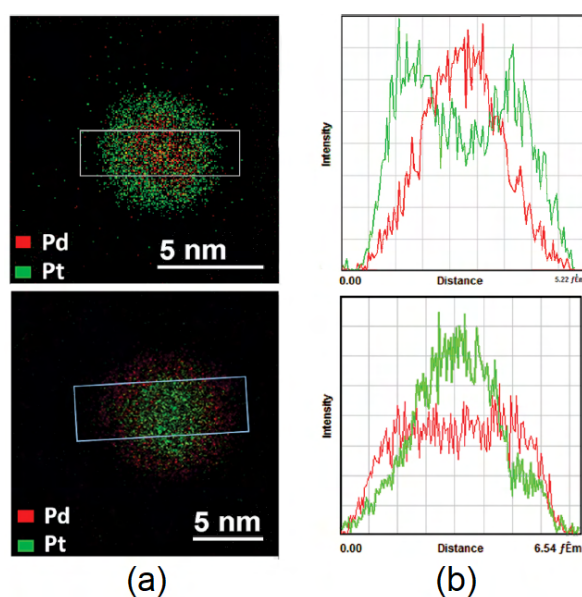


**Figure 3.4.1:** Images of a (PtPd)@Pt NP (top row) and a (PtPd)@Pd NP (bottom row). (a) STEM-EDX mapping of the chemical composition of the NP. The colors are based on the local chemical composition, where Pt is in green and Pd in red. The rectangle in the panel indicates the area from which the profiles are extracted. (c) EDX composition profiles of Pt (in green) and Pd (in red).

Reproduced from D. Nelli, A. Krishnadas, R. Ferrando and Chloé Minnai, *One-Step Growth of Core–Shell (PtPd)@Pt and (PtPd)@Pd Nanoparticles in the Gas Phase*, *J. Phys. Chem. C*, 124:14338–14349, 2020.

Pd-rich NP the opposite holds. The EDX composition profiles in Fig. 3.4.1(c) confirm this evaluation, and show that, while the shell is almost pure, both elements are present in the central region in similar proportions; however, we notice that it is difficult to extrapolate the exact composition of the core by using EDX techniques. The size of such core-shell NPs is in the range 4–10 nm; all NPs fcc have crystalline structure.

In summary, two different chemical ordering types have been obtained, in which the minority element of the initial metallic vapour always concentrates in the central part of the structure, while the shell is strongly enriched in the majority element. This corresponds to the formation of (PtPd)@Pd and of (PtPd)@Pt core–shell structures in the Pd-rich and Pt-rich cases, respectively. These are the most abundant structures in both samples; other observed structures include small sub-2 nm NPs with Pt-Pd composition close to 50%-50% and intermixed chemical ordering, and NPs mainly constituted by the majority element with small contamination of the minority element.

### 3.4.2 EQUILIBRIUM CHEMICAL ORDERING IN Pt-Pd NANOPARTICLES

To understand whether the two experimentally observed core-shell arrangements are equilibrium or out-of-equilibrium chemical ordering types for Pt-Pd NPs, we have performed global optimization searches. We have considered different sizes, namely 201, 586, 1289, 2406, and 4033 atoms, corresponding to sizes from 1.7 to 5.2 nm, which are in the range of interest of our experiments.

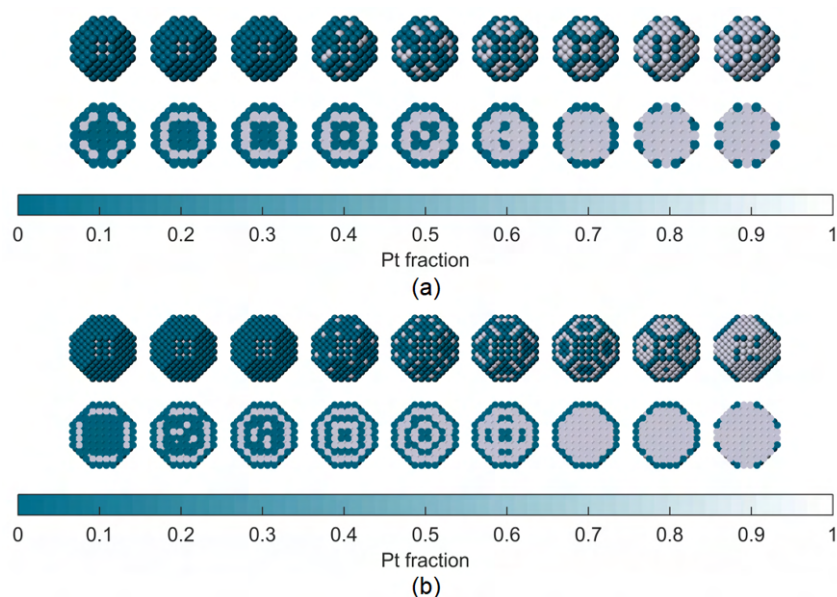


**Figure 3.4.2:** Equilibrium structures for (a)  $\text{TO}_{201}$  and (b)  $\text{TO}_{586}$  nanoparticles at various compositions. The composition is expressed as Pt fraction. For each composition, the image in the top row shows the cluster surface, and the image in the bottom row shows a cross section. Here and in the following figures Pt and Pd atoms are colored in white and blue, respectively. Reproduced from D. Nelli, A. Krishnadas, R. Ferrando and Chloé Minnai, *One-Step Growth of Core–Shell (PtPd)@Pt and (PtPd)@Pd Nanoparticles in the Gas Phase*, *J. Phys. Chem. C*, 124:14338–14349, 2020.

For 201 and 586 atoms we have checked various compositions increasing the Pt fraction from 0.1 to 0.9 in steps of 0.1, whereas for larger sizes we have considered only compositions  $\text{Pt}_{0.2}\text{Pd}_{0.8}$  and  $\text{Pt}_{0.8}\text{Pd}_{0.2}$ . As already mentioned, all experimentally observed Pt-Pd NPs exhibit fcc geometric structures; therefore, here we have considered the fcc TO shape. The geometric shape has been kept unchanged during the simulations (apart from small distortions due to local minimization) while the chemical ordering has been optimized by exchange moves between Pt and Pd atoms (see Section 2.2.2), starting from a randomly intermixed distribution. The acceptance temperature of exchange moves has been set to 100 K. For each system and composition, at least three independent simulations of length  $10^6$  steps have been made.

The lowest-energy chemical arrangements for  $\text{TO}_{201}$  and  $\text{TO}_{586}$  NPs are shown in Fig. 3.4.2. At both sizes we can observe clear tendencies to Pd surface segregation and Pt subsurface segregation. However, such tendencies are not extreme, since for some compositions the central region of the NP contains some Pd atoms even if the surface is not completely made of Pd (see the structures at 0.4, 0.5, and 0.6 Pt fraction in both Fig. 3.4.2(a) and (b)); conversely, in some cases few Pt atoms occupy inner sites even if the subsurface is not completely made of Pt (see the structure at 0.2 Pt fraction in Fig. 3.4.2(b)). At some compositions we can also observe multi-shell arrangements with some degree of local ordering.

The lowest-energy chemical arrangements obtained for  $\text{TO}_{1289}$ ,  $\text{TO}_{2496}$ , and  $\text{TO}_{4033}$  are shown in Fig. 3.4.3. For all sizes, in the Pd-rich case the surface is completely made of Pd, the subsurface

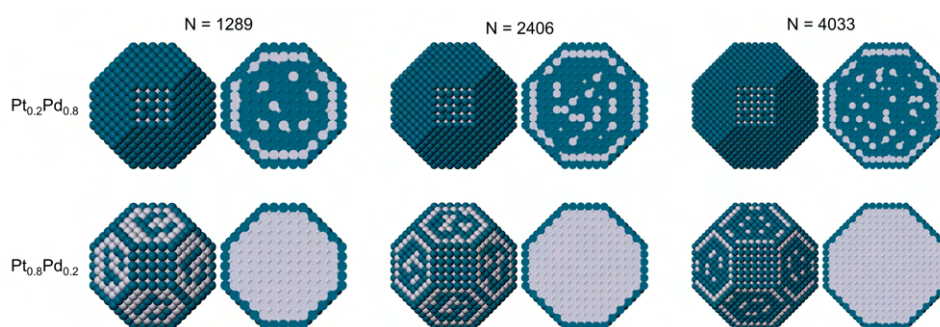


**Figure 3.4.3:** Equilibrium structures for  $\text{TO}_{1289}$ ,  $\text{TO}_{2406}$  and  $\text{TO}_{4033}$ , at  $\text{Pt}_{0.2}\text{Pd}_{0.8}$  and  $\text{Pt}_{0.8}\text{Pd}_{0.2}$  composition. For each structure, the image on the left shows the cluster surface, and the image on the right shows a cross section.

Adapted from D. Nelli, A. Krishnadas, R. Ferrando and Chloé Minnai, *One-Step Growth of Core–Shell (PtPd)@Pt and (PtPd)@Pd Nanoparticles in the Gas Phase*, *J. Phys. Chem. C*, 124:14338–14349, 2020.

is enriched in Pt, and the core is almost randomly intermixed, whereas in the Pt-rich case all Pd atoms are at the surface of the NP. Our optimized structures strongly resemble those in Ref. [96], in which Monte Carlo simulations for Pt–Pd fcc clusters up to 1289 atoms have been performed, and the Pd surface and Pt subsurface segregation has been pointed out, as well as the formation of ordered multi-shell structures at small sizes. In [96] a different parametrization for the SMATB potential has been used, based on DFT data obtained for small clusters; the agreement between the results supports the reliability of our model.

Let us now discuss whether the experimentally observed NPs are at equilibrium or not. To this end, we point out that in none of the structures in Figs. 3.4.2 and 3.4.3 the minority element is concentrated in the NP core. This is evident in the Pt-rich case, in which Pd atoms are mostly on the surface of the NP, but it is true also in the Pd-rich case, in which a large fraction of the Pt atoms is in the subsurface layer. The results of our global optimization searches therefore allow us to establish that the experimentally observed core–shell arrangements are out-of-equilibrium configurations, and therefore are the results of kinetic trapping phenomena taking place during the growth. On the other hand, the experimental sub-2 nm NPs, which exhibit intermixed chemical ordering, are likely to be at the equilibrium.

### 3.4.3 MULTI-STEP OUT-OF-EQUILIBRIUM GROWTH PATHWAY OF CORE-SHELL NANOALLOYS

The inversion of core–shell chemical ordering depending on vapour composition was previously observed in laser-vaporization growth of Au–Ag NPs of 2–3 nm sizes [97]. In that case, the authors have proposed the following explanation: since bimetallic Au–Ag small clusters are energetically more favorable than their elemental counterparts, they will be predominant in the first stage of vapor condensation; these clusters will then aggregate to form the seeds of the NP growth, i.e., the experimentally observed alloyed cores. The higher stability of binary small clusters was proved by DFT calculations on Au–Ag dimers, trimers, and tetramers. After the formation of the seeds, the metallic vapor is depleted of the minority element; in the final stage of the growth, the remaining

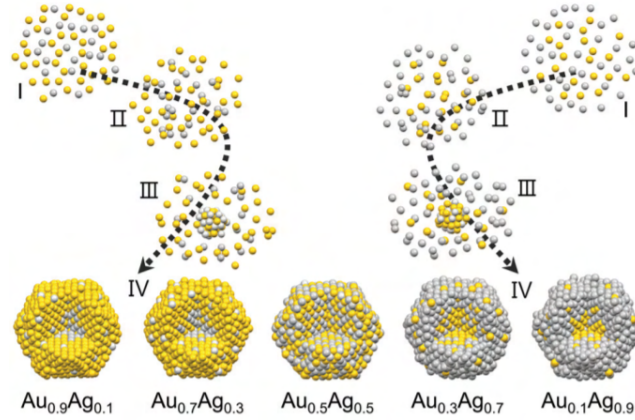


**Figure 3.4.4:** Schematic representation of the multi-step growth pathway of composition-tunable core-shell NPs, in the case of Au-Ag.

Reproduced from T.-W. Liao, A. Yadav, K.-J. Hu, J. van der Tol, S. Cosentino, F. D’Acapito, R. E. Palmer, C. Lenardi, R. Ferrando, D. Grandjean and P. Lievens, *Unravelling the nucleation mechanism of bimetallic nanoparticles with composition-tunable core-shell arrangement*, *Nanoscale*, 10:6684-6694, 2018.

vapor condenses forming a shell enriched in the majority element around the intermixed cores. A schematic representation of such multi-step growth process is shown in Fig. 3.4.4, reproduced from Ref. [97].

We have verified whether this explanation could be applied to our Pt–Pd growth, where NPs are considerably larger than the Au–Ag ones in Ref. [97]. This is indeed the case, as we show in the following. To validate the multi-step growth process as previously described, we have calculated the mixing energy of small Pt–Pd NPs with different compositions to show that mixed alloys with  $\sim 50\%$ – $50\%$  composition are the most energetically favorable and thus the most likely to be formed in the early growth stages. Then, we have performed growth simulations starting from a mixed Pt–Pd seed and depositing either Pt or Pd atoms to simulate the final growth stage in Pt-rich and Pd-rich atmospheres and to show that (PtPd)@Pt and (PtPd)@Pd out-of-equilibrium core-shell arrangements can be obtained, respectively.

Mixing energy calculations have been performed for small Pt–Pd clusters of size of 50 atoms and varying composition. For each composition, we have performed global optimization simulations in order to find the best isomer. In this case, Brownian and exchange moves (see Section 2.2.2) have been combined to optimize geometric shape and chemical ordering at the same time. The proportion between Brownian and exchange moves have been set to 90%-10%, and acceptance temperatures were 2000 K and 100 K, respectively. For each composition, at least 3 independent simulations of length  $5 \times 10^4$  steps have been made. The energy of the global minima have been used to evaluate the mixing energy, defined as [13]

$$E_{\text{mix(Pt}_m\text{Pd}_n)}} = E_{\text{b(Pt}_m\text{Pd}_n)}} - \frac{m}{N}E_{\text{b(Pt}_N)}} - \frac{n}{N}E_{\text{b(Pd}_N)}} , \quad (3.2)$$



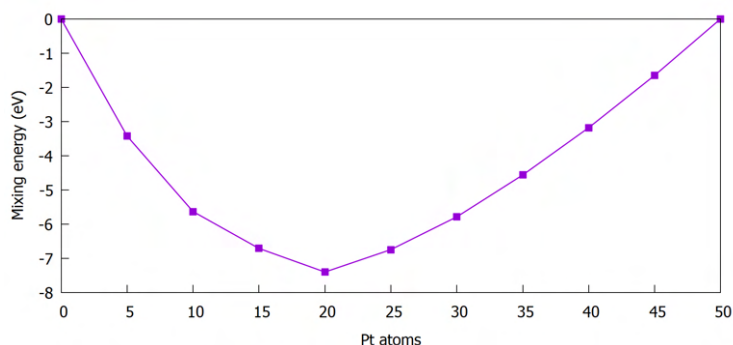


**Figure 3.4.5:** Mixing energy calculated for small Pt-Pd clusters of 50 atoms. Reproduced from D. Nelli, A. Krishnadas, R. Ferrando and Chloé Minnai, *One-Step Growth of Core–Shell (PtPd)@Pt and (PtPd)@Pd Nanoparticles in the Gas Phase*, *J. Phys. Chem. C*, 124:14338–14349, 2020.

where  $E_b$  is the binding energy and  $N = m + n$  is the total number of atoms. The mixing energy allows us to understand whether the formation of bimetallic or monometallic clusters is more favourable during the early stage of nanoparticle growth. In particular, if  $E_{\text{mix}(\text{Pt}_m\text{Pd}_n)} < 0$ , the formation of a collection of  $N$   $\text{Pt}_m\text{Pd}_n$  bimetallic clusters is energetically more favorable than the formation of a collection of  $m$   $\text{Pt}_N + n$   $\text{Pd}_N$  mono-metallic clusters. Vice versa, if  $E_{\text{mix}(\text{Pt}_m\text{Pd}_n)} > 0$ , mono-metallic clusters are energetically more favorable. The behavior of  $E_{\text{mix}}$  is shown in Fig. 3.4.5.  $E_{\text{mix}}$  is negative for all compositions, with a minimum for  $\text{Pt}_{20}\text{Pd}_{30}$ . Therefore, the mixing of Pt and Pd atoms is energetically favorable, and thus we expect that, in the early stages of the NP growth, bimetallic clusters will appear more frequently than mono-metallic ones, and more frequently than what would result from a simple combinatorial count of equally probable configurations (see Ref. [97] for details on this point). Among them, clusters with composition in a range close to 50%–50%, i.e., compositions close to the minimum of the mixing energy, will be the most abundant. Mixing energy calculations for smaller Pt–Pd clusters have been performed previously [98], obtaining the same type of results.

In order to study the final stage of the NP formation, we have performed MD growth simulations starting from a mixed Pt–Pd seed. The seed of our simulations is the lowest-energy structure for Pt–Pd  $\text{TO}_{201}$  at 50%–50% composition (see Fig. 3.4.2(a)). The size of the chosen seed is representative of the experimentally observed sub-2 nm population and, in some cases, of the cores of the NPs of the largest population, while the composition is close to the minimum value for the mixing energy. We have considered the lowest-energy configuration since we assume that, because of its small size and because of the high temperatures in the early stage of the gas-phase growth, the seed is able to fully equilibrate.

We have performed two simulation series, in order to mimic the growth of the initial mixed NP in either a Pt-rich or Pd-rich metallic vapour. In the first one, Pt atoms have been deposited on the starting seed with deposition rate of 0.1 atoms/ns, up to a final size of  $\sim 1000$  atoms; temperatures in the range 300–800 K have been selected, and 5 simulations per temperature have been performed.

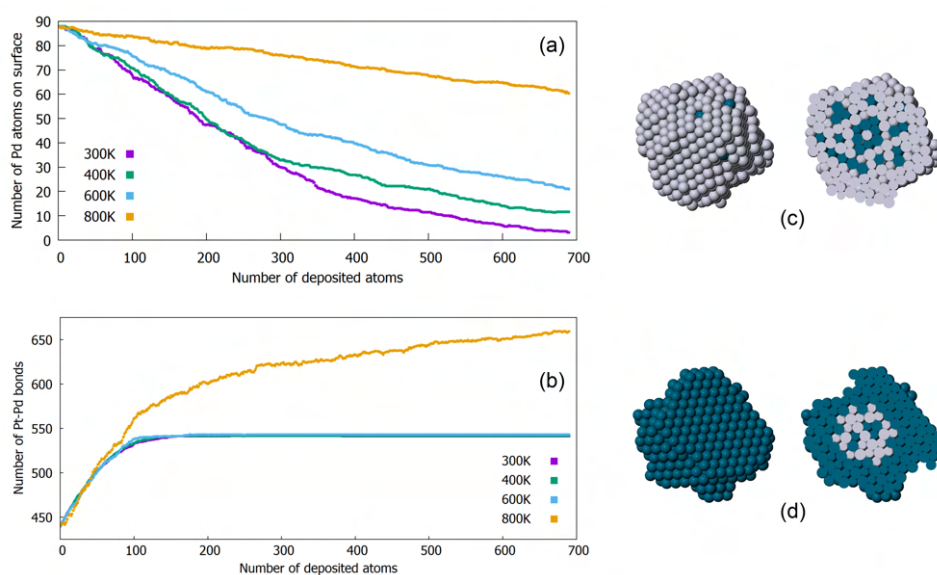


**Figure 3.4.6:** Graphs obtained for (a) Pt and (b) Pd deposition (average over five independent simulations). Core–shell structures with the outer shell enriched in (c) Pt and (d) Pd. These structures have been obtained at the end of two growth simulations at 300 K with deposition of Pt and Pd, respectively. For each structure, the image on the left shows the cluster surface, and the image on the right shows a cross section.

Reproduced from D. Nelli, A. Krishnadas, R. Ferrando and Chloé Minnai, *One-Step Growth of Core–Shell (PtPd)@Pt and (PtPd)@Pd Nanoparticles in the Gas Phase*, *J. Phys. Chem. C*, 124:14338–14349, 2020.

In the second simulation series the same growth conditions have been set, but Pd atoms have been deposited. The aim of the simulations was to verify whether it is possible to obtain a stable outer shell made of either Pt or Pd surrounding the mixed Pt–Pd seed. Actually, we have shown that both types of core–shell arrangements are out-of-equilibrium, so that they might transform under the action of equilibrium driving forces. In the Pt-rich case, at equilibrium, all Pd atoms are on the NP surface; thus, the formation of a Pt outer shell may be prevented by the tendency of Pd atoms to segregate to the surface. To evaluate this effect, we have monitored the number of Pd atoms on the surface of the NP during the simulations. The results are shown in Fig. 3.4.6(a). At 300, 400, and 600 K we can see a significant decrease of the number of Pd atoms on the surface, and therefore we can state that, at these temperatures, the deposited Pt atoms succeed in covering the Pd atoms of the starting seed, and a stable Pt shell can actually be obtained. At 800 K we do not see a similarly significant decrease, as the majority of Pd atoms of the initial seed are able to “float” on the deposited Pt atoms and to stay on the surface.

Let us now analyze the Pd deposition case. We have shown that in Pd-rich equilibrium structures Pt atoms are randomly mixed in the interior part of the NP and enrich the subsurface layer. Therefore, in this case the formation of a Pd thick outer shell may be prevented by the tendency of Pt atoms to distribute throughout the volume of the cluster, and especially below the surface. To evaluate this effect, we have monitored the number of heterogeneous Pt–Pd bonds. The results are shown in Fig. 3.4.6(b). The behaviour at 300, 400, and 600 K is the same: in the first part of the

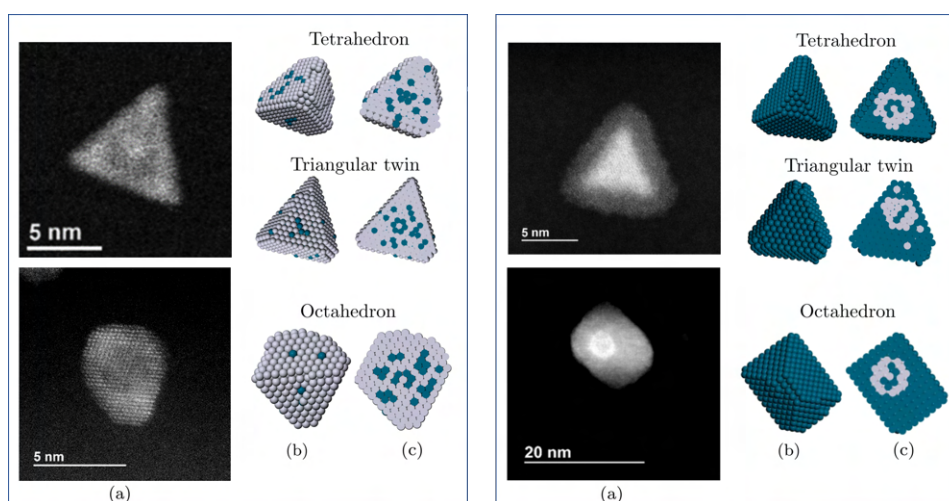


**Figure 3.4.7:** Comparison between typical structures of (PtPd)@Pt (left frame) and (PtPd)@Pd (right frame) NPs grown experimentally (a) and by MD simulations (b–c): tetrahedra/triangular twins and octahedra. For both: (a) HAADF-STEM image of the observed NP; (b) cluster surface and (c) cross section of the corresponding structure obtained in growth simulations with deposition of Pt atoms and Pd atoms, respectively.

Reproduced from D. Nelli, A. Krishnadas, R. Ferrando and Chloé Minnai, *One-Step Growth of Core–Shell (PtPd)@Pt and (PtPd)@Pd Nanoparticles in the Gas Phase*, *J. Phys. Chem. C*, 124:14338–14349, 2020.

simulations the number of mixed bonds increases since the deposited Pd atoms come into contact with the Pt atoms on the surface of the starting seed; after the first Pd layer is completed, the number of Pt–Pd bonds remains constant until the end of the simulations, meaning that Pt atoms do not mix any further. Therefore, at these temperatures, Pd atoms cover the starting seed layer by layer, and a thick pure Pd shell is formed. On the other hand, at 800 K the number of bimetallic bonds increases for the whole duration of the simulations, meaning that the Pt atoms of the seed mix with the deposited Pd atoms. At this temperature, we can still identify a Pt-enriched core (generally off-centered), but many Pt atoms are dissolved in the Pd growing shell.

In summary, the results of the growth simulations show that core–shell arrangements with mixed core and outer shell enriched in either Pt or Pd can be obtained by depositing Pt or Pd atoms, respectively, on a mixed Pt–Pd seed. In Figs. 3.4.6(c,d) we can see core–shell structures of the two types, obtained at 300 K. The purity of the outer shell depends on the growth temperature. At higher temperatures, the tendency toward equilibration is stronger, and therefore the purity of the shell is lower. However, we can state that in both cases there is a wide range of temperatures, from 300 K to a transition temperature between 600 and 800 K, in which the core–shell arrangement is actually obtained. This result is in agreement with the growth model described previously. In particular, it demonstrates that the formation of the seed and of the shell must occur at different times: the seed is formed in the early stage of the growth, which is known to take place at high temperatures, whereas the outer shell must form at a later stage, when the temperature of the metallic vapor has decreased; otherwise, the NP would equilibrate and the shell would not be stable enough to be observed in the experiments.

Here we have focused on the evolution of the chemical ordering during the growth process. Regarding the geometric shapes, different types of fcc structures have been obtained at the end of our MD simulations, namely Oh, Th and triangular twins; some of them are shown in Fig. 3.4.7, in which they are compared to the NPs produced experimentally, for both the Pt-rich and Pd-rich growth conditions. The growth mechanisms of such geometric motifs and their relationship with the growth parameters are the same as we have described in details in Section 3.3.

# 4

## Chemical ordering transformations in nanoalloys: atomic diffusion and equilibration pathways

OUT-OF-EQUILIBRIUM chemical ordering patterns are often obtained in the synthesis of nanoalloys. This is typically due to kinetic trapping phenomena taking place during the nanoparticle growth; a meaningful example has been given in Section 3.4, in which we have described the spontaneous formation of out-of-equilibrium core-shell arrangements from a two-component atomic vapour. Through the fine tuning of the experimental growth conditions it is possible to exploit such kinetic trapping phenomena in order to obtain some specific chemical ordering types. Moreover, sophisticated synthesis techniques can be employed to achieve an even better control on the final chemical ordering [99].

The out-of-equilibrium structures are expected to evolve towards more favourable configurations, and to eventually reach thermodynamic equilibrium, through the diffusion of the two atomic species within the nanoparticle volume. A deep understanding of such equilibration processes is highly desirable. Firstly, in view of possible technological applications, a clear knowledge of the thermodynamic stability of the produced phases under the typical operating conditions is needed. Moreover, the underlying physical processes of chemical ordering transformations are often peculiar to nanoscale systems, and are therefore of great interest for basic science research. The equilibration of nanoalloy chemical ordering has indeed been the subject of several experimental [100–110] and theoretical studies [111–114] in the recent years.

In this chapter, we present our results on the evolution of nanoalloys starting from out-of-equili-

brium chemical arrangements. These results have been obtained by MD-based simulation techniques. Chemical ordering equilibration processes have been analysed at different time and length scales.

In the first case, we have focused on the very fundamental process of intra-nanoparticle diffusion, i.e. the displacement of one atom of species A within a volume occupied by atoms of species B. To this end, we have simulated the diffusion of a single-atom impurity of either Ag or Au within otherwise pure nanoparticles of Co, Cu, Ni, Pt and Rh. The diffusion pathways have been analysed step by step, by focusing on the displacement of the impurity between adjacent internal sites. In this way, we have been able to identify a new elementary diffusion mechanism, which is peculiar to nanoparticles, and specifically to the icosahedral geometry. Our results are shown and discussed in the first part of the chapter, along with a brief description of the MetaD scheme that we have employed to accelerate the diffusion of the impurity at room temperature.

In the second case, we have considered phase-separating bimetallic systems such as Au-Co, Ag-Ni and Ag-Cu, and we have studied their evolution from strongly out-of-equilibrium intermixed configurations towards the most favourable core-shell arrangement. Here the main focus was not on the diffusion of individual atoms, but on the overall equilibration pathways of the chemical ordering. Such transformations involve the concerted displacements of many atoms and, sometimes, are combined with significant structural rearrangements of the nanoparticle. Again, our simulations have allowed us to identify some interesting kinetic behaviours that are peculiar to nanoscale systems; they are analysed in details in the second part of the chapter.

#### 4.1 ELEMENTARY DIFFUSION MECHANISMS IN ICOSAHEDRAL NANOPARTICLES

Atomic diffusion is the underlying process of chemical ordering transformations in nanoalloys. In general, diffusion is enhanced at the nanoscale. Diffusion processes are typically activated at lower temperatures than those needed for the correspondent bulk system, and much faster rates are measured [115, 116]. A significant increase in the diffusion rate when decreasing the NP size has been observed both in experiments [117] and in MD simulations [118–120]. Moreover, MD simulations have allowed to identify the main diffusion mechanisms in NPs. In these mechanisms the role of the surface is always of primary importance. In most cases, the whole process begins with the disordering of the surface layer: surface atoms diffuse easily, and the motion is eventually transmitted to the atoms in the inner layers, therefore allowing for the rearrangement of the two atomic species [118, 119, 121]. A second mechanism is possible, which requires the presence of vacancies within the cluster volume; in this case, atoms can diffuse by jumping to unoccupied neighboring sites [120–123]. Again, vacancies first appear on the surface, where defects are created more easily, and then migrate inward through subsequent filling steps.

We have studied the diffusion in the case of a single-atom impurity of Ag or Au moving within otherwise pure magic-size icosahedral clusters of Co, Cu, Ni, Pt and Rh. Our simulations have revealed unexpected diffusion pathways, in which the displacement of the impurity is coupled with

the creation of vacancies in the central part of the cluster. Such diffusion mechanism is indeed quite different from the vacancy-mediated diffusion processes described in the literature; in the following, we will analyse it in details, and we will show that it can be related to the presence of non-homogeneous compressive stress in the inner part of the icosahedral structure<sup>1</sup>.

Our results have been obtained through two different simulation techniques. Along with standard MD, we have employed MetaD simulations, which have been necessary to observe the impurity diffusion at room temperature within an affordable simulation time. A general presentation of the MetaD technique has been provided in Section 2.3.2, in which we have pointed out that the CVs must be carefully chosen according to the system under study. Here we have employed a recently proposed CV set, which is particularly appropriate to study transition pathways from an initial configuration towards a target configuration. The form and main properties of these CVs will be described, with particular attention to the choice of the optimal CV parameters for our study.

We remark that in our case MetaD simulations have been used only to accelerate the kinetics of rare events that are not observed in standard MD simulations at room temperature, whereas the estimation of free energy barriers has not been attempted. As discussed in Section 2.3.2, the reconstruction of the free energy profile requires the achievement of the diffusive regime at some stage of the simulation, during which the system is able to move freely in the space of the CVs and to go back and forth between the initial and the final configurations of the transition. However, the diffusive regime has not been reached in our MetaD simulations. We believe that this is due to two reasons: firstly, as we will see, the initial configurations of our simulations are very high in energy, so that returning back is highly unlikely; secondly, we have put no constraints forbidding arbitrary deformations of the clusters, so that in long MetaD simulations the added bias potential, which forces the system to go away from the already visited regions of the CV space, easily leads to unphysical cluster shapes, and finally even to the breaking of the cluster into pieces.

Finally, we note that all the results presented below have been obtained by means of the atomistic Gupta potential. Work is in process to evaluate the energetics of the diffusion processes by more sophisticated methods, such as DFT.

#### 4.1.1 ENERGY AND STRESS EFFECTS OF THE IMPURITY PLACEMENT WITHIN THE ICOSAHEDRAL MATRIX

We have considered perfect icosahedral clusters of sizes 147, 309, 561 and 923 atoms. The clusters are completely made of Co, Ni, Pt or Rh, with the exception of a single-atom impurity of Ag (in Co, Cu and Ni clusters) or Au (in Co, Pt and Rh clusters). The largest Ih sizes (561 and 923) have been considered only for Au-Co. Here we will mostly focus on the two smaller Au-Co clusters; results obtained for the other systems and sizes will be commented briefly.

First, we have considered all possible positions of the impurity within the Ih matrix, and we have

---

<sup>1</sup>Results have been published in Ref. [124] and in Ref. [125]. Most results have been achieved thanks to the close collaboration with Fabio Pietrucci (Sorbonne University, Paris, France).

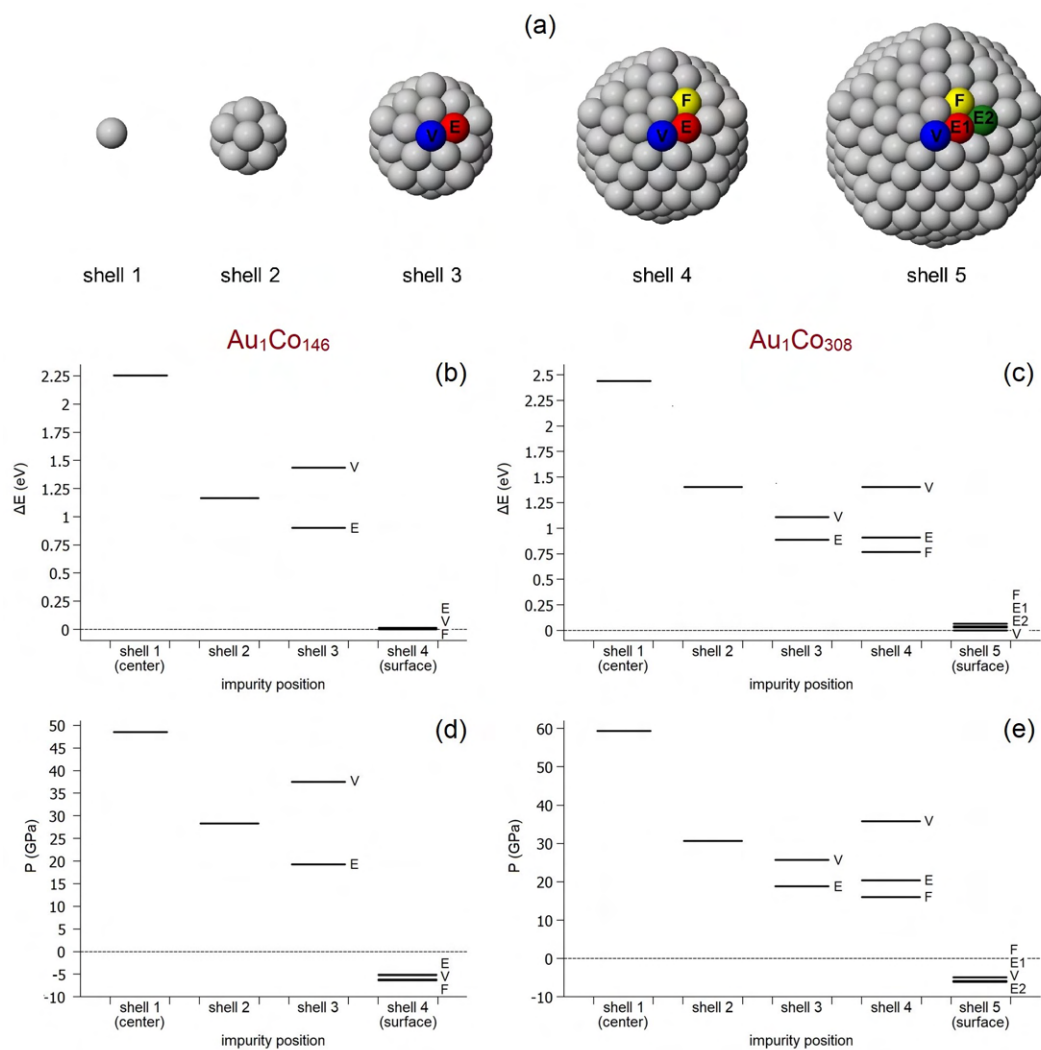


**Figure 4.1.1:** (a) Inequivalent sites in the first five Ih shells. Energy of (b)  $\text{Au}_1\text{Co}_{146}$  and (c)  $\text{Au}_1\text{Co}_{308}$  Ih clusters as a function of the Au impurity position. In the case of shells 3–5, all the possible inequivalent sites are considered, as in (a). For each system, the reference value of the energy corresponds to the best placement of the impurity in the cluster, which is in one of the surface sites. Energy differences from this minimum value are displayed. Atomic pressure on the impurity for (d)  $\text{Au}_1\text{Co}_{146}$  and (e)  $\text{Au}_1\text{Co}_{308}$  Ih clusters as a function of the Au impurity position. Adapted from D. Nelli, F. Pietrucci and R. Ferrando, *Impurity diffusion in magic-size icosahedral clusters*, *J. Chem. Phys.*, 155:144304, 2021.



calculated the total energy of the cluster in each case. The energy of the  $\text{Au}_1\text{Co}_{146}$  and  $\text{Au}_1\text{Co}_{308}$  clusters as a function of the impurity position is shown in Fig. 4.1.1(b, c). We can observe an overall decrease in total energy as the impurity is put into ever more external shells. Surface sites are the most energetically favourable for the placement of the impurity, as a consequence of the lower surface energy of Au compared to Co [40]. In the inner part of the Ih, vertex sites, i.e. sites belonging to the fivefold symmetry axes, are always the least favourable. The other bimetallic systems considered in this study exhibit a similar energy profile, with the only exception of Au-Rh: the best placement for the Au impurity is on the surface as in the other cases, but here the central site turns out to be more energetically favourable than sites in the second shell (i.e. sites that are neighbours of the central site).

The energy behaviour observed in Fig. 4.1.1(b, c) can be explained on the basis of atomic stress effects. In Ih NPs, interatomic distances are contracted in the radial direction [14], resulting in compressive stress on the atoms placed in the inner sites [13]. The degree of contraction, and thus of compressive stress, is larger in the shells closer to the center, the pressure on the central atom being particularly high [126, 127]. The Ih matrix is therefore a non-homogeneous environment, and the placement on the impurity in the different sites can strongly affect the total energy of the cluster. In general, we expect the energy to improve as the local pressure on the impurity goes closer to zero. Here, the atomic radius of the impurity is larger compared to the atoms building up the Ih matrix, the lattice mismatch being 15% for Au-Co and in the range 4-16% for the other bimetallic systems. The compressive stress on the impurity inside the cluster is therefore even higher, resulting in a more striking energy difference between the different sites.

To quantify the effect of stress, we have calculated the local pressure on the impurity from its atomic stress tensor. The atomic stress tensor on a selected atom  $i$  is defined as [128]

$$\sigma_i^{ab} = -\frac{1}{3V_i} \sum_{j \neq i} \frac{\partial E_i}{\partial r_{ij}} \frac{r_{ij}^a r_{ij}^b}{r_{ij}}, \quad (4.1)$$

in which  $a, b = x, y, z$ ,  $E_i$  is the atomic energy of the  $i$ -th atom calculated according to Gupta potential,  $V_i$  is the volume of the  $i$ -th atom in its bulk crystal structure and  $r_{ij}$  is the distance between atoms  $i$  and  $j$ . The eigenvalues of this symmetric  $3 \times 3$  matrix correspond to the principal stress components  $p_{i,k}$  ( $k = 1, 2, 3$ ). The isotropic pressure on atom  $i$  is calculated as the sum of the three principal stress components [129]. The derivation of the atomic stress tensor, as provided in Ref. [128], is reported in Appendix B.

In Fig. 4.1.1(d, e) we show the local pressure on the impurity for  $\text{Au}_1\text{Co}_{146}$  and  $\text{Au}_1\text{Co}_{308}$  as a function of the impurity position. The behaviours of the pressure and of the energy look very much alike, showing that atomic stress effects are indeed the cause of the energy difference between different inner Ih sites. As expected, the highest value of the atomic pressure is found in the center; then, the pressure on the impurity gradually decreases as it occupies more and more external shells. We note that the pressure on the impurity is negative for all surface sites, i.e. tensile stress is present in the NP surface, as it is well known in the literature [13]. Again, all bimetallic systems exhibit a

similar pressure profile. The atomic pressure on the Au impurity in Au-Rh clusters is smaller in the second shell than in the center, as in the other systems; in this case, however, the replacement of Au with Rh in the central site actually causes an increase in the central pressure for both Ih sizes, and, as a consequence, also in the total energy.

The results shown in Fig. 4.1.1 represent a reference point for the study of the diffusion pathways of the impurity within the Ih matrix, which we will present in the following. Essentially, if we initially place the impurity in any of the inner sites, we expect that it will diffuse toward the cluster surface in order to reach the most energetically favourable position. The driving force for the diffusion is the relaxation of the local stress in the volume around the impurity, which progressively decreases as the impurity moves toward the external layers.

#### 4.1.2 METADYNAMICS SIMULATIONS FOR THE STUDY OF IMPURITY DIFFUSION: FORM AND PARAMETERS OF THE COLLECTIVE VARIABLES

The impurity has been initially placed in the central site of the Ih, and the evolution has been studied by MD simulations at constant temperature. Firstly, two independent simulations at room temperature ( $T = 300$  K) with a duration of  $10 \mu\text{s}$  have been run for  $\text{Au}_1\text{Co}_{146}$ ,  $\text{Au}_1\text{Co}_{308}$ ,  $\text{Ag}_1\text{Cu}_{146}$  and  $\text{Ag}_1\text{Cu}_{308}$ ; in these simulations no significant changes have been observed, neither in the impurity position within the cluster nor in the overall geometry. Perfect Ih with the impurity occupying the central site are therefore metastable configurations, whose lifetime at room temperature exceeds the maximum timescale we are able to reach by our MD simulations.

To accelerate the impurity diffusion process we have exploited two different approaches: we have increased the temperature of the MD simulations and we have performed MetaD simulations at room temperature. MD simulations have been performed at different temperatures, from room temperature up to a maximum value below the melting point. In general, rising the temperature modifies the free energy landscape of the system and therefore may produce evolution pathways that are unlikely at lower temperatures. For this reason we have performed MetaD simulations at room temperature, as well. The combination of the two methods have allowed us to identify a more complete collection of possible evolution pathways, thus providing an overall view of the impurity diffusion process.

Before showing the simulation results, it is useful to describe the CVs employed in our MetaD simulations, as well as the procedure we have followed to set the CV parameters. We remind that a proper choice of the CVs is required to ensure the efficiency and the accuracy of the MetaD simulations.

The CVs chosen are the path CVs [130] combined with the PIV metric [131], as proposed in Ref. [132]. This scheme has been successfully employed in the computational study of several different systems [132–134], and here it has been applied for the first time to NPs.

The path CVs are defined from a reference evolution pathway, consisting of the initial and final states of the studied transition, and, optionally, of a discrete set of putative intermediate configurations. Here we have considered only two reference structures, i.e. the chosen starting configuration

(A) and the lowest energy structure for the NP (B). Path CVs for the running configuration X are defined in the following way [130]:

$$\begin{aligned} s_X &= \frac{e^{-\lambda \mathcal{D}_{AX}} + 2e^{-\lambda \mathcal{D}_{BX}}}{e^{-\lambda \mathcal{D}_{AX}} + e^{-\lambda \mathcal{D}_{BX}}}, \\ z_X &= -\lambda^{-1} \ln \left( e^{-\lambda \mathcal{D}_{AX}} + e^{-\lambda \mathcal{D}_{BX}} \right), \end{aligned} \quad (4.2)$$

where  $\mathcal{D}_{AX}$  and  $\mathcal{D}_{BX}$  are the distances between the running structure and the two reference structures, according to some properly chosen metric. The  $s$ -variable tracks the progress of the evolution towards the selected final structure, as it increases as the system moves away from A and approaches B, whereas  $z$  is a measure of the distance from the reference pathway since it takes high values when the system explores configurations distant from both A and B. For the parameter  $\lambda$  we have used  $\lambda = 2.3/\mathcal{D}_{AB}$ ,  $\mathcal{D}_{AB}$  being the distance between the two reference structures, which ensures smooth and well-resolved evolution pathways in the  $s$ - $z$  plane [132].

In the framework of the path CVs, a metric for the calculation of distances between different configurations of the system is required. Here we have employed the metric introduced in Ref. [131] which we will briefly describe in the following; we will use the same notation as in Ref. [131], to which reference should be made for a more detailed explanation.

In this metric, each configuration of a system of size  $N$  is associated to a vector  $\mathbf{v}$  of  $\frac{1}{2}N(N-1)$  components, corresponding to the total number of possible atomic pairs; the vector is built in the following way

$$\mathbf{v} = \text{sort}(C_{ij}) = \text{sort}(C(|\mathbf{R}_i - \mathbf{R}_j|)), \quad i > j, \quad (4.3)$$

where  $\mathbf{R}_i$  ( $\mathbf{R}_j$ ) are the Cartesian coordinates of atom  $i$  ( $j$ ), and  $C_{ij}$  is a monotonically decreasing function of the interatomic distance  $d_{ij} = |\mathbf{R}_i - \mathbf{R}_j|$ . The vector  $\mathbf{v}$  includes all the elements from the upper triangular part of the symmetric matrix  $C$ . These elements are sorted in ascending order within each block characterized by the pairing of the same elements. The sorting operation ensures the invariance of  $\mathbf{v}$  under the permutation of identical atoms; for this reason,  $\mathbf{v}$  is called *permutation invariant vector* (PIV). Finally, distances between configurations are computed as squared Euclidean distances between their PIVs.

The matrix  $C$  in Eq. (4.3) is called *adjacency matrix*; each entry refers to a specific pair of atoms and provides its level of connection, which is here evaluated by a function  $C(d_{ij})$  of the interatomic distance. This function, also called *switching function*, monotonically decreases from one (maximum level of connection) to zero (no connection) as the spatial distance between the two atoms increases. Different choices for the switching function are possible; in this work we have used the decreasing sigmoid function

$$f_{\text{switch}}(r) = \frac{1 - (r/r_o)^n}{1 - (r/r_o)^m}. \quad (4.4)$$

The parameters  $r_o$ ,  $m$  and  $n$  can be adjusted to select the range of interatomic distances in which the switching function actually decays from one to zero; in this way it is possible to focus the metric on

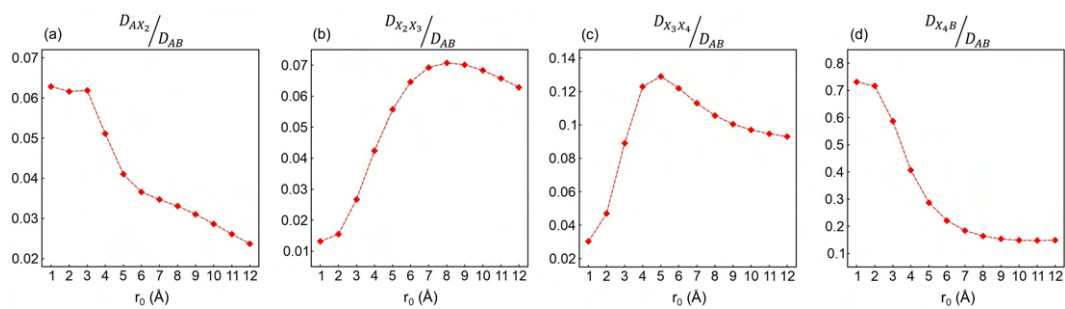


**Figure 4.1.2:** Relative distances calculated for (a) A- $X_2$ , (b)  $X_2$ - $X_3$ , (c)  $X_3$ - $X_4$  and (d)  $X_4$ -B for different values of the parameter  $r_0$  of the switching function.

Reproduced from D. Nelli, F. Pietrucci and R. Ferrando, *Impurity diffusion in magic-size icosahedral clusters*, *J. Chem. Phys.*, 155:144304, 2021.

the range of distances that are relevant for the transition we are studying.

The choice of the parameters of the switching function is indeed crucial to ensure the efficiency of MetaD simulations. In general, the transition pathway must be well-resolved in the CV space, i.e. the metadynamics CVs must be able to distinguish between the most relevant configurations appearing during the evolution. The path CVs defined in Eq. (4.2), together with the choice of the parameter  $\lambda$  already discussed, ensure that the two reference structures are always well separated in the  $s$ - $z$  plane; it is easy to verify that  $s_A \simeq 1.1$  and  $s_B \simeq 1.9$ , regardless of the details of the metric. However, we need to ensure that the intermediate configurations of the transition, for which we have  $1.1 \lesssim s_X \lesssim 1.9$ , are sufficiently resolved as well. This is possible if distances between intermediate configurations are reasonably large according to the chosen metric. Strictly speaking, as the parameter  $\lambda$  is chosen as a function of the distance  $D_{AB}$  between the two reference structures, what is actually relevant in the building of the path CVs is the *relative distance*: if we consider two intermediate configurations X and Y, the quantity we have to evaluate is the ratio  $D_{XY}/D_{AB}$ . Optimal values of the parameters of the switching function are therefore those that provide large relative distances between intermediate structures.

In this study the parameters  $m$  and  $n$  have been fixed to 6 and 3, respectively. Here we will describe the protocol we have used for the choice of  $r_0$ ; data refer to the system  $\text{Au}_1\text{Co}_{308}$ .

Firstly, a set of putative intermediate configurations have to be selected. Here, in the first reference structure (A) the Au impurity is in the center of the Ih whereas in the second one (B) Au is on the surface, on the vertex site; it is therefore reasonable to choose configurations in which Au is placed in the different Ih shells, as those considered in Fig. 4.1.1(c, e). We have selected one configuration per shell, namely  $X_k$ , with  $k = 1, 2, 3, 4, 5$  referring to the number of the shell in which the impurity is placed. When multiple sites are present in the same shell, we have always considered the vertex site (see Fig. 4.1.1(a)). Of course we have  $X_1 \equiv \text{A}$  and  $X_5 \equiv \text{B}$ .

We have considered different values of  $r_0$  in the range 1-12 Å and, for those values, we have evaluate the relative distances between all pairs of adjacent structures  $D_{X_k X_{k+1}}/D_{AB}$  with  $k = 1, 2, 3, 4$ . Results are shown in Fig. 4.1.2.

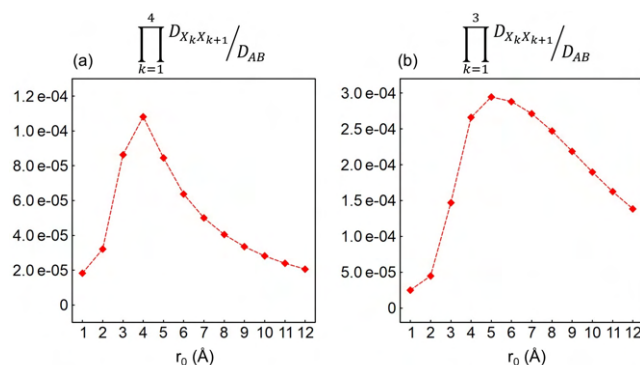


**Figure 4.1.3:** Product of the relative distances between adjacent configurations of the  $X_k$  set. In (a) all the relative distances of Fig. 4.1.2 are considered, whereas in (b) we do not take into account the relative distance between  $X_4$  and B. Reproduced from D. Nelli, F. Pietrucci and R. Ferrando, *Impurity diffusion in magic-size icosahedral clusters*, *J. Chem. Phys.*, 155:144304, 2021.

Before analysing the results of Fig. 4.1.2, it is useful to make some general remarks on the PIVs of the chosen structures. All configurations in the  $X_k$  set exhibit the same overall geometry, as they differ only in the position of the Au impurity within the Ih matrix. As a consequence, changes in PIV terms referring to the Co-Co pairs between the different configurations are small. On the other hand, we expect a quite large variation in the Au-Co terms, which therefore mostly affect the calculation of pair distances. To rationalize the behaviour of the calculated relative distances we have thus to focus on the effect of the parameter  $r_0$  on the Au-Co PIV terms.

Two different trends are observed. In the case of A- $X_2$  and  $X_4$ -B, the relative distance takes its maximum value for  $r_0 = 1$  Å and then decreases as  $r_0$  is increased (see Fig. 4.1.2(a, d)). Such behaviour is consistent with short-range differences between the two structures of each pair; in particular, the structures can be well-distinguished if we focus on the first neighbours range of interatomic distances. This is clear for the  $X_4$ -B configuration pair: Au occupies an inner site when in  $X_4$  and a surface site when in B, therefore the number of its first neighbours is different in the two configurations. Regarding A- $X_1$ , the number of Au first neighbours does not change since Au is placed in the inner part of the cluster in both cases. However, the values of the distances of the first neighbours are slightly different: when Au is in the compressed central site all of its twelve first neighbours are 2.45 Å apart, whereas when it is placed in the second shell the average first neighbours distance is 2.53 Å. The difference is indeed small, but it can be detected by a properly chosen metric; here values of  $r_0$  in the range 1-3 Å are able to distinguish the two configurations to an acceptable degree.

Relative distances calculated for  $X_2$ - $X_3$  and  $X_3$ - $X_4$  exhibit a rather different behaviour, as shown in Fig. 4.1.2(b, c). Small values are obtained when  $r_0$  is small; then the distance increases with  $r_0$ , and the maximum is reached for  $r_0 = 8$  Å and 5 Å, respectively. In configurations  $X_2$ ,  $X_3$  and  $X_4$  Au is placed in inner sites with similar first neighbours distances, therefore short-range effects poorly affect the distance between structures. In this case, the largest relative distances are obtained for higher values of  $r_0$ , which are able to detect the different position of Au within the whole Ih matrix.

We have calculated the product of all relative distances as a function of  $r_o$ ; optimal values of the parameter  $r_o$  are those which maximize this quantity, therefore ensuring sufficiently large adjacent pair distances between all the putative intermediate structures. Results are shown in Fig 4.1.3(a), in which we can identify the maximum value in correspondence of  $r_o = 4 \text{ \AA}$ . In Fig 4.1.3(b) we show the results of the same calculation, but without taking into account the relative distance between  $X_4$  and B. For this pair of configurations, quite large relative distances are obtained for all the considered values of  $r_o$  (see the comparison between Fig. 4.1.2(d) and Fig. 4.1.2(a-c)), therefore it is reasonable to focus on the contribution of the other pairs only. In this case, the maximum of the product of the relative distances is shifted to slightly larger values of  $r_o$  and the peak is more broadened; good values of  $r_o$  are in the range 4-7  $\text{\AA}$ .

Similar results for the optimal values of  $r_o$  have been found for all the considered systems. In our MetaD simulations we have therefore decided to employ  $r_o = 4 \text{ \AA}$  in all cases.

In the case of  $\text{Au}_1\text{Co}_{308}$  the value  $r_o = 10 \text{ \AA}$  has been tested as well, but non-physical trajectories have been obtained, in which the cluster disintegrates after few simulation steps. This behaviour is due to the inability of the metric to distinguish between different configurations in the early stages of the evolution (see Fig. 4.1.2(a)), which are therefore all located in a small region of the  $s$ - $z$  plane. After some MetaD steps, a high bias potential is deposited in this small area; the resulting forces on the system are huge, and the system is eventually destroyed. The bad results obtained in this simulation set further demonstrate the importance of the correct setting of the CV parameters for the efficiency of the MetaD technique.

The parameters of the Gaussian deposition during the MetaD simulation have been set to: Gaussian height  $\delta = 0.01$  or  $0.10$  eV, Gaussian width  $(\sigma_s, \sigma_z) = (0.02, 0.1)$ , deposition stride 10 or 100 ps. As anticipated, the simulation temperature has been set to 300 K. MetaD simulations have been performed using our own MD code interfaced with the PLUMED plugin [135]<sup>2</sup>.

#### 4.1.3 IMPURITY DISPLACEMENT AND INTERNAL VACANCY CREATION: A SINGLE-STEP COLLECTIVE PROCESS

Here we describe a new diffusion mechanism, that we have observed in the displacement of the impurity from the central site to the second Ih shell. The lowest temperature at which the diffusion is activated on our timescale depends on the system: for example, it is 400 K for  $\text{Au}_1\text{Co}_{146}$  and 500 K for  $\text{Au}_1\text{Co}_{308}$ . In MetaD simulations at room temperature we have always observed the diffusion of the impurity, which begins after few simulation steps; this indeed confirms the efficiency of our MetaD scheme.

The diffusion process has been analysed at the atomic level. Interestingly, we have found that both in MD and MetaD simulations the migration of the impurity to the second shell is coupled with the formation of a *vacancy* in the central site, and with an adatom emerging on the surface. The clusters before and after the impurity displacement are shown in Fig. 4.1.4(a, c) and 4.1.4(e,

<sup>2</sup>The set-up of the metadynamics code has been handled by Fabio Pietrucci (Sorbonne University, Paris, France)

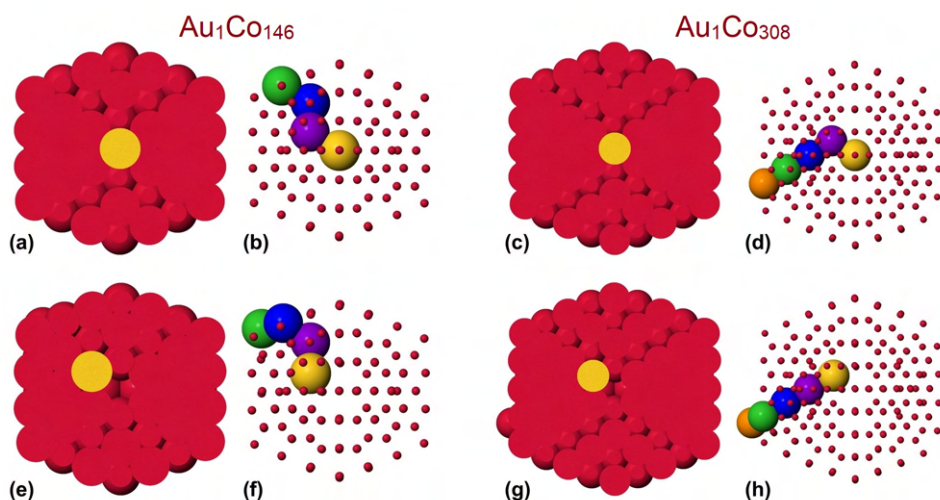


**Figure 4.1.4:** Snapshots of the migration of the impurity from the center to the second shell in the case of Au<sub>1</sub>Co<sub>146</sub> (on the right) and Au<sub>1</sub>Co<sub>308</sub> (on the left). On the top and bottom row we show the cluster before and after the impurity migration, respectively. (a,c) Starting configuration, with the Au impurity occupying the central site. (e,g) The impurity moves to one of the sites in second shell; the central site left by the impurity is not occupied by any Co atom, so that a vacancy is created. (b,d,f,h) Atoms involved in the diffusion process.

Reproduced from D. Nelli, F. Pietrucci and R. Ferrando, *Impurity diffusion in magic-size icosahedral clusters*, *J. Chem. Phys.*, 155:144304, 2021.

g), respectively. In Fig. 4.1.4(e, g) we can see that the impurity has moved to one of the sites in the second shell; the central site left by the impurity is not occupied by any Co atom, so that a vacancy is created.

Ih structures with a central vacancy have been predicted by global optimization searches for Lennard-Jones clusters [136–139], Cu [126], Ag [126], Au [140, 141], Al [141–143], Pt [141] and Pb [144] clusters modelled by atomistic potentials and for Ag clusters also at the DFT level [41]. The presence of the vacancy has been proved to release the strong compressive stress in the central site of the Ih, therefore stabilizing the structure [126]. Ih missing the central atom have also been observed in freezing MD simulations of Au NPs [145, 146]. On the experimental side, mass spectra obtained for methane clusters synthesized in helium nanodroplets exhibits peaks at Ih magic sizes, but the peak corresponding to the three-shell Ih is shifted from size 55 to 54 [147]; this is consistent with the presence of a vacancy, which is expected to be at the center on the basis of energy considerations.

Here we can see the dynamic process of creation of the central vacancy, as a consequence of the impurity diffusion. A previous study on single-atom impurity diffusion in NPs has indeed described the formation of inner vacancies in Ih clusters during the diffusion process [123]. In Ref. [123], an Ag atom has been initially placed in the central site of an otherwise pure Cu Ih of size 147 atoms, and the diffusion of the impurity has been studied by means of atomistic MD simulation at  $T = 700$  K. A detailed description of the impurity diffusion process has been provided: first, the surface of the cluster becomes partially disordered on one side, and a vacancy appears in the subsurface

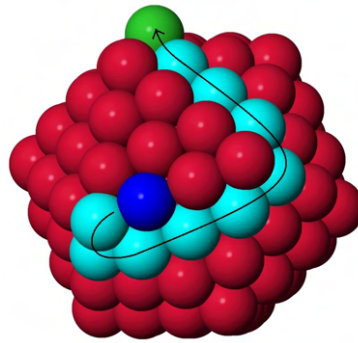


**Figure 4.1.5:** Surface of  $\text{Au}_1\text{Co}_{146}$  after the process of impurity diffusion and central vacancy formation, as obtained in one of our simulations. The dark blue atom is the one coming up from the subsurface shell. The adatom (coloured in green) emerges quite far away from the dark blue one. All light blue atoms are displaced by one position during the process.

layer; the vacancy migrates to the second shell and comes into contact with the Ag atom, which is still in the central site; the Ag atom jumps to the empty site in the second shell, so that the vacancy is displaced in the centre; finally, the structure reverts to the perfect Ih geometry, with ordered surface. In this mechanism, the vacancy first appears in the subsurface layer and then moves inwards until it reaches the central site; the whole process involves three steps, taking place at different times. The initial formation of the vacancy requires the partial disordering of the cluster surface, and therefore many atoms are involved during this vacancy-mediated diffusion process.

Here we have observed a rather different process. The vacancy is created directly in the center of the Ih, at the same time as the impurity migrates to the second shell. In contrast to what described in Ref. [123], the vacancy does not play the role of promoter of the diffusion of the impurity, but it is a product of the diffusion itself. The whole process can be described as a push-like mechanism, in which the migration of the impurity to the second shell induces a concerted displacement of a row of atoms in the outward direction. The outer atom of the row, i.e. the one belonging to the cluster surface prior to the diffusion, is expelled from the Ih matrix and becomes an adatom; in some cases it is again incorporated into the surface through the well-known rosette reconstruction [23]. In Fig. 4.1.4(b, d) and 4.1.4(f, h) the clusters are again shown before and after the impurity displacement, respectively. All the atoms involved in the diffusion process are highlighted. The remaining Co atoms (displayed as small spheres in the figure) do not change their position during the process; in particular, no surface disordering is observed. We do not observe a preferential direction for the displacement, for example along a fivefold symmetry axis; instead, moving atoms are often rather misaligned, as in the case displayed in Fig. 4.1.4(b, f). We remark that the processes of Fig. 4.1.4 are only representative examples of the family of diffusion mechanisms, which may take place also through more complex displacements. Specifically, it frequently happens that the adatom pops up on the surface in positions that are far away from the emerging subsurface atom. In this case a concerted movement of many surface atoms is observed, as shown in Fig. 4.1.5.

Sometimes the creation of surface defects precedes the diffusion of the impurity: one or more



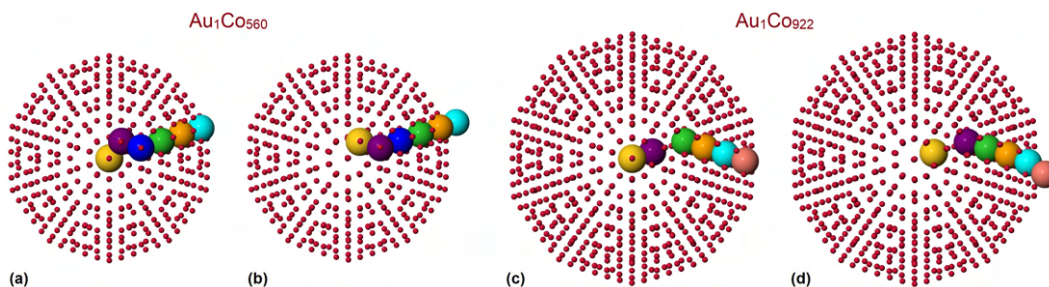


**Figure 4.1.6:** Snapshots of the migration of the Au impurity from the center to the second shell within Co Ih clusters, obtained in MetaD simulations at room temperature. The displacement of the impurity is coupled to the formation of a vacancy in the central site and to the appearance of a Co adatom on the surface. (a-b) Starting and final configuration of the diffusion process for  $\text{Au}_1\text{Co}_{560}$ . (c-d) Same, but for  $\text{Au}_1\text{Co}_{922}$ . Atoms involved in the diffusion process are highlighted. Reproduced from D. Nelli, *Central vacancy creation in icosahedral nanoparticles induced by the displacement of large impurities*, accepted in *Eur. Phys. J. Appl. Phys.*

vertex atoms are detached and diffuse on the cluster surface, or are incorporated into it through some reconstruction process. In that case, the collective displacement described before takes place in the direction of a missing vertex, so that the empty site on the surface is filled by an atom coming from the subsurface shell.

Even though the stability of the central vacancy in Ih clusters has been extensively discussed in the literature, the one-step creation process here described, in which the vacancy directly appears in the central site, is somewhat unexpected. By comparison, the formation of the vacancy in the subsurface layer as described in Ref. [123] is less impressive, since defects frequently appear in the surface of NPs, due to the low coordination and enhanced mobility of surface atoms. The formation of defects inside the NP is much less common. As a matter of fact, the combined process of impurity diffusion and vacancy formation inside the cluster can be easily explained on the basis of stress considerations alone. The atom initiating the whole process is the impurity, which moves to the second shell in order to release its initially strong compressive stress; as a consequence, a vacancy appears in the central site. Normally one would expect an inner vacancy to be almost instantaneously filled by one of its neighbouring atoms. Here, this does not happen due to its favourable position. The relative stability of the vacancy indeed prevents atoms in the second shell to move to the central site. Due to the suppression of atomic movement towards the center of the cluster, the collective displacement triggered by the impurity can only proceed outwards, so that one atom is eventually expelled, as previously described. Actually, each atom involved in such displacement reduces its local pressure; this kind of motion is more favourable than inner circular motions needed to fill the central vacancy, in which atoms moves within the same shell or inward, i.e. towards sites with similar or higher degree of compression. The filling of the central vacancy actually takes place in our simulations, but on much longer timescales.

The same kind of impurity diffusion and vacancy formation process takes place also in other bimetallic systems (Ag-Cu, Ag-Co, Ag-Ni and Au-Rh), and in Au-Co clusters of larger sizes, as we

have found in our room temperature MetaD simulations. In Fig. 4.1.6 we show the cluster before and after the impurity diffusion process, for Au-Co Ih of size 561 and 923 atoms. At size 923 we observe some peculiarity in the moving atomic row. As we can see in Fig. 4.1.4(c-d), the highlighted atomic row is interrupted in correspondence of the third shell: as observed at smaller sizes, the Au impurity replaces one of the atoms in the second shell, but this atom (in purple) passes through the third shell and stops in the fourth shell, where it replaces the green atom. The third shell is unchanged at the end of the process. This behaviour has been observed in all our simulations for  $\text{Au}_1\text{Co}_{922}$ , with different positions of the interruption in the atomic row.

The evaluation of the energy barriers associated to the observed diffusion processes is surely interesting. However, such processes are quite complex: in some cases they take place through two steps (vertex detachment and successive displacement of the impurity at a later time), and in general there are several different diffusion mechanisms, in which different inner atoms are involved; often, a large number of surface atoms is displaced, as the adatom pops up quite far from the atom emerging from the subsurface shell (see Fig. 4.1.5). For this reason, the estimate of the energy barriers by methods such as Nudged Elastic Band (NEB) [148] is rather cumbersome, as one should take into account many different diffusion processes. On the other hand, since the diffusive regime has not been reached in our MetaD simulations, the estimate of the barrier through MetaD-based methods does not give satisfactory results. Therefore we have decided to evaluate the activation barriers by means of the well-known Arrhenius plot.

First we have considered the case of  $\text{Au}_1\text{Co}_{146}$ , in which the diffusion process takes place through a single step at all temperatures. We have run 30 independent MD simulations at four different temperatures (450, 500, 550 and 600 K), we have evaluated the average time for the first occurrence of the event at each temperature and we have made the Arrhenius plot of the rate  $r_{\text{vf}}$  of the process of vacancy formation:

$$r_{\text{vf}} = r_{\text{vf}}^{\circ} \exp\left(-\frac{E_a}{k_B T}\right) \quad (4.5)$$

where  $r_{\text{vf}}^{\circ}$  is the frequency prefactor and  $E_a$  is the activation barrier. The activation barrier turns out to be  $E_a = (0.97 \pm 0.03)$  eV, and  $r_{\text{vf}}^{\circ} \sim 10^{17} \text{ s}^{-1}$ . We note that the calculated prefactor is quite large, which may be due to two reasons; firstly,  $E_a$  is an effective barrier which takes into account several similar diffusion processes, and not a single well-defined process; secondly, each diffusion process involves the concerted displacement of many atoms.

We have tried the same kind of activation barrier evaluation for other systems, namely  $\text{Au}_1\text{Co}_{308}$ ,  $\text{Ag}_1\text{Cu}_{146}$  and  $\text{Ag}_1\text{Cu}_{308}$ . In these cases one should keep in mind that in our high-temperature MD simulations process does not take place through a single step, but the displacement of the impurity is preceded by the detachment of a vertex atom. The estimated energy barrier refers to such combined process; that estimate should reflect the energy difference between the highest saddle point encountered during the whole process and the starting configuration. The highest barrier is that of the rate limiting process, which we observe to be the one in which the impurity moves from the center to the second shell by a collective displacement. Given these caveats, for  $\text{Au}_1\text{Co}_{308}$  and

Ag<sub>1</sub>Cu<sub>146</sub> we have obtained  $E_a = (1.16 \pm 0.04)$  eV and  $(2.1 \pm 0.2)$  eV, respectively. In the case of Ag<sub>1</sub>Cu<sub>308</sub> the temperature range in which it is possible to observe the process in our MD time scale is very limited, so that we have been unable to produce a reliable estimate of the barrier.

To study the following steps of the diffusion process, we have performed new simulations, with the impurity initially placed in the second and third shell of the perfect Ih matrix, without central vacancies. In this case, simulations have been performed only for Au-Co and Ag-Cu clusters of sizes 147 and 309 atoms. The initial placement in third shell has been considered only for the 309-atoms Ih; in that case, both inequivalent starting sites have been considered (see Fig. 4.1.1(a)). Again, in 10  $\mu$ s-long MD simulations at room temperature the systems do not display any significant evolution, so that MD simulations at higher temperatures and MetaD simulations were necessary to study the diffusion process. In all cases we have observed diffusion pathways similar to that previously described, in which the migration of the impurity to the outer shell takes place together with the formation of an internal vacancy. The vacancy appears in the site originally occupied by the impurity. The position of the vacancy suggests that its formation is again due to a push-like mechanism initiated by the impurity, which has indeed been confirmed by the short-timescale analysis of the simulations. Again, small surface reconstructions have sometimes been observed before the diffusion, especially at high temperatures.

The observed diffusion pathways have been analysed in terms of energy and atomic pressure on the impurity. In Fig. 4.1.7 we show the energy and pressure profiles calculated during the different steps of the evolution, for Au<sub>1</sub>Co<sub>146</sub> and Au<sub>1</sub>Co<sub>308</sub>. Energy and pressure levels corresponding to perfect Ih configurations (without the vacancy) are displayed as continuous lines, whereas for configurations with the central vacancy dashed lines are used.

The displacement of the impurity from the center to the second shell is associated with a significant decrease of the total energy of the clusters, for both Au-Co systems; however, we notice that the configuration obtained after the diffusion (impurity in the second shell, central vacancy) is less energetically favourable than its perfectly Ih counterpart (impurity in the second shell, no central vacancy). On the other hand, we observe a major improvement of the atomic pressure on the impurity, which decreases by tens of GPa in both cases. As regards the subsequent diffusion steps, we observe that the displacement of the impurity, with the formation of the vacancy in the second and third shell, always increases significantly the energy of the system. However, as observed for the impurity migration from the central site, the local pressure on the impurity decreases during the process. Furthermore, if we compare the two possible configurations (with and without the vacancy) for any given impurity position, we find that the presence of the vacancy is always associated to lower values of the atomic pressure on the impurity. This effect is able to temporarily stabilize the vacancy, which is not immediately filled and therefore can actually be observed in our simulations. In some simulations we have observed the subsequent migration of the vacancy from the second shell to the more favourable central site, whereas we have never observed the vacancy migration from the third shell inwards.

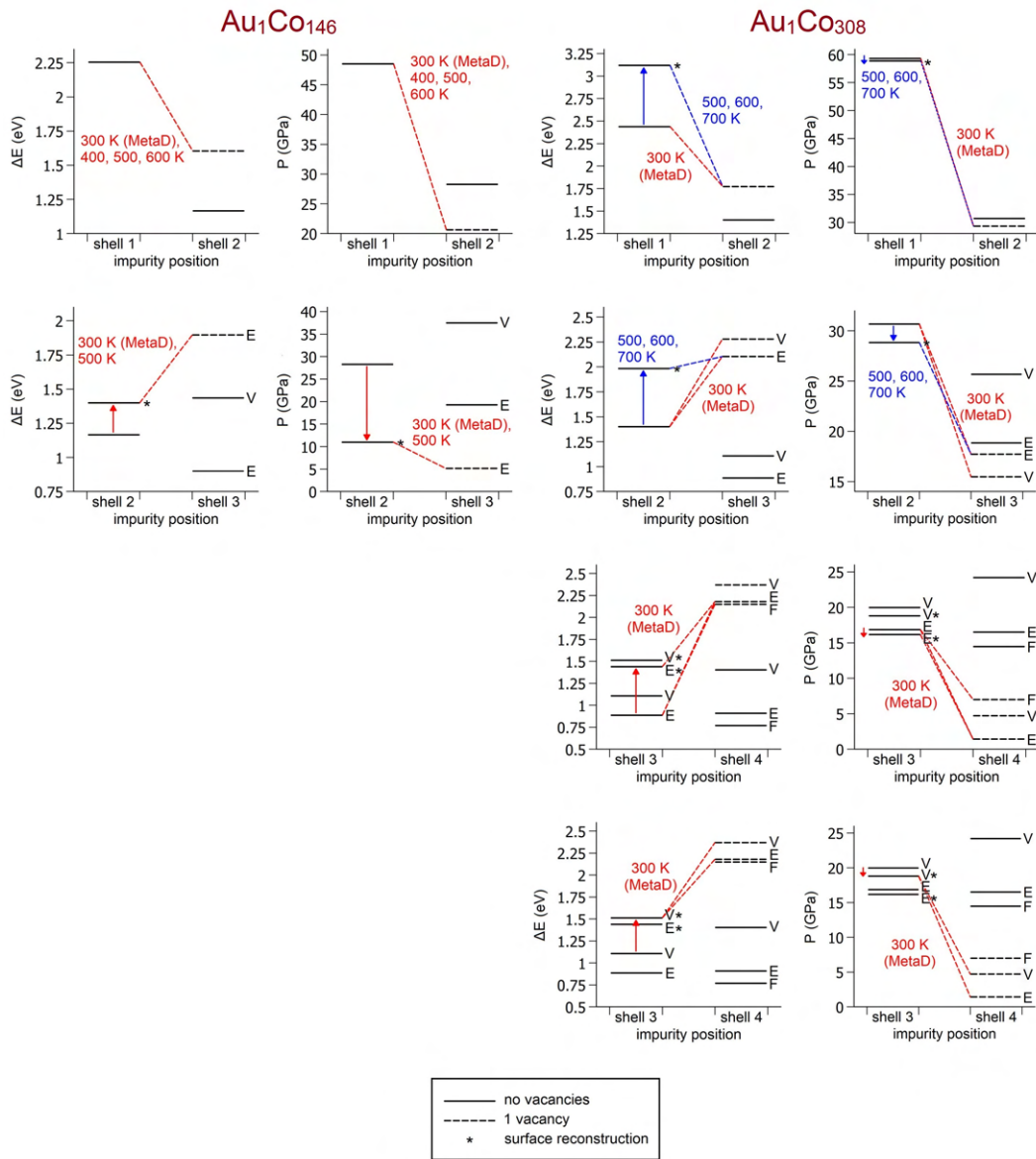


**Figure 4.1.7:** Energy and atomic pressure on the impurity during the impurity diffusion process for  $\text{Au}_1\text{Co}_{146}$  and  $\text{Au}_1\text{Co}_{308}$ . First line: displacement from the center to the second shell. Second line: displacement from the second to the third shell. Third and fourth line: displacement from the third to the fourth shell, starting from edge and vertex site, respectively (only for  $\text{Au}_1\text{Co}_{308}$ ). Energy differences from the best impurity placement on the cluster surface are displayed. Energy and pressure levels corresponding to perfect Ih and Ih with with one vacancy in the central site are displayed with continuous and dashed lines, respectively. Levels corresponding to perfect Ih with adatoms or minor surface reconstructions are marked with a star. All possible diffusion pathways observed in simulations at different temperatures are shown, in which the cluster keeps the perfect Ih geometry.

*Adapted from D. Nelli, F. Pietrucci and R. Ferrando, Impurity diffusion in magic-size icosahedral clusters, J. Chem. Phys., 155:144304, 2021.*

The pressure profiles in Fig. 4.1.7 confirm that the driving force for the impurity diffusion within the Ih matrix is the release of the compressive stress on the impurity itself. Configurations with an inner vacancy are indeed effective in this sense, as the pressure on the impurity is much lower compared to the initial value. In the two-steps process observed at  $T > 300$  K, the initial surface reconstruction corresponds to a rather large increase of the cluster energy and has small effects on the local pressure on the impurity; however, if one surface vertex is removed, the atomic row which has to be “pushed” outwards by the impurity is shorter by one atom, and the energy barrier of the process is expected to be lower as well. Therefore, at temperatures in which such minor surface reconstruction is activated, it always precedes the migration of the impurity, actually accelerating the diffusion process.

The analysis of MD and MetaD simulations with different initial placements of the impurity gives us a general idea of the whole diffusion process. By putting together the simulation results, we can describe overall diffusion pathways, from the central site to the subsurface shell of the Ih matrix. At each step of the diffusion a vacancy can appear. Since in each simulation set the impurity has been placed in a perfect Ih (without inner vacancies), so far we have actually assumed that the vacancy created at each step is filled before the following step begins. However, due to the already discussed stability of inner vacancies in Ih clusters (particularly high in the case of the central vacancy), we cannot exclude the possibility that they survive during the whole diffusion process. This has been indeed observed in our simulations, as we will briefly discuss in the following.

We have initially placed the impurity in the central site and we have let the system evolve until the completion of the diffusion, i.e. until the impurity has reached the NP surface. Different diffusion pathways have been observed. In our simulations, the central vacancy created during the first step of the diffusion is often filled while the impurity is in the second shell; however, sometimes it is still present when the impurity migrates to the third shell, and sometimes it even survives until the impurity arrives on the surface. Such behaviour can be observed for all the considered systems.

In Fig. 4.1.8 we show two possible diffusion pathways, obtained for  $\text{Au}_1\text{Co}_{146}$  in two independent MetaD simulations at room temperature. For both pathways we show the evolution in the space of MetaD CVs, i.e. in the  $s$ - $z$  plane, and the behaviour of the total energy of the cluster (in (a, b) and (c, d), respectively). In (e, f), snapshots of the fundamental evolution steps are shown as well, in which we can see the Au impurity gradually migrating from the center to the surface of the cluster. In the first case (left panel of Fig. 4.1.8) the central vacancy created during the initial diffusion step is filled while the Au atom is still in the second shell; as the Au atom migrates to the third shell, a second vacancy appears in the second shell, which is again filled before the subsequent diffusion step takes place. At the end of the evolution the Au atom reaches the cluster surface, but the lowest energy configuration is not obtained, as some surface defects (rosette reconstruction) are still present. In the second case (right panel of Fig. 4.1.8) the central vacancy is maintained during the whole diffusion process, so that again the final structure does not correspond to the best configuration for this system. Here the migration of Au from the second to the third shell takes

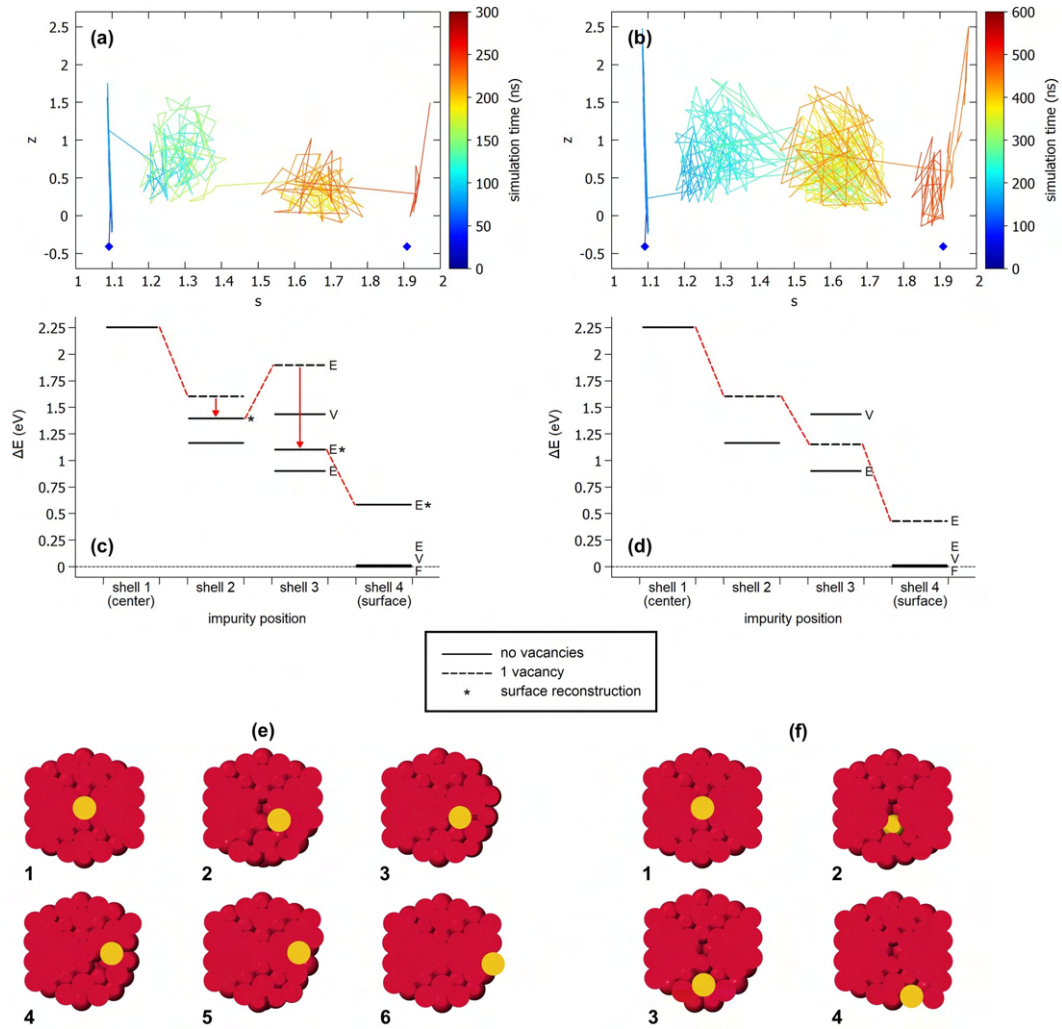


**Figure 4.1.8:** Possible diffusion pathways obtained for Au<sub>1</sub>Co<sub>146</sub> in two independent MetaD simulations at room temperature. For each pathway (on the left and right panel of the figure) we show: (a,b) evolution in the space of the MetaD CVs, i.e. the  $s$ - $z$  plane; the blue dots in the bottom part of the graphs represent the starting configuration (on the left) and the desired final configuration of the process, i.e. the global minimum (on the right); (c,d) total energy of the cluster during the diffusion process; the reference value of the energy corresponds to the best placement of the impurity in the cluster; (e,f) snapshots of the fundamental steps of the evolution. The MetaD parameters used in both simulations are: Gaussian height  $\delta = 0.10$  eV, Gaussian width  $(\sigma_s, \sigma_z) = (0.02, 0.1)$ , deposition stride 100 ps. Reproduced from D. Nelli, F. Pietrucci and R. Ferrando, *Impurity diffusion in magic-size icosahedral clusters*, *J. Chem. Phys.*, 155:144304, 2021.

place without the formation of a further vacancy.

Now we briefly analyse the progression of the two MetaD simulations in the  $s$ - $z$  plane, as displayed in Fig. 4.1.8(a, b). In both cases we can easily identify four well-separated regions through which the system passes during the evolution. Such regions in the CV space are associated to the placement of the Au impurity in the four different Ih shells, and therefore the sudden jumps between adjacent CV regions correspond to the migration of Au between adjacent shells. The ability to discriminate between configurations in which the impurity occupies different Ih shells is a crucial property of the chosen CVs, which indeed guarantees the efficiency of our MetaD simulations in accelerating the process of impurity diffusion towards the surface. We note that for any given placement of the impurity, different possible configurations are not so easily distinguishable. Configurations with or without the vacancy, even though rather different regarding the total energy of the cluster, are placed in the same region of the  $s$ - $z$  plane, so that the vacancy filling process is not easily identified by solely looking at the behaviour of the CVs during the evolution. In short, the CVs used in this work are strongly sensitive to the position of the impurity within the Ih matrix, but less sensitive to the presence of a vacancy and to other fine details of the cluster structure, such as some surface reconstructions.

In some evolution pathways we have observed the contemporary presence of multiple vacancies inside the cluster, each one created during a different diffusion step. This last scenario happens frequently in MetaD simulations at room temperature; configurations with two or three vacancies have been observed also in MD simulations at high temperatures, for short times. Multiple vacancies are typically associated to high energy values, therefore they are expected not to frequently appear during the evolution, and to be poorly stable. We believe that the probability of creation of multiple vacancies during the diffusion is somewhat overestimated by MetaD: probably, in MetaD simulations the migration of the impurity towards the surface is accelerated to a higher degree than the vacancy-filling process, and therefore a new vacancy appears before the one created in the previous diffusion step is filled.

#### 4.1.4 OTHER IMPURITY DIFFUSION PROCESSES

Finally, we discuss the occurrence of other diffusion pathways in our simulations. In such pathways, the nanoparticle geometric structure is significantly deformed: the cluster temporarily takes a liquid-like configuration, at least on one side, and the impurity quickly diffuses towards the surface; the perfect Ih geometry is then restored, as described in Ref. [123]. Such disordered-mediated diffusion processes have been observed in high-temperature MD simulations for Au-Co and Ag-Cu systems, being more frequent for initial position of the impurity closer to the cluster surface. It has never been observed in MetaD simulations at room temperature of Au-Co, Ag-Cu, Ag-Co, Ag-Ni and Au-Rh clusters, in which the diffusion of the impurity is always coupled to the formation of the internal vacancy in the perfect Ih, as described above.

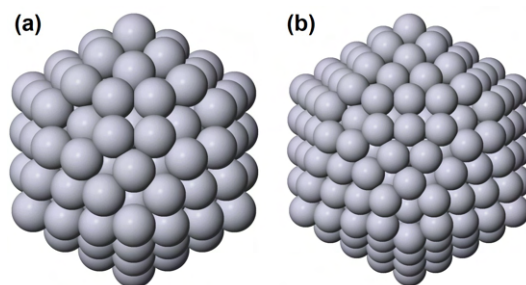


**Figure 4.1.9:** Most favourable rosette-like reconstructions for Pt Ih: (a) Ih of size 147, in which two fivefold vertices are replaced by hexagonal rings; (b) Ih of size 309, in which three vertices are replaced.

*Reproduced from D. Nelli, Central vacancy creation in icosahedral nanoparticles induced by the displacement of large impurities, accepted in Eur. Phys. J. Appl. Phys.*

size	system	$E_{\text{rosette}} - E_{\text{Ih}}$
147	Co	+0.58
	Cu	+1.41
	Ni	+2.09
	Pt	-0.22
	Rh	+4.05
309	Co	+0.73
	Cu	+1.96
	Ni	+2.93
	Pt	-0.54
	Rh	+5.54

**Table 4.1.1:** Energy difference (in eV) between Ih displaying the rosette-like surface reconstructions shown Fig. 4.1.9 and perfect Ih of the same size. Data refer to pure clusters.

*Reproduced from D. Nelli, Central vacancy creation in icosahedral nanoparticles induced by the displacement of large impurities, accepted in Eur. Phys. J. Appl. Phys.*



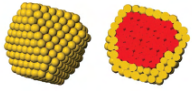
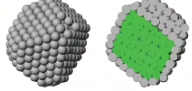
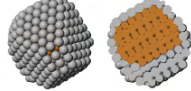
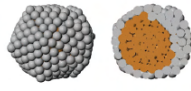
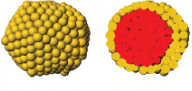
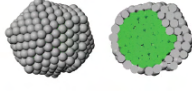
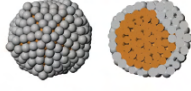
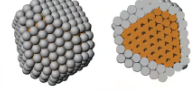
The only exception is the Au-Pt system, as in all our room temperature MetaD simulations the Pt Ih matrix partially deforms while the Au impurity is still in the central site, and the impurity then diffuses outwards within such deformed region. The activation of deformation-mediated diffusion processes at room temperature is due to the instability of the perfect Ih geometry. The tendency to rosette-like surface reconstructions has indeed been observed for pure Pt Ih clusters, also at the DFT level [23]. The most favourable rosette-like reconstructions for Pt Ih of size 147 and 309 are shown in Fig. 4.1.9.

To check the stability of the Ih matrix, we have evaluated the energy of the structures of Fig. 4.1.9 for pure Co, Cu, Ni, Pt and Rh, and we have compared it to the energy of the perfect Ih of the same size. Data are reported in Table 4.1.1. In all cases the reconstruction of the Ih surface is largely energetically unfavourable, except for Pt clusters, in which the presence of rosette motifs lowers the total energy of the cluster. Energy calculations are in agreement with the results of MetaD simulations, in which the disordering of the surface at room temperature is observed only for Au-Pt. Our results show that the stability of the Ih matrix against surface reconstruction is essential for the observation of the combined process of impurity diffusion and central vacancy formation. If the Ih surface is unstable, other pathways are more likely, in which the structure is partially deformed. We point out that our simulations are able to reproduce both types of diffusion processes; this further confirms the effectiveness of our MetaD scheme in the study of the diffusion of impurities within NPs.

## 4.2 CHEMICAL ORDERING EQUILIBRATION PATHWAYS IN PHASE-SEPARATING BIMETALLIC SYSTEMS

In Section 4.1, we have studied nanoalloy equilibration by focusing on the diffusion of a single atom within a volume occupied by atoms of a different species. This approach, though helpful to identify the elemental steps of chemical ordering transformations, is actually difficult to apply in more complex cases. Single-atom displacements are hardly distinguishable at the typical timescale and space resolution of the experiments; also in computer simulations, if a large number of atoms of the two species is considered, following the diffusion pathway of each one is not feasible in practical terms. Therefore a different approach has to be employed, in which the main focus is not on the diffusion of individual atoms, but on the transformations of the overall chemical ordering. The results that we will present in the following have been obtained through such approach.

We have simulated the evolution of three systems, namely Au-Co, Ag-Ni and Ag-Cu nanoalloys, from the same type of initial out-of-equilibrium configuration, with the aim of comparing their evolution pathways towards equilibrium. The three systems indeed share a few common features: they present very weak bulk miscibility [149–151], and lattice mismatch above 10%, with the element of larger atomic size (either Au or Ag) also presenting lower cohesive and surface energy. These features are driving forces towards phase separation at the nanoscale, leading to Au and Ag surface segregation and finally to the formation of core-shell Co@Au [40, 51, 152–157], Ni@Ag [22, 41, 42, 56, 158–160], and Cu@Ag [22, 41, 42, 51, 56, 114, 129, 161–170] structures at equi-

	Au <sub>293</sub> Co <sub>293</sub>	Ag <sub>293</sub> Ni <sub>293</sub>	Ag <sub>293</sub> Cu <sub>293</sub>	Ag <sub>280</sub> Cu <sub>281</sub>
Lowest energy structure				
Best structure of competing motif				
$\Delta E$	2.35	0.46	0.60	0.24

**Figure 4.2.1:** Low-energy structures. For each composition we show both the lowest energy structure (which is fcc for Au<sub>293</sub>Co<sub>293</sub>, Ag<sub>293</sub>Ni<sub>293</sub> and Ag<sub>293</sub>Cu<sub>293</sub>, and Ih for Ag<sub>280</sub>Cu<sub>281</sub>) and the best structure of the competing motif (which is Ih for Au<sub>293</sub>Co<sub>293</sub>, Ag<sub>293</sub>Ni<sub>293</sub> and Ag<sub>293</sub>Cu<sub>293</sub>, and fcc for Ag<sub>280</sub>Cu<sub>281</sub>). In all cases, both NP surface view and NP cross-section are shown. Ag, Au, Co, Ni and Cu atoms are coloured in grey, yellow, red, green and orange, respectively.  $\Delta E$  is the energy difference (in eV) between the global minimum and the best isomer of the competing motif.

Reproduced from D. Nelli and R. Ferrando, *Core-shell vs. multi-shell formation in nanoalloy evolution from disordered configurations*, *Nanoscale*, 11:13040, 2019.

librium, if the composition is sufficiently rich in either Au or Ag to fully cover the core.

We have considered NPs of diameters between 2.5 and 3 nm, a size range which is investigated in several experiments, and of 50%–50% composition. The initial chemical ordering has been chosen to be randomly intermixed, and the evolution towards the equilibrium core-shell arrangement has been studied by means of MD simulations at different temperatures. Our simulations have shown that, in spite of the similarities between the three bimetallic systems, their approach to equilibrium follows quite different pathways, with different intermediate metastable configurations appearing during the evolution. Moreover, we have found that chemical ordering transformations can occur through collective processes, in which multiple atoms are involved, and which can induce a sudden transformation of the NP shape. We have also pointed out the influence of the NP geometric structure in the speed of chemical ordering equilibration<sup>3</sup>.

Our results, that will be extensively discussed in the following, have indeed shed some light on chemical ordering equilibration pathways in nanoalloys, in the case of phase-separating bimetallic systems. Work is in progress to study chemical ordering transformations in systems with tendency towards intermixing, such as Au-Cu, Au-Ag and Pt-Pd.

#### 4.2.1 FROM RANDOMLY INTERMIXED TO CORE-SHELL CHEMICAL ORDERING

The initial configurations of our MD simulations are the TO of 586 atoms and, for Ag-Cu, also the Ih of 561 atoms; the reason behind the choice of the Ih structure in the case of Ag-Cu will become clear later. As anticipated, in all cases we have considered a 50%–50% composition and a randomly intermixed chemical ordering. Such initial structures are very far from the typical equilibrium con-

<sup>3</sup>Results have been published in Ref. [58]

configurations, for all temperatures that we have considered. A better reference for the equilibrium configurations, especially for low temperatures, is given by the lowest-energy structures as found by our global optimization searches (see Section 2.2 for details on the global optimization procedure). These are always phase-separated, of the core-shell type, with cores of Co, Ni or Cu and shells of Ag or Au, as shown in Fig. 4.2.1. For  $\text{Au}_{293}\text{Co}_{293}$ ,  $\text{Ag}_{293}\text{Ni}_{293}$  and  $\text{Ag}_{293}\text{Cu}_{293}$  the lowest-energy structures are always of fcc type, with off-center cores which are fully covered by a thin shell of either Au or Ag. This shell is mostly an atomic skin and it can be thicker on one side of the NP. These structures are in close energetic competition with Ih structures (also shown in Fig. 4.2.1) presenting either chiral shells (for Au-Co and Ag-Ni) or anti-Mackay shells (for Ag-Cu). For  $\text{Ag}_{280}\text{Cu}_{281}$ , fcc and Ih structures are again in close competition, but in this case the Ih with chiral shell is slightly lower in energy. We note that since fcc and Ih motifs are quite close in energy, it is possible that, at high temperatures, entropic effect reverse the stability order [171]. We also note that the structures in Fig. 4.2.1 are putative global minima; we do not exclude that structures of even lower energy can be found by further calculations. However we expect that the overall chemical ordering will always be of the same core-shell type.

MD simulations have been performed for temperatures in the range 300-700 K, with a duration of 5-10  $\mu\text{s}$  each. The evolution of the structures from their initial configuration has been described by monitoring the compositions of the different regions within the NP. Three regions have been considered: the surface and the subsurface, which correspond to single atomic layers, and the interior region, which is formed by atoms that belong neither to the surface nor to the subsurface. Moreover, since we are considering systems with tendency to phase separation, we have also monitored the connectivity of the aggregates of Au and Ag (the meaning of connectivity will be explained in the following).

#### 4.2.2 SURFACE SEGREGATION AND SHAPE TRANSFORMATIONS IN THE FIRST STAGE OF THE EVOLUTION

In the case of Au-Co and Ag-Ni, it is possible to clearly distinguish a first step in the evolution of the nanoparticle chemical ordering, in which Au and Ag atoms quickly segregate to the surface. During this first evolution step, significant transformations of the overall geometric shape take place, too. In fact, even though the cluster has initially a TO shape, the obtained final configurations are mostly of the Ih family. Specifically, the Ih geometry has been obtained in all simulations of Ag-Ni nanoparticles, at all the considered temperatures ( $T = 300, 400, 500, 600$  and  $700$  K), and in all simulations of Au-Co at  $T = 300, 400$  and  $500$  K; at  $600$  K, the fcc-to-Ih shape transformation has been observed in 4/5 simulations, whereas in one case the final structure was of fcc type.

The observed shape transformations actually take place in the very first part of our simulations: in all cases, the initial configuration transforms very quickly (less than 10 ns) into a structurally disordered liquidlike configuration, which then reorganizes into a defective Ih cluster. We note that even though the initial structures and the lowest-energy structures are both fcc, the evolution is almost always towards a different structural motif. This is due to the formation of several regions

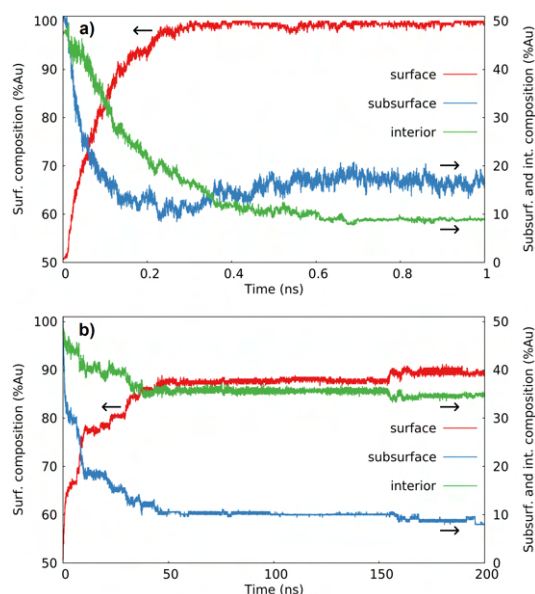


**Figure 4.2.2:** Evolution of surface, subsurface and inner compositions of Au-Co in the first part of typical simulations at (a)  $T = 600$  K and (b)  $T = 300$  K. Surface composition scale is on the left of the panels, while subsurface and inner composition scale is on the right of the panels. *Reproduced from D. Nelli and R. Ferrando, Core-shell vs. multi-shell formation in nanoalloy evolution from disordered configurations, Nanoscale, 11:13040, 2019.*

of local fivefold symmetry in the disordered structures, which tend naturally to evolve to the full fivefold symmetry axes of the Ih symmetry.

The first stage of the evolution has been analysed quantitatively. In Fig. 4.2.2 we show the behaviour of the composition of the surface layer, of the subsurface layer and of the inner part of the Au-Co cluster for typical simulations at the highest and at the lowest temperatures, i.e.  $T = 600$  K and 300 K. In both cases, inner Au atoms migrate fast to the surface, and surface Co atoms incorporate in the subsurface, so that the composition of these layers becomes strongly Au-rich and Co-rich, respectively. At 600 K, the surface layer becomes 100% Au within 500 ps in all five simulations we have made. On the other hand, at 300 K, reaching 90% of Au at the surface has required times between 100 and 600 ns. Typical time scales for reaching a threshold of 90% at 400 and 500 K are 10–20 ns and 1–2 ns, respectively. Our simulations also show that the rearrangement process is not limited to the two external layers, as we can see by analyzing the evolution of the composition of the inner part. At all temperatures, there is an initial drop of the inner Au content, whose time scale is the same as for changes in composition of the surface and subsurface layers. This coincidence indicates that the Au atoms are simultaneously migrating towards the surface layer from both the subsurface layer and the inner part of the cluster. A similar behaviour has been observed in the first stage of the evolution of the Ag-Ni cluster. We note that the structural transition to the disordered liquidlike configuration and the segregation of Au and Ag atoms to the nanoparticle surface to form a complete Au/Ag skin take place at the same time, suggesting that these two effects are strongly

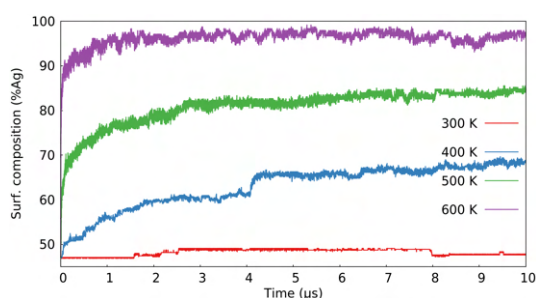


**Figure 4.2.3:** Evolution of the composition of the surface layer of Ag-Cu in typical simulations at four different temperatures ( $T = 300, 400, 500$  and  $600$  K).

Reproduced from D. Nelli and R. Ferrando, *Core-shell vs. multi-shell formation in nanoalloy evolution from disordered configurations*, *Nanoscale*, 11:13040, 2019.

correlated; this point will be better analysed in the following.

The evolution of both geometric structure and chemical ordering in Ag-Cu is much slower than in Au-Co and Ag-Ni. In Fig. 4.2.3 we show the evolution of the composition of the surface layer of  $\text{Ag}_{293}\text{Cu}_{293}$  for representative simulations at the different temperatures. At 300 K there is essentially no change in surface composition in the whole duration of the simulation, so that the surface layer stays essentially at 50% Ag–50% Cu. This is quite different from the cases of Au-Co (see Fig. 4.2.2) and of Ag-Ni, in which the segregation to the surface layer leads to a composition close to 90% Au or Ag within few tens of ns. In order to achieve a comparable composition of the cluster surface, one has to simulate at much higher temperatures, close to 600 K. Some migration of Ag to the surface indeed already takes place at 400 and 500 K, but it is a phenomenon which involves only the surface and subsurface layers (which becomes enriched in Cu), without any substantial migration of Ag from deeper locations. This is shown by the data reported in Fig. 4.2.4, in which the quantity of Ag atoms in the inner part of the cluster exhibits no variation at 400 K (see Fig. 4.2.4(a)), and a rather slow variation at 500 and 600 K (see Fig. 4.2.4(b, c)). In all these case, the geometric structure keeps a somewhat distorted TO shape, without any evidence of the (temporary) formation of metastable liquidlike configurations, which has been instead observed in both Au-Co and Ag-Ni clusters. For observing such liquidlike configurations, and the subsequent structural transformation to Ih, one has to increase the temperature to 650 K. At this temperature, the fast migration of Ag atoms from the inner part of the cluster to the surface has been observed (see Fig. 4.2.4(d)).

Our results on the evolution of Ag-Cu clusters indeed confirm the correlation between structural disordering and surface segregation of Ag atoms: when the transformation to the liquidlike configuration is activated, the composition of the surface layer evolves quickly, due to the migration of Ag atoms from the inner part of the NP; conversely, when such structural transformation does not occur, the migration of Ag atoms is restricted to the most external layers, and the evolution of the chemical ordering is therefore much slower.

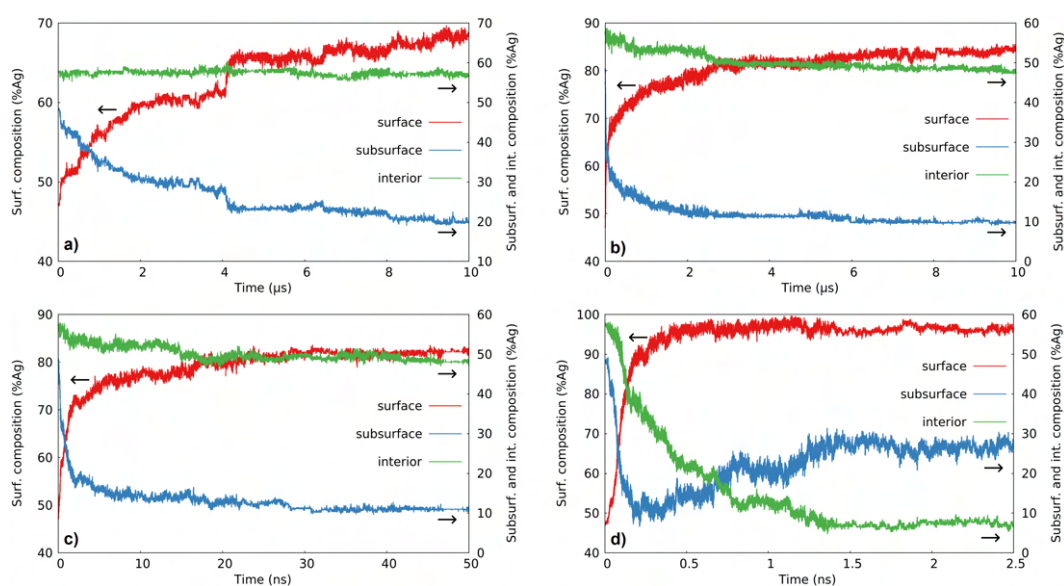


**Figure 4.2.4:** Evolution of surface, subsurface and inner composition of Ag-Cu in typical simulations at (a)  $T = 400\text{ K}$ , (b)  $T = 500\text{ K}$ , (c)  $T = 600\text{ K}$  and (d)  $T = 650\text{ K}$ . Surface composition scale is on the left of the panels, while subsurface and inner composition scale is on the right of the panels.

Reproduced from D. Nelli and R. Ferrando, *Core-shell vs. multi-shell formation in nanoalloy evolution from disordered configurations*, *Nanoscale*, 11:13040, 2019.

#### 4.2.3 FORMATION OF DIFFERENT TYPES OF THREE-SHELL INTERMEDIATE CONFIGURATIONS

In the previous section we have discussed the evolution of the NP surface; here we describe the evolution of the internal region, as obtained in our MD simulations. Specifically, we will focus on the possible intermediate chemical ordering types appearing during the evolution towards the equilibrium core-shell arrangement, which are different for the three systems.

Firstly, we analyse the behaviour of the Au-Co system. On our time scale, the complete evolution to the equilibrium Co@Au core-shell configuration has been achieved only at 600 K. For lower temperatures, the structure evolves rather quickly to a metastable three-shell configuration of the Au@Co@Au type, but then it remains trapped there. In Au@Co@Au structures, the central part of the NP is enriched in Au, whereas the intermediate part, comprising also the subsurface layer, is mostly Co, and it is covered by the Au-skin. The complete transformation pathway leading to the equilibration of chemical ordering, as observed in our simulations at 600 K, takes place through a series of steps. The different evolution stages are shown in Fig. 4.2.5(a1-e1).

First of all, an almost complete Au-skin is formed, together with a subsurface enrichment in Co. This process takes place through the transformation of the cluster into a metastable liquidlike structure (see Fig. 4.2.5(b1), top row), as already discussed in the previous section. In the inner part of the cluster, Au atoms form a ramified aggregate which is still connected to the Au-skin, usually through several branches (Fig. 4.2.5(b1), bottom row). The newly formed Au-skin becomes gradually better ordered, with well-developed facets, as can be seen by comparing the cluster surfaces of Fig. 4.2.5(b1) and (c1).

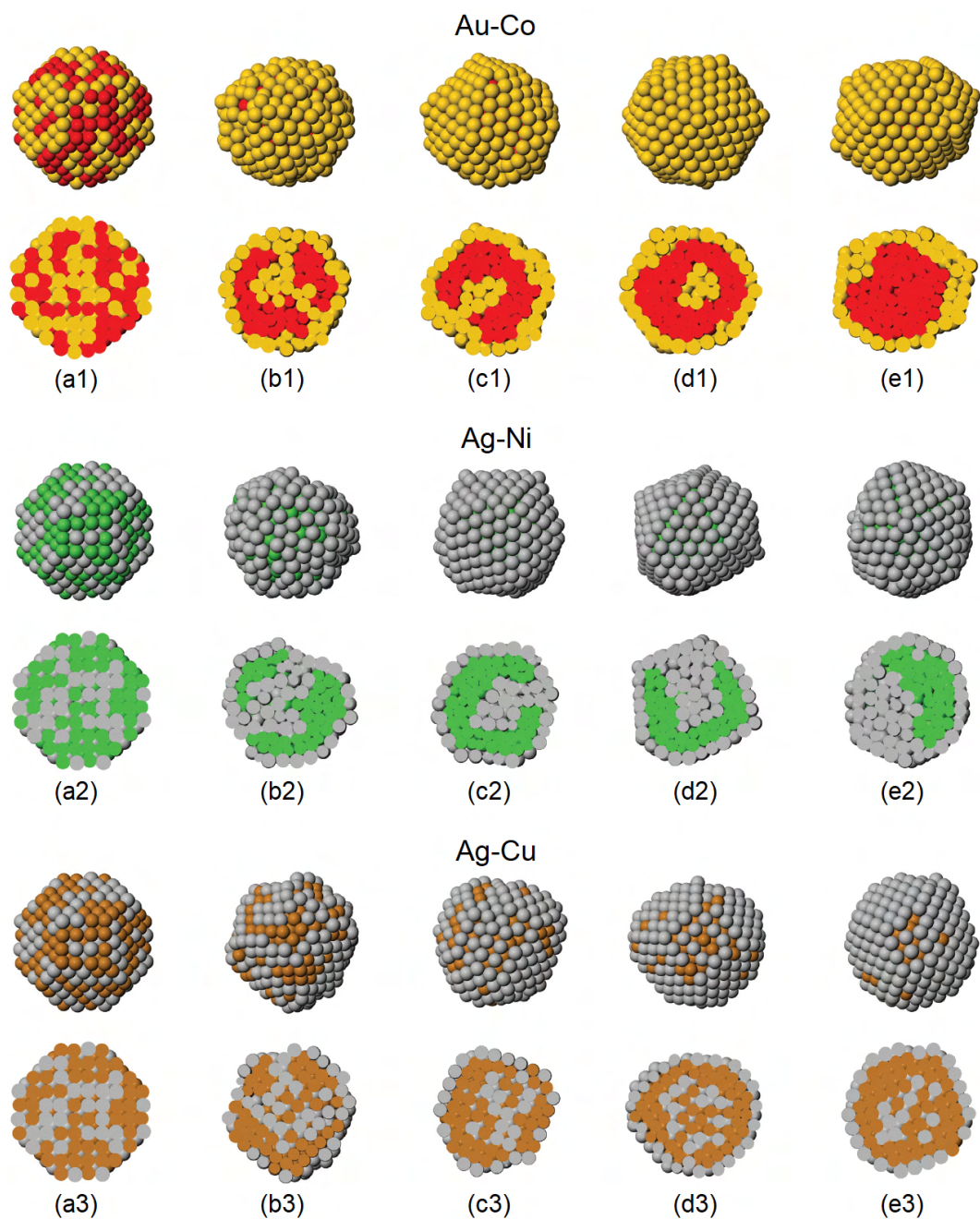


**Figure 4.2.5:** Equilibration stages of chemical ordering in typical simulations of Au-Co, Ag-Ni and Ag-Cu at  $T = 600\text{K}$ . For each configuration, the image in the top row shows the cluster surface and the image in the bottom row shows a cross-section. (a1, a2, a3) Starting configurations for the three systems; images of Au-Co evolution taken after (b1) 0.7 ns, (c1) 1.7 ns, (d1) 15 ns and (e1) 4  $\mu\text{s}$ ; images of Ag-Ni evolution taken after (b1) 0.3 ns, (c1) 200 ns, (d1) 3.5  $\mu\text{s}$  and (e1) 9  $\mu\text{s}$ ; images of Ag-Cu evolution taken after (b1) 1.4 ns, (c1) 8 ns, (d1) 200 ns and (e1) 1  $\mu\text{s}$ .

*Adapted from D. Nelli and R. Ferrando, Core-shell vs. multi-shell formation in nanoalloy evolution from disordered configurations, Nanoscale, 11:13040, 2019.*

A second stage follows on a slower time scale, in which the inner ramified Au aggregate tends to become more compact. The connecting branches are gradually eliminated (see Fig. 4.2.5 (b1), in which a single branch is left), together with the migration of some Au atoms towards the cluster surface. At the end of the second stage, the connecting branches have disappeared (even though a single branch may occasionally reform) and a true Au@Co@Au three-shell structure is formed, with well separated Au-skin and Au-core, and a Co intermediate shell. In the final third stage, the Au atoms in the core migrate towards the surface to reach the Co@Au equilibrium chemical ordering; in this stage we have observed a rather frequent formation and elimination of connecting branches with short lifetime; when connecting branches are present, the Au atoms of the inner core are able to progressively migrate to the surface. This is a slower process, which is however completed well before the end of our 600 K simulations in four cases over five. The only exception is the simulation in which the geometric structure is fcc, which is still of Au@Co@Au chemical ordering after 5  $\mu$ s. This may indicate a slower evolution of chemical ordering in fcc structures compared to Ih ones, a point which will be examined in more details later.

At lower temperatures, the first stage is always completed, as discussed in the previous section. Depending on the temperature, the simulations end either with configurations corresponding to the incomplete second stage (for  $T = 300$  and 400 K) or to the incomplete third stage ( $T = 500$  K).

The evolution of the inner part of the cluster has been analyzed more accurately, by monitoring the connectivity of the Au part, i.e. by determining whether Au atoms form a single connected aggregate comprising both the inner part and the Au-skin or not. Here, two Au atoms are considered as being connected if they are nearest neighbours, i.e. if their distance does not exceed the nearest-neighbour distance in bulk Au multiplied by 1.15, which is 3.31 Å. Two Au atoms belong to the same aggregate if they can be connected by a chain of nearest-neighbour Au–Au bonds. When a single aggregate has been found, with Au atoms in the central part of the cluster, we have counted how many branches connect these inner atoms with the Au skin. We note that in the perfect Au@Co@Au arrangement, there are no connecting branches so that we have two Au aggregates well separated by an intermediate Co shell.

At  $T = 500$  K, connecting branches are gradually eliminated, at a slower rate than at 600 K. Once the perfect Au@Co@Au arrangement is reached, a single branch may reform but no evolution to the Co@Au equilibrium chemical ordering has been accomplished on the 10  $\mu$ s time scale of the simulations. For  $T = 400$  and 300 K the evolution is even slower.

The results concerning the evolution of chemical ordering in Au-Co clusters are summarized in Table 4.2.1. We remark the distinction between the average and the perfect Au@Co@Au chemical ordering: in the average Au@Co@Au chemical ordering, the inner part is strongly enriched in Au, the intermediate part is strongly enriched in Co, and the surface contains essentially only Au, but connecting branches are present; in the perfect Au@Co@Au chemical ordering, the central Au aggregate is fully separated from the surface Au shell by a few layers of Co. As we will discuss in the following, this distinction is crucial for discussing the different behaviour of Ag-Ni with respect to



$T$ (K)	$n_{\text{core-shell}}$	$n_{3\text{-shell}}$		$\bar{n}_{\text{branch}}$
		average	perfect	
600	4	5	5	0
500	0	5	4	0.6
400	0	5	1	1.6
300	0	5	0	5

**Table 4.2.1:** Summary of the results for the evolution of chemical ordering in Au-Co NPs. For each temperature, 5 simulations have been made.  $n_{\text{core-shell}}$  is the number of simulations in which the equilibrium Co@Au chemical ordering has been reached;  $n_{3\text{-shell}}$  is the number of simulations in which the Au@Co@Au chemical ordering has been reached, at least for some time; we distinguish between average and perfect Au@Co@Au chemical ordering, i.e. with or without connecting branches between the Au core and the Au shell.  $\bar{n}_{\text{branch}}$  is the average number of connecting branches present in the last  $\mu\text{s}$  of the simulations. For  $T = 300, 400$  and  $500$  K,  $\bar{n}_{\text{branch}}$  has been calculated by averaging over all five simulations, since none of them have completed the transformation to the Co@Au chemical ordering. For  $T = 600$  K,  $\bar{n}_{\text{branch}}$  has been calculated using the only simulation which has not completed the transition to Co@Au.

*Reproduced from D. Nelli and R. Ferrando, Core-shell vs. multi-shell formation in nanoalloy evolution from disordered configurations, Nanoscale, 11:13040, 2019.*

Au-Co. In Au-Co, the perfect Au@Co@Au is formed for some time in all simulations at  $T = 600$  K and in four simulations over five at  $T = 600$  K. In Table 4.2.1 we also report the quantity  $\bar{n}_{\text{branch}}$ , defined as the number of connecting branches averaged over time in the last  $\mu\text{s}$  of the simulations.  $\bar{n}_{\text{branch}}$  clearly decreases with temperature, and therefore the compactness of the Au inner aggregate increases.

The evolution of the Ag-Ni cluster during a typical simulation at  $T = 600$  K is shown in Fig. 4.2.5 (a2-e2). In the first stage of the simulation, the behaviour resembles strongly that of Au-Co, with the transition to liquidlike structures, a fast segregation of Ag to complete an Ag-skin, and the formation of an average Ag@Ni@Ag three-shell arrangement, as we can see from comparison between Fig. 4.2.5 (b2) and (b1). However, the subsequent evolution shows important differences. At variance with all simulations of Au-Co at the same temperature, the perfect Ag@Ni@Ag chemical ordering is never obtained at any stage of the simulation, because at least one thick connecting branch is always present (see Fig. 4.2.5 (c2, d2)). Another difference is related to the final configuration, which is still somewhat incomplete. This configuration, shown in Fig. 4.2.5 (e2), can still be classified as average Ag@Ni@Ag. Instead, a true Ni@Ag would resemble to the final structure obtained for Au-Co in the same conditions (Fig. 4.2.5 (e1)), and to the optimal chemical ordering of Ag-Ni as reported in Fig. 4.2.1. In summary, the approach towards equilibrium is slower compared to Au-Co, and it involves the formation of different intermediate three-shell arrangements.

The behaviour of Ag-Cu is even more different, as it is evident by comparing the snapshots reported in Fig. 4.2.5 (a3-e3) to those in (a1-e1) and (a2-e2), all taken from simulations at the same temperature  $T = 600$  K. Besides the evolution of surface composition, which has been already

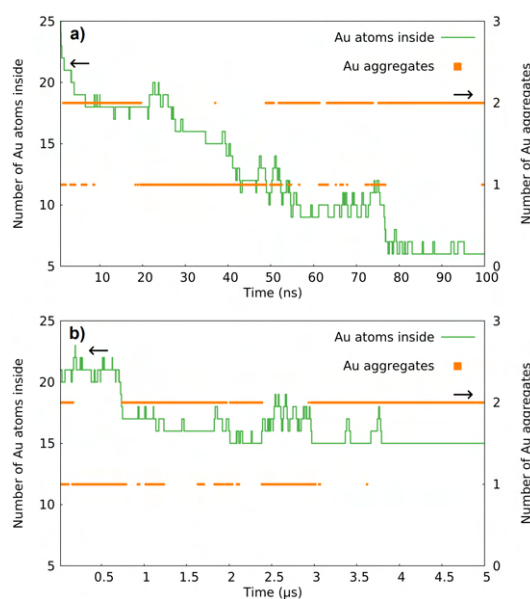


**Figure 4.2.6:** Evolution of the number of Au atoms in the internal part of the cluster and of the number of Au aggregates in two simulations of Au-Co at  $T = 600$  K: (a) Ih-shaped NP and (b) fcc-shaped NP. In both panels, the very initial stage of the simulation, in which the number of internal Au atoms drops from  $\sim 70$  to  $\sim 25$ , is not shown.

Reproduced from D. Nelli and R. Ferrando, *Core-shell vs. multi-shell formation in nanoalloy evolution from disordered configurations*, *Nanoscale*, 11:13040, 2019.

discussed, in Fig. 4.2.5(a3-e3) we can follow the formation of an average three-shell chemical ordering, in which the Ag aggregate in the inner part is much less compact than the corresponding aggregates of Au and Ag in Au-Co and Ag-Ni. The non-compact character of the Ag aggregate is maintained until the end of the simulation. This behaviour is consistent with a weaker tendency to phase separation in Ag-Cu compared to the other systems.

#### 4.2.4 EFFECT OF GEOMETRIC SHAPE ON THE CHEMICAL ORDERING EQUILIBRATION: FCC VS. IH

The results on the evolution of the inner part Au-Co clusters suggest that chemical ordering equilibration is faster in NP of Ih geometric shape compared to fcc ones. In fact, whereas all Ih nanoparticles have been able to reach the equilibrium Co@Au arrangement well before the end of our simulations at  $T = 600$  K, the fcc NP has not been able to equilibrate at the same simulation temperature; instead, it has remained trapped in a metastable Au@Co@Au configuration. Here we analyse this point in more details.

In Fig. 4.2.6 we show the evolution of the number Au atoms in the inner part of the cluster and of the number Au aggregates, for both an Ih-shaped (Fig. 4.2.6(a)) and the fcc-shaped NP (Fig. 4.2.6(b)) at 600 K. In both cases, the perfect Au@Co@Au is formed for some time. Here the perfect Au@Co@Au corresponds to the times in which two Au aggregates are counted, whereas a single Au aggregate indicates the presence of at least a connecting branch between the Au inner atoms and the Au shell. In simulation (a), the structure fluctuates for some time between the per-

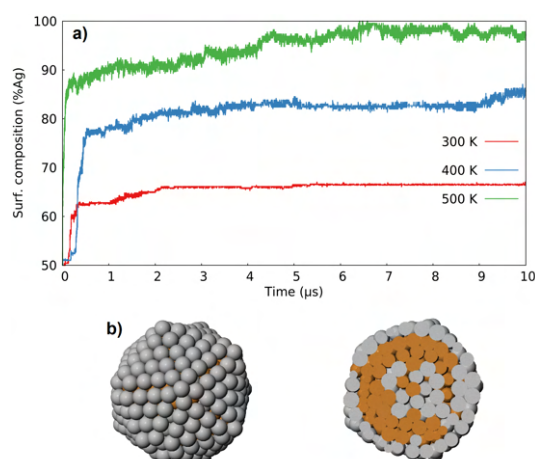


**Figure 4.2.7:** (a) Evolution of surface composition of Ag-Cu clusters of Ih shape at  $T = 300$ , 400 and 500 K. (b) Final snapshot from a simulation at 500 K. Both the cluster surface and its cross section are shown.

Reproduced from D. Nelli and R. Ferrando, *Core-shell vs. multi-shell formation in nanoalloy evolution from disordered configurations*, *Nanoscale*, 11:13040, 2019.

fect Au@Co@Au arrangement and configurations in which a single connecting branch is present. The presence of a connecting branch is associated with the migration of some Au atoms towards the cluster surface, indicated by a drop in the number of internal Au atoms in the figure. This leads to the equilibrium Co@Au arrangement on a time scale of  $0.1 \mu\text{s}$ . In simulation (b), the formation of connecting branches is not associated to a significant migration of Au atoms towards the outer shell. For this reason the simulation terminates with the perfect Au@Co@Au chemical ordering. These two different behaviours clearly indicate that Au atoms migrate more easily to the surface in Ih than in fcc NPs.

A second evidence of the influence of geometric shape in the speed of chemical ordering equilibration has been found in the case of Ag-Cu. Since the slow evolution of Ag-Cu clusters in the temperature range 300–600 K seems to be correlated to the absence of structural transformations to Ih shapes, we have run some simulations starting from an Ag-Cu Ih cluster, and we have compared the chemical ordering equilibration in this new simulation set to what we have observed for fcc clusters. We have considered an Ih cluster of almost the same size of the TO (561 atoms, i.e. a magic size for the Ih, instead of 586), with initially random chemical ordering. From this type of initial configuration, we have run two independent simulations of  $10 \mu\text{s}$  each at  $T = 300$ , 400 and 500 K. As shown in Fig. 4.2.7(a), the segregation of Ag atoms to the surface layer is considerably faster in the Ih than in the fcc cluster. We have not observed the formation of liquidlike configurations like those found for Au-Co and Ag-Ni; therefore the type of evolution is qualitatively the same for Ag-Cu Ih and fcc clusters (below 650 K). Let us compare the evolution of surface composition in these two clusters at  $T = 300$  K. After  $10 \mu\text{s}$ , the composition of the surface layer in the fcc cluster is still 50% Ag, exactly as at the beginning of the simulation (see Fig. 4.2.3). On the contrary, for the Ih cluster, surface composition grows quickly to about 60% and continues growing surpassing

65% Ag towards the end of the simulation. The faster evolution in the Ih is confirmed at higher temperatures, with final surface compositions of 80% and 95% Ag at 400 and 500 K, respectively, to be compared to 65% and 80% Ag in the fcc cluster. Another difference between the evolution of the Ih and that of the fcc cluster is that in the Ih inner Ag atoms are more involved in the migration towards the surface. Also during the evolution of the Ih cluster, the average Ag@Cu@Ag three-shell chemical ordering is often reached (see Fig. 4.2.7(b)), but there is no evidence of the formation of the perfect Ag@Cu@Ag arrangement.

The different speed of chemical ordering equilibration in fcc and Ih clusters can be easily explained if we consider the atomic pressure in the internal region. As already discussed in Section 4.1.1, atoms in the inner sites of Ih clusters undergo high compressive stress; in systems with lattice mismatch, compressive stress is higher for atoms with larger radius, i.e. Au atoms in Au-Co and Ag atoms in Ag-Ni and Ag-Cu. To release the stress, Au and Ag atoms migrate from the internal region of the initially intermixed configuration towards the more external layers, in which lower values of the atomic pressure are typically found. In fcc clusters, interatomic distances are closer to the bulk values, and therefore the inner compressive stress is much lower than in Ih clusters. As a consequence, even though the best placement for Au and Ag atoms is in the surface, inner sites turn out to be less energetically unfavourable, so that Au and Au atoms can remain trapped there for longer times.

#### 4.2.5 COMPARISON BETWEEN AU-CO, AG-NI AND AG-CU EQUILIBRATION PATHWAYS

In summary, our simulations have shown that, in spite of the strong similarities between the three considered bimetallic systems, the approach to equilibrium from metastable intermixed configurations takes place in different ways. The differences are of both quantitative and qualitative character.

Quantitative differences are well summarized in Fig. 4.2.8, in which we report the time scales of the migration of Au or Ag to the surface layer in the different systems. Specifically, we show the average time  $t_s$  needed to reach the threshold of 70% in Au or Ag in the surface layer, as a function of the simulation temperature.  $t_s$  has been calculated by averaging over ten simulations for  $T \geq 400$  K, whereas for  $T = 300$  K we have averaged over those simulations in which the liquidlike behaviour has been observed; for those simulations in which this has not happened we have decided to report the single-simulation datum. It is clear that the evolution is slower in these cases. Comparing the different systems, it turns out that the fastest migration is achieved in Ag-Ni, followed by Au-Co and then by Ag-Cu. In Ag-Cu, migration of Ag to the surface layer is faster in the Ih than in the fcc cluster.

Qualitative differences are well appreciated in the formation of metastable liquidlike configurations and in the types of three-shell structures produced during the evolution. Liquidlike configurations are quite often observed in the initial stages of the evolution of both Au-Co and Ag-Ni, but not of Ag-Cu. As a consequence, Au-Co and Ag-Ni initial fcc structures quickly transform with high probability into Ih already at low temperatures, while, in the same temperature range, Ag-Cu

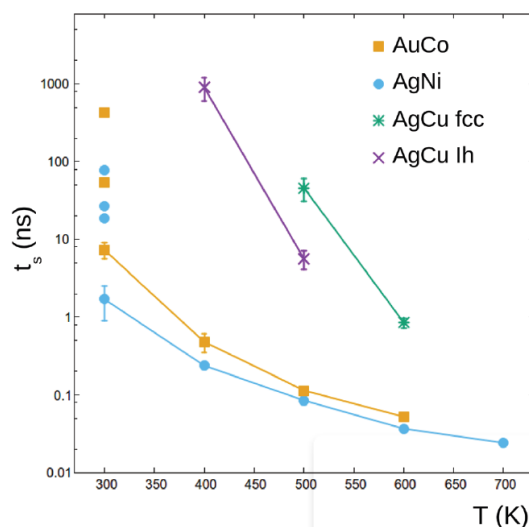


**Figure 4.2.8:** Surface segregation for the different systems as a function of temperature.  $t_s$  is the time at which the composition of the surface layer surpasses the threshold of 70% in Au or Ag. For Au-Co and Ag-Ni at  $T = 300$  K there are some scattered points which correspond to a few simulations (2 for Au-Co and 3 for Ag-Ni) in which the NP has not transformed into a metastable liquidlike structure in the first stages of the simulation. We note also that in Ag-Cu, the threshold has never been reached for  $T < 500$  K and  $T < 400$  K for fcc and lh structures, respectively.

Reproduced from D. Nelli and R. Ferrando, *Core-shell vs. multi-shell formation in nanoalloy evolution from disordered configurations*, *Nanoscale*, 11:13040, 2019.

NPs keep their geometric motif for the whole duration of the simulation.

Regarding the metastable three-shell structures, we have observed the formation of both average and perfect Au@Co@Au structures, while we have observed only average Ag@Ni@Ag and Ag@Cu@Ag. Moreover, these average Ag@Ni@Ag and Ag@Cu@Ag arrangements are quite different. In Ag@Ni@Ag, the central part of the NP contains Ag atoms which form a compact aggregate connected to the Ag surface layer by a single thick branch. In Ag@Cu@Ag, the central part of the NP is enriched in Ag, but the Ag aggregate is much less compact, with some Cu atoms dissolved in it. Connecting branches to the Ag surface shell are thin and irregular.

Differences in the equilibration time scales and pathways can be explained on the basis of rather fine details of the interaction between atomic species in the three systems. When comparing Ag-Cu, Ag-Ni and Au-Co phase diagrams, it turns out that Ag-Ni presents the most extreme tendency to phase separation, followed by Au-Co and by Ag-Cu. The same type of trend is found also for the difference in surface energy between the elements of the clusters, which is considerably larger in Ag-Ni and Au-Co than in Ag-Cu [172]. These trends are well reproduced by our model, for both phase separation and surface energies. As a consequence, intermixed configurations are farther from equilibrium in Ag-Ni than in Au-Co, and in Au-Co than in Ag-Cu, as it turns out from the energy differences between our intermixed initial configurations and the global minima. These differences are of about 100, 80 and 50 eV in Ag-Ni, Au-Co, and Ag-Cu, respectively. The stronger non-equilibrium character of the intermixed configurations in Au-Co and Ag-Ni triggers the for-

mation of liquidlike configurations in the initial part of the simulations. In liquidlike structures mobility is enhanced and the migration of Au and Ag to the surface is facilitated. The evolution of the internal part of the NP can be explained on the basis of the same considerations: the Au/Ag aggregate is more compact in the case of Ag-Ni, in which the tendency towards phase separation is stronger, followed by Au-Co and then by Ag-Cu, thus originating the different types of three-shell arrangements described previously.

# 5

## Kinetic trapping and equilibration in the coalescence of pure Au and alloyed Pt-Pd nanoparticles

COALESCENCE is a phenomenon that takes place in the last stage of nanoparticle synthesis. In coalescence, two or more preformed clusters collide and merge to form a single larger aggregate. It can occur during the formation in the gas phase or in solution, or after the deposition of the produced nanoparticles on a solid substrate. Usually, coalescence events negatively affect the quality of the samples produced in the growth experiments, as they introduce some degree of polydispersity, and often cause the formation of nanoparticles with irregular shapes. For this reason, synthesis techniques are commonly designed to limit such events as much as possible; for example, in wet chemistry methods nanoparticles are protected by ligands in order to induce electrostatic repulsion and thus prevent coalescence and agglomeration. However, coalescence can also be exploited to produce specifically tailored structures; a possible application is the production of nanoalloys with Janus or core-shell chemical ordering by inducing the coalescence of two monometallic clusters of different species [173–175].

In both cases, a precise understanding of coalescence processes is highly desirable. Firstly, it is necessary to know what are the experimental conditions in which coalescence is either negligible or dominant, in order to be able to tune the coalescence degree according to the desired purpose. In addition, it is important to understand the elemental physical mechanisms at the basis of coalescence phenomena, in the case of both mono- and bi-metallic systems; computer simulations are particularly useful in this sense, as they can provide a description of such phenomena at the atomic

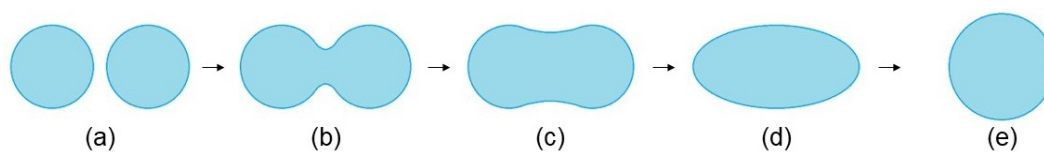


**Figure 5.0.1:** Schematic representation of the stages of the coalescence process: (a) initially separated well-formed clusters; (b) formation of the sintering neck; (c) the neck becomes larger and larger; (d) elongated structure without neck; (e) fully equilibrated structure.

level [176].

During coalescence, the shape of the newly formed aggregate evolves from an initial configuration that is strongly out of equilibrium towards more compact structures. A schematic representation of the coalescence stages is shown in Fig. 5.0.1. The two clusters come into contact and form a so-called sintering neck (Fig. 5.0.1(b)), which becomes larger and larger through the diffusion of atoms from each subunit (Fig. 5.0.1(c)). In a later stage, the coalescing aggregate is more compact, the two initial clusters cannot be identified anymore but the shape is still elongated (Fig. 5.0.1(d)). At the end of the process, full equilibrium is approached, so that it is almost impossible to guess that the structure has originated from a coalescence event (Fig. 5.0.1(e)). Kinetic trapping effects can take place, which slowdown the evolution of the coalescing aggregate; in this case, the coalescence process stops at some intermediate stage, corresponding to peculiar out-of-equilibrium structures in which the two colliding units are still distinguishable. In general, the coalescence speed and final outcome may be influenced by the initial features of the colliding units, such as their geometric structure and relative size, and their mutual orientation. However, this issue has not been deeply investigated in the literature.

In this chapter, we present the results of our MD simulations of the coalescence of mono- and bi-metallic nanoparticles. In the first case, we have simulated the coalescence of two small Au clusters, for which we have considered all the most common geometric shapes, i.e. decahedra, icosahedra and truncated octahedra. Our simulations do reveal a persistent influence of the structure and relative orientation of the initial colliding clusters on the final coalesced aggregates. Moreover, they show that aggregate reshaping occurs by a variety of specific transformation pathways, which often involve the concerted displacements of many atoms.

In the second case, we have studied the final stages of the nanoparticle growth process analysed in Section 3.4, in which the coalescence between different Pt-Pd structures may occur. Our simulations have allowed us to single out the key steps through which the coalescence process takes place. The simulation results are in agreement with experimental observations of Pt-Pd nanoalloys grown in the gas phase; in particular, they have shown that some specific core-shell arrangements observed in the experiments can originate from coalescence processes.



## 5.1 MEMORY EFFECTS IN THE COALESCENCE OF AU CLUSTERS

Coalescence has been the subject of several simulation works, both for clusters of a single species [177–185] and of two different species [61, 169, 174, 175, 186]. In these works, most of the attention has been devoted to analyze the formation and evolution of the neck between coalescing units and, in the case of different species, to the evolution of chemical ordering. By contrast, the evolution of the aggregate structural motif during the coalescence process has not been analyzed in details, so that it is still to be understood to a large extent. In principle, this evolution may depend on several factors, including the initial state of the colliding units (i.e. their shapes and their relative orientation) and on temperature. We have tried to shed some light on these aspects, in the case of the coalescence of Au clusters. Specifically, we have employed MD simulations at constant temperature to follow the evolution pathways of the coalescing aggregate and to determine to what extent the initial state of the colliding units influences the resulting structural motif at the end of the simulation. To this end, we have simulated on longer time scales than in previous works, choosing for every simulation a duration of 1.4  $\mu$ s. For comparison, the typical time scales of previous MD simulations of coalescence are in the range 0.1–35 ns [179, 184, 185]. We have considered several types of initial states, and for each of them, we have run a large number of independent simulations to accumulate significant statistics (details on the statistical analysis of our data are given in the Appendix of Ref. [187]).

We have observed different degrees of equilibration of the coalesced NP, depending on the selected simulation temperature. The main finding of our simulations is that, even at quite high temperatures, the final result of the coalescence process is still clearly influenced by both the initial structures and the initial relative orientation of the colliding clusters. In some cases such memory effect is quite subtle: even though the final shape is very regular, and the two colliding units cannot be identified anymore, the geometric motif depends on the collision type in a statistically significant way. In the following we will present these results, and we will describe some of the atomic-level reshaping mechanisms which occur in the first stage of the coalescence process, as observed in our simulations<sup>1</sup>.

### 5.1.1 LOWEST-ENERGY GEOMETRIC STRUCTURES BEFORE AND AFTER THE COALESCENCE

We have simulated the collisions of two clusters of the same size, i.e. 147 atoms. The initial units used in the coalescence simulations are shown in Fig. 5.1.1. The choice of these relatively small sizes has allowed us to perform a large number of long MD simulations with a reasonable computational effort. Specifically, size 147 has been chosen because it is a widely studied geometric magic size for the Mackay Ih, the Ino Dh and the cuboctahedron [14]. However, none of these structures is the global minimum for Au clusters, but, according to both our atomistic model and DFT calculations

---

<sup>1</sup>Results have been published in Ref. [187]. Here, experimental TEM images of Au nanoparticles have been provided by Richard E. Palmer and Zhiwei Wang (Swansea University, UK)

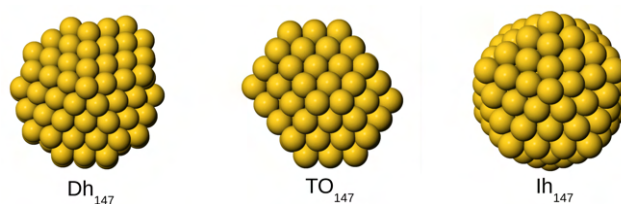


**Figure 5.1.1:** Elementary units used in the different types of collisions. These are low-energy isomers of the Dh, TO and Ih motifs at size 147.

Reproduced from D. Nelli, G. Rossi, Z. Wang, R. E. Palmer and R. Ferrando, *Structure and orientation effects in the coalescence of Au clusters*, *Nanoscale*, 12:7688, 2020.

[40], the lowest energy structures are defective Marks Dh, obtained by adding one atom to the perfect Marks Dh of size 146. There are several quasi-degenerate ways (within 0.1 eV) to produce 147-atom defective Dh, one of which is shown in Fig. 5.1.1. These lowest-energy Dh are in rather close competition with the fcc structures, while the perfect Mackay Ih is much higher in energy, by about 1.8 eV.

Before analyzing the coalescence process and the final outcome of the MD simulations, we have made global optimization searches for the most stable clusters corresponding to the final aggregate size of 294 atoms (see Section 2.2 for details on the global optimization procedure). The lowest-energy structures for the principal motifs are shown in Fig. 5.1.2. The lowest-energy structures have been used as references to check whether the coalescing clusters have approached equilibrium or not during our simulations. The global minimum for size 294 is a Marks Dh (Fig. 5.1.2(a)), with some defects and/or asymmetries, since the final size is not a magic geometric size for the Marks Dh. The best TO (Fig. 5.1.2(b)) is 0.21 eV above the global minimum, and it is practically degenerate with an fcc structure presenting a single twin plane, shown in Fig. 5.1.2(c) (see also Fig. 1.1.2 in Section 1.1.2). Finally, the best (incomplete) Ih (Fig. 5.1.2(d)) is considerably higher in energy, 1.97 eV above the global minimum. The unfavourable character of Ih structures in this size range is in agreement with previous calculations and experiments [188]. These results are also in good agreement with recent DFT calculation which have predicted that Dh structures are lower in energy than Ih ones already starting from the size of 147 atoms [40]. We note that the best Dh in Fig. 5.1.2(a) is rather well separated from the second-best Dh (by 0.18 eV), while there are several fcc structures, presenting either a stacking fault or a twin plane, whose energies lie within 0.05 eV of the best fcc isomer.

### 5.1.2 MOLECULAR DYNAMICS COALESCENCE SIMULATIONS

Coalescence has been studied by MD simulations, using a time step of 7 fs. The colliding clusters have been initially placed close to each other (separated by few Å) without any relative velocity, so that their collision is simply due to the attractive forces between them. Simulations have been performed at constant temperature (in the NVT statistical ensemble). Constant-temperature simulations mimic conditions in which the coalescing clusters can efficiently get rid of the heat excess due

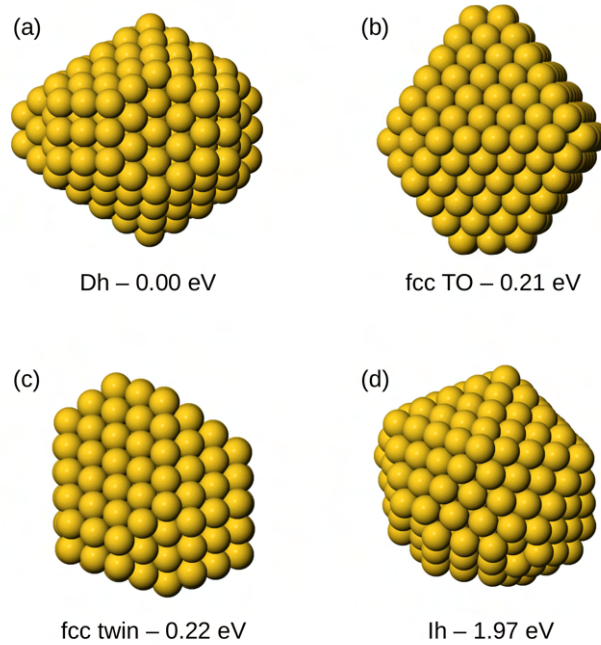


**Figure 5.1.2:** Lowest-energy structures for  $\text{Au}_{294}$  clusters: (a) defective Marks Dh, (b) defective fcc TO, (c) somewhat asymmetric fcc twin. (d) Defective Ih. Energy differences from the global minimum structure (the Dh) are given in eV.

Reproduced from D. Nelli, G. Rossi, Z. Wang, R. E. Palmer and R. Ferrando, *Structure and orientation effects in the coalescence of Au clusters*, *Nanoscale*, 12:7688, 2020.

to the condensation. This corresponds to physical situations in which the clusters are embedded in a dense inert gas or deposited on a weakly-interacting substrate. Another possibility could be to simulate the coalescence process at constant energy (in the NVE ensemble). However we note that previous work the coalescence of palladium clusters [184] have shown that NVT and NVE simulations give qualitatively the same type of results. Different simulation temperatures have been employed, namely 400, 500, 525, 550 and 575 K.

The structures of Fig. 5.1.1 have been used as the initial configurations for six different types of collisions:  $\text{Dh} \leftrightarrow \text{Dh}$ ,  $\text{TO} \leftrightarrow \text{TO}$ ,  $\text{Ih} \leftrightarrow \text{Ih}$ ,  $\text{Dh} \leftrightarrow \text{TO}$ ,  $\text{Dh} \leftrightarrow \text{Ih}$ ,  $\text{TO} \leftrightarrow \text{Ih}$ . The initial orientations of the clusters have been chosen at random, as in Fig. 5.1.3. In order to study the influence of the initial orientation of the colliding units, we have also considered some well-defined relative orientations. This has been done for the  $\text{Dh} \leftrightarrow \text{TO}$  and  $\text{TO} \leftrightarrow \text{TO}$  collisions, for which we have chosen initial configurations with the Dh initially facing fcc clusters either by  $(111)$  facets or by Marks re-entrant vertices (rev) and the TO facing TO or Dh clusters either by  $(111)$  or  $(100)$  facets. This gives six possible types of initial configurations, which are shown in Fig. 5.1.4.

In the following, we will analyze mostly the results obtained at 400 and 500 K. The evolution of the coalescing aggregates is quite different for the two simulation temperatures, as anticipated

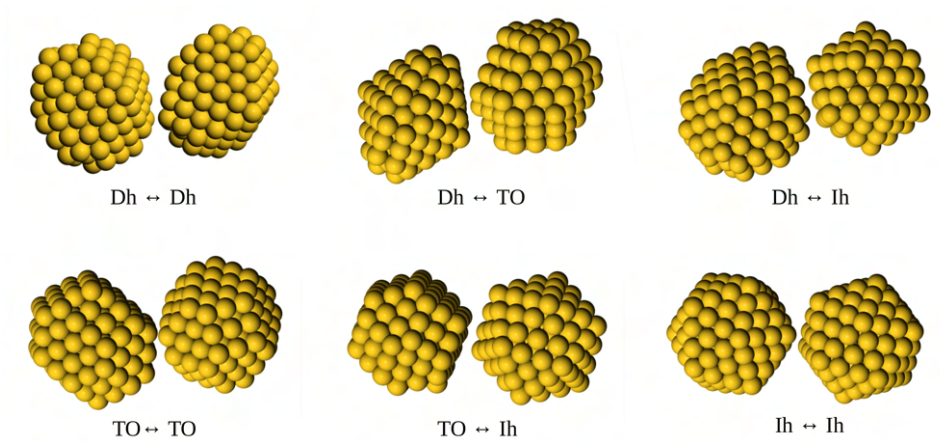


**Figure 5.1.3:** Examples of initial configurations of the different types of collisions with randomly chosen orientations.  
 Reproduced from D. Nelli, G. Rossi, Z. Wang, R. E. Palmer and R. Ferrando, *Structure and orientation effects in the coalescence of Au clusters*, *Nanoscale*, 12:7688, 2020.

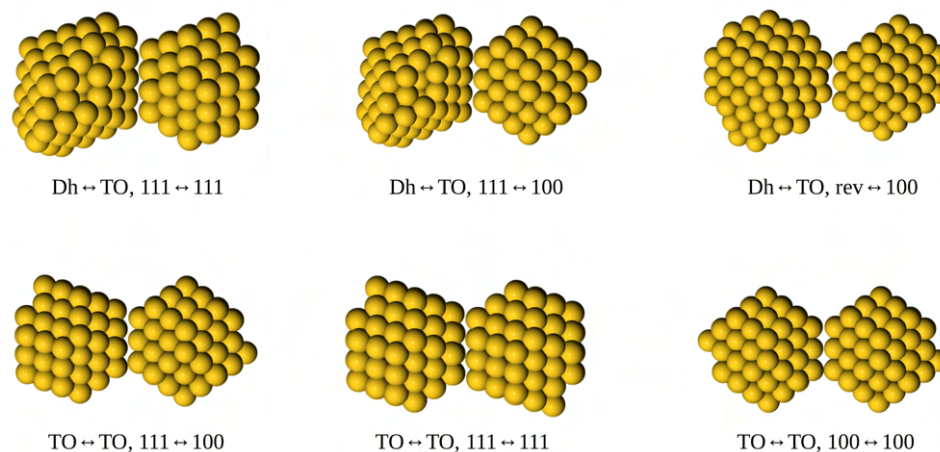


**Figure 5.1.4:** Initial configurations of the  $Dh \leftrightarrow TO$  and  $TO \leftrightarrow TO$  collisions with specific orientations.  
 Reproduced from D. Nelli, G. Rossi, Z. Wang, R. E. Palmer and R. Ferrando, *Structure and orientation effects in the coalescence of Au clusters*, *Nanoscale*, 12:7688, 2020.

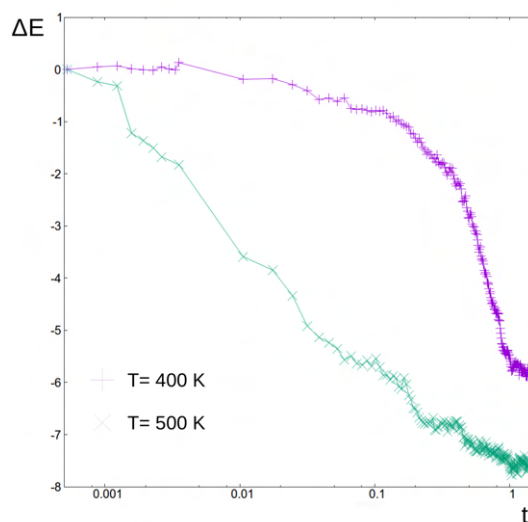


**Figure 5.1.5:** Behaviour of the average potential energy of coalesced cluster at 400 and 500 K as a function of the simulation time  $t$  (in  $\mu\text{s}$ ).  $\Delta E$  (in eV) is the energy difference between the energy of the cluster and its initial energy. Data are taken averaging over 10 independent simulations at each temperature, starting from the same initial configuration. *Reproduced from D. Nelli, G. Rossi, Z. Wang, R. E. Palmer and R. Ferrando, Structure and orientation effects in the coalescence of Au clusters, Nanoscale, 12:7688, 2020.*

in Fig. 5.1.5. In this figure, we report the evolution of the potential energy of the coalesced aggregate with time, averaged over 10 independent simulations at each temperature. All simulations have started from the same initial configuration, and, in all cases, an energy decrease with time has been observed, corresponding to the rearrangement of the coalesced cluster towards more compact structures. The results in Fig. 5.1.5 show that the rearrangement kinetics is faster at 500 K than at 400 K by about one order of magnitude, as one can estimate by comparing the value of  $\Delta E$  at 400 K and 1  $\mu\text{s}$  with the one obtained at 500 K and 0.1  $\mu\text{s}$ . The final energy at 500 K is lower by about 2 eV than at 400 K. From about 1  $\mu\text{s}$  on, the structures at 500 K are quite close to the best ones obtained by our global optimization searches, while the final structures at 400 K are quite different, as we will show in the next section.

### 5.1.3 COALESCENCE AT 400 K: PECULIAR KINETICALLY-TRAPPED STRUCTURES

For this temperature, we have performed more than 100 simulations of duration 1.4  $\mu\text{s}$ . We have simulated three types of collisions, namely  $Dh \leftrightarrow Dh$ ,  $Dh \leftrightarrow TO$  and  $TO \leftrightarrow TO$ , for several random initial orientations of the clusters. The main results obtained at this temperature can be summarized as follows. For all initial structures and mutual orientations, the coalesced cluster evolves significantly away from the initial configuration (see the lowering of the energy in Fig. 5.1.5); however, the final structure is always much less compact and significantly higher in energy (typically between 1 and 3 eV) than the best structures of the corresponding motif found in our global optimization searches (see Fig. 5.1.2). The lowest-energy structures of the different motifs have never

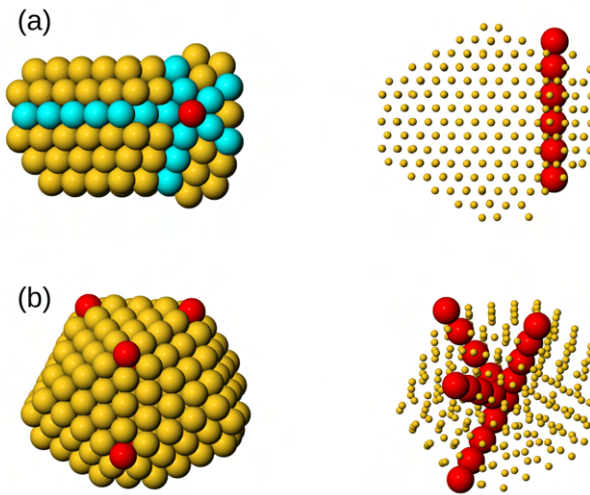


**Figure 5.1.6:** Examples of final configurations in simulations at 400 K. Each structure is shown in two views. (a) Comet star cluster, obtained in a  $Dh \leftrightarrow TO$  collision, in which the Dh part has remained fairly unchanged, and a twin plane has formed in the fcc part. (b) Fragment of the 561-atom Ih, with four fivefold local symmetry axes. In both (a) and (b): in the left panel atoms belonging to twin planes are colored in cyan, and atoms of the fivefold axis are colored in red; in the right panel, atoms of the fivefold axis are represented by bigger red spheres, other atoms by yellow small spheres. Here and in the following figures, all images are shown after local minimization to eliminate the effects of vibrations.

*Reproduced from D. Nelli, G. Rossi, Z. Wang, R. E. Palmer and R. Ferrando, Structure and orientation effects in the coalescence of Au clusters, Nanoscale, 12:7688, 2020.*

been reached, at any stage of the simulations. A variety of irregular structures was formed instead.

In Fig. 5.1.6 we report some of the most frequent final structures produced in  $Dh \leftrightarrow Dh$  and  $Dh \leftrightarrow TO$  collisions. These comprise clusters in which there is a single fivefold axis in a peripheral position, as in the comet-star cluster of Fig. 5.1.6(a), bidecahedral ( $Dh_2$ ) and tridecahedral ( $Dh_3$ ) clusters [189, 190] (see Section 5.1.4 for details about these structures) and clusters with several local fivefold symmetry axes [190] (such as the Ih fragment of Fig. 5.1.6(b)). In  $TO \leftrightarrow TO$  collisions, structures with several stacking faults and/or hcp zones have been frequently produced, often with quite elongated shapes (not shown in the figure). These results indicate that, for all initial cluster shapes and relative orientations, the time scale of our simulations is far too short to achieve equilibration of the clusters at this temperature.

#### 5.1.4 COALESCENCE AT 500 K: INTRA-MOTIF VS. INTER-MOTIF EQUILIBRATION

At  $T = 500$  K we have considered all six types of collisions. Firstly, the initial orientations of the clusters have been chosen at random, as in Fig. 5.1.3. For each type of collision, 50 independent simulations have been made, in order to accumulate significant statistics for the events (again, we refer to the Appendix of Ref. [187] for the detailed statistical analysis).

A summary of the results is given in Table 5.1.1, in which we report the resulting structures after

Colliding clusters	Structure at 140 ns				Structure at 1.4 $\mu$ s			
	Dh	fcc	Ih	Dh <sub>2</sub> /Dh <sub>3</sub>	Dh	fcc	Ih	Dh <sub>2</sub> /Dh <sub>3</sub>
Dh $\leftrightarrow$ Dh	24	8	0	18	37	12	0	1
Dh $\leftrightarrow$ TO	14	15	0	21	30	19	0	1
Dh $\leftrightarrow$ Ih	18	8	1	23	35	13	0	2
TO $\leftrightarrow$ TO	8	39	0	3	5	45	0	0
TO $\leftrightarrow$ Ih	17	28	1	4	20	30	0	0
Ih $\leftrightarrow$ Ih	22	9	14	5	35	11	4	0

**Table 5.1.1:** Intermediate and final structures (at 140 ns and 1.4  $\mu$ s, respectively) for simulations at constant temperature  $T = 500$  K of collisions between clusters with random initial orientations.

Reproduced from D. Nelli, G. Rossi, Z. Wang, R. E. Palmer and R. Ferrando, *Structure and orientation effects in the coalescence of Au clusters*, *Nanoscale*, 12:7688, 2020.

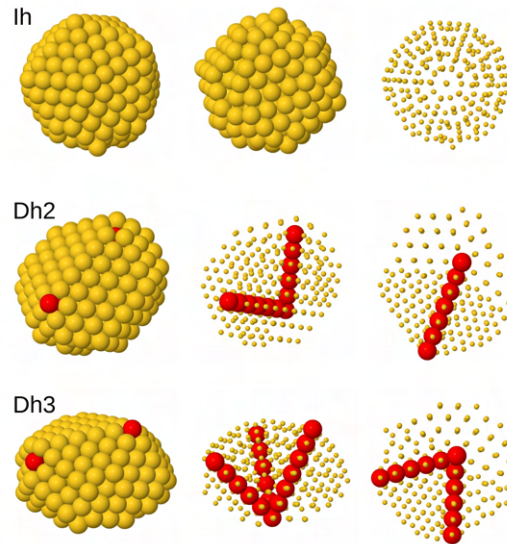


**Figure 5.1.7:** Snapshots of some Ih, Dh<sub>2</sub> and Dh<sub>3</sub> structures found in the coalescence simulations at  $T = 500$  K. Each structure is represented in three views. In the Dh<sub>2</sub> and Dh<sub>3</sub> structures (images taken after 140 ns), the atoms along local fivefold symmetry axes are shown in red. The third view of Dh<sub>2</sub> and Dh<sub>3</sub> structures is taken along one of the fivefold axis to show the Dh arrangement around it.

Reproduced from D. Nelli, G. Rossi, Z. Wang, R. E. Palmer and R. Ferrando, *Structure and orientation effects in the coalescence of Au clusters*, *Nanoscale*, 12:7688, 2020.

a time corresponding to 10% of the final time (i.e. at 140 ns from start) and at the end of the simulations (i.e. at 1.4  $\mu$ s). These structures fall into four motifs, Dh, fcc, Ih and polydecahedra (specifically Dh<sub>2</sub> and Dh<sub>3</sub>). Ih, Dh<sub>2</sub> and Dh<sub>3</sub> structures from the simulations are shown in Fig. 5.1.7. In fcc structures, we include also clusters with twin planes and/or stacking faults. Regarding the frequency of the different motifs in the final structures, our results show that Dh structures are more likely than fcc ones when at least one of the initial clusters is a Dh, and also in Ih $\leftrightarrow$ Ih collisions. On the other hand, final fcc structures are by far dominant when colliding two fcc clusters, and still quite likely when colliding a TO with an Ih. Finally, Ih and Dh<sub>2</sub>/Dh<sub>3</sub> structures appear infrequently as the final result of the coalescence process.

Let us now analyze more closely the evolution of the clusters during the coalescence process at different times. The most evident difference between the results at 140 ns and 1.4  $\mu$ s is that in the former case we frequently observe Dh<sub>2</sub>/Dh<sub>3</sub> structures, while in the latter Dh<sub>2</sub>/Dh<sub>3</sub> clusters are almost absent. This means that Dh<sub>2</sub>/Dh<sub>3</sub> structures evolve into simple Dh or fcc structures as the simulation time increases. As one may expect, Dh<sub>2</sub>/Dh<sub>3</sub> structures are more frequently observed in simulations in which at least one of the starting clusters is a Dh. We note however that the frequency of Dh<sub>2</sub>/Dh<sub>3</sub> structures is comparable in Dh $\leftrightarrow$ Dh and Dh $\leftrightarrow$ TO coalescence, even though in the latter a single fivefold axis is initially present. This implies that new fivefold axes can form in the initial stages of the simulations, with an appreciable frequency. A new fivefold axis often forms when an amorphous liquid-like zone is created in the initial part of the simulation (see also Section 5.1.6 where these types of processes are discussed). As shown in freezing simulations of liquid droplets [190], local fivefold symmetry points are common in the liquid state, so that complex arrangements of fivefold symmetry axes can be formed during freezing. However, structures with multiple fivefold axes of different orientations are strongly strained and quite high in energy [190], so that they rather easily evolve into structures with a single fivefold axis. This picture is confirmed by the results of our simulations.

In the collisions in which neither of the initial clusters is Dh, the formation of Dh<sub>2</sub>/Dh<sub>3</sub> structures is much less frequent. In Ih $\leftrightarrow$ Ih collisions we often find a pure Ih (shown in Fig. 5.1.7, top row) at 140 ns, which then is likely to evolve into a Dh with time. Generally, the Ih transforms directly into a Dh, without intermediate steps like Dh<sub>2</sub> or Dh<sub>3</sub>. The two-step transformation Ih $\rightarrow$ Dh<sub>2</sub>/Dh<sub>3</sub> $\rightarrow$ Dh is observed only in one simulation. Since Dh<sub>2</sub>/Dh<sub>3</sub> intermediate structures rarely form, in TO $\leftrightarrow$ TO and TO $\leftrightarrow$ Ih collisions, the evolution towards the final structure is more direct and usually faster.

In the simulations in which the coalesced cluster presents Dh<sub>2</sub>/Dh<sub>3</sub> structures, frequent back-and-forth transitions Dh<sub>2</sub> $\rightarrow$ Dh<sub>3</sub> and Dh<sub>3</sub> $\rightarrow$ Dh<sub>2</sub> are observed. In these transitions, the third fivefold axis, which is likely to be in peripheral position, is eliminated and reformed. The evolution to the final Dh structure is then obtained by the elimination of one of the fivefold axes in the Dh<sub>2</sub>. Once the Dh structure is achieved, the transition back to Dh<sub>2</sub>, i.e. the formation of a reasonably stable second fivefold axis, is not observed. In some simulations Dh structures are metastable and evolve into fcc structures. This happens only when the Dh fivefold axis is near to the cluster surface, while transformations from Dh clusters with centered axis to fcc clusters are never observed. Also



Colliding clusters and orientation	Structure at 140 ns				Structure at 1.4 $\mu$ s			
	Dh	fcc	Ih	Dh <sub>2</sub> /Dh <sub>3</sub>	Dh	fcc	Ih	Dh <sub>2</sub> /Dh <sub>3</sub>
Dh $\leftrightarrow$ TO, random	14	15	0	21	30	19	0	1
Dh $\leftrightarrow$ TO, 111 $\leftrightarrow$ 111	13	29	3	5	19	31	0	0
Dh $\leftrightarrow$ TO, 111 $\leftrightarrow$ 100	31	11	1	7	37	12	1	0
Dh $\leftrightarrow$ TO, rev $\leftrightarrow$ 100	15	29	1	5	18	30	1	1
TO $\leftrightarrow$ TO, random	8	39	0	3	5	45	0	0
TO $\leftrightarrow$ TO, 111 $\leftrightarrow$ 100	9	35	0	6	12	37	0	1
TO $\leftrightarrow$ TO, 111 $\leftrightarrow$ 111	0	49	0	1	1	49	0	0
TO $\leftrightarrow$ TO, 100 $\leftrightarrow$ 100	3	47	0	0	3	47	0	0

**Table 5.1.2:** Intermediate and final structures structures (at 140  $\mu$ s and 1.4  $\mu$ s, respectively) for simulations at constant temperature  $T = 500$  K for collisions of clusters with selected initial orientations. The data for Dh $\leftrightarrow$ TO and TO $\leftrightarrow$ TO collisions with random orientations (taken from Table 5.1.1) are repeated here for comparison. Reproduced from D. Nelli, G. Rossi, Z. Wang, R. E. Palmer and R. Ferrando, *Structure and orientation effects in the coalescence of Au clusters*, *Nanoscale*, 12:7688, 2020.

the fcc $\rightarrow$ Dh transition is never observed, in spite of the fact that there are Dh structures lower in energy than any fcc structure.

Regarding the degree of equilibration of the coalesced structure at the end of the simulations, the results in Table 5.1.1 show that the probability of achieving the different final structures depends on the structures of the initial colliding units, so that our results are largely incompatible with the hypothesis of full equilibration. This indicates that equilibration between the different motifs (inter-motif equilibration), specifically between Dh and fcc motifs, has not been achieved even at  $T = 500$  K on our simulation time scale. Of course, in full inter-motif equilibration no influence of the initial colliding structures would be retained. On the other hand, we have found evidence of a good degree of equilibration within each motif (intra-motif equilibration), especially as regards Dh structures. In fact, of the 162 simulations ending with Dh structures, 91 (i.e. 56%) simulations have reached, at least for some period of time, the lowest-energy Dh (see Fig. 5.1.2). Of the 130 simulations ending with fcc structures, 24 reached either the best fcc or the best single twin or defective structures (within 0.05 eV from the best fcc), corresponding to 18% of the simulation ending in this motif. We recall that at  $T = 400$  K none of the simulations reached anything close to the lowest-energy structures of Dh and fcc motifs.

In order to better understand the influence of the initial state on the coalescence process, we have also considered collisions of clusters with initially well-defined relative orientations instead of randomly chosen orientations. We have focused on Dh $\leftrightarrow$ TO and TO $\leftrightarrow$ TO collisions, and we have selected mainly facet-to-facet orientations, as described in Section 5.1.2 (see Fig. 5.1.4). The

relevance of such initial states is supported by the results in Ref. [191], indicating the occurrence of an oriented attachment mechanism of coalescing clusters in solution. In this mechanism, NPs undergo continuous rotation and interaction until they find a perfect lattice match to attach.

For each type of collision we have run 50 independent simulations of 1.4  $\mu\text{s}$  each, and we have made the same type of analysis as in the case of randomly oriented collisions. The results of these simulations are given in Table 5.1.2, where we also report for comparison the relevant data for randomly oriented collisions. The main result of these simulations is that the final outcomes do depend on the initial orientations of the clusters, at a high level of significance as shown by the statistical analysis reported in the Appendix of Ref. [187]. In particular, for Dh $\leftrightarrow$ TO collisions with 111 $\leftrightarrow$ 111 and rev $\leftrightarrow$ 100 orientations, we have found a significant increase in fcc structures compared with the case of random orientations; in this case, final fcc structures are indeed even more likely than Dh structures. The origin of this result will be discussed below, by analyzing in details a Dh $\leftrightarrow$ TO, 111 $\leftrightarrow$ 111 collision.

In TO $\leftrightarrow$ TO collisions with 111 $\leftrightarrow$ 100 orientation we have found the opposite result, i.e. a significant increase of final Dh outcomes, whose origin will be again analyzed below. For other TO $\leftrightarrow$ TO orientations the data are compatible with the random case. We can also notice that an fcc final structure is always preferred for collisions between the same type of facet.

From the analysis of the intermediate structures at 140 ns, it follows that in Dh $\leftrightarrow$ TO collisions, summed over all specific orientations, there is a significant decrease of Dh<sub>2</sub>/Dh<sub>3</sub> structures, compared with the random orientation case. This indicates more direct and faster evolution to the final structures. The faster evolution towards equilibrium is also supported by the fact that the lowest energy structures have been reached slightly more often than in randomly oriented collisions: the lowest energy Dh structures have been reached in 56 out of 90 cases (62% compared with 56%) and the lowest energy fcc structures have been reached reached in 49 out of 206 cases (24% compared with 18%).

In general, the results in Table 5.1.2 indicate some increase of the number of fcc structures in the simulation time between 140 ns and 1.4  $\mu\text{s}$ , showing that some Dh or Dh<sub>2</sub>/Dh<sub>3</sub> structures evolve into fcc as the simulations progress. On the contrary, fcc $\rightarrow$ Dh transformations have not been observed, in agreement with the results of randomly oriented collisions.

#### 5.1.5 COALESCENCE ABOVE 500 K: INTER-MOTIF EQUILIBRATION DUE TO INITIAL RANDOMIZATION

Here we investigate the coalescence for higher temperatures than 500 K in order to check whether inter-motif equilibration can be achieved on our simulation time scale. To this end, we have chosen Dh $\leftrightarrow$ Dh and TO $\leftrightarrow$ TO collisions, which have given the most incompatible results at  $T = 500$  K. For each collision type we have performed 50 independent simulations for  $T = 525, 550$  and  $575$  K. The results about the final outcome of the simulations are reported in Table 5.1.3. At  $T = 525$  K the results are still incompatible with inter-motif equilibration at a very high significance level, while

temperature	colliding clusters	final structure		
		Dh	fcc	L
525 K	Dh↔Dh	39	11	0
525 K	TO↔TO	12	38	0
550 K	Dh↔Dh	31	19	0
550 K	TO↔TO	25	25	0
575 K	Dh↔Dh	39	10	1
575 K	TO↔TO	35	15	0

**Table 5.1.3:** Final structures at  $T > 500$  K. L denotes liquid structures.

Reproduced from D. Nelli, G. Rossi, Z. Wang, R. E. Palmer and R. Ferrando, *Structure and orientation effects in the coalescence of Au clusters*, *Nanoscale*, 12:7688, 2020.

the data at 550 and 575 K are compatible with full equilibration.

A few remarks are necessary in order to explain these results. First of all, the isolated 147-atom units would be all melted at 550 K and 575 K. In fact, we have performed heating simulations of isolated 147-atom clusters, heating them from 300 K to 600 K with a heating rate of  $1 \text{ K ns}^{-1}$ , finding that the melting range of these isolated clusters is between 515 and 540 K, which is compatible with the experimental results reported in Ref. [192]. Since  $T = 550$  and 575 K are above the melting range of the colliding units, at the beginning of the simulations the coalescing aggregate is very likely to pass through a liquid-state stage which may last for several tens of ns. Then the aggregate solidifies, because for size 294 the melting temperature is higher than for size 147. At 550 K, clusters maintain their solid state after solidifying, while at 575 K, which is just at the beginning of the melting range of size 294, clusters may fluctuate back and forth between the liquid and the solid state, but being solid for most of the time. In fact, one simulation out of 50 terminates with the cluster in the liquid state. Inter-motif equilibration between Dh and TO structures mostly occurs through the randomization and memory loss taking place in the liquid state of the initial part of the simulations.

Solid–solid transitions between fcc and Dh motifs are absent at 550 K and somewhat rare at 575 K, where we have observed 12 fcc→Dh transformations in the solid state, plus 7 transformations after fluctuations back to the liquid state. Solid-state fcc→Dh transformations can occur through a variety of different pathways, made of complex sequences of steps, each step involving the concerted motion of several atoms. Work is in progress to analyse more deeply these transformation pathways. We note finally that the results of our simulations suggest a melting range between 575 and 600 K for size 294, which is again compatible with the results of Ref. [192].

#### 5.1.6 STRUCTURAL REARRANGEMENT PATHWAYS OF THE COALESCED AGGREGATE

Here we show few examples of possible evolution pathways of the nanoparticle during the coalescence process, as observed in our MD simulations; through such processes, the nanoparticle

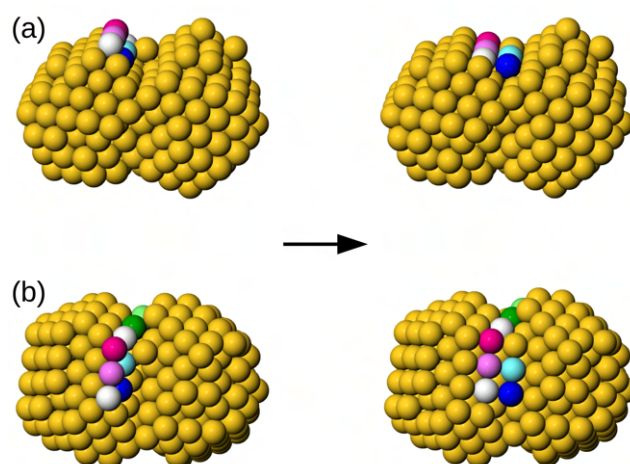


**Figure 5.1.8:** Collective diffusion process to fill a groove: (a) side view (b) top view. The process involves a total of eight atoms (shown in different colors), but only two atoms are finally displaced inside the groove. The time between the initial and final image is 0.5 ps. Reproduced from D. Nelli, G. Rossi, Z. Wang, R. E. Palmer and R. Ferrando, *Structure and orientation effects in the coalescence of Au clusters*, *Nanoscale*, 12:7688, 2020.

gradually achieves a more compact and regular shape compared to the initial far-from-equilibrium configuration.

Firstly, we note that most structural transformations, including (but not only) the elimination of the neck between the colliding clusters in the initial stages of the simulations [176], do not occur by atom detachment  $\rightarrow$  diffusion  $\rightarrow$  reattachment to higher-coordination sites, as often assumed in analytical models and simulations of coalescence [183, 193]. On the contrary, rearrangement processes in these solid–solid structural transitions are in most cases collective, involving the concerted displacement of several atoms instead of single-atom surface diffusion [171, 194]. An example of a collective process for filling out the neck is given in Fig. 5.1.8. This example is only representative of a wide variety of collective processes which take place during cluster rearrangement, including the concerted displacement of atomic rows, the gliding of adatom islands and of atomic planes, and small relative rotations of the different parts of the cluster.

Here we focus on coalescence processes in which the initial units have well-defined mutual orientation. The first example we discuss is the mechanism of fcc structure formation in Dh $\leftrightarrow$ TO, 111 $\leftrightarrow$ 111 collisions. In Fig. 5.1.9 we report snapshots from a simulation showing a typical rearrangement pathway leading to the disappearance of the fivefold axis of the initial Dh. This takes place by small concerted displacements of many atoms, which reorient the decahedral part in such a way that its close-packed planes become parallel to those of the fcc part. At the same time, the fivefold axis slightly distorts and finally loses its fivefold character. Since the initial fivefold axis is not parallel to the close-packed planes of the fcc part, the initial structure is highly strained. The subsequent rearrangements lead to a decrease of strain with a net energy gain.

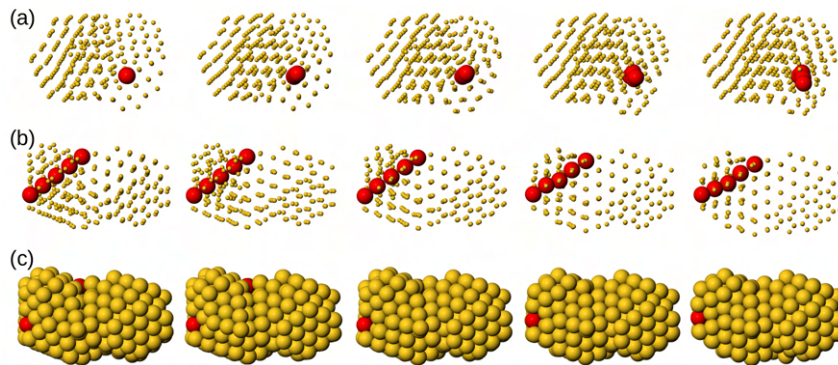


**Figure 5.1.9:** Snapshots from a simulation of  $Dh \leftrightarrow TO$ ,  $111 \leftrightarrow 111$  coalescence at  $T = 500$  K. The atoms in red are those of the fivefold axis of the Dh. The same sequence is shown three times: (a) view along the initial orientation of the fivefold axis of the decahedral part; (b) view perpendicular to the close-packed planes that are finally formed; (c) the same as in (b) but with all atoms represented by big spheres. From left to right, one can follow the distortion of the fivefold axis (which is no longer locally fivefold in the fourth and fifth snapshots of the sequence), plus the nucleation of new parallel close-packed planes in the part which was initially decahedral. The transformation process is very fast (1.5 ps in total from the first to the fifth image) and takes place by many concerted small displacements of atoms.

Reproduced from D. Nelli, G. Rossi, Z. Wang, R. E. Palmer and R. Ferrando, *Structure and orientation effects in the coalescence of Au clusters*, *Nanoscale*, 12:7688, 2020.

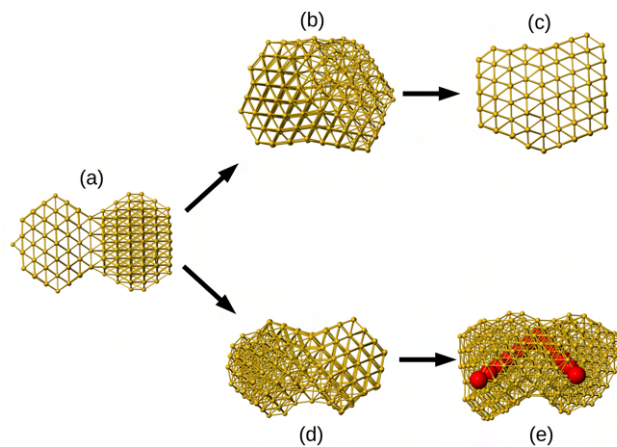


**Figure 5.1.10:** Snapshots from two simulations of  $TO \leftrightarrow TO$ ,  $111 \leftrightarrow 100$  coalescence at  $T = 500$  K. All clusters are shown in the ball-and-stick representation to better distinguish disordered parts from regions with well-developed crystalline planes. In the initial configuration (a) the two crystal lattices are rotated with respect to each other. In the first collision (sequence (a) → (b) → (c)) this leads to the fast formation of an amorphous part (b), which extends to almost half of the total volume. Finally in (c) a single lattice is formed, still with several stacking faults. This will evolve towards a less defective fcc structure in the remainder of the simulation. The process from (a) to (c) is relatively fast at this temperature, taking place in about 40 ns. In the second collision (sequence (a) → (d) → (e)) we can see the formation of a partially amorphous structure in (d), which then evolves to the Dh2 structure (e), in which atoms of the fivefold axes are shown by big spheres. After this fast evolution (a few ns) the structure rearranges into a single Dh on a much longer time scale.

Reproduced from D. Nelli, G. Rossi, Z. Wang, R. E. Palmer and R. Ferrando, *Structure and orientation effects in the coalescence of Au clusters*, *Nanoscale*, 12:7688, 2020.

Other interesting evolution pathways can be observed in the  $\text{TO} \leftrightarrow \text{TO}$  collision with  $111 \leftrightarrow 100$  orientation (see Fig. 5.1.10); here the crystal lattices of the colliding units are initially rotated with respect to each other. This misorientation often leads to the formation of an amorphous part, whose character may even be liquid-like [176], and whose extent may be comparable to that of the whole cluster at these sizes. This amorphous part may then evolve (i) with the formation of a series of parallel close-packed planes, leading to an fcc structure, or (ii) with the formation of one or two fivefold axes, generating Dh or Dh2 structures, which may further evolve.

## 5.2 EQUILIBRATION STEPS IN THE COALESCENCE OF Pt-Pd CRYSTALLINE NANOPARTICLES

In Section 5.1 we have shown that the final outcome of coalescence, as well as the possible intermediate configurations which form during the process, are strongly influenced by the structural motif of the two colliding units. On the other hand, in this section we have focused on the coalescence of crystalline fcc NPs, with the aim of precisely identifying the different stages of the equilibration of the coalesced aggregate. The system we have analysed is Pt-Pd; specifically, we have considered the final stages of the growth of Pt-Pd NPs produced in the gas phase (see Section 3.4), in which coalescence events may occur in flight, before deposition on the solid substrate. As in Section 3.4, a comparison between experimental and simulation data has been provided. We also remark that the experimental parameters of the NP growth have been finely tuned in order to increase the number of coalescence events among the produced NPs, and therefore to allow a more complete observation of the coalescence stages; a detailed description of such coalescence-tuning procedure can be found in Ref. [195].

Both the equilibration of the geometric structure and of the chemical ordering of the coalesced NP have been analysed. We have found that the equilibration of chemical ordering always occurs over longer time scales compared to the equilibration of the shape. The result of such time scale difference is the formation of peculiar configurations, in which the overall shape is highly compact whereas the chemical ordering is still far from full equilibrium; these structures have been observed in both experimental images and MD simulations. Moreover, all steps of geometric structure equilibration have been identified through the analysis of a large number of MD simulations at the atomic level, again with the help of experimental images of NPs acquired at different stages of the coalescence process<sup>2</sup>.

### 5.2.1 SHAPE EVOLUTION DURING COALESCENCE

In Section 3.4 we have shown that the chemical ordering of the Pt-Pd NPs depends on the composition of the atomic vapour from which they originate, being either Pt-rich or Pd-rich. Here we have

---

<sup>2</sup>Experiments have been conceived, performed and analysed by Chloé Minnai (Okinawa Institute of Science and Technology Graduate University, Okinawa, Japan). Experimental and simulation results have been published in Ref. [195].

focused on the Pd-rich case, in which the most commonly observed NPs are completely made of Pd or are of the core-shell (PtPd)@Pd type, and exhibit crystalline fcc structure. The coalescence between these two configurations has been studied by MD simulations, as described in Section 5.1.2. Specifically, two simulation sets have been performed. Firstly, we have simulated the coalescence of a pure Pd<sub>976</sub> cluster and Pd-rich Pt<sub>645</sub>Pd<sub>1280</sub> one (with (PtPd)@Pd chemical ordering); for both clusters the perfect TO shape has been selected, and a random mutual orientation has been chosen. The total size of the aggregate is of about 3000 atoms, corresponding to linear sizes of 5-6 nm during the evolution, which is in the size range of the experiments. Simulations of this type are quite cumbersome from a computational point of view so that we have been able to run only a few of them. Therefore, in order to accumulate a more complete statistics allowing quantitative estimates, we have performed coalescence simulations for smaller sizes, of about 800 atoms in total (linear sizes of 3-4 nm during the coalescence process). Also in this second case, the two colliding clusters have perfect TO geometry and random relative orientation; the chosen compositions are Pd<sub>201</sub> and Pt<sub>100</sub>Pd<sub>305</sub>. A range of temperatures from 500 to 900 K has been considered. We remark that, as already discussed for the growth of Pt and Pt-Pd NPs, the temperature at which the evolution takes place in the experiments is not known exactly; therefore in our simulations we have considered different temperatures, belonging to a reasonable range of values. We also note that the simulation temperature has to be chosen accordingly to the size of the system: here, in the case of larger NPs simulations at quite high temperatures (750-900 K) have been necessary in order to observe a significant evolution within the time scale of our simulations; for smaller NPs, major rearrangements have been observed already at 500 K. The time scale of our simulations is up to 3  $\mu$ s for the larger coalesced aggregates, and up to 10  $\mu$ s for the smaller ones. We remark that, to our knowledge, here we present the longest coalescence simulations ever made by MD. For the simulation at larger sizes, we have used the version of our MD code running on GPUs.

In Fig. 5.2.1 we report snapshots from coalescence of the two NPs of larger size at  $T = 750$  K. The first rearrangement step in the coalescence process leads to the alignment of atomic columns. Here, an atomic column is a straight row of atoms connected by nearest-neighbour bonds. This first step is quite fast, since the atomic columns align along a common direction ( $z$  direction in Fig. 5.2.1), on a time scale of a few ns, which is much shorter than the time at which the snapshot of Fig. 5.2.1 (b) is taken. Even though all columns are aligned along  $z$ , in Fig. 5.2.1 (b) and (c) the close-packed atomic planes that are perpendicular to  $x$ - $y$  do not form a sequence of parallel planes extending to the whole aggregate. In fact, in Fig. 5.2.1 (b) and (c) three zones, separated by two non-parallel twin planes, can be singled out. There is a first larger zone on the bottom left part of the coalescing aggregate, which derives from the original Pt<sub>645</sub>Pd<sub>1280</sub> unit. In that zone, all close-packed planes are parallel to the  $x$ - $z$  plane. The second zone is smaller and it is between the two twin planes (which are enclosed by the black and red rectangles in the figure). In this second zone, all close-packed planes are again parallel to the  $x$ - $z$  plane. In the third zone, which derives from Pd<sub>976</sub>, the close-packed planes are tilted with respect to those of the other zones, so that they are not parallel to the  $x$ - $z$  plane. As the

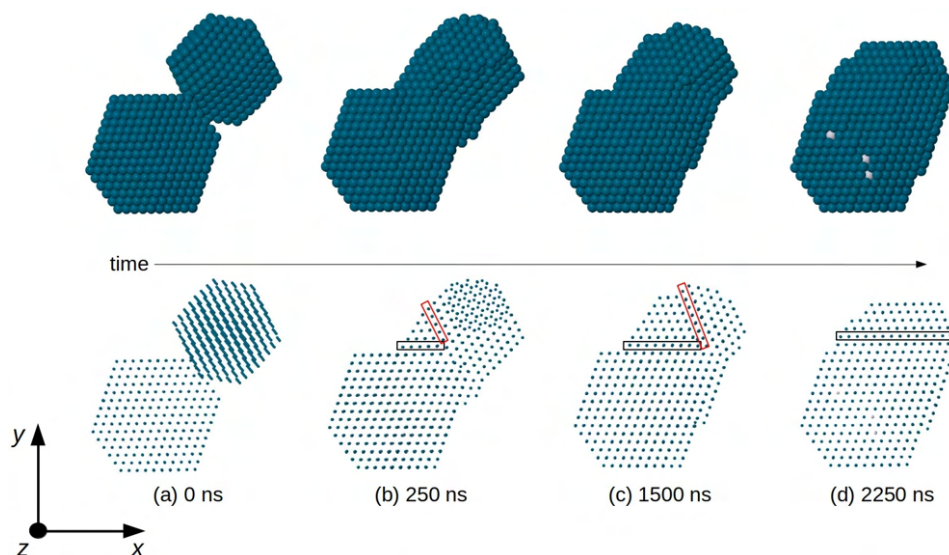


**Figure 5.2.1:** Snapshots from a coalescence simulation of  $\text{Pd}_{976}$  and  $\text{Pt}_{645}\text{Pd}_{1280}$  at  $T = 750$  K. Here and in the following figures Pd and Pt atoms are colored in blue and white, respectively. In the top row, we show the NP surface, which is almost completely made of Pd atoms. In the bottom row, the same images are shown by representing the atoms by small spheres, so that the atomic columns can be seen. (a) Initial configuration: the NPs are randomly oriented, so that atomic columns of  $\text{Pd}_{976}$  are not parallel to those of  $\text{Pt}_{645}\text{Pd}_{1280}$ . (b) The two NPs very quickly rearrange their orientations so that all atomic columns become parallel to the  $z$  direction. This happens well before the time (250 ns) of this snapshot. Two non-parallel twin planes (enclosed by the black and red rectangles) separate different fcc fragments of the aggregate. The close-packed planes to the right of the red rectangle do not present the same orientation as the planes of the remaining part of the aggregate. An island on hcp stacking is visible in the top right corner. (c) The twin plane enclosed by the red rectangle shifts to the right, so that the fragment with misoriented planes becomes smaller and smaller and finally (d) disappears. In (d) all close-packed planes are parallel (to the  $xz$  plane), but the twin plane enclosed by the black rectangle is still there. In (d), top row, some isolated white spots show very few Pt atoms appearing at the NP surface.

Reproduced from D. Nelli, M. Cerbelaud, R. Ferrando and C. Minnai, *Tuning the coalescence degree of Pt-Pd nanoalloys*, *Nanoscale Adv.*, 3:836, 2021.



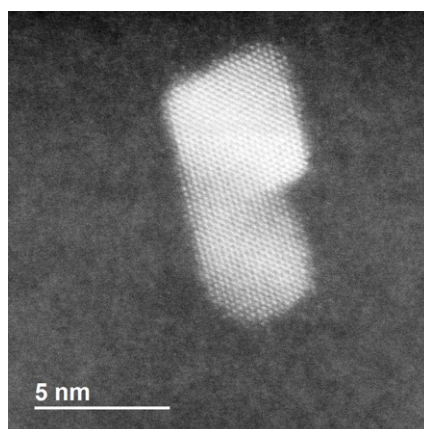


**Figure 5.2.2:** HRTEM-STEM image of a coalescing NP of elongated shape in which atomic close-packed planes are very well aligned, forming a single sequence of planes spanning the whole NP.

Reproduced from D. Nelli, M. Cerbelaud, R. Ferrando and C. Minnai, *Tuning the coalescence degree of Pt-Pd nanoalloys*, *Nanoscale Adv.*, 3:836, 2021.

simulation proceeds, the twin plane in the red rectangle progressively shifts to the right, so that the third zone becomes smaller and smaller, and finally disappears (Fig. 5.2.1(d)). This process ends with an elongated aggregate with all close-packed planes parallel to  $x$ - $z$ . It takes place on a time scale of a few  $10^3$  ns, being therefore much slower than the alignment of atomic columns, but faster than the scale of shape rounding. This hierarchy of time scales is experimentally confirmed by the frequent observation of NPs in which the close-packed planes are very well aligned, but the overall shape is quite elongated, as in the TEM image shown in Fig. 5.2.2.

In summary, the sequence shown in Fig. 5.2.1 suggests that the evolution of the shape of the coalesced aggregate takes place through a three-steps process: (i) alignment of the atomic columns of the two subunits (Fig. 5.2.1(b)); (ii) alignment of close-packed planes (Fig. 5.2.1(d)); (iii) structural rearrangement in a compact geometric shape (not shown in the figure). To validate this scheme we have performed and analysed multiple MD simulation of the coalescence of NPs of smaller sizes, as anticipated.

For each simulation, we have identified the times at which the three different evolution steps have been completed. The alignment time of atomic columns and of closed-packed planes are the times in which configurations such as Fig. 5.2.1(b) and Fig. 5.2.1(d) have been achieved for the first time, respectively. To identify the characteristic time of the third step, i.e. the achievement of a compact shape, we have considered the evolution of the *asphericity* of the aggregate. It is a geometric parameter defined from the eigenvalues of the gyration tensor, as  $b = \lambda_1^2 - 1/2(\lambda_2^2 + \lambda_3^2)$ , where  $\lambda_1$  is the largest of the three eigenvalues. The asphericity is always non-negative and zero only when the eigenvalues are all equal, i.e. when the aggregate is spherically symmetric. The use of this parameter is particularly appropriate in this case, since the equilibrium structure of the coalesced NP is expected to be the quasi-spherical TO shape.

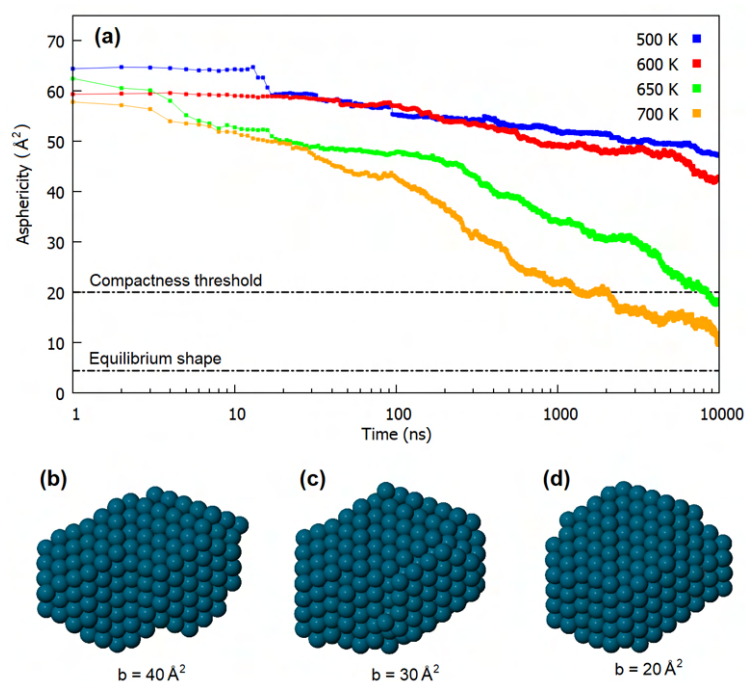


**Figure 5.2.3:** Shape evolution in the coalescence of Pd<sub>201</sub> and Pt<sub>100</sub>Pd<sub>305</sub>. (a) Evolution of the asphericity of the aggregate at different temperatures. For each temperature we show the average over 10 independent simulations. (b) - (c) - (d) Structures obtained during a simulation at 650 K, corresponding to decreasing values of the asphericity. Structure in (d) corresponds to the chosen compactness threshold of  $b = 20 \text{ \AA}^2$ .

Reproduced from D. Nelli, M. Cerbelaud, R. Ferrando and C. Minnai, *Tuning the coalescence degree of Pt-Pd nanoalloys*, *Nanoscale Adv.*, 3:836, 2021.

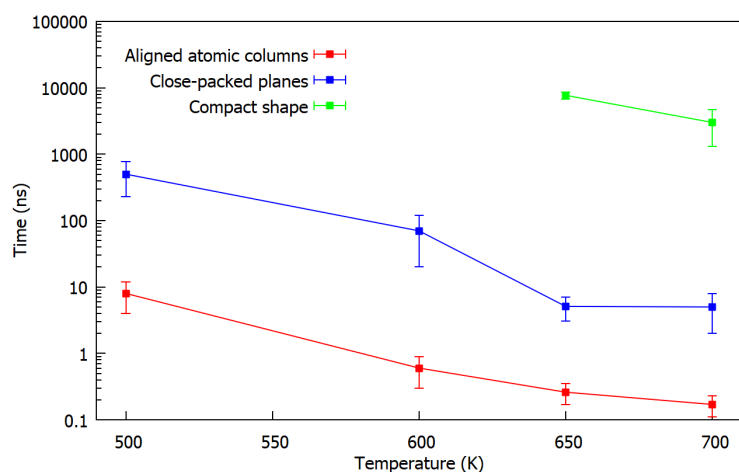


**Figure 5.2.4:** Characteristic times of the three steps (alignment of columns, alignment of close-packed planes, rounding of the shape) of the evolution during the coalescence Pd<sub>201</sub> with Pt<sub>100</sub>Pd<sub>305</sub>. For each temperature we show the average over 10 independent simulations. The graph shows that the three steps are well-separated in time at all temperatures.

Reproduced from D. Nelli, M. Cerbelaud, R. Ferrando and C. Minnai, *Tuning the coalescence degree of Pt-Pd nanoalloys*, *Nanoscale Adv.*, 3:836, 2021.

In Fig. 5.2.3(a) we show the behaviour of the asphericity of the coalescing aggregates at different temperatures, whereas in Fig. 5.2.3(b-d) we show some snapshots from an evolution sequence obtained at 650 K. These structures exhibit aligned close-packed planes and are therefore representative of the final stage of the shape evolution process. The corresponding asphericity values are reported below each structure. The figure shows that the asphericity decreases during the simulations, as the aggregate goes from the initially elongated shape towards a more compact one. We point out that the difference in the initial values of the curves in Fig. 5.2.3(a) are simply due to statistical fluctuations in the very first steps of the simulations. Here we assume that the third step of the evolution is reasonably completed when the asphericity has reached the value  $b = 20 \text{ \AA}^2$ , i.e. when structures such as the one in Fig. 5.2.3(d) have been achieved. This structure is still rather different from the equilibrium TO shape, for which we have calculated  $b = 4.44 \text{ \AA}^2$ . However, it exhibits a fairly good degree of compactness, especially in comparison to the previous stages of the evolution. We notice that the chosen threshold is reached only at the highest temperatures (650 and 700 K) in the time scale of our simulations.

The results are summarized in Fig. 5.2.4, in which the characteristic times of the three different steps of the evolution are shown as a function of the simulation temperature. For each temperature we show the average values over 10 independent simulations. The graph shows that the three different steps previously identified are well-separated in time at all temperatures.

### 5.2.2 FORMATION OF NANOALLOYS WITH OFF-CENTERED CORES

The sequence at 900 K shows a complete evolution of the nanoparticle shape towards a TO structure. The NP becomes more and more compact with increasing time, and reaches a truly compact shape already on a time scale of  $\sim 250$  ns. However, equilibrium is not completely reached. Chemical ordering is not the optimal one, because the Pd-rich core still remains in off-center position. The equilibration of chemical ordering is therefore quite slow even at this temperature, so that coalescence can lead to structures which closely resemble the experimental image of Fig. 5.2.6. In the sequence at 800 K, shape equilibration is not yet completed after 3000 ns. The NP structure is still somewhat ellipsoidal at the end of the simulation, and the Pt-rich core is clearly off-center also in this case.

Here we focus on the evolution of the chemical ordering during coalescence. In Fig. 5.2.5 we show representative snapshots of the coalescence process between  $\text{Pd}_{976}$  and  $\text{Pt}_{645}\text{Pd}_{1280}$ , i.e. the same colliding units considered in Section 5.2.5. We remark that the largest NP has core-shell (PtPd)@Pd chemical ordering, with a Pd surface layer and a randomly intermixed inner part. Here higher temperatures are considered than in the simulations shown in Section 5.2.5; specifically, in the two simulations of Fig. 5.2.5, the system is evolved at a constant temperature of 900 and 800 K for 1.5 and 3  $\mu\text{s}$ , respectively.

The same behaviour is observed in the coalescence of smaller NPs: in all simulations, the final

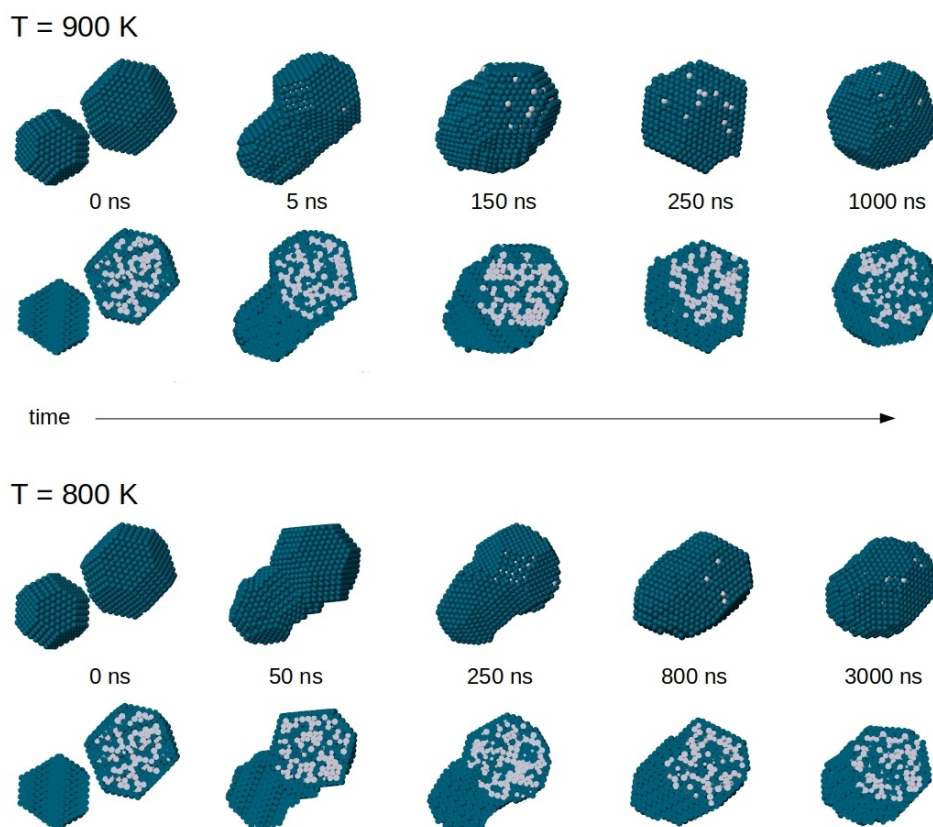


**Figure 5.2.5:** Snapshots from coalescence simulations of  $\text{Pd}_{976}$  and  $\text{Pt}_{645}\text{Pd}_{1280}$  at  $T = 900$  and  $800$  K. The initial configuration is the same in both cases. For each structure, two views are shown: in the top row we present the cluster surfaces, in the bottom row we present cross sections to show chemical ordering inside the NPs.

Reproduced from D. Nelli, M. Cerbelaud, R. Ferrando and C. Minnai, *Tuning the coalescence degree of Pt-Pd nanoalloys*, *Nanoscale Adv.*, 3:836, 2021.

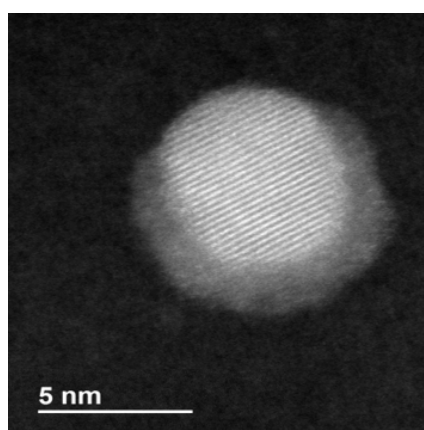


**Figure 5.2.6:** HAADF-STEM image of a  $(\text{PtPd})@\text{Pd}$  NP with off-centered core, that has probably originated from the coalescence between a symmetric  $(\text{PtPd})@\text{Pd}$  NP and a pure Pd one.

Reproduced from D. Nelli, M. Cerbelaud, R. Ferrando and C. Minnai, *Tuning the coalescence degree of Pt-Pd nanoalloys*, *Nanoscale Adv.*, 3:836, 2021.

structure after 10  $\mu\text{s}$  exhibits core-shell chemical ordering with off-centered Pt-Pd mixed core. To quantify this effect, we have calculated the distance between the geometric center of the whole aggregate and the geometric center of the distribution of Pt atoms, which roughly corresponds to the center of the Pt-Pd mixed core. We have also monitored the mean distance of Pt atoms from Pt geometric center, as a measure of the core compactness. We have analysed the simulations at 650 and 700 K, i.e. the ones in which the coalesced aggregate has achieved a fairly compact shape (see Section 5.2.1). After 10  $\mu\text{s}$ , the distance between the centers of the core and of the whole NP is 5.81 Å and 5.11 Å on average at 650 and 700 K, respectively. It is a significant off-center displacement compared to the NP radius, which is in the range of 15-16 Å for these NPs. Moreover, the mean distance of Pt atoms from Pt geometric centre does not change during the evolution at 650 K and increases only slightly at 700 K (plus 1.9% by the end of the simulation, on average), meaning that the Pt-Pd mixed core keeps the same size as at the beginning of the coalescence process, without significant diffusion of its atoms within the coalescing aggregate.

In summary, our simulations show that equilibrium shape is attained well before equilibrium chemical ordering. This is due to the fact that shape can attain equilibrium by atomic-level processes which involve the displacement of surface and subsurface atoms, while chemical ordering needs also the occurrence of diffusion events in the inner part of the aggregate. The latter are much slower than the former, as already shown in Chapter 4 for the equilibration of phase-separating systems.

# 6

## Surface stress relaxation and shape transformations in Au-Pd nanoalloys

ATOMIC STRESS is present, to some degree, in all nanoparticles. The origin of stress at the atomic level is *strain*: in strained structures, interatomic distances are either contracted or expanded with respect to the ideal lattice spacing of the bulk crystal, corresponding to compressive (positive) or tensile (negative) stress, respectively. In crystalline nanoparticles, strain and stress are present in the proximity of the surface, because of the contracted distance between surface and subsurface layers. Noncrystalline structures are much highly strained; the most extreme case among those relevant to our systems is the icosahedron, in which interatomic distances become more and more contracted while approaching the central site, and are expanded at the surface, thus resulting in a strongly non-homogenous stress distribution within the nanoparticle volume. Moreover, the environment around an atomic site of a nanoparticle is often strongly anisotropic, so that stress can be anisotropic as well and even of different types in different directions.

In some cases, stress effects may strongly affect the equilibrium and kinetic behaviours of nanoparticles and nanoalloys; in Chapter 4 we have shown that inner vacancies are stabilized in icosahedral clusters, and may appear during diffusion processes, due to the relaxation of the strong compressive stress in the central region; moreover, we have shown that, in the case of phase-separating nanoalloys, intra-nanoparticle diffusion and surface segregation are faster in icosahedral structures than in fcc ones, again due to the higher level of internal stress. Other examples of such effects can be found in the literature; among them, we mention the influence of stress relaxation effects in the

equilibrium chemical ordering of nanoalloys [27, 41, 51, 129].

In this chapter, we show how shape changes in nanoparticles might be obtained by using atomic stress to stabilize or destabilize specific structural motifs. Such possibility has been suggested for the first time in Ref. [28] on the basis of theoretical considerations concerning the relaxation of internal stress. At variance with Ref. [28], here we present a case in which *surface stress* relaxation at the atomic level is the cause of the shape changes; specifically, we will demonstrate that the shape of Au-Pd nanoparticles can be controlled by varying the Au content in nanoparticles of Pd-rich compositions, changing it from fcc truncated octahedral structures to icosahedral ones. As we will see, these Au atoms are preferentially placed in the surface layer, and therefore influence surface stress. In addition to our theoretical calculations, the observation of a large number of Au-Pd nanoparticles grown in the gas phase has unambiguously shown that these stress-induced shape changes can indeed be experimentally achieved. Such experimental results will be briefly presented in the following (a more detailed analysis can be found in Ref. [196]); then, we will focus on our computational results, which have been able to rationalize the experimental findings and, as anticipated, to highlight the major role atomic stress effects<sup>1</sup>.

At variance with the previous chapters of this thesis, which are mainly devoted to kinetic trapping effects taking place during the nanoparticle evolution, here we describe a phenomenon mainly caused by thermodynamic equilibrium driving forces. In this way, we are able to provide a more complete overview of the possible behaviours of nanoparticles and nanoalloys. We remark that, in general, equilibrium and kinetic effects are in close competition, therefore leading to an even wider spectrum of complex and interesting phenomena.

#### 6.0.1 TO → IH MORPHOLOGY TRANSITION IN AU-PD NANOALLOYS GROWN IN THE GAS PHASE

Au-Pd NPs have been synthesized by inert gas-aggregation sputtering deposition. Specifically, the synthesis technique is the same employed for producing the Pt-Pd NPs we have analysed in Sections 3.4 and 5.2; in this case, Pd and Au targets have been used. The powers applied to the two targets have been varied to obtain different compositions of the metallic vapor, from pure Pd to three Pd-rich compositions: Au<sub>15</sub>Pd<sub>85</sub>, Au<sub>25</sub>Pd<sub>75</sub>, and Au<sub>35</sub>Pd<sub>65</sub> (in atomic percentage). For each composition, a series of different experiments has been made, corresponding to different residence times of the clusters in the aggregation zone. Here we do not dwell on the experimental details, for which we again refer to Ref. [196]; however, as we will see, the residence time of the NPs in the aggregation zone is an essential parameter to correctly interpret the experimental findings, therefore it is useful to briefly discuss this point. Basically, the residence time can be increased by increasing the length of the aggregation zone ( $L_{AZ}$ ); alternatively, the pressure difference  $\Delta P$  between the source and the deposition chamber can be decreased, thus decreasing the acceleration of the NPs from the acceleration zone to the deposition chamber (see Fig. 3.1.1 in Chapter 3). In both cases,

---

<sup>1</sup>Experiments have been conceived, performed and analysed by Chloé Minnai (Okinawa Institute of Science and Technology Graduate University, Okinawa, Japan). Experimental and simulation results have been published in Ref. [196]

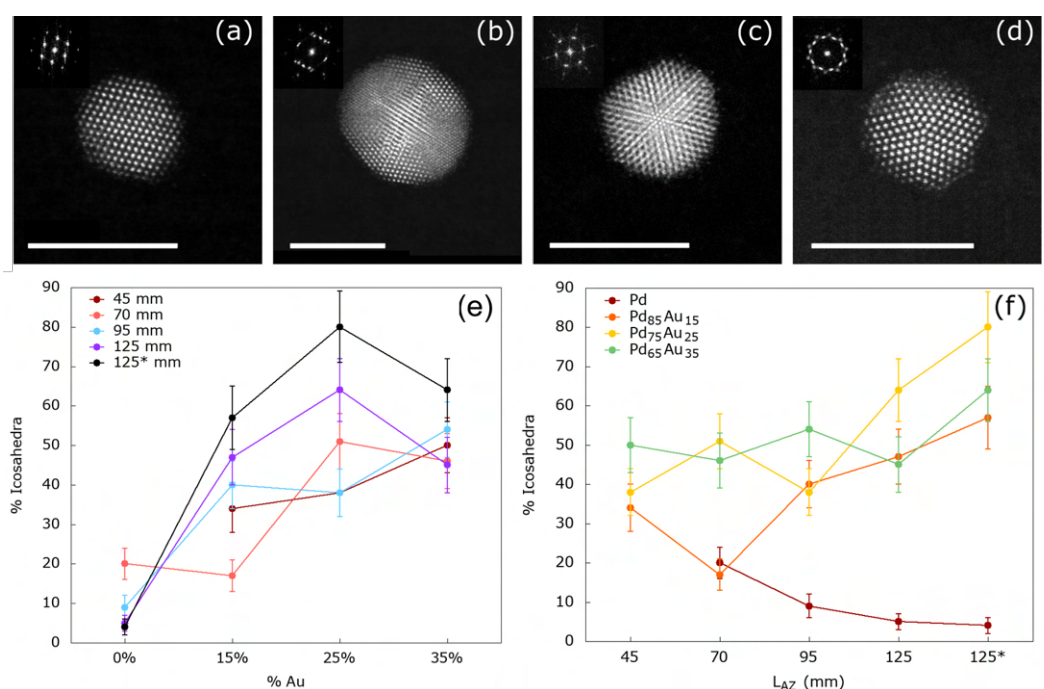


**Figure 6.0.1:** (a–d) Atomic-resolution HAADF–STEM image of Au-Pd NPs. The scale bar is of 5 nm. (a) TO NP; (b, c) Ih NPs oriented with a three- and two-fold axis parallel to the electron beam, respectively; (d) Dh NP along fivefold symmetry axis. (e) Evolution of the percentage of Au-Pd Ih NPs (%Icosahedra) on the total of Ih+fcc structures, as a function of the chemical composition of the distribution. Each curve refers to a different growth condition. The legend indicates the length of the aggregation zone ( $L_{AZ}$ ) at which the distribution is grown. The pressure in the deposition chamber is  $P_{DC} = 6 \times 10^{-4}$  mbar for the first four curves and  $P_{DC} = 7 \times 10^{-3}$  mbar in the last one. (f) Evolution of %Icosahedra as a function of  $L_{AZ}$ .  $P_{DC} = 6 \times 10^{-4}$  mbar for the first four  $L_{AZ}$  values and  $P_{DC} = 7 \times 10^{-3}$  mbar for the last point marked as “125\*mm”. Note that (e) and (f) show the same data set plotted in two different ways. Reproduced from D. Nelli, C. Roncaglia, R. Ferrando and C. Minnai, *Shape Changes in AuPd Alloy Nanoparticles Controlled by Anisotropic Surface Stress Relaxation*, *J. Phys. Chem. Lett.*, 12:4609-4615, 2021.

we can expect the growth to become closer to thermodynamic equilibrium conditions, because the growing NPs have more time to rearrange toward equilibrium structures during their growth [197].

In the produced samples, three different structural motifs have been identified: crystalline fcc TO, Ih and Dh. Some examples of these structures are shown in Fig. 6.0.1(a–d). Since in all samples the number of Dh structures has turned out to be much smaller than that of TO or Ih, we have decided to focus on the analysis of the abundances of the TO and Ih structures. In the following, the quantity %Icosahedra indicate the percentage of Ih with respect to the sum of the Ih and TO structures. Let us analyze first how the relative abundance %Icosahedra evolves as a function of composition of the nominal Au-Pd composition of the sample. Data are reported in Fig. 6.0.1(e), for the different growth conditions. In pure Pd distributions TO are by far dominant over Ih, being always between 5 and 20 times more abundant. However, if the Au content is increased, Ih structures are observed more and more frequently; the maximum abundance is reached for the



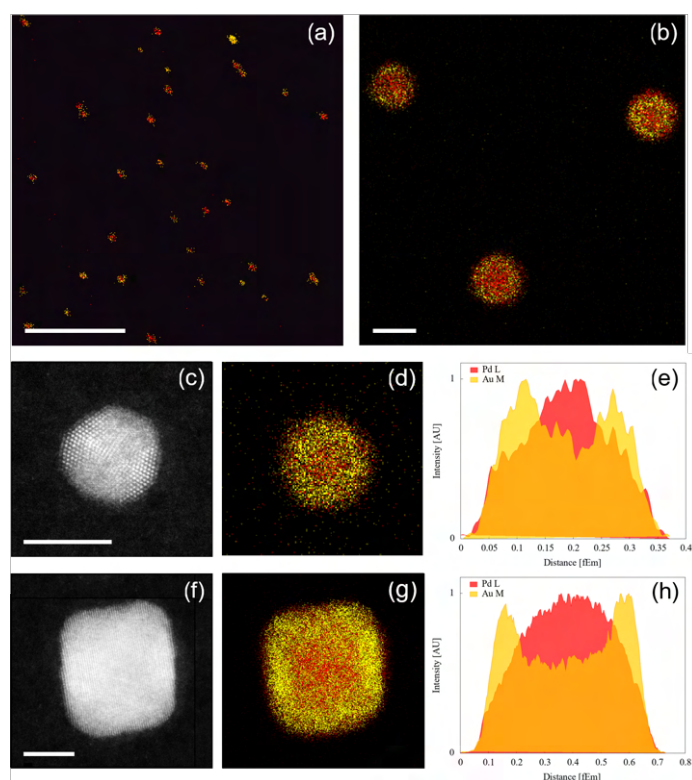


**Figure 6.0.2:** Elemental mapping of  $\text{Au}_{25}\text{Pd}_{75}$  NPs at different magnifications. The colors are based on the chemical composition of the NPs where Au is in yellow and Pd in red. (a) Low magnification mapping showing that all the particles have a mixed composition. The size distribution is  $3.9 \pm 0.6$  nm. Scale bar 50 nm. (b) Higher magnification mapping showing that Au tends to enrich the surface of the NP surface. Scale bar 5 nm. (c, f) HAADF-STEM images of Au-Pd NPs with Ih and TO structures, respectively. The elemental mapping acquired on the same particles (d, g) and the composition profiles (e, h) clearly show that Au atoms distribute at the surface of the particles. Scale bars 5 nm.

Reproduced from D. Nelli, C. Roncaglia, R. Ferrando and C. Minnai, *Shape Changes in AuPd Alloy Nanoparticles Controlled by Anisotropic Surface Stress Relaxation*, *J. Phys. Chem. Lett.*, 12:4609-4615, 2021.

composition  $\text{Au}_{25}\text{Pd}_{75}$ , where, depending on the growth conditions, Ih can be up to four times more abundant than TO. A further increase of the Au content to  $\text{Au}_{35}\text{Pd}_{65}$  causes on average some decrease of %Icosahedra.

In Fig. 6.0.1(f), we report %Icosahedra as a function of the growth conditions at a fixed composition. By increasing  $L_{AZ}$  and then decreasing  $\Delta P$  when the maximum value of  $L_{AZ}$  is reached, one gradually increases the dwell time in the aggregation zone, and therefore the equilibration degree of the grown NPs. Two different types of behaviors can be identified: for pure Pd distributions, %Icosahedra decreases when the growth becomes closer to equilibrium; on the contrary, for the distributions containing Au atoms, %Icosahedra tends to increase when going toward equilibrium. These results indicate that the dominance of TO over Ih in pure Pd and the opposite dominance of Ih over TO, which is especially evident for  $\text{Au}_{25}\text{Pd}_{75}$ , are likely to be related, at least to some extent,

to the thermodynamic equilibrium abundances of these structural motifs.

A further important aspect of the experimental characterization of the samples is the determination of the NP chemical ordering. Au and Pd are known to present a strong tendency toward intermixing in their bulk equilibrium phase diagram [198]. At the nanoscale, equilibrium chemical ordering is expected to be influenced also by the tendency of Au to some degree of surface segregation, as found by several simulations results, at both the atomistic and DFT level [43, 199, 200]. On the experimental side, the tendency of the surface placement of Au has been observed in Au-Pd TO NP grown by wet-chemistry techniques [201]. The EDX characterization of the grown NPs is reported in Fig. 6.0.2. An overall inspection of the samples by EDX (see the images in Fig. 6.0.1(a, b) which show portions of a sample at different magnifications) unambiguously demonstrates that true Au-Pd nanoalloys are grown, without evidence for the formation of separated Au and Pd elemental NPs. In addition, the EDX results confirm that the external part of Au-Pd nanoalloys is enriched in Au, for both Ih and fcc structures, as shown in parts Fig. 6.0.1(c–e) and (f–h), respectively.

In summary, experimental results show that a quite sharp TO  $\rightarrow$  Ih transition takes place because of the replacement of a relatively modest proportion of Pd atoms with Au atoms, with the Au atoms preferentially distributed in the NP shell. The TO  $\rightarrow$  Ih transition becomes more evident when growth is closer to equilibrium.

#### 6.0.2 EQUILIBRIUM STRUCTURES FOR SMALL-SIZE AU-PD NANOALLOYS

In order to determine whether Ih or TO structures are favorable at equilibrium, we have performed global optimization searches, and we have calculated free energy differences by the harmonic superposition approximation (HSA) [13, 202]. Here we describe our procedure in details.

We have considered four sizes, namely  $N = 150, 200, 250$  and  $300$ . For each size we have initially considered ten different compositions from pure Pd to pure Au, increasing the Au content in the NP by steps of 10%. For each composition we have performed at least three full global searches, in which geometric structure and chemical ordering have been optimized simultaneously by combining Brownian and exchange moves (see Section 2.2.2) with relative proportion of 80%-20%. By comparing the results obtained at the different compositions we have identified, for each size, the best structures of the two considered geometric motifs (Ih and TO). These structures have then been employed in a new set of global optimization searches at fixed geometry, in which only the chemical ordering has been optimized. In this set we have increased the number of intermediate compositions in the Pd-rich region. All our simulations were  $10^6$  steps long, and acceptance temperatures have been set to 2000 K and 100 K, respectively for Brownian and exchange moves.

In Fig. 6.0.3 we show the best TO and Ih for each of the four considered sizes ( $N = 150, 200, 250$  and  $300$ ), as obtained in the first set of our global optimization searches. We note that at size  $N = 150$  and  $300$  Ih structures are very close to the perfect Ih of 147 and 309 atoms, respectively.

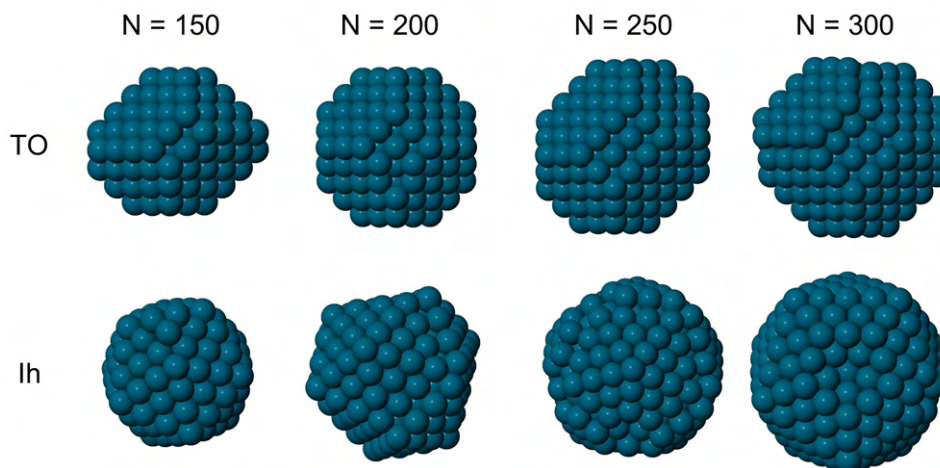


**Figure 6.0.3:** Best TO and Ih for  $N = 150, 200, 250$  and  $300$  obtained in the global optimization searches. Here we show pure Pd clusters.

Adapted from the Supplementary Information of D. Nelli, C. Roncaglia, R. Ferrando and C. Minnai, *Shape Changes in AuPd Alloy Nanoparticles Controlled by Anisotropic Surface Stress Relaxation*, *J. Phys. Chem. Lett.*, 12:4609-4615, 2021.

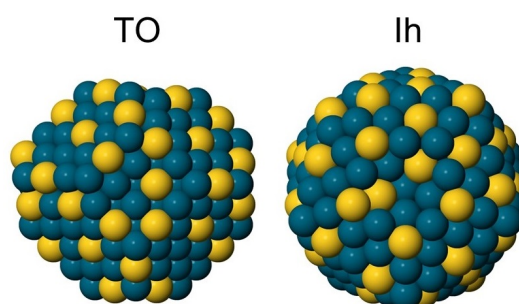


**Figure 6.0.4:** Best chemical ordering for  $\text{Au}_{50}\text{Pd}_{250}$ . Au and Pd atoms are colored in yellow and blue, respectively. Au atoms are placed in the surface layer.

Adapted from the Supplementary Information of D. Nelli, C. Roncaglia, R. Ferrando and C. Minnai, *Shape Changes in AuPd Alloy Nanoparticles Controlled by Anisotropic Surface Stress Relaxation*, *J. Phys. Chem. Lett.*, 12:4609-4615, 2021.

At size  $N = 200$  and  $250$ , Ih structures are intermediate between the two perfect Ih clusters, with the presence of an incomplete outer shell. In Fig. 6.0.4 we show the results of the optimization of chemical ordering in the case of  $\text{Au}_{50}\text{Pd}_{250}$ . This composition is representative of all the Pd-rich compositions that have been analysed. In both geometric structures all Au atoms are placed on the NP surface, in agreement with the experiments and with the computational results in the literature. Moreover, we note that the Au-Pd surface layer presents an intermixed arrangement.

Free energy differences have been calculated starting from the best structures obtained in the global optimization. In the HSA, the free energy  $F_s$  of a local minimum  $s$  of the potential energy landscape is given by the sum of translational, symmetry, vibrational and rotational contributions, added to the energy  $E_s$  of the potential well bottom [13]

$$F_s = E_s + F_{tr,s} + F_{sym,s} + F_{vib,s} + F_{rot,s}. \quad (6.1)$$

The translational term  $F_{tr,s}$  does not depend on the structure, so that it cancels in free energy differences. The other terms are given by

$$\begin{aligned} F_{sym,s} &= k_B T \ln(h_s) \\ F_{vib,s} &= k_B T \sum_{i=1}^{3N-6} \ln \left( 2 \sinh \left( \frac{\hbar \omega_{i,s}}{2k_B T} \right) \right) \\ F_{rot,s} &= -\frac{3}{2} k_B T \ln \left( \frac{2\pi k_B T \bar{I}_s}{\hbar^2} \right), \end{aligned} \quad (6.2)$$

where  $h_s$  is the order of the symmetry group,  $\omega_{i,s}$  are the non-zero normal-mode frequencies, and  $\bar{I}_s$  is the geometric average of the principal inertia moments.

For each of the four considered NP sizes, we have calculated the free energy difference  $\Delta F = F_{Ih} - F_{TO}$  between the best Ih and the best TO structure, for different Pd-rich compositions at different temperatures. Additional details on the calculation procedure of the different contributions to the free energy can be found in the Supplementary Information of Ref. [196]<sup>2</sup>. The  $\Delta F$  results are reported in Fig. 6.0.5.  $\Delta F$  is always positive in pure Pd NPs, reflecting the stronger stability of TO structures with respect to Ih ones. But at increasing Au content,  $\Delta F$  becomes negative, showing a transition to Ih structures. This effect is very strong for  $N = 150$  and  $N = 300$ , which are close to magic Ih sizes, whereas it is still present but weaker for  $N = 200$ , which is very close to the magic TO size 201. On the other hand, for  $N = 250$ , which is far from all magic sizes, the effect is quite strong too. These results therefore show that Ih structures become energetically favorable in Pd-rich AuPd nanoalloys (see the results for  $T = 0$  K) and that entropic contributions, mainly due to the vibrational term, tend to further stabilize Ih structures for increasing temperature. This confirms that the experimentally observed transition is mainly caused by thermodynamic equilibrium

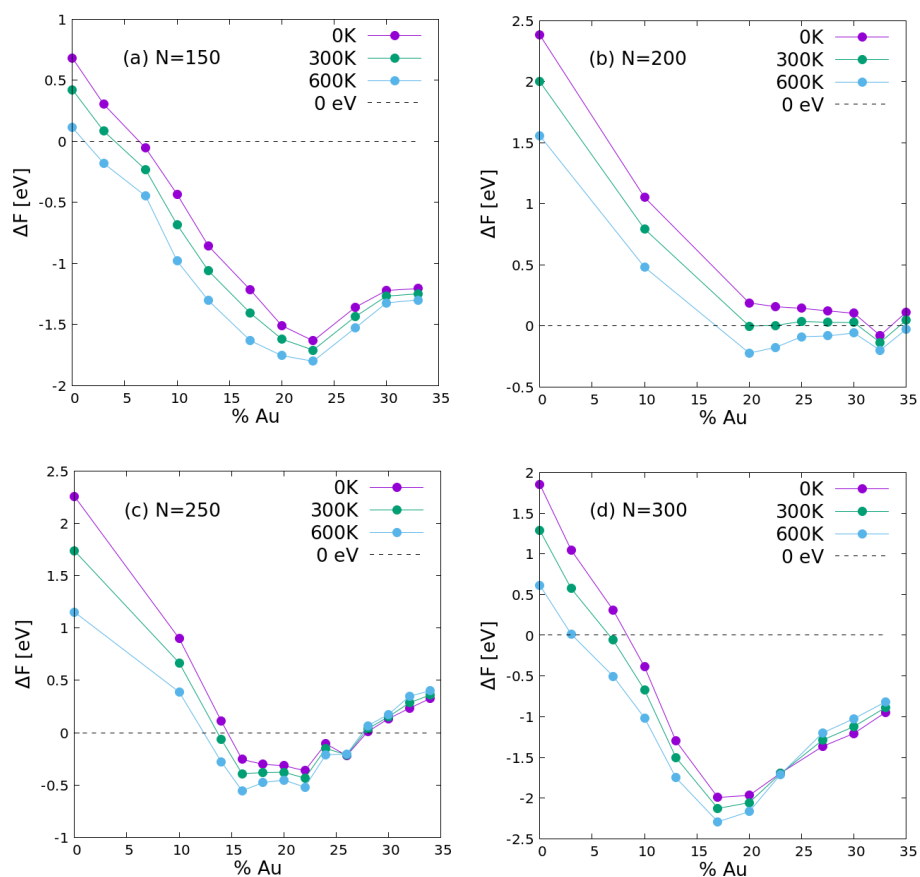


**Figure 6.0.5:** Free energy differences  $\Delta F = F_{Ih} - F_{TO}$  between the best Ih and TO structures for different sizes and Pd-rich compositions. For  $\Delta F < 0$  the Ih is favored over the TO at the thermodynamic equilibrium, while for  $\Delta F > 0$  the opposite holds.

Reproduced from D. Nelli, C. Roncaglia, R. Ferrando and C. Minnai, *Shape Changes in AuPd Alloy Nanoparticles Controlled by Anisotropic Surface Stress Relaxation*, *J. Phys. Chem. Lett.*, 12:4609-4615, 2021.

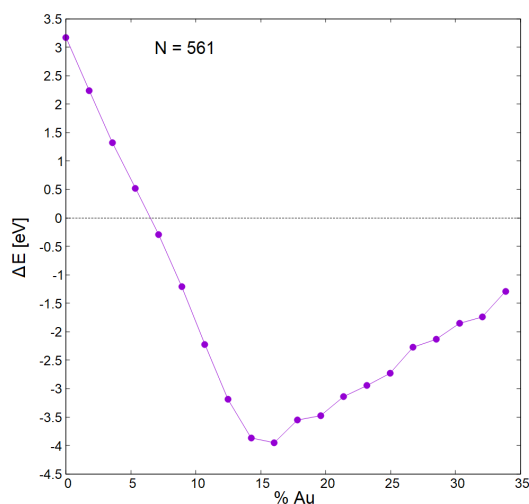


**Figure 6.0.6:** Energy difference  $\Delta E$  between the best Ih and TO structures for different Pd-rich compositions at size 561 atoms.

Reproduced from the Supplementary Information of D. Nelli, C. Roncaglia, R. Ferrando and C. Minnai, *Shape Changes in AuPd Alloy Nanoparticles Controlled by Anisotropic Surface Stress Relaxation*, *J. Phys. Chem. Lett.*, 12:4609-4615, 2021.

driving forces.

Results for Au-Pd nanoalloys of 561 atoms show that the TO  $\rightarrow$  Ih transition is present even at larger sizes. In this case, we have calculated the energy difference  $\Delta E$  between the perfect Ih of 561 atoms and the best TO structure of the same size, for different Pt-rich compositions. Results are shown in Fig. 6.0.6. For pure Pd NPs  $\Delta E$  is positive, but it decreases while increasing the Au content and it takes negative values for a wide composition range. We therefore observe the same inversion of the relative stability of Ih and TO already discussed for NPs of smaller sizes. We point out that, in this case, we have not calculated the free energy difference between the two structures but the difference between the energies obtained from our chemical ordering optimization searches. Anyway, we expect the entropic contribution to further stabilize Ih structures at higher temperatures, as already seen at smaller sizes. Finally, we note that even in this case all Au atoms are placed in the surface of the optimized NPs for all the considered compositions and for both geometric shapes.

### 6.0.3 PHYSICAL DRIVING FORCE FOR THE TO $\rightarrow$ IH TRANSITION: RELAXATION OF ATOMIC-LEVEL SURFACE STRESS

The question which arises from our results is: why Ih structures become energetically favorable when replacing surface Pd atoms with Au atoms? In the following we will show that the relaxation of atomic stress is the key to understand this point.

We have considered atoms placed in the surface sites of Ih and TO nanoparticles, as those shown in Fig. 6.0.7(a) and (b), respectively. For these atoms, we have calculated the three principal stress

<sup>2</sup>Free energy calculations have been made by Cesare Roncaglia (University of Genoa, Italy)

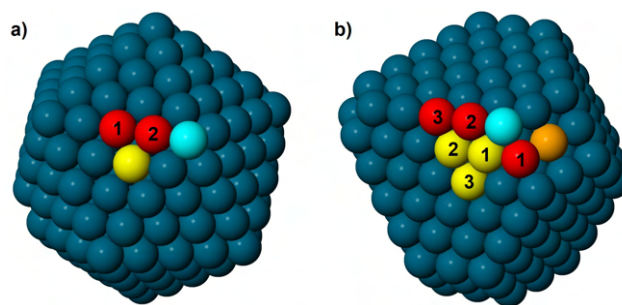


**Figure 6.0.7:** Sites at which Pd atoms are replaced by Au atoms in (a) the best 300-atom pure Pd Ih and (b) the best 300-atom pure Pd TO. Vertex sites are in cyan, edge sites in red, (111)-terrace sites in yellow and (100)-terrace sites in orange. In these sites the data of Table 6.0.1 are calculated.

Reproduced from D. Nelli, C. Roncaglia, R. Ferrando and C. Minnai, *Shape Changes in AuPd Alloy Nanoparticles Controlled by Anisotropic Surface Stress Relaxation*, *J. Phys. Chem. Lett.*, 12:4609-4615, 2021.

components, i.e. the eigenvalues of the atomic stress tensor of Eq. 4.1. All calculations have been performed on locally minimized structures. In all cases, one component ( $p_r$  in the following) lies approximately in radial direction, while the other two components are transverse, lying close to the surface plane for terrace sites. In the following  $p_t$  indicates the arithmetic mean of the transverse components.

The results for atoms in the sites of Fig. 6.0.7 are given in Table 6.0.1. For pure Pd NPs, all stress components are negative, corresponding to tensile stress in all directions. The absolute magnitude of the tensile stress is considerably larger in the Ih than in the fcc TO NP, especially for terrace sites and some edge sites, due to the expanded distances in the (111)-like Ih surfaces compared to ideal (111) surfaces. When a Pd atom is replaced by a larger atom like Au, the strong tensile stress in the Ih relaxes very well, especially in terrace sites where all stress components get close to zero: the sum of the moduli  $|p_r| + 2|p_t|$  decreases from about 8 GPa to less than 1 GPa. On the contrary, in the TO structure, the Au impurity well relaxes only the radial component  $p_r$ , while the components in the surface plane become strongly positive, so that  $|p_r| + 2|p_t|$  increases from 2-4 to 6-8 GPa. For this reason, the energy gain due to the impurity is considerably larger in Ih terraces than in fcc (111) terraces. We note that in the fcc TO structure, placement of Au atoms is more favorable at edges and vertices than on (111) terraces, in agreement with experimental observations and DFT calculations [199, 201], while in the Ih terrace sites are slightly more favorable.

In summary, these results show that the replacement of Pd atoms with Au atoms in surface sites is more effective in the Ih, so that after replacing a sufficient number of atoms the Ih structure becomes energetically favorable against the TO.

Our analysis indicates that the main driving force for the experimentally observed TO  $\rightarrow$  Ih shape change derives from the equilibrium energetics for varying composition. However, in NP growth, kinetic effects are usually expected to occur to some extent, as extensively discussed in Chapter 3. Therefore, our finally observed NPs may in principle present some form of kinetic trapping, because

structure	site	$\Delta E$	bonds	$p_r$		$p_t$		$ p_r  + 2 p_t $		
				Pd	Au	Pd	Au	Pd	Au	$\Delta$
Ih	111	-0.537	9	-4.13	-0.12	-1.90	0.25	7.93	0.62	-7.31
	edge_1	-0.518	8	-4.31	-1.16	-1.83	-0.02	7.97	1.20	-6.77
	edge_2	-0.510	8	-3.25	-0.54	-1.47	0.67	6.19	1.88	-4.31
	vertex	-0.448	6	-2.19	-0.65	-1.39	0.05	4.97	0.75	-4.22
TO	111_1	-0.411	9	-1.07	0.15	-0.46	4.01	1.99	8.17	6.18
	111_2	-0.402	9	-1.19	0.18	-0.86	3.53	2.91	7.24	4.33
	111_3	-0.384	9	-1.77	0.16	-1.13	2.99	4.03	6.14	2.11
	100	-0.459	8	-2.04	-0.40	-1.57	0.71	5.18	1.82	-3.36
	edge_1	-0.457	7	-2.16	-0.48	-1.46	0.45	5.08	1.38	-3.70
	edge_2	-0.453	7	-2.45	0.02	-1.17	0.57	4.79	1.16	-3.63
	edge_3	-0.448	7	-2.65	0.07	-1.18	0.46	5.01	0.99	-4.02
	vertex	-0.441	6	-2.22	-0.50	-1.41	-0.04	5.04	0.58	-4.46

**Table 6.0.1:** Radial and transversal atomic stress values ( $p_r$  and  $p_t$ , see text) in the sites of Fig. 6.0.7. In the “Pd” columns, we report the stress values for the atomic sites in the pure Pd NP, whereas in the “Au” columns we report the stress values after replacing the Pd atom with an Au atom.  $\Delta E$  and  $\Delta$  are the energy gain and the variation of  $|p_r| + 2|p_t|$  due to the replacement, respectively. Energies are in eV and stress values in GPa.

Reproduced from D. Nelli, C. Roncaglia, R. Ferrando and C. Minnai, *Shape Changes in AuPd Alloy Nanoparticles Controlled by Anisotropic Surface Stress Relaxation*, *J. Phys. Chem. Lett.*, 12:4609-4615, 2021.



the time scale for attaining equilibrium becomes longer and longer as a NP grows in size, so that it may happen that the growing NPs equilibrate up to some critical size of at least 2-3 nm in our case, and then they grow by a kind of *template growth* [203]. In template growth, the geometric structure is selected in the first part of the growth (in which equilibrium shapes are formed) and then preserved as the NP grows further. This point is currently under investigation.

In conclusion, our results show that atomic-level stress can be used to induce shape changes in NPs, by either stabilizing or destabilizing specific structural types. In Au-Pd, the size mismatch between the larger Au atoms and the smaller Pd atoms is used to very well relax the tensile stress of the expanded surfaces of Ih NPs, while size mismatch induces a less efficient relaxation in the surfaces of fcc TO NPs because of compressive stress in the terrace planes. We believe that simple physical mechanisms of this type can be effective for a wide class of binary systems, for both gas phase and wet chemistry synthesis methods.

## Conclusions

In this Ph.D. thesis, different examples of nonequilibrium phenomena have been analysed and discussed, in the case of both mono- and bi-metallic NPs. Such phenomena have been studied by different computational techniques and, in some cases, simulation results have been compared with experimental observations. Our simulations have allowed us to identify some general trends in the evolution of NPs and nanoalloys, which we briefly summarize here.

1. **Equilibrium vs. kinetic driving forces.** In all process analysed in this thesis, a close competition between equilibrium and kinetic driving forces takes place during the NP evolution. We have shown that the outcomes of such competition depend on the conditions of the evolution, namely the temperature and, in the case of growth processes, the rate at which atoms are deposited on the growing NP. By tuning these conditions in our MD simulations, we have been able to identify different regimes, in which either equilibrium or kinetic effects are dominant. In the latter case, different kinds of kinetic trapping effects have been observed. Metastable surface defects have been proved to be responsible of the octahedron-to-tetrahedron growth pathway in Pt NPs, in which the symmetry of the growing structure is broken in a very specific way and, at the same time, the NP moves further and further away from equilibrium while growing. These results have allowed the explanation of the long-standing problem of the formation of metallic tetrahedral NPs. The simulations have also demonstrated that Pt octahedra grow instead of tetrahedra when the growth conditions are closer to equilibrium. Kinetic trapping effects are also responsible of the formation of peculiar composition-tunable core-shell configurations in the growth Pt-Pd nanoalloys, in which a mixed Pt-Pd core is surrounded by a shell of the majority element. Different types of metastable out-of-equilibrium chemical arrangements have been obtained for other bimetallic systems at some stage of their evolution: three-shell arrangements have been observed during the evolution of Au-Co, Ag-Cu and Ag-Ni nanoalloys from out-of-equilibrium intermixed configurations; coalescing Pt-Pd NPs have taken core-shell arrangements with off-centered core.
2. **Equilibration time scales: structural vs. chemical rearrangements.** In the case of bimetallic NPs, we have systematically observed relevant differences between the equilibration time scale of the overall geometric shape and of the chemical ordering, the latter being much longer in all cases. Accordingly, in our simulations we have often observed NP configura-

tions in which the shape is rather compact and fairly close to the optimal one, but the chemical ordering is strongly out-of-equilibrium. Such structures have been obtained during the evolution of Au-Co, Ag-Cu and Ag-Ni NPs, and during the growth and the coalescence of Pt-Pd NPs: in most cases, the out-of-equilibrium chemical arrangements mentioned in the previous point are coupled to compact and regular geometric shapes, close to the one of the global minimum.

- 3. Collective processes.** Both shape and chemical ordering rearrangements taking place during NP and nanoalloy equilibration have been proved to occur through mechanisms of collective character, in which several atoms change their positions at the same time in a concerted way. Conversely, while single-atom processes have been observed, they were not among the most effective causes of shape rearrangement. An example of collective process is the transformation of Au-Co and Ag-Ni intermixed nanoalloys into disordered liquidlike structures, and the simultaneous migration of multiple Au and Ag atoms towards the NP surface. A second example is the filling of the sintering neck of coalescing Au NPs, which have been found to take place through the concerted displacement of several atoms, and not by single-atom detachment, surface diffusion and reattachment as often assumed in the literature. A third example is the displacement of impurities from the center of an icosahedron.
- 4. Stress effects.** In the case of noncrystalline icosahedral NPs, stress effects have been proved to play a major role. This has been verified for both equilibrium properties and kinetic behaviours, for different bimetallic systems with some degree of size mismatch between the two atomic species. Unexpected diffusion pathways have been identified in the case of large single-atom impurities moving within icosahedral clusters, which involve the sudden creation of internal vacancies; our calculations have shown that the atomic-level driving force for such pathways is the relaxation of the compressive stress on the impurity. Moreover, we have shown that chemical ordering equilibration is faster in Au-Co and Ag-Cu icosahedral NPs compared to crystalline fcc NPs of similar size; this behaviour is again due to internal stress relaxation driving forces, which are much stronger in icosahedra compared to fcc structures. Finally, our calculations have demonstrated that surface stress effects are responsible of the fcc-to-Ih shape transformation experimentally observed in Au-Pd NPs while increasing the Au content. In particular, we have shown that this transformation is caused by the relaxation of the anisotropic surface stress obtained by placing Au impurities in the icosahedral surface.

In conclusion, our simulation results have contributed to the the study of the nonequilibrium behaviours of NPs and nanoalloys. Some interesting evolution phenomena have been extensively described and clearly explained for the first time, and, in some cases, our calculations have allowed to achieve a deeper understanding of the experimental observations. Anyway, the subject is wide, complex and of great actual interest; our aim is to further pursue this study, by analysing new phenomena and systems, and by employing new simulation techniques.

# A

## Parameters of the SMATB force field

Here we report the parameters of the SMATB potential used for modelling the metallic systems studied in this thesis. The parameters are those in Eq. 2.2, plus the cutoff distances as defined in Section 2.1.

	$p$	$q$	$A$ (eV)	$\xi$ (eV)	$r_o$ (Å)	$r_{c1}$ (Å)	$r_{c2}$ (Å)
Pt-Pt	10.6120	4.004	0.29750	2.6950	2.77	3.91737	4.79778
Pd-Pd	10.8670	3.742	0.17460	1.7180	2.75	3.88909	4.76314
Pt-Pd	10.7395	3.873	0.23605	2.2065	2.76	3.90323	4.78046

**Table A.0.1:** Parameters of SMATB potential for Pt and Pt-Pd. From Ref. [204].

	$p$	$q$	$A$ (eV)	$\xi$ (eV)	$r_o$ (Å)	$r_{c1}$ (Å)	$r_{c2}$ (Å)
Au-Au	10.35	4.178	0.210	1.818	2.88	4.07294	4.98831
Co-Co	8.80	2.960	0.189	1.907	2.50	3.53553	4.33013
Au-Co	10.66	3.113	0.141	1.614	2.69	4.07294	4.33013

**Table A.0.2:** Parameters of SMATB potential for Au-Co. From Ref. [157].

	$p$	$q$	$A$ (eV)	$\xi$ (eV)	$r_o$ (Å)	$r_{c1}$ (Å)	$r_{c2}$ (Å)
Ag-Ag	10.85	3.180	0.1031	1.1895	2.890	4.08708	5.00563
Cu-Cu	10.55	2.430	0.0894	1.2799	2.560	3.62039	4.43405
Ag-Cu	10.70	2.805	0.0977	1.2275	2.725	4.08708	4.43405

**Table A.0.3:** Parameters of SMATB potential for Ag-Cu. From Ref. [164].

	$p$	$q$	$A$ (eV)	$\xi$ (eV)	$r_o$ (Å)	$r_{c1}$ (Å)	$r_{c2}$ (Å)
Ag-Ag	10.790	3.190	0.10433	1.194019	2.890	4.08708	5.00563
Co-Co	9.210	2.975	0.175700	1.843000	2.500	3.53553	4.33013
Ag-Co	10.001	3.085	0.15202	1.431900	2.695	4.08708	4.33013

**Table A.0.4:** Parameters of SMATB potential for Ag-Co. From Ref. [205].

	$p$	$q$	$A$ (eV)	$\xi$ (eV)	$r_o$ (Å)	$r_{c1}$ (Å)	$r_{c2}$ (Å)
Ag-Ag	10.850	3.180	0.1031	1.1895	2.89	4.08708	5.00563
Ni-Ni	11.340	2.270	0.0958	1.5624	2.49	3.52139	4.31281
Ag-Ni	11.095	2.725	0.0960	1.3400	2.69	4.08708	4.31281

**Table A.0.5:** Parameters of SMATB potential for Ag-Ni. From Ref. [205].

	$p$	$q$	$A$ (eV)	$\xi$ (eV)	$r_o$ (Å)	$r_{c1}$ (Å)	$r_{c2}$ (Å)
Au-Au	10.229	4.036	0.2061	1.790	2.88400	4.07859	4.99523
Pt-Pt	10.612	4.004	0.2795	2.695	2.77470	3.92402	4.80592
Au-Pt	10.420	4.020	0.2500	2.200	2.82935	4.07859	4.80592

**Table A.0.6:** Parameters of SMATB potential for Au-Pt. From Ref. [206].

	$p$	$q$	$A$ (eV)	$\xi$ (eV)	$r_o$ (Å)	$r_{c1}$ (Å)	$r_{c2}$ (Å)
Au-Au	12.500	3.5500	0.2061	0.129097	2.8843	4.99575	5.76860
Rh-Rh	18.450	1.8670	0.2795	0.062891	2.6891	6.01307	6.58699
Au-Rh	9.529	1.7893	0.2500	0.120341	2.7867	6.01307	6.58699

**Table A.0.7:** Parameters of SMATB potential for Au-Rh. From Ref. [207].

	$p$	$q$	$A$ (eV)	$\xi$ (eV)	$r_o$ (Å)	$r_{c1}$ (Å)	$r_{c2}$ (Å)
Au-Au	10.139	4.033	0.2096	1.8153	2.88400	4.07859	4.99523
Pd-Pd	11.000	3.794	0.1715	1.7019	2.75064	3.88999	4.76425
Au-Pd	10.569	3.913	0.2764	2.0820	2.82732	4.07859	4.76425

**Table A.0.8:** Parameters of SMATB potential for Au-Pd. From Ref. [43].

# B

## Atomic stress and pressure

Here we report the derivation of the atomic stress tensor, which follows the one in Ref. [128].

### B.1 HYDROSTATIC PRESSURE

The hydrostatic pressure  $p_i$  acting on atom  $i$  can be defined as follows:

$$p_i = -\frac{dE_i}{dV_i}, \quad (\text{B.1})$$

where  $E_i$  is the energy of atom  $i$  and  $V_i$  is its volume. This definition can be applied when atomic energies and volumes can be attributed, at least in principle, for example as in the case of atomistic models.

Let us evaluate the local pressure in terms of atomic coordinates. Our system consists of  $N$  atoms of relative distances  $r_{mn}$ . In general  $E_i$  depends on all distances  $r_{ij}$ , with  $j = 1, \dots, N$  and  $j \neq i$ . The atom has an initial volume  $V_{oi}$  and we expand all initial distances  $r_{oij}$  uniformly by a factor  $a$ . We have

$$\begin{aligned} r_{ij} = r_{oij} &\rightarrow r'_{ij} = ar_{oij}, \\ V_i = V_{oi} &\rightarrow V'_i = a^3 V_{oi}, \\ E_i(r_{oi1}, \dots, r_{oin}) &\rightarrow E_i(a r_{oi1}, \dots, a r_{oin}). \end{aligned} \quad (\text{B.2})$$

Now the local pressure can be evaluated by

$$p_i = -\frac{dE_i}{da} \frac{da}{dV_i}, \quad (\text{B.3})$$

calculated in  $\alpha = 1$ . But

$$\frac{da}{dV_i} = \left( \frac{dV_i}{da} \right)^{-1} = \frac{1}{3\alpha^2 V_{oi}} = \frac{1}{3V_{oi}}, \quad (\text{B.4})$$

and

$$\frac{dE_i}{da} = \sum_{j \neq i} \frac{dE_i}{dr_{ij}} \frac{dr_{ij}}{da} = \sum_{j \neq i} \left( \frac{dE_i}{dr_{ij}} \right)_{r_{ij}=r_{oij}} r_{oij}, \quad (\text{B.5})$$

when calculated in  $\alpha = 1$ . Dropping the subscript  $o$  and simplifying the notation we have finally

$$p_i = -\frac{1}{3V_i} \sum_{j \neq i} \frac{dE_i}{dr_{ij}} r_{ij}. \quad (\text{B.6})$$

Let us now consider a specific example, a binary system of species A and B interacting by a SMATB potential. In this case

$$E_i = \sum_{j, r_{ij} \leq r_c} A_{ij} e^{-p_{ij} \left( \frac{r_{ij}}{r_{oij}} - 1 \right)} - \sqrt{\sum_{j, r_{ij} \leq r_c} \xi_{ij}^2 e^{-2q_{ij} \left( \frac{r_{ij}}{r_{oij}} - 1 \right)}}. \quad (\text{B.7})$$

The parameters  $p_{ij}$ ,  $q_{ij}$ ,  $A_{ij}$ ,  $\xi_{ij}$ ,  $r_{oij}$  depend indeed on the atomic species of the pair only. Therefore  $p_{ij}$  can be either  $p_{AA}$  or  $p_{BB}$  or  $p_{AB}$ , and the same holds for all other parameters. As for  $r_{oij}$ ,  $r_{oAA}$  and  $r_{oBB}$  are the equilibrium distances in the bulk pure crystals at zero temperature, and  $r_{oAB} = (r_{oAA} + r_{oBB})/2$ .  $r_c$  is an appropriate cutoff distance so that the sum has contributions from all neighbours of atom  $i$  that are within  $r_c$ .

The derivatives in Eq.(B.6) are

$$\frac{dE_i}{dr_{ik}} = -\frac{p_{ik} A_{ik}}{r_{oik}} e^{-p_{ik} \left( \frac{r_{ik}}{r_{oik}} - 1 \right)} + \frac{q_{ik} \xi_{ik}^2}{r_{oik}} \frac{e^{-2q_{ik} \left( \frac{r_{ik}}{r_{oik}} - 1 \right)}}{\sqrt{\sum_{j, r_{ij} \leq r_c} \xi_{ij}^2 e^{-2q_{ij} \left( \frac{r_{ij}}{r_{oij}} - 1 \right)}}}. \quad (\text{B.8})$$

The volume  $V_i$  in Eq.(B.6) is usually chosen as the atomic volume in the bulk lattice of one of the two elements (the *host* element) and is therefore a constant  $\Omega$ . Putting

$$D(i)^{-1} = \sqrt{\sum_{j, r_{ij} \leq r_c} \xi_{ij}^2 e^{-2q_{ij} \left( \frac{r_{ij}}{r_{oij}} - 1 \right)}}, \quad (\text{B.9})$$



we obtain

$$p_i = \frac{1}{3\Omega} \sum_{k, r_{ik} \leq r_c} \frac{r_{ik}}{r_{oik}} \left[ p_{ik} A_{ik} e^{-p_{ik} \left( \frac{r_{ik}}{r_{oik}} - 1 \right)} - q_{ik} \xi_{ik}^2 D(i) e^{-2q_{ik} \left( \frac{r_{ik}}{r_{oi}} - 1 \right)} \right]. \quad (\text{B.10})$$

More generally, the form of the potential is

$$E_i = \sum_{j \neq i} \phi_{ij}(r_{ij}) - \sqrt{\sum_{j \neq i} \psi_{ij}^2(r_{ij})}, \quad (\text{B.11})$$

where

$$\begin{aligned} \phi_{ij}(r_{ij}) &= A_{ij} e^{-p_{ij} \left( \frac{r_{ij}}{r_{oij}} - 1 \right)} & r_{ij} \leq r_{1ij} \\ &= a_{5ij}(r_{ij} - r_{2ij})^5 + a_{4ij}(r_{ij} - r_{2ij})^4 + a_{3ij}(r_{ij} - r_{2ij})^3 & r_{1ij} < r_{ij} \leq r_{2ij}, \\ &= 0 & r_{ij} > r_{2ij} \\ \psi_{ij}(r_{ij}) &= \xi_{ij} e^{-q_{ij} \left( \frac{r_{ij}}{r_{oij}} - 1 \right)} & r_{ij} \leq r_{1ij} \\ &= x_{5ij}(r_{ij} - r_{2ij})^5 + x_{4ij}(r_{ij} - r_{2ij})^4 + x_{3ij}(r_{ij} - r_{2ij})^3 & r_{1ij} < r_{ij} \leq r_{2ij} \\ &= 0 & r_{ij} > r_{2ij}. \end{aligned} \quad (\text{B.12})$$

$r_{1ij}$  and  $r_{2ij}$  are cutoff distances. The coefficients of the polynomials ( $a_{5ij}$ ,  $a_{4ij}$ ,  $a_{3ij}$  and  $x_{5ij}$ ,  $x_{4ij}$ ,  $x_{3ij}$ ) are chosen to insure a continuous function with continuous derivative in all points. All these quantities depend on the atomic species involved in the pair  $ij$ .

The derivative is

$$\frac{dE_i}{dr_{ik}} = \frac{d\phi_{ik}}{dr_{ik}} - \psi_{ik} \frac{d\psi_{ik}}{dr_{ik}} D(i), \quad (\text{B.13})$$

with

$$D(i)^{-1} = \sqrt{\sum_{j \neq i} \psi_{ij}^2(r_{ij})}, \quad (\text{B.14})$$

and

$$\begin{aligned} \frac{d\phi_{ik}}{dr_{ik}} &= -\frac{p_{ik} A_{ik}}{r_{oik}} e^{-p_{ik} \left( \frac{r_{ik}}{r_{oik}} - 1 \right)} & r_{ik} \leq r_{1ik} \\ &= 5a_{5ik}(r_{ik} - r_{2ik})^4 + 4a_{4ik}(r_{ik} - r_{2ik})^3 + 3a_{3ik}(r_{ik} - r_{2ik})^2 & r_{1ik} < r_{ik} \leq r_{2ik} \\ &= 0 & r_{ik} > r_{2ik}, \\ \frac{d\psi_{ik}}{dr_{ik}} &= -\frac{q_{ik} \xi_{ik}}{r_{oik}} e^{-q_{ik} \left( \frac{r_{ik}}{r_{oik}} - 1 \right)} & r_{ik} \leq r_{1ik} \\ &= 5x_{5ik}(r_{ik} - r_{2ik})^4 + 4x_{4ik}(r_{ik} - r_{2ik})^3 + 3x_{3ik}(r_{ik} - r_{2ik})^2 & r_{1ik} < r_{ik} \leq r_{2ik} \\ &= 0 & r_{ik} > r_{2ik}. \end{aligned} \quad (\text{B.15})$$

Finally

$$p_i = -\frac{1}{3V_i} \sum_{k \neq i} r_{ik} \left[ \frac{d\phi_{ik}}{dr_{ik}} - \psi_{ik} \frac{d\psi_{ik}}{dr_{ik}} D(i) \right]. \quad (\text{B.16})$$

## B.2 STRESS TENSOR

Now we generalize the approach to arbitrary deformations. Let us consider an arbitrary homogeneous infinitesimal deformation in which all coordinates  $\mathbf{r}_{ij}$  are transformed as follows

$$\mathbf{r}_{ij} \rightarrow (\underline{I} + \underline{\varepsilon})\mathbf{r}_{ij}, \quad (\text{B.17})$$

where  $\underline{I}$  and  $\underline{\varepsilon}$  are the identity matrix and the infinitesimal strain tensor, respectively. In terms of components

$$r_{ij}^a \rightarrow \sum_b (\delta^{ab} + \varepsilon^{ab}) r_{ij}^b. \quad (\text{B.18})$$

In our system the total energy is written as a sum of atomic contributions  $E_i$  which depend on the distances  $r_{ij}$ .

$$E = \sum_i E_i(\{r_{ij}\}). \quad (\text{B.19})$$

Let us evaluate the change in energy of  $E_i$  due to the transformation.

$$\delta E_i = \sum_{j \neq i} \frac{\partial E_i}{\partial r_{ij}} \delta r_{ij}, \quad (\text{B.20})$$

where  $\delta r_{ij}$  is the change in the distance between atoms  $i$  and  $j$ . To the first order in  $\underline{\varepsilon}$  one has

$$\delta r_{ij} = \sqrt{[(\underline{I} + \underline{\varepsilon})\mathbf{r}_{ij}] \cdot [(\underline{I} + \underline{\varepsilon})\mathbf{r}_{ij}]} - r_{ij} = \sqrt{r_{ij}^2 + 2\mathbf{r}_{ij} \cdot \underline{\varepsilon}\mathbf{r}_{ij}} - r_{ij} = \frac{\mathbf{r}_{ij} \cdot \underline{\varepsilon}\mathbf{r}_{ij}}{r_{ij}}, \quad (\text{B.21})$$

which, in terms of components reads

$$\delta r_{ij} = \frac{1}{r_{ij}} \sum_{ab} r_{ij}^a \varepsilon^{ab} r_{ij}^b, \quad (\text{B.22})$$

so that

$$\delta E_i = \sum_{j \neq i} \sum_{ab} \frac{1}{r_{ij}} \frac{\partial E_i}{\partial r_{ij}} r_{ij}^a \varepsilon^{ab} r_{ij}^b, \quad (\text{B.23})$$

and the change in total energy is given by

$$\delta E = \sum_i \delta E_i = \sum_{i,j \neq i} \sum_{ab} \frac{1}{r_{ij}} \frac{\partial E_i}{\partial r_{ij}} r_{ij}^a \varepsilon^{ab} r_{ij}^b = \sum_{ab} \varepsilon^{ab} \sum_{i,j \neq i} \frac{1}{r_{ij}} \frac{\partial E_i}{\partial r_{ij}} r_{ij}^a r_{ij}^b. \quad (\text{B.24})$$

From the theory of elasticity the change in total energy is given by the trace of the product of the (symmetric) stress tensor  $\underline{\sigma}$  with the infinitesimal strain tensor

$$\delta E = \sum_{ab} \sigma^{ab} \varepsilon^{ab}, \quad (\text{B.25})$$

so that the stress tensor can be written as

$$\sigma^{ab} = \sum_{i,j \neq i} \frac{\partial E_i}{\partial r_{ij}} \frac{r_{ij}^a r_{ij}^b}{r_{ij}}, \quad (\text{B.26})$$

which can be written as a sum of atomic stress tensors  $\underline{\sigma}_i$

$$\sigma^{ab} = -3 \sum_i V_i \sigma_i^{ab}, \quad (\text{B.27})$$

with  $V_i$  volume of the  $i$ -th atom and

$$\sigma_i^{ab} = -\frac{1}{3V_i} \sum_{j \neq i} \frac{\partial E_i}{\partial r_{ij}} \frac{r_{ij}^a r_{ij}^b}{r_{ij}}. \quad (\text{B.28})$$

Here the factor  $-1/3$  has been included so that the hydrostatic pressure is exactly the trace of the atomic stress tensor, and the tensions and the pressure are of common sign, as we show below.

The stress tensor is symmetric and therefore can be diagonalized. In the basis of the principal axes (which changes from atom to atom) it has the form

$$\frac{-1}{3V_i} \sum_{j \neq i} \begin{pmatrix} \frac{\partial E_i}{\partial r_{ij}} \frac{x_{ij}^2}{r_{ij}} & 0 & 0 \\ 0 & \frac{\partial E_i}{\partial r_{ij}} \frac{y_{ij}^2}{r_{ij}} & 0 \\ 0 & 0 & \frac{\partial E_i}{\partial r_{ij}} \frac{z_{ij}^2}{r_{ij}} \end{pmatrix}$$

Comparing this tensor with Eq. (B.6) we find that the pressure is proportional to the trace of the tensor (note that the trace is invariant under rotations).

$$p_i = \text{Tr}(\underline{\sigma}_i). \quad (\text{B.29})$$

The diagonal elements of the strain tensor give the energy change due to a unidirectional deformation along a single coordinate axis. This can be seen by repeating for a unidirectional deformation the same procedure that derives the hydrostatic pressure from a uniform isotropic deformation.

### B.3 ENERGY AND FORCES

We have

$$E = \sum_i E_i = \sum_i \left[ \sum_{j, r_{ij} \leq r_c} A_{ij} e^{-p_{ij} \left( \frac{r_{ij}}{r_{oij}} - 1 \right)} - \sqrt{\sum_{j, r_{ij} \leq r_c} \xi_{ij}^2 e^{-2q_{ij} \left( \frac{r_{ij}}{r_{oij}} - 1 \right)}} \right], \quad (\text{B.30})$$

and

$$f_{i,a} = - \frac{\partial E}{\partial r_{i,a}}, \quad (\text{B.31})$$

with  $a = 1, 2, 3$  enumerates the components of the vector  $\mathbf{r}_i$ . We can separate attractive and binding parts

$$f_{i,a} = f_{i,a}^r + f_{i,a}^b, \quad (\text{B.32})$$

with

$$f_{i,a}^r = 2 \sum_{k, r_{ik} \leq r_c} \frac{A_{ik} p_{ik}}{r_{oik} r_{ik}} (r_{i,a} - r_{k,a}) e^{-p_{ik} \left( \frac{r_{ik}}{r_{oik}} - 1 \right)}, \quad (\text{B.33})$$

and

$$f_{i,a}^b = - \sum_{k, r_{ik} \leq r_c} \frac{\xi_{ik}^2 q_{ik}}{r_{oik} r_{ik}} (r_{i,a} - r_{k,a}) [D(i) + D(k)] e^{-2q_{ik} \left( \frac{r_{ik}}{r_{oik}} - 1 \right)}, \quad (\text{B.34})$$

with  $D(i)$  given by

$$D(i)^{-1} = \sqrt{\sum_{j, r_{ij} \leq r_c} \xi_{ij}^2 e^{-2q_{ij} \left( \frac{r_{ij}}{r_{oij}} - 1 \right)}}. \quad (\text{B.35})$$

## Bibliography

- [1] Denis Uzio and Gilles Berhault. Factors governing the catalytic reactivity of metallic nanoparticles. *Catalysis Reviews*, 52(1):106–131, 2010.
- [2] Rongchao Jin. The impacts of nanotechnology on catalysis by precious metal nanoparticles. *Nanotechnology Reviews*, 1(1):31–56, 2012.
- [3] Vincenzo Amendola, Roberto Pilot, Marco Frasconi, Onofrio M Maragò, and Maria Antonia Iati. Surface plasmon resonance in gold nanoparticles: a review. *Journal of Physics: Condensed Matter*, 29(20):203002, apr 2017.
- [4] Natalie A. Frey, Sheng Peng, Kai Cheng, and Shouheng Sun. Magnetic nanoparticles: synthesis, functionalization, and applications in bioimaging and magnetic energy storage. *Chem. Soc. Rev.*, 38:2532–2542, 2009.
- [5] Kai Wu, Diqing Su, Jinming Liu, Renata Saha, and Jian-Ping Wang. Magnetic nanoparticles in nanomedicine: a review of recent advances. *Nanotechnology*, 30(50):502003, sep 2019.
- [6] Erik C. Dreaden, Alaaldin M. Alkilany, Xiaohua Huang, Catherine J. Murphy, and Mostafa A. El-Sayed. The golden age: gold nanoparticles for biomedicine. *Chem. Soc. Rev.*, 41:2740–2779, 2012.
- [7] A. L. González, Cecilia Noguez, J. Beránek, and A. S. Barnard. Size, shape, stability, and color of plasmonic silver nanoparticles. *The Journal of Physical Chemistry C*, 118(17):9128–9136, 2014.
- [8] Maria Losurdo, Maria M. Giangregorio, Giuseppe V. Bianco, Alexandra A. Suvorova, Charlie Kong, Sergey Rubanov, Pio Capezzuto, Josef Humlicek, and Giovanni Bruno. Size dependence of the dielectric function of silicon-supported plasmonic gold nanoparticles. *Phys. Rev. B*, 82:155451, Oct 2010.
- [9] Claire Deeb, Xuan Zhou, Jérôme Plain, Gary P. Wiederrecht, Renaud Bachelot, Milo Russell, and Prashant K. Jain. Size dependence of the plasmonic near-field measured via single-nanoparticle photoimaging. *The Journal of Physical Chemistry C*, 117(20):10669–10676, 2013.
- [10] K. Lance Kelly, Eduardo Coronado, Lin Lin Zhao, and George C. Schatz. The optical properties of metal nanoparticles: the influence of size, shape, and dielectric environment. *J. Phys. Chem. B*, 107:668–677, 2003.
- [11] Radha Narayanan and Mostafa A. El-Sayed. Catalysis with transition metal nanoparticles in colloidal solution: nanoparticle shape dependence and stability. *The Journal of Physical Chemistry B*, 109(26):12663–12676, 2005.

- [12] Simon Mostafa, Farzad Behafarid, Jason R. Croy, Luis K. Ono, Long Li, Judith C. Yang, Anatoly I. Frenkel, and Beatriz Roldan Cuenya. Shape-dependent catalytic properties of Pt nanoparticles. *Journal of the American Chemical Society*, 132(44):15714–15719, 2010.
- [13] R. Ferrando. *Structure and Properties of Nanoalloys*. Frontiers of Nanoscience, Volume 10. Elsevier, 2016.
- [14] F. Baletto and R. Ferrando. Structural properties of nanoclusters: Energetic, thermodynamic, and kinetic effects. *Rev. Mod. Phys.*, 77:371–423, 2005.
- [15] R. Ferrando, J. Jellinek, and R. L. Johnston. Nanoalloys: From theory to applications of alloy clusters and nanoparticles. *Chem. Rev. (Washington, DC)*, 108:845–910, 2008.
- [16] R. T. Johnson and R. D. Dragsdorf. The martensitic transformation in cobalt. *Journal of Applied Physics*, 38:618–626, 1967.
- [17] F. Baletto, R. Ferrando, A. Fortunelli, F. Montalenti, and C. Mottet. Crossover among structural motifs in transition and noble-metal clusters. *J. Chem. Phys.*, 116:3856, 2002.
- [18] S. Ino. Stability of multiply-twinned particles. *J. Phys. Soc. Jpn.*, 27:941–953, 1969.
- [19] A. Howie and L. D. Marks. Elastic strains and the energy balance for multiply twinned particles. *Phil. Mag. A*, 49:95–109, 1984.
- [20] A. L. Mackay. A dense non-crystallographic packing of equal spheres. *Acta Crystallogr.*, 15:916–918, 1962.
- [21] I. A. Harris, R. S. Kidwell, and J. A. Northby. Structure of charged argon clusters formed in a free jet expansion. *Phys. Rev. Lett.*, 53:2390, 1984.
- [22] D. Bochicchio and R. Ferrando. Size-dependent transition to high-symmetry chiral structures in AgCu, AgCo, AgNi, and AgAu nanoalloys. *Nano Lett.*, 10:4211–4216, 2010.
- [23] E. Aprà, F. Baletto, R. Ferrando, and A. Fortunelli. Amorphization mechanism of icosahedral metal nanoclusters. *Phys. Rev. Lett.*, 93:065502, 2004.
- [24] L. L. Wang and D. D. Johnson. Predicted trends of core-shell preferences for 132 late transition-metal binary-alloy nanoparticles. *J. Am. Chem. Soc.*, 131:14023–14029, 2009.
- [25] G. Rossi, A. Rapallo, C. Mottet, A. Fortunelli, F. Baletto, and R. Ferrando. Magic polyicosahedral core-shell clusters. *Phys. Rev. Lett.*, 93:105503, 2004.
- [26] D. Wang, H.L. Xin, R. Hovden, H. Wang, Y. Yu, D.A. Muller, F.J. DiSalvo, and H.D. Abruna. Structurally ordered intermetallic platinum–cobalt core-shell nanoparticles with enhanced activity and stability as oxygen reduction electrocatalysts. *Nature Mater.*, 12:81, 2013.
- [27] J. Pirart, A. Front, D. Rapetti, C. Andreazza-Vignolle, P. Andreazza, C. Mottet, and R. Ferrando. Reversed size-dependent stabilization of ordered nanophases. *Nature Communications*, 10:1982, 2019.
- [28] E. Panizon, D. Bochicchio, G. Rossi, and R. Ferrando. Tuning the structure of nanoparticles by small concentrations of impurities. *Chem. Mater.*, 26:3354–3356, 2014.
- [29] M. P. Allen and D. J. Tildesley. *Computer Simulation of Liquids*. Clarendon, Oxford, 1987.

- [30] D. Frenkel and B. Smit. *Understanding Molecular Simulation from Algorithms to Applications*. Academic Press, 2002.
- [31] R. M. Martin. *Electronic Structure - Basic Theory and Practical Methods*. Cambridge University Press, 2004.
- [32] E. Engel and R.M. Dreizler. *Density Functional Theory – An Advanced Course*. Springer-Verlag Berlin Heidelberg, 2011.
- [33] F. Cyrot-Lackmann and F. Ducastelle. Binding energies of transition-metal atoms adsorbed on a transition metal. *Phys. Rev. B*, 4:2406–2412, 1971.
- [34] R. P. Gupta. Lattice relaxation at a metal surface. *Phys. Rev. B*, 23:6265, 1981.
- [35] V. Rosato, M. Guillopé, and B. Legrand. Thermodynamical and structural properties of f.c.c. transition metals using a simple tight-binding model. *Phil. Mag. A*, 59:321, 1989.
- [36] D. Spanjaard and M.-C. Desjonqueres. *Concepts in surface physics, second edition*. Springer Verlag, 2002.
- [37] Daniele Rapetti. Master’s thesis, University of Genoa, 2017.
- [38] F. Cleri and V. Rosato. Tight-binding potentials for transition metals and alloys. *Phys. Rev. B*, 48:22, 1993.
- [39] M. J. López and J. Jellinek. On the problem of fitting many-body potentials. i. the minimal maximum error scheme and the paradigm of metal systems. *J. Chem. Phys.*, 110:8899–8911, 1999.
- [40] Juan-Pedro Palomares-Baez, Emanuele Panizon, and Riccardo Ferrando. Nanoscale effects on phase separation. *Nano Letters*, 17(9):5394–5401, 2017.
- [41] K. Laasonen, E. Panizon, D. Bochicchio, and R. Ferrando. Competition between icosahedral motifs in agcu, agni, and agco nanoalloys: A combined atomistic-dft study. *J. Phys. Chem. C*, 117:26405–26413, 2013.
- [42] E. Panizon and R. Ferrando. Strain-induced restructuring of the surface in core@shell nanoalloys. *Nanoscale*, 8:15911–15919, 2016.
- [43] Faye Pittaway, Lauro Oliver Paz-Borbón, Roy L. Johnston, Haydar Arslan, Riccardo Ferrando, Christine Mottet, Giovanni Barcaro, and Alessandro Fortunelli. Theoretical studies of palladium–gold nanoclusters: Pd–au clusters with up to 50 atoms. *The Journal of Physical Chemistry C*, 113(21):9141–9152, 2009.
- [44] J. P. K. Doye and D. J. Wales. Calculation of thermodynamic properties of small lennard-jones clusters incorporating anharmonicity. *J. Chem. Phys.*, 102:9659, 1995.
- [45] D. J. Wales. *Energy Landscapes*. Cambridge University Press, 2003.
- [46] D. J. Wales and J. P. K. Doye. Global optimization by basin-hopping and the lowest energy structures of lennard-jones clusters containing up to 110 atoms. *J. Phys. Chem. A*, 101:5111–5116, 1997.

- [47] Z. Li and H. A. Scheraga. Monte-carlo-minimization approach to the multiple-minima problem in protein folding. *Proc. Natl. Acad. Sci. U.S.A.*, 84:6611–6615, 1987.
- [48] J. P. K. Doye and D. J. Wales. Thermodynamics of global optimization. *Phys. Rev. Lett.*, 80:1357, 1998.
- [49] Richard H. Byrd, Peihuang Lu, Jorge Nocedal, and Ciyou Zhu. A limited memory algorithm for bound constrained optimization. *SIAM Journal on Scientific Computing*, 16(5):1190–1208, 1995.
- [50] G. Rossi and R. Ferrando. Searching for low-energy structures of nanoparticles: a comparison of different methods and algorithms. *J. Phys. Cond. Mat.*, 21:084208, 2009.
- [51] D. Bochicchio and R. Ferrando. Morphological instability of core-shell metallic nanoparticles. *Phys. Rev. B*, 87:165435, 2013.
- [52] D. Bochicchio, R. Ferrando, E. Panizon, R. Novakovic, and G. Rossi. Chemical ordering in magic-size ag–pd nanoparticles. *Phys. Chem. Chem. Phys.*, 16:26478–26484, 2014.
- [53] G. Rossi and R. Ferrando. Global optimization by excitable walkers. *Chem. Phys. Lett.*, 423:17–22, 2006.
- [54] Nicolas Combe, Pablo Jensen, and Alberto Pimpinelli. Changing shapes in the nanoworld. *Phys. Rev. Lett.*, 85:110–113, 2000.
- [55] F. Baletto, C. Mottet, and R. Ferrando. Reentrant morphology transition in the growth of free silver nanoclusters. *Phys. Rev. Lett.*, 84:5544–5547, 2000.
- [56] F. Baletto, C. Mottet, and R. Ferrando. Growth of three-shell onionlike bimetallic nanoparticles. *Phys. Rev. Lett.*, 90:135504, 2003.
- [57] F. Calvo, A. Fortunelli, F. Negreiros, and D. J. Wales. Communication: Kinetics of chemical ordering in ag–au and ag–ni nanoalloys. *J. Chem. Phys.*, 139:111102, 2013.
- [58] Diana Nelli and Riccardo Ferrando. Core-shell vs. multi-shell formation in nanoalloy evolution from disordered configurations. *Nanoscale*, 11:13040–13050, 2019.
- [59] Kevin Rossi, Luca Pavan, YeeYeen Soon, and Francesca Baletto. The effect of size and composition on structural transitions in monometallic nanoparticles. *Eur. Phys. J. B*, 91(33), 2018.
- [60] Xin Qi, Zihao Chen, Tianyu Yan, and Kristen A. Fichthorn. Growth mechanism of five-fold twinned ag nanowires from multiscale theory and simulations. *ACS Nano*, 13:4647–4656, 2019.
- [61] Lucas M. Farigliano, Marcos A. Villarreal, Ezequiel P. M. Leiva, and S. Alexis Paz. Thermodynamics of nanoparticle coalescence at different temperatures via well-tempered metadynamics. *The Journal of Physical Chemistry C*, 124(43):24009–24016, 2020.
- [62] Jonathan Amodeo, Fabio Pietrucci, and Julien Lam. Out-of-equilibrium polymorph selection in nanoparticle freezing. *The Journal of Physical Chemistry Letters*, 11(19):8060–8066, 2020.



- [63] Kristen A. Fichthorn, Zihao Chen, Zhifeng Chen, Robert M. Rioux, Myung Jun Kim, and Benjamin J. Wiley. Understanding the solution-phase growth of Cu and Ag nanowires and nanocubes from first principles. *Langmuir*, 37:4419–4431, 2021.
- [64] Hongcheng Peng, Weihong Qi, Siqi Li, and Wenhai Ji. Modeling the phase stability of Janus, core-shell, and alloyed Ag-Cu and Ag-Au nanoparticles. *J. Phys. Chem. C*, 119(4):2186–2195, 2015.
- [65] Kristen A. Fichthorn and Tianyu Yan. Shapes and shape transformations of solution-phase metal particles in the sub-nanometer to nanometer size range: Progress and challenges. *The Journal of Physical Chemistry C*, 125:3668–3679, 2021.
- [66] Arthur F. Voter, Francesco Montalenti, and Timothy C. Germann. Extending the time scale in atomistic simulation of materials. *Annual Rev. Mater. Res.*, 32:321–346, 2002.
- [67] Alessandro Laio and Michele Parrinello. Escaping free-energy minima. *Proceedings of the National Academy of Sciences*, 99(20):12562–12566, 2002.
- [68] Marcos A. Villarreal, Oscar A. Oviedo, and Ezequiel P. M. Leiva. A straightforward approach for the determination of the maximum time step for the simulation of nanometric metallic systems. *Journal of Chemical Theory and Computation*, 8(5):1744–1749, 2012.
- [69] F. Baletto, C. Mottet, and R. Ferrando. Molecular dynamics simulations of surface diffusion and growth on silver and gold clusters. *Surf. Sci.*, 446:31–45, 2000.
- [70] Alessandro Laio and Francesco L. Gervasio. Metadynamics: a method to simulate rare events and reconstruct the free energy in biophysics, chemistry and material science. *Rep. Progr. Phys.*, 71:126601, 2008.
- [71] Giovanni Bussi and Alessandro Laio. Using metadynamics to explore complex free-energy landscapes. *Nature Reviews Physics*, 2(4):200–212, Apr 2020.
- [72] L. Pavan, K. Rossi, and F. Baletto. Metallic nanoparticles meet metadynamics. *J. Chem. Phys.*, 143:184304, 2015.
- [73] Anna L. Gould, Kevin Rossi, C. Richard A. Catlow, Francesca Baletto, and Andrew J. Logsdail. Controlling structural transitions in AuAg nanoparticles through precise compositional design. *The Journal of Physical Chemistry Letters*, 7(21):4414–4419, 2016.
- [74] Kevin Rossi and Francesca Baletto. The effect of chemical ordering and lattice mismatch on structural transitions in phase segregating nanoalloys. *Phys. Chem. Chem. Phys.*, 19:11057–11063, 2017.
- [75] Yu Xia, Diana Nelli, Riccardo Ferrando, Jun Yuan, and Z. Y. Li. Shape control of size-selected naked platinum nanocrystals. *Nat. Commun.*, 12:3019, 2021.
- [76] Diana Nelli, Anjana Krishnadas, Riccardo Ferrando, and Chloé Minnai. One-step growth of core-shell (PtPd)@Pt and (PtPd)@Pd nanoparticles in the gas phase. *The Journal of Physical Chemistry C*, 124(26):14338–14349, 2020.
- [77] Hellmut Haberland, Martin Karrais, Martin Mall, and Yonca Thurner. Thin films from energetic cluster impact: A feasibility study. *J. Vac. Sci. Technol. A*, 10:3266–3271, 1992.

- [78] S. Pratontep, S. J. Carroll, C. Xirouchaki, M. Streun, and R. E. Palmer. Size-selected cluster beam source based on radio frequency magnetron plasma sputtering and gas condensation. *Rev. Sci. Instrum.*, 76:045103, 2005.
- [79] D. B. Williams and C. B. Carter. *Transmission Electron Microscopy: A Textbook for Materials Science*. Springer, Berlin, 2009.
- [80] J. Goldstein, Dale E. Newbury, David C. Joy, Charles E. Lyman, P. Echlin, E-Lifshin, L. Sawyer, and J. R. Michael. *Scanning Electron Microscopy and X-ray Microanalysis*. Springer Science + Business Media Inc., New York, 2003.
- [81] Sergio Mejía-Rosales, Arturo Ponce, and Miguel José-Yacamán. Experimental techniques for structural characterization, 2013. In *Nanoalloys - From fundamentals to emergent applications* Chapter 2, pages 113-145. Edited by F. Calvo. Elsevier, Amsterdam.
- [82] Yi Wang, Shuifen Xie, Jingyue Liu, Jinho Park, Cheng Zhi Huang, and Younan Xia. Shape-controlled synthesis of palladium nanocrystals: A mechanistic understanding of the evolution from octahedrons to tetrahedrons. *Nano Letters*, 13(5):2276–2281, 2013.
- [83] G. Wulff. Xxv. zur frage der geschwindigkeit des wachsthums und der auflösung der kristallflächen. *Z. Krist.*, 34(1):449–530, 1901.
- [84] L. D. Marks and L. Peng. Nanoparticle shape, thermodynamics and kinetics. *J. Phys. Condensed Matter*, 28:053001, 2016.
- [85] Marie Villarba and Hannes Jónsson. Diffusion mechanisms relevant to metal crystal growth: Pt/pt(111). *Surface Science*, 317(1):15–36, 1994.
- [86] Armin Götzhäuser and Gert Ehrlich. Atom movement and binding on surface clusters: Pt on pt(111) clusters. *Phys. Rev. Lett.*, 77:1334–1337, Aug 1996.
- [87] El yakout El koraychy, Diana Nelli, Cesare Roncaglia, Chloé Minnai, and Riccardo Ferrando. Growth of size-matched nanoalloys - a comparison of auag and ptpd. *submitted*.
- [88] John Perdew, Kieron Burke, and Matthias Ernzerhof. Generalized gradient approximation made simple. *Phys. Rev. Lett.*, 77:3865–3868, 1997.
- [89] John P. Perdew, Adrienn Ruzsinszky, Gábor I. Csonka, Oleg A. Vydrov, Gustavo E. Scuseria, Lucian A. Constantin, Xiaolan Zhou, and Kieron Burke. Restoring the density-gradient expansion for exchange in solids and surfaces. *Phys. Rev. Lett.*, 100:136406, 2008.
- [90] R.G. Parr and W. Yang. *Density-Functional Theory of Atoms and Molecules*. Oxford University Press, 1994.
- [91] P. Giannozzi, S. Baroni, N. Bonini, M. Calandra, R. Car, C. Cavazzoni, D. Ceresoli, G. L. Chiarotti, M. Cococcioni, I. Dabo, A. Dal Corso, S. de Gironcoli, S. Fabris, G. Fratesi, R. Gebauer, U. Gerstmann, C. Gougoussis, A. Kokalj, M. Lazzeri, L. Martin-Samos, N. Marzari, F. Mauri, R. Mazzarello, S. Paolini, A. Pasquarello, L. Paulatto, C. Sbraccia, S. Scandolo, G. Sclauzero, A. P. Seitsonen, A. Smogunov, P. Umari, and R. M. Wentzcovitch. Quantum espresso: a modular and open-source software project for quantum simulations of materials. *J. Phys. Condens. Matter*, 21:395502, 2009.

- [92] S. C. Wang and G. Ehrlich. Structure, stability, and surface diffusion of clusters: Irx on ir(111). *Surface Science*, 239(3):301–332, 1990.
- [93] El yakout El koraychy, Cesare Roncaglia, Diana Nelli, and Riccardo Ferrando. Growth mechanisms from tetrahedral seeds to multiply twinned au particles revealed by atomic level simulations. *submitted*.
- [94] H. Okamoto. Pd-pt (palladium-platinum). *J. Phase Equil.*, 12:617–618, 1991.
- [95] J. L. Rousset, A. J. Renouprez, and A. M. Cadrot. Ion-scattering study and monte carlo simulations of surface segregation in pd-pt nanoclusters obtained by laser vaporization of bulk alloys. *Phys. Rev. B*, 58:2150–2156, Jul 1998.
- [96] A. De Clercq, S. Giorgio, and C. Mottet. Pd surface and pt subsurface segregation in pt1-cPd nanoalloys. *Journal of Physics: Condensed Matter*, 28(6):064006, jan 2016.
- [97] Ting-Wei Liao, Anupam Yadav, Kuo-Juei Hu, Johan van der Tol, Salvatore Cosentino, Francesco D’Acapito, Richard E. Palmer, Cristina Lenardi, Riccardo Ferrando, Didier Grandjean, and Peter Lievens. Unravelling the nucleation mechanism of bimetallic nanoparticles with composition-tunable core-shell arrangement. *Nanoscale*, 10:6684–6694, 2018.
- [98] L. O. Paz-Borbón, A. Gupta, and R. L. Johnston. Dependence of the structures and chemical ordering of pd-pt nanoalloys on potential parameters. *J. Mater. Chem.*, 18:4154–4164, 2008.
- [99] Philipp Thaler, Alexander Volk, Daniel Knez, Florian Lackner, Georg Haberfehlner, Johannes Steurer, Martin Schnedlitz, and Wolfgang E. Ernst. Synthesis of nanoparticles in helium droplets—a characterization comparing mass-spectra and electron microscopy data. *The Journal of Chemical Physics*, 143(13):134201, 2015.
- [100] Tianlong Wen and Kannan M. Krishnan. Thermal stability and morphological transformations of aucore-coshell nanocrucibles. *J. Phys. Chem. C*, 114:14838–14842, 2010.
- [101] S. Liu, Z. Sun, Q. Liu, L. Wu, Y. Huang, T. Yao, J. Zhang, T. Hu, M. Ge, F. Hu, Z. Xie, G. Pan, and S. Wei. Unidirectional thermal diffusion in bimetallic cu@au nanoparticles. *ACS Nano*, 8:1886–1892, 2014.
- [102] A. Bruma and Z. Y. Li. Thermal induced structural transformation of bimetallic AuPd nanoparticles. *Journal of Physics: Conference Series*, 522:012079, jun 2014.
- [103] Miaofang Chi, Chao Wang, Yinkai Lei, Guofeng Wang, Dongguo Li, Karren L. More, Andrew Lupini, Lawrence F. Allard, Nenad M. Markovic, and Vojislav R. Stamenkovic. Surface faceting and elemental diffusion behaviour at atomic scale for alloy nanoparticles during *in situ* annealing. *Nature Communications*, 6:8925, 2015.
- [104] Cecile S. Bonifacio, Sophie Carenco, Cheng Hao Wu, Stephen D. House, Hendrik Bluhm, and Judith C. Yang. Thermal stability of core-shell nanoparticles: A combined *in situ* study by xps and tem. *Chemistry of Materials*, 27(20):6960–6968, 2015.
- [105] Maximilian Lasserus, Martin Schnedlitz, Daniel Knez, Roman Messner, Alexander Schiffmann, Florian Lackner, Andreas W. Hauser, Ferdinand Hofer, and Wolfgang E. Ernst. Thermally induced alloying processes in a bimetallic system at the nanoscale: Agau sub-5 nm core-shell particles studied at atomic resolution. *Nanoscale*, 10:2017–2024, 2018.

- [106] Min Tang, Beien Zhu, Jun Meng, Xun Zhang, Wentao Yuan, Ze Zhang, Yi Gao, and Yong Wang. Pd-pt nanoalloy transformation pathways at the atomic scale. *Materials Today Nano*, 1:41–46, 2018.
- [107] Martin Schnedlitz, Ricardo Fernandez-Perea, Daniel Knez, Maximilian Lasserus, Alexander Schiffmann, Ferdinand Hofer, Andreas W. Hauser, Maria Pilar de Lara-Castells, and Wolfgang E. Ernst. Effects of the core location on the structural stability of ni-au core-shell nanoparticles. *The Journal of Physical Chemistry C*, 123(32):20037–20043, 2019.
- [108] Zhemin Wu, Min Tang, Xiaoyan Li, Sai Luo, Wentao Yuan, Beien Zhu, Hui Zhang, Hangsheng Yang, Yi Gao, and Yong Wang. Surface faceting and compositional evolution of pd@au core-shell nanocrystals during in situ annealing. *Phys. Chem. Chem. Phys.*, 21:3134–3139, 2019.
- [109] Martin Schnedlitz, Daniel Knez, Maximilian Lasserus, Ferdinand Hofer, Ricardo Fernández-Perea, Andreas W. Hauser, María Pilar de Lara-Castells, and Wolfgang E. Ernst. Thermally induced diffusion and restructuring of iron triade (fe, co, ni) nanoparticles passivated by several layers of gold. *The Journal of Physical Chemistry C*, 124(30):16680–16688, 2020.
- [110] Fan Li, Yuan Zong, Yanling Ma, Mingxu Wang, Wen Shang, Peng Tao, Chengyi Song, Tao Deng, Hong Zhu, and Jianbo Wu. Atomistic imaging of competition between surface diffusion and phase transition during the intermetallic formation of faceted particles. *ACS Nano*, 15(3):5284–5293, 2021.
- [111] J. L. Rodríguez-López, J. M. Montejano-Carrizales, and M. José-Yacamán. Molecular dynamics study of bimetallic nanoparticles: the case of auxcuy alloy clusters. *Applied Surface Science*, 219(1):56–63, 2003.
- [112] J. M. Martínez De La Hoz, R. C. Tovar, and P. B. Balbuena. Size effect on the stability of cu-ag nanoalloys. *Mol. Sim.*, 35:785–794, 2009.
- [113] M. Chandross. Energetics of the formation of cu-ag core-shell nanoparticles. *Modelling Simul. Mater. Sci. Eng.*, 22:075012, 2014.
- [114] F. Berthier, A. Tadjine, and B. Legrand. Ageing of out-of-equilibrium nanoalloys by a kinetic mean-field approach. *Phys. Chem. Chem. Phys.*, 17:28193–28199, 2015.
- [115] H. Mori, M. Komatsu, K. Takeda, and H. Fujita. Spontaneous alloying of copper into gold atom clusters. *Philosophical Magazine Letters*, 63(3):173–178, 1991.
- [116] H. Yasuda and H. Mori. Spontaneous alloying of zinc atoms into gold clusters and formation of compound clusters. *Phys. Rev. Lett.*, 69:3747–3750, 1992.
- [117] H. Yasuda and H. Mori. Cluster-size dependence of alloying behavior in gold clusters. *Z. Phys. D: At. Mol. Clusters*, 31:131–134, 1994.
- [118] Y. Shimizu, S. Sawada, and K. S. Ikeda. Classical dynamical simulation of spontaneous alloying. *Eur. Phys. J. D*, 4:365–372, 1998.
- [119] Yasushi Shimizu, Kensuke S. Ikeda, and Shin-ichi Sawada. Spontaneous alloying in binary metal microclusters: A molecular dynamics study. *Phys. Rev. B*, 64:075412, Jul 2001.

- [120] F Delogu. The mechanism of chemical disordering in  $\text{Cu}_3\text{Au}$  nanometre-sized systems. *Nanotechnology*, 18(23):235706, may 2007.
- [121] T. Niiyama, S. Sawada, K. S. Ikeda, and Y. Shimizu. A numerical study upon the atomistic mechanisms of rapid diffusion in nanoclusters. *Chem. Phys. Lett.*, 503:252–255, 2011.
- [122] Tomohiro Shibata, Bruce A. Bunker, Zhenyuan Zhang, Dan Meisel, Charles F. Vardeman, and J. Daniel Gezelter. Size-dependent spontaneous alloying of  $\text{Au-Ag}$  nanoparticles. *Journal of the American Chemical Society*, 124(40):11989–11996, 2002.
- [123] Riccardo Ferrando. Mass transport in nanoalloys studied by atomistic models. *Diffusion Foundations*, 12:23–37, 11 2017.
- [124] Diana Nelli, Fabio Pietrucci, and Riccardo Ferrando. Impurity diffusion in magic-size icosahedral clusters. *The Journal of Chemical Physics*, 155(14):144304, 2021.
- [125] Nelli, Diana. Central vacancy creation in icosahedral nanoparticles induced by the displacement of large impurities. *Eur. Phys. J. Appl. Phys.*, 97:18, 2022.
- [126] C. Mottet, G. Tréglia, and B. Legrand. New magic numbers in metallic clusters: an unexpected metal dependence. *Surf. Sci.*, 383:L719–L727, 1997.
- [127] C. Mottet, G. Rossi, F. Baletto, and R. Ferrando. Single impurity effect on the melting of nanoclusters. *Phys. Rev. Lett.*, 95:035501, 2005.
- [128] V. Vitek and T. Egami. Atomic level stresses in solids and liquids. *Physica Status Solidi B*, 144:145–156, 1987.
- [129] R. Ferrando. Symmetry breaking and morphological instabilities in core-shell metallic nanoparticles. *J. Phys. Condens. Matter*, 27:013003, 2015.
- [130] Davide Branduardi, Francesco Luigi Gervasio, and Michele Parrinello. From a to b in free energy space. *The Journal of Chemical Physics*, 126(5):054103, 2007.
- [131] Grégoire A. Gallet and Fabio Pietrucci. Structural cluster analysis of chemical reactions in solution. *The Journal of Chemical Physics*, 139(7):074101, 2013.
- [132] S. Pipolo, M. Salanne, G. Ferlat, S. Klotz, A. M. Saitta, and F. Pietrucci. Navigating at will on the water phase diagram. *Phys. Rev. Lett.*, 119:245701, Dec 2017.
- [133] M. Fitzner, G. C. Sosso, F. Pietrucci, S. Pipolo, and A. Michaelides. Pre-critical fluctuations and what they disclose about heterogenous crystal nucleation. *Nature Communications*, 8:2257, 2017.
- [134] S. Schaack, Ph. Depondt, M. Moog, F. Pietrucci, and F. Finocchi. How methane hydrate recovers at very high pressure the hexagonal ice structure. *The Journal of Chemical Physics*, 152(2):024504, 2020.
- [135] Gareth A. Tribello, Massimiliano Bonomi, Davide Branduardi, Carlo Camilloni, and Giovanni Bussi. Plumed 2: New feathers for an old bird. *Computer Physics Communications*, 185(2):604–613, 2014.
- [136] L. L. Boyer and J. Q. Broughton. Statics and dynamics of icosahedrally twinned and single-crystal fcc clusters. *Phys. Rev. B*, 42:11461–11468, Dec 1990.

- [137] Sergei V. Krivov. Hierarchical global optimization of quasiseparable systems: Application to lennard-jones clusters. *Phys. Rev. E*, 66:025701, Aug 2002.
- [138] Xueguang Shao, Yuhong Xiang, and Wensheng Cai. Formation of the central vacancy in icosahedral lennard-jones clusters. *Chemical Physics*, 305(1):69–75, 2004.
- [139] Yuhong Xiang, Longjiu Cheng, Wensheng Cai, and Xueguang Shao. Structural distribution of lennard-jones clusters containing 562 to 1000 atoms. *The Journal of Physical Chemistry A*, 108(44):9516–9520, 2004.
- [140] N. T. Wilson and R.L. Johnston. Modelling gold clusters with an empirical many-body potential. *Eur. Phys. J. D*, 12(XXX):161–169, 2000.
- [141] Ali Sebetci and Ziya B Güvenç. Global minima of AlN, AuN and PtN,  $n \leq 80$ , clusters described by the voter–chen version of embedded-atom potentials. *Modelling and Simulation in Materials Science and Engineering*, 13(5):683–698, may 2005.
- [142] Lesley D. Lloyd, Roy L. Johnston, Christopher Roberts, and Thomas V. Mortimer-Jones. Geometry optimisation of aluminium clusters using a genetic algorithm. *ChemPhysChem*, 3(5):408–415, 2002.
- [143] Jan-Ole Joswig and Michael Springborg. Genetic-algorithms search for global minima of aluminum clusters using a sutton-chen potential. *Phys. Rev. B*, 68:085408, Aug 2003.
- [144] Jonathan P.K. Doye. Lead clusters: Different potentials, different structures. *Computational Materials Science*, 35(3):227–231, 2006.
- [145] Yanting Wang, S. Teitel, and Christoph Dellago. Melting and equilibrium shape of icosahedral gold nanoparticles. *Chemical Physics Letters*, 394(4):257–261, 2004.
- [146] Yanting Wang, S. Teitel, and Christoph Dellago. Melting of icosahedral gold nanoclusters from molecular dynamics simulations. *The Journal of Chemical Physics*, 122(21):214722, 2005.
- [147] Christian Leidlmair, Peter Bartl, Harald Schöbel, Stephan Denifl, Shengfu Yang, Andrew M. Ellis, and Paul Scheier. Ionization of methane clusters in helium nanodroplets. *ChemPhysChem*, 13(2):469–476, 2012.
- [148] Graeme Henkelman and Hannes Jónsson. Improved tangent estimate in the nudged elastic band method for finding minimum energy paths and saddle points. *J. Chem. Phys.*, 113:9978, 2000.
- [149] H. Okamoto, T. B. Massalski, T. Nishizawa, and M. Hasebe. The au-co (gold-cobalt) system. *Bulletin of Alloy Phase Diagrams*, 6(5):449–454, 1985.
- [150] A. Nash and P. Nash. The ag-ni (silver-nickel) system. *Bull. Alloy Phase Diagrams*, 8:119–121, 1987.
- [151] P. R. Subramanian and J. H. Perepezko. The ag-cu (silver-copper) system. *Journal of Phase Equilibria*, 14(1):62–75, Feb 1993.

- [152] V. Dupuis, A. Hillion, A. Robert, O. Loiselet, G. Khadra, P. Capiod, C. Albin, O. Boisron, D. Le Roy, L. Bardotti, F. Tournus, and A. Tamion. Bottom-up strategies for the assembling of magnetic systems using nanoclusters. *Journal of Nanoparticle Research*, 20(5):128, May 2018.
- [153] Y.-H. Xu and J.-P. Wang. Direct gas-phase synthesis of heterostructured nanoparticles through phase separation and surface segregation. *Adv. Mater.*, 20:994, 2008.
- [154] D. Wang and Y. Li. One-pot protocol for au-based hybrid magnetic nanostructures via a noble-metal-induced reduction process. *J. Am. Chem. Soc.*, 132:6280, 2012.
- [155] Alvaro Mayoral, Daniel Llamasa, and Yves Huttel. A novel co@au structure formed in bimetallic core@shell nanoparticles. *Chem. Commun.*, 51:8442–8445, 2015.
- [156] V. Dupuis, G. Khadra, A. Hillion, A. Tamion, J. Tuaille-Combes, L. Bardotti, and F. Tournus. Intrinsic magnetic properties of bimetallic nanoparticles elaborated by cluster beam deposition. *Phys. Chem. Chem. Phys.*, 17:27996–28004, 2015.
- [157] A. Rapallo, J. A. Olmos-Asar, O. A. Oviedo, M. Luduena, R. Ferrando, and M. M. Mariscal. Thermal properties of co/au nanoalloys and comparison of different computer simulation techniques. *J. Phys. Chem. C*, 116:17210–17218, 2012.
- [158] H. Portales, L. Saviot, E. Duval, M. Gaudry, E. Cottancin, M. Pellarin, J. Lermé and M. Broyer. Resonant raman scattering by quadrupolar vibrations of ni-ag core-shell nanoparticles. *Phys. Rev. B*, 65:165422, 2002.
- [159] Y. Mahara, H. Ishikawa, J. Ohyama, K. Sawabe, Y. Yamamoto, S. Arai, and A. Satsuma. Enhanced co oxidation activity of ni@ag core-shell nanoparticles. *Chem. Lett.*, 43:910–912, 2014.
- [160] M. Molayem, V. G. Grigoryan, and M. Springborg. Theoretical determination of the most stable structures of nimag bimetallic nanoalloys. *J. Phys. Chem. C*, 115:7179–7192, 2011.
- [161] C. Langlois, D. Alloyeau, Y. Le Bouar, A. Loiseau, T. Oikawa, C. Mottet, and C. Ricolleau. Growth and structural properties of cuag and copt bimetallic nanoparticles. *Faraday Disc.*, 138:375–391, 2008.
- [162] C. Langlois, Z. Y. Li, J. Yuan, D. Alloyeau, J. Nelayah, D. Bochicchio, R. Ferrando, and C. Ricolleau. Transition from core-shell to janus chemical configuration for bimetallic nanoparticles. *Nanoscale*, 4:3381–3388, 2012.
- [163] M. Tchapyguine, T. Andersson, Ch. Zhang, and O. Björneholm. Core-shell structure disclosed in self-assembled cu-ag nanoalloy particles. *J. Chem. Phys.*, 138:104303, 2013.
- [164] F. Baletto, C. Mottet, and R. Ferrando. Growth simulations of silver shells on copper and palladium nanoclusters. *Phys. Rev. B*, 66:155420, 2002.
- [165] M. Molayem, V. G. Grigoryan, and M. Springborg. Global minimum structures and magic clusters of cu<sub>m</sub> ag<sub>n</sub> nanoalloys. *J. Phys. Chem. C*, 115:22148–22162, 2011.
- [166] P. Lu, M. Chandross, T. J. Boyle, B. G. Clark, and P. Vianco. Equilibrium cu-ag nanoalloy structure formation revealed by in situ scanning transmission electron microscopy heating experiments. *APL Mater.*, 2:022107, 2014.

- [167] F. Lequien, J. Creuze, F. Berthier, I. Braems, and B. Legrand. Superficial segregation, wetting, and dynamical equilibrium in bimetallic clusters: A monte carlo study. *Phys. Rev. B*, 78:075414, 2008.
- [168] S. Nunez and R. L. Johnston. Structures and chemical ordering of small cu-ag clusters. *J. Phys. Chem. C*, 114:13255–13266, 2010.
- [169] Panagiotis Grammatikopoulos, Joseph Kioseoglou, Antony Galea, Jerome Vernieres, Maria Benelmekki, Rosa E. Diaz, and Mukhles Sowwan. Kinetic trapping through coalescence and the formation of patterned ag-cu nanoparticles. *Nanoscale*, 8:9780–9790, 2016.
- [170] J. Magnus Rahm and Paul Erhart. Understanding chemical ordering in bimetallic nanoparticles from atomic-scale simulations: The competition between bulk, surface, and strain. *The Journal of Physical Chemistry C*, 122(49):28439–28445, 2018.
- [171] F. Baletto, A. Rapallo, G. Rossi, and R. Ferrando. Dynamical effects in the formation of magic cluster structures. *Phys. Rev. B*, 69:235421, 2004.
- [172] H. L. Skriver and N. M. Rosengaard. Surface energy and work function of elemental metals. *Phys. Rev. B*, 46:7157–7168, 1992.
- [173] C.E. Blackmore, N.V. Rees, and R.E. Palmer. Modular construction of size-selected multiple-core pt-tio<sub>2</sub> nanoclusters for electro-catalysis. *Phys. Chem. Chem. Phys.*, 17:28005–28009, 2015.
- [174] M. M. Mariscal, S. A. Dassie, and E. P. M. Leiva. Collision as a way of forming bimetallic nanoclusters of various structures and chemical compositions. *J. Chem. Phys.*, 123:184505, 2005.
- [175] S. A. Paz, E. P. M. Leiva, J. Jellinek, and M. M. Mariscal. Properties of rotating nanoalloys formed by cluster collision: A computer simulation study. *J. Chem. Phys.*, 134:094701, 2012.
- [176] Panagiotis Grammatikopoulos, Mukhles Sowwan, and Joseph Kioseoglou. Computational modeling of nanoparticle coalescence. *Advanced Theory and Simulations*, 2:1900013, 2019.
- [177] Huilong Zhu. Sintering processes of two nanoparticles: A study by molecular dynamics simulations. *Philosophical Magazine Letters*, 73(1):27–33, 1996.
- [178] Laurent J. Lewis, Pablo Jensen, and Jean-Louis Barrat. Melting, freezing, and coalescence of gold nanoclusters. *Phys. Rev. B*, 56:2248–2257, 1997.
- [179] S Arcidiacono, N.R Bieri, D Poulidakos, and C.P Grigoropoulos. On the coalescence of gold nanoparticles. *International Journal of Multiphase Flow*, 30(7):979 – 994, 2004. A Collection of Papers in Honor of Professor G. Yadigaroglu on the Occasion of his 65th Birthday.
- [180] J. Rogan, R. Ramírez, A. H. Romero, and M. Kiwi. Rearrangement collisions between gold clusters. *The European Physical Journal D - Atomic, Molecular, Optical and Plasma Physics*, 28:219–228, 2004.
- [181] G. Bilalbegovic. Assemblies of gold icosahedra. *Computational Materials Science*, 31(1):181 – 186, 2004.



- [182] Denitsa Alamanova, Valeri G Grigoryan, and Michael Springborg. Formation of stable products from cluster–cluster collisions. *Journal of Physics: Condensed Matter*, 19(34):346204, 2007.
- [183] Teck H. Lim, David McCarthy, Shaun C. Hendy, Kevin J. Stevens, Simon A. Brown, and Richard D. Tilley. Real-time tem and kinetic monte carlo studies of the coalescence of decahedral gold nanoparticles. *ACS Nano*, 3(11):3809–3813, 2009.
- [184] Panagiotis Grammatikopoulos, Cathal Cassidy, Vidyadhar Singh, and Mukhles Sowwan. Coalescence-induced crystallisation wave in pd nanoparticles. *Scientific Reports*, 4:5779, 2014.
- [185] Kayoung Yun, Jaegab Lee, and Ho-Seok Nam. Effect of temperature on coalescence behavior of unsupported gold nanoparticles. *Electronic Materials Letters*, Aug 2018.
- [186] H. Y. Kim, S. H. Lee, H. G. Kim, J. H. Ryu, and H. M. Lee. Molecular dynamic simulation of coalescence between silver and palladium clusters. *Mater. Trans.*, 48:455–459, 2007.
- [187] Diana Nelli, Giulia Rossi, Zhiwei Wang, Richard E Palmer, and Riccardo Ferrando. Structure and orientation effects in the coalescence of au clusters. *Nanoscale*, 12(14):7688–7699, 2020.
- [188] Charles L. Cleveland, Uzi Landman, Thomas G. Schaaff, Marat N. Shafigullin, Peter W. Stephens, and Robert L. Whetten. Structural evolution of smaller gold nanocrystals: The truncated decahedral motif. *Phys. Rev. Lett.*, 79:1873–1876, 1997.
- [189] Kenji Koga. Novel bidecahedral morphology in gold nanoparticles frozen from liquid. *Phys. Rev. Lett.*, 96:115501, 2006.
- [190] G. Rossi and R. Ferrando. Freezing of gold nanoclusters into poly-decahedral structures. *Nanotechnology*, 18:225706, 2007.
- [191] Dongsheng Li, Michael H. Nielsen, Jonathan R. I. Lee, Cathrine Frandsen, Jillian F. Banfield, and James J. De Yoreo. Direction-specific interactions control crystal growth by oriented attachment. *Science*, 336(6084):1014–1018, 2012.
- [192] D.M. Foster, Th. Pavloudis, J. Kioseoglou, and R.E. Palmer. Atomic-resolution imaging of surface and core melting in individual size-selected au nanoclusters on carbon. *Nature Communications*, 10:2583, 2019.
- [193] F. A. Nichols and W. W. Mullins. Morphological changes of a surface of revolution due to capillarity-induced surface diffusion. *Journal of Applied Physics*, 36(6):1826–1835, 1965.
- [194] G. Caratti, R. Ferrando, R. Spadacini, and G. E. Tommei. Noise-activated diffusion in the egg-carton potential. *Phys. Rev. E*, 54:4708–4721, 1996.
- [195] Diana Nelli, Manuella Cerbelaud, Riccardo Ferrando, and Chloé Minnai. Tuning the coalescence degree in the growth of pt–pd nanoalloys. *Nanoscale Adv.*, 3:836–846, 2021.
- [196] Diana Nelli, Cesare Roncaglia, Riccardo Ferrando, and Chloé Minnai. Shape changes in aupd alloy nanoparticles controlled by anisotropic surface stress relaxation. *The Journal of Physical Chemistry Letters*, 12(XXX):4609–4615, 2021.

- [197] Simon R Plant, Lu Cao, and Richard E Palmer. Atomic structure control of size-selected gold nanoclusters during formation. *Journal of the American Chemical Society*, 136(21):7559–7562, 2014.
- [198] H. Okamoto and T. B. Massalski. The au–pd (gold-palladium) system. *Bull. Alloy Phase Diagrams*, 6:229–235, 1985.
- [199] Sergey M. Kozlov, Gábor Kovács, Riccardo Ferrando, and Konstantin M. Neyman. How to determine accurate chemical ordering in several nanometer large bimetallic crystallites from electronic structure calculations. *Chem. Sci.*, 6:3868–3880, 2015.
- [200] Gábor Kovács, Sergey M. Kozlov, and Konstantin M. Neyman. Versatile optimization of chemical ordering in bimetallic nanoparticles. *The Journal of Physical Chemistry C*, 121(20):10803–10808, 2017.
- [201] Haijun Zhang, Tatsuya Watanabe, Mitsutaka Okumura, Masatake Haruta, and Naoki Toshima. Catalytically highly active top gold atom on palladium nanocluster. *Nature Materials*, 11(1):49–52, Jan 2012.
- [202] J. P. K. Doye and F. Calvo. Entropic effects on the size dependence of cluster structure. *Phys. Rev. Lett.*, 86:3570–3573, 2001.
- [203] Dawn M. Wells, Giulia Rossi, Riccardo Ferrando, and Richard E. Palmer. Metastability of the atomic structures of size-selected gold nanoparticles. *Nanoscale*, 7:6498–6504, 2015.
- [204] A. Rapallo, G. Rossi, R. Ferrando, A. Fortunelli, B. C. Curley, L. D. Lloyd, G. M. Tarbuck, and R. L. Johnston. Global optimization of bimetallic cluster structures. i. size-mismatched ag-cu, ag-ni, and au-cu systems. *J. Chem. Phys.*, 122:194308, 2005.
- [205] Z. Kuntová, G. Rossi, and R. Ferrando. Melting of core-shell ag-ni and ag-co nanoclusters studied via molecular dynamics simulations. *Phys. Rev. B*, 77:205431, 2008.
- [206] D. Bochicchio, F. Negro, and R. Ferrando. Competition between structural motifs in gold-platinum nanoalloys. *Comput. Theor. Chem.*, 1021:177, 2013.
- [207] Giulia Rossi and Riccardo Ferrando. Combining shape-changing with exchange moves in the optimization of nanoalloys. *Computational and Theoretical Chemistry*, 1107:66 – 73, 2017.